The Evolution of Upper Ocean Thermal Structure at 10°N, 125°W during 1997-1998

by

J. Thomas Farrar

Submitted to the MIT/WHOI Joint Program in Physical Oceanography
in partial fulfillment of the requirements for the degree of

Master of Science

at the

MASSACHUSETTS INSTITUTE OF TECHNOLOGY

September 2003

Author .....
MIT/WHOI Joint Program in Physical Oceanography
August 8, 2003

Certified by .....
Robert Weller
Senior Scientist, Woods Hole Oceanographic Institution
Thesis Supervisor

Accepted by .....
Carl Wunsch
Chairman, Joint Committee for Physical Oceanography

The Evolution of Upper Ocean Thermal Structure at 10°N, 125°W during 1997-1998

by

J. Thomas Farrar

Submitted to the MIT/WHOI Joint Program in Physical Oceanography
on August 8, 2003, in partial fulfillment of the
requirements for the degree of
Master of Science

Abstract

In this thesis I have endeavored to determine the factors and physical processes that controlled SST and thermocline depth at 10°N, 125°W during the Pan American Climate Study (PACS) field program. Analysis based on the PACS data set, TOPEX/Poseidon sea surface height data, European Remote Sensing satellite wind data, and model simulations and experiments reveals that the dominant mechanisms affecting the thermocline depth and SST at the mooring site during the measurement period were local surface fluxes, Ekman pumping, and vertical mixing associated with enhancement of the vertical shear by strong near-inertial waves in the upper ocean superimposed upon intra-seasonal baroclinic Rossby waves and the large scale zonal flow.

Thesis Supervisor: Robert Weller
Title: Senior Scientist, Woods Hole Oceanographic Institution

Acknowledgments

Most importantly, I would like to express my thanks to my wife, Shelly. Without her support, patience, and good humor, I might have produced a much weaker thesis.

I owe special thanks to my advisor, Bob Weller. Besides granting me, a graduate student, access to a phenomenal data set, Bob has provided excellent guidance and support. I am grateful to be able to learn from someone who is such a fine scientist and a good guy.

I did not take part in the collection of the mooring data (and had only a minor role in processing), and I am indebted to Weller and the members of the Upper Ocean Processes (UOP) group group whose committment to collection of high quality data is a valuable service to oceanography, meteorology, and society at large. All told, the mooring cruises required the efforts of 28 scientific crew and the ship's crew of three vessels. B.S. Way and W.M. Ostrom participated in all three cruises. Many others participated from shore in the preparation of instrumentation for the ships and moorings and in the data processing and compilation of data reports. The importance of these contributions to the present study cannot be overstated. The present study would not be possible without the scientific and managerial skill of chief scientists R. Weller and S. Anderson, the concerted effort of the members of the WHOI UOP group, and the generous funding provided by the National Oceanic and Atmospheric Administration (NOAA).

Finally, I would like to thank my parents, both of whom have done a great deal to instill in me the qualities that have allowed me to complete this thesis. My mother, Ann, has greatly contributed to my academic development. My father, John, has given me a love of science, from chemistry to astronomy to debugging automotive electrical systems. Moreover, both had an instrumental role in helping me to realize that, despite the fact that almost everyone in my hometown works in a plastics factory, I have plenty of alternative options for employment. I am thrilled to have stumbled into the exciting and stimulating field of physical oceanography.

This work was funded under NOAA Grant NA17RJ1223 and I also gratefully

acknowledge receipt of an MIT Presidential Fellowship in 2000-2001.

Contents

Chapter 1

Introduction

In this thesis I have endeavored to determine the factors and physical processes that controlled SST and thermocline depth at 10°N, 125°W during the Pan American Climate Study (PACS) field program. Analysis based on the PACS data set, TOPEX/Poseidon sea surface height data, European Remote Sensing satellite wind data, and model simulations and experiments reveals that the dominant mechanisms affecting the thermocline depth and SST at the mooring site during the measurement period were local surface fluxes, Ekman pumping, and vertical mixing associated with enhancement of the vertical shear by first mode baroclinic intraseasonal Rossby waves and strong near-inertial waves in the upper ocean.

Although this thesis will utilize a variety of data sets, this study relies heavily on the high quality mooring-based upper ocean and surface meteorology data set collected as part of the Pan American Climate Study (PACS) during 1997 and 1998 in the eastern tropical Pacific Ocean. With temporal resolution of 15 minutes or better, state-of-the-art meteorological packages on the mooring provided the first accurate time series of air-sea fluxes of freshwater, heat, and momentum from the region, and closely spaced temperature, salinity, and velocity measurements on the upper 200 m of the mooring provided the most detailed record of the variability of the upper ocean from the region to date. Additional data sets utilized in this thesis are the gridded TOPEX/Poseidon sea surface height anomaly and European Remote Sensing scatterometer wind fields distributed through the World Ocean Circulation

Experiment (WOCE) program. We also make use of the extensive data set provided by the Tropical Atmosphere Ocean (TAO) mooring array (McPhaden et al., 1998).

This chapter is organized as follows. Section 1.1 introduces the PACS mooring program. Section 1.2 reviews the climatology of the eastern tropical Pacific and discuss the motivation for the PACS program. Section 1.3 provides an overview of the eastern tropical Pacific during the 1997-1998 El Niño/La Niña event. Section 1.4 discusses some aspects of our current understanding of the role of off-equatorial variability in El Niño and La Niña. The chapter concludes with a brief summary of the thesis and a statement of objectives.

1.1 The Pan American Climate Study

The overarching goal of PACS is to gain understanding of the relationship between sea surface temperature variability in the tropical oceans and the climate of the American continents in order to improve the skill of seasonal to interannual climate forecasts. Sea surface temperature (SST) in the eastern tropical Pacific Ocean is believed to exert a profound influence on the weather and climate of North and South America (Ropelewski and Halpert, 1986, 1989, 1996; Livezey et al., 1997; Livezey and Smith, 1999; Magaña et al., 1999; Pielke and Lansea, 1999; Smith and O'Brien, 2001). Furthermore, tropical Pacific SST is thought to be an important factor in global climate anomalies (Cane, 1998; Shukla, 1998). Pacific SST is believed to determine the strength and location of the Inter-Tropical Convergence Zone (ITCZ), which may in turn influence the jet stream, storm activity, and precipitation over North America (Montroy, 1997). Mechanisms of coupling between the ITCZ and the underlying ocean have been discussed by numerous investigators (e.g. Emanuel, 1987; Neelin et al., 1987; Mitchell and Wallace, 1992; Chang and Philander, 1994), but the details of this coupling are not well understood (Li, 1997).

The primary goal of the PACS mooring deployment was to improve our understanding of the processes that govern the evolution of sea surface temperature in the eastern tropical Pacific Ocean. A thorough understanding of the processes governing

SST evolution in the region requires an account of how the seasonal cycle of radiation, evaporation, and precipitation is modulated by the annual migration of the ITCZ and how these dependencies may change during ENSO[1] events. There is substantial debate over the extent to which higher frequency meteorological forcing can influence the onset, strength, and duration of ENSO events. In addition, we require quantitative estimates of the relative roles of local surface heat flux, freshwater flux, turbulent heat flux, and advection in determining SST and thermocline depth.

As part of the PACS field program, two moorings were deployed in the eastern tropical Pacific from May, 1997 to September, 1998. One was placed at 10°N in the eastern Pacific warm pool, near the northernmost climatological location of the ITCZ. The other mooring was placed at 3°S in the Equatorial Cold Tongue. The field program was designed to gather data with which to study the seasonal cycle in these two contrasting regimes. This thesis will address the measurements made at 10°N; the measurements from 3°S will be addressed elsewhere. The largest El Niño event on record occurred while the moorings were deployed, and the mooring records constitute the first in-situ time series of air-sea fluxes of heat, freshwater, and momentum during from the region such an event. In addition, the mooring time series have very high vertical and temporal resolution of upper ocean temperature, salinity, and velocity. So, the mooring records provide a unique opportunity to examine air-sea interaction and other processes that govern the evolution of the upper ocean during an ENSO event.

1.2 Climatology of the Eastern Tropical Pacific

The SST field of the eastern tropical Pacific typically exhibits a strong meridional asymmetry with large seasonal and interannual variability. The climatological seasonal cycle of SST is illustrated in figure 1-1 (Levitus and Boyer, 1994). Sea surface temperatures are much cooler in the eastern than western Pacific, except for a band

[1]ENSO stands for El Niño and the Southern Oscillation and is used here to refer to El Niño and related phenomena such as La Niña.

of warm water that spans the Pacific north of the equator. In the eastern Pacific, this warm water extends westward from the coast of Central America, and is referred to as the eastern Pacific warm pool. The warm pool roughly coincides with the location of the eastward-flowing North Equatorial Counter-Current (NECC). The ITCZ is a persistent feature in the eastern tropical Pacific, found over the warm pool. This is not surprising because large scale deep convection usually occurs over water exceeding 27.5°C (Graham and Barnett, 1987). The ITCZ and warm pool move north and south annually between 2 and 12°N, reaching a northernmost point late in the boreal summer. In contrast to the eastern Pacific warm pool, the Equatorial Cold Tongue (ECT) is a prominent feature found just south of the equator from May to September. Note that the ECT, the eastern Pacific warm pool, and the sharp front at their interface are blurred and obscured by the spatial and temporal smoothing involved in the computation of the climatology shown in figure 1-1.

Seasonal changes in the distribution and strength of the equatorial current system, ocean thermal structure, surface winds, the ITCZ, and other meteorological parameters occur in concert. Convection in the ITCZ is fueled by the convergence of the northeast and southeast trade winds over areas of high SST. The northeast trades are strongest during the northern hemisphere winter when the ITCZ is farthest south, while the southeast trades are strongest during the summer. From February to April, the ITCZ is at its southernmost point near the equator, the southeast trades are weak, and the northeast trades are strong (Wyrtki, 1974). The strong northeast trades induce northward Ekman transport north of the ITCZ; convergence and divergence of the Ekman transport produces a trough in the thermocline near 10°N and a ridge in the thermocline near 3°N. From May to July, the ITCZ is moving northward as the the northeast trades weaken and the southeast trades strengthen. During this time, the strengthening southeast trades lead to upwelling off of the South American coast and the formation of the ECT, which persists until September or October. In August-October, the ITCZ is near its northernmost latitude (10-12°N), the northeast trades are weak, and the southeast trades are strong. The strong southeast trades promote upwelling near the equator, contributing to the intensification of the South

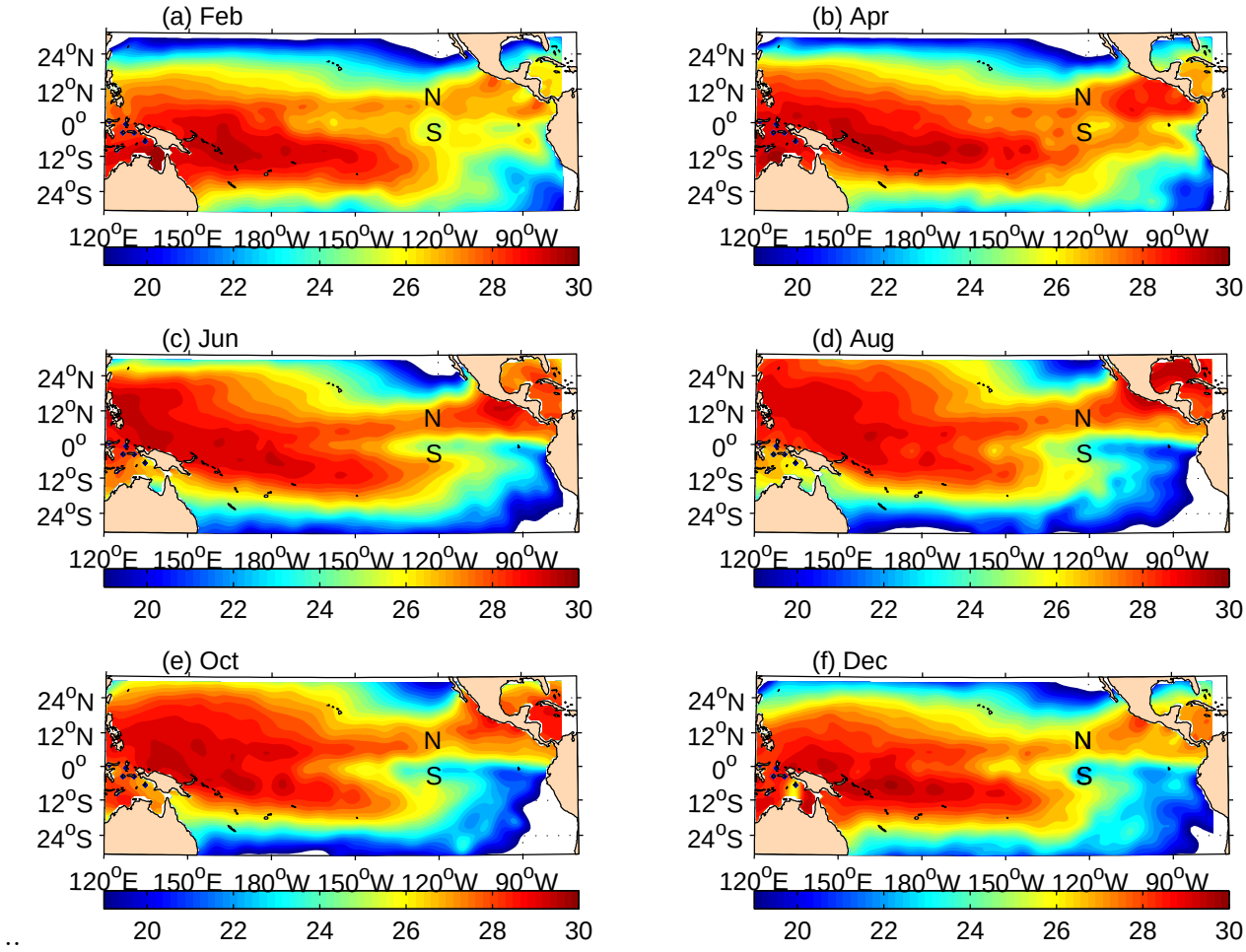

..

Figure 1-1: Levitus SST climatology for the tropical Pacific. The color scale ranges from 19 to 30°C. The PACS mooring locations are marked 'N' and 'S'.

Equatorial Current (SEC). At the same time, the wind stress curl of the ITCZ/trade wind system also causes a thermocline ridge near 10°N, intensifying the NEC and NECC. From November to January, the ITCZ moves southward as the northeast trades strengthen and the southeast trades weaken to begin the cycle again.

While there is apparent coupling of SST, the trade winds, the ITCZ, the eastern Pacific warm pool, and the equatorial cold tongue, many of the details of this coupling are not known. Dynamic coupling of the ocean and atmosphere is generally due to air-sea fluxes of heat, freshwater, and momentum. However, there are a number of unanswered questions about how the ITCZ modulates these fluxes on time scales ranging from diurnal to interannual and what role these modulations may play in air-sea interaction. Contrary to the mental picture of the ITCZ that we may form based on climatologies, the ITCZ is not a solid band of cloud cover that stretches across the Pacific. Rather, it is a region where convection is likely to occur, where convection is modulated by diurnal heat fluxes, westward propagating easterly waves, the Madden-Julian Oscillation, and atmospheric Rossby waves propagating from mid-latitudes (Gray and Jacobson, 1977; Gu and Zhang, 2002; Kiladis and Weickmann, 1992a, b; Kiladis, 1998). While it is believed that the annual migration of the ITCZ modulates air-sea fluxes in the eastern tropical Pacific, the manner in which the surface forcing varies inside and outside of the ITCZ is not well known.

The PACS mooring program was undertaken to provide accurate and concurrent time series of air-sea fluxes and upper ocean behavior in two contrasting regions of the eastern tropical Pacific that are thought to be important to large scale weather and climate patterns. Both moorings augment the TAO array along 125°W. One mooring was placed at 10°N in the eastern Pacific warm pool near the northernmost climatological location of the ITCZ. The other mooring was placed at 3°S where the equatorial cold tongue appears annually.

1.3 Overview of the Tropical Pacific in 1997-1998

The strongest ENSO event on record occurred during 1997 and 1998 while the PACS moorings were deployed (e.g. McPhaden, 1999a, b). As measured by the Southern Oscillation Index (SOI), the El Niño warm event of 1997 reached full strength around December, 1997, and the event abruptly terminated by mid-May, 1998. Figure 1-2 shows an SST time series from a TAO buoy in the eastern equatorial Pacific which graphically illustrates the anomalous character of the El Niño episode; SST in the eastern equatorial Pacific was exceptionally high between May, 1997 and May, 1998. By May, 1997 the the trade winds in the western equatorial Pacific had weakened and the El Niño event was beginning to develop; corresponding to the weakening trades, the Walker circulation shifted eastward toward the dateline (Wang and Weisberg, 2000). So, the PACS moorings were deployed just as the El Niño event was beginning to unfold.

Within a few months of the mooring deployment (i.e. May to July, 1997), SST had become anomalously high in the eastern equatorial Pacific and westerly wind anomalies had progressed as far eastward as 120°W (Wang and Weisberg, 2000; Kessler, 2001). The westerly wind anomalies at the equator were accompanied by northerly anomalies north of the equator, extending to about 14°N (Wang and Weisberg, 2000). Coincident with the warm SSTs and weakened trades, the ITCZ had developed an unusually large meridional span and was found farther south than usual. By late 1997 and early 1998, sea surface temperature anomalies in the eastern equatorial Pacific were near maximum levels and the equatorial westerly wind anomalies were beginning to weaken and move southward (McPhaden, 1999; Wang and Weisberg, 2000). This southward movement of the equatorial westerly wind anomalies was accompanied by a southward movement of the northerly anomalies found north of the equator. During the spring of 1998, the El Niño event began its decay as the westerly anomalies shifted south of the equator (bringing the equatorial zonal wind to near normal strength) and the cold tongue emerged once again in the eastern Pacific in May, 1998.

Figure 1-3 shows the SST field at various times during 1997 and 1998. The

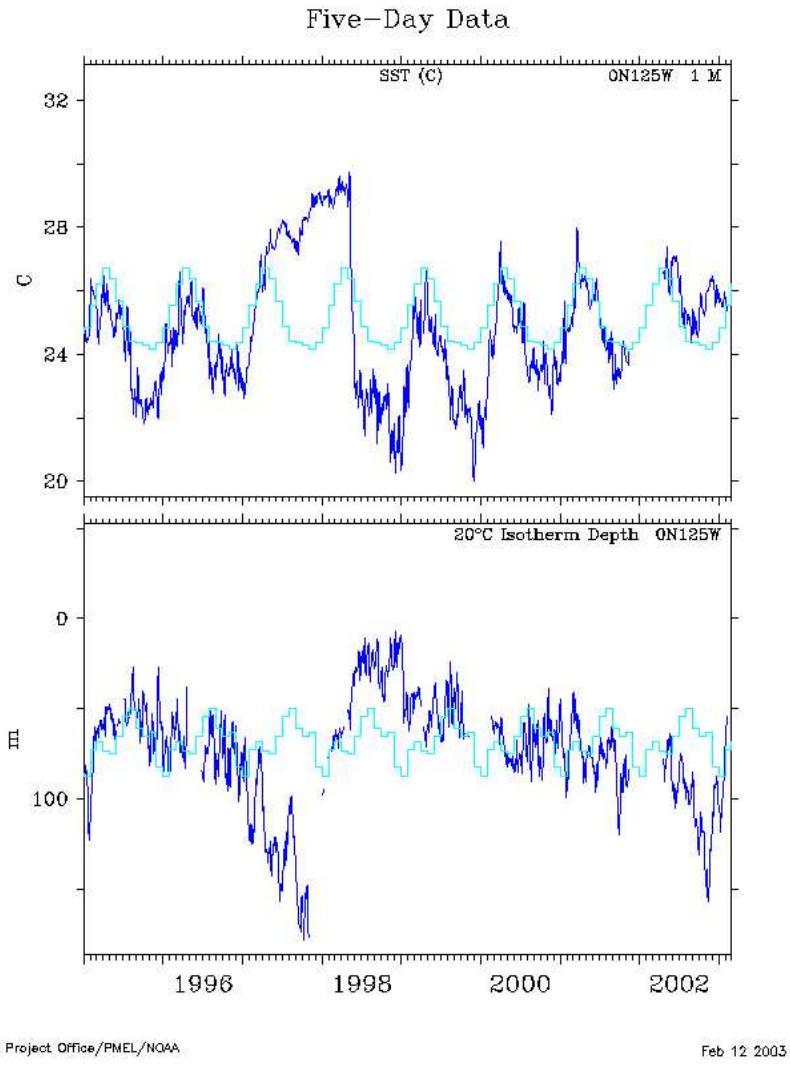

Figure 1-2: SST (top panel) and 20°C isotherm depth (bottom panel) at the TAO buoy at 0°N, 125°W in the eastern equatorial Pacific. The turquoise lines show the climatological seasonal cycle at the site. Note that the relatively weak El Niño event of 2002 is also evident. (Adapted from McPhaden (1999); plot courtesy of TAO/PMEL.)

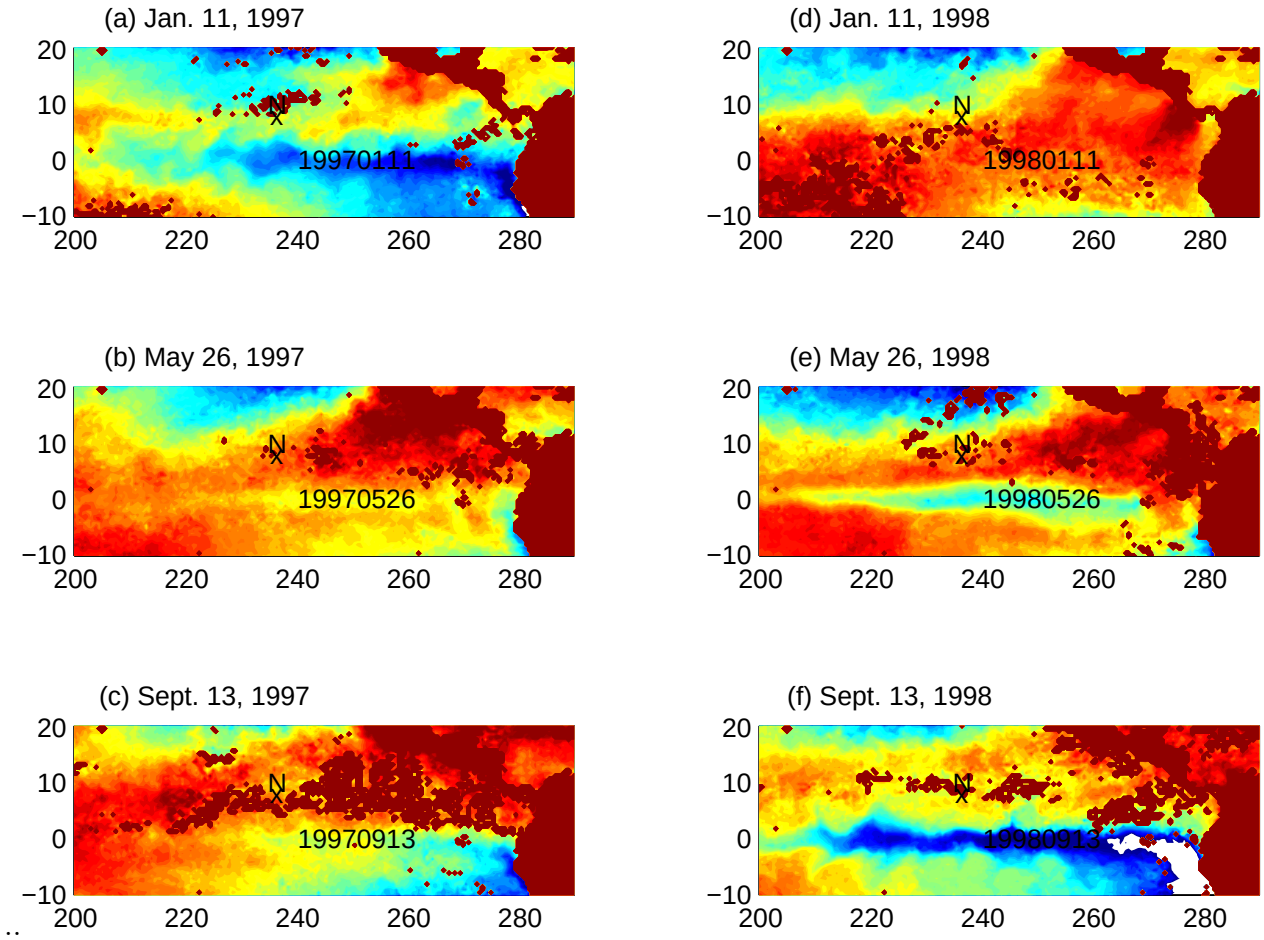

Figure 1-3: WOCE AVHRR SST. The left and right columns show corresponding times during 1997 and 1998. The color scale ranges from 21 to 30 degrees C. Dark red indicates land and areas that were obscured by clouds during the measurement interval.

equatorial eastern tropical Pacific SST was somewhat cooler than usual in early 1997 (figure 1-3(a)), but by May, 1997 it was clear that an El Niño was unfolding as the Equatorial Cold Tongue (ECT) failed to appear between May and September (compare 1-3(b) to 1-3(e)). Equatorial sea surface temperatures were still unusually high in early 1998, but the El Niño warm event abruptly terminated around May, 1998 when the trade winds resumed and facilitated the return of the cold tongue.

While discussions of El Niño commonly focus on anomalous conditions at the equator, there were also significant anomalies outside of the equatorial band. Figure 1-4 shows about eight years of the TAO record of SST and 20°C isotherm depth at 8°N, 125°W. In the tropical Pacific, the 20°C isotherm depth is thought to be a good proxy for thermocline depth (Kessler and Taft, 1987), and in this thesis we will frequently take the 19° or 20°C isotherm depth to represent the thermocline depth. Again, by May, 1997 SST had become anomalously high. In contrast to the equatorial behavior, the thermocline in the off-equatorial eastern Pacific was anomalously shallow during 1997, but it rapidly deepened during early 1998, reaching depth anomalies of over 40 m by March 1, 1998.

Large excursions from the climatological seasonal cycle were also observed at 10°N, 125°W. Figure 1-5 shows SST and 20°C isotherm depth time series measured during the PACS field program. The 20°C isotherm depth was calculated by linear interpolation between the closely spaced temperature sensors on the mooring. The climatological seasonal cycle is also shown (Levitus and Boyer, 1994). As was the case at 8°N, in 1997 the thermocline at 10°N was anomalously shallow and SST was high, while in 1998 the thermocline was anomalously deep and SST was near normal. Note that the motion of the thermocline at 8 and 10°N is about 180° out of phase with that at 0°N, 125°W (compare figures 1-4 and 1-5 to figure 1-2). We will further discuss this anti-phasing of the thermocline between the equator and 8 to 10°N in section 1.4.

The zonal scale of the off-equatorial deepening of the thermocline in early 1998 is almost the width of the Pacific Ocean. Figure 1-6(a) shows thermocline depth (represented by the 20°C isotherm) from the TAO array along 8°N; the thermocline

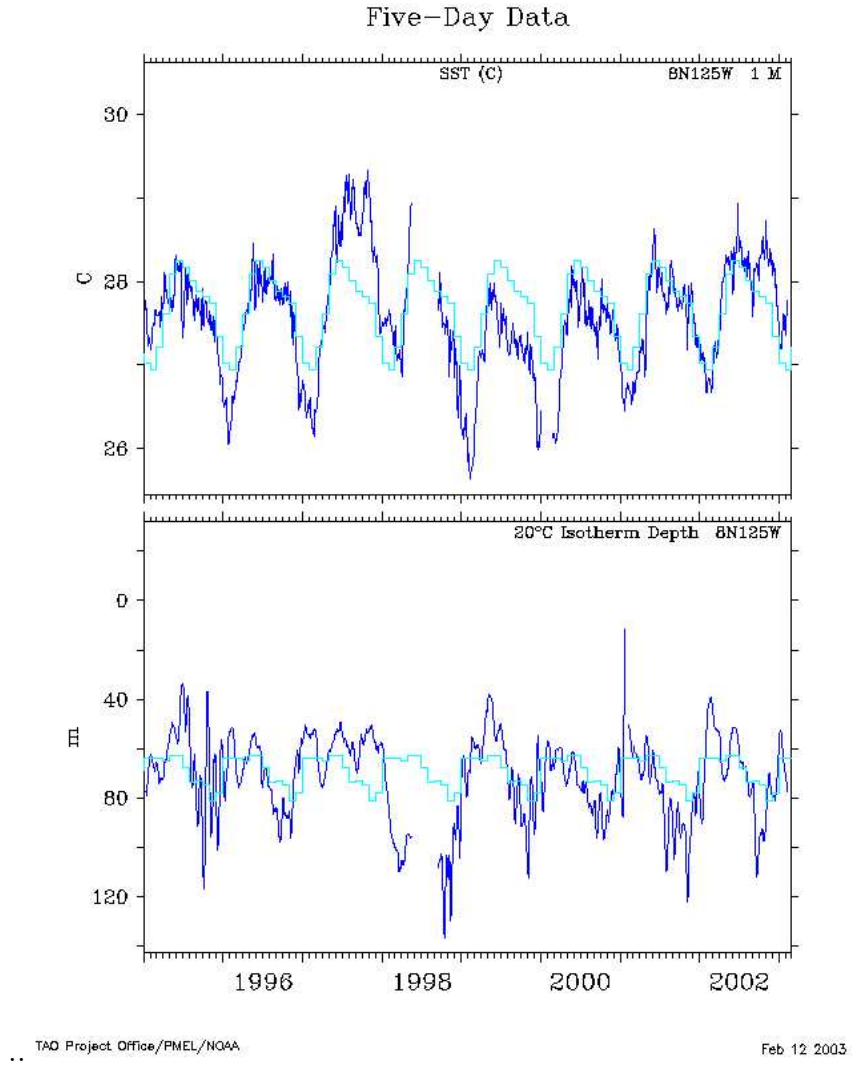

Figure 1-4: SST (top panel) and 20°C isotherm depth (bottom panel) at 8°N, 125°W for the period 1996-1999 (blue lines). The mean seasonal cycle is shown in turquoise. (Plot courtesy of TAO/PMEL.)

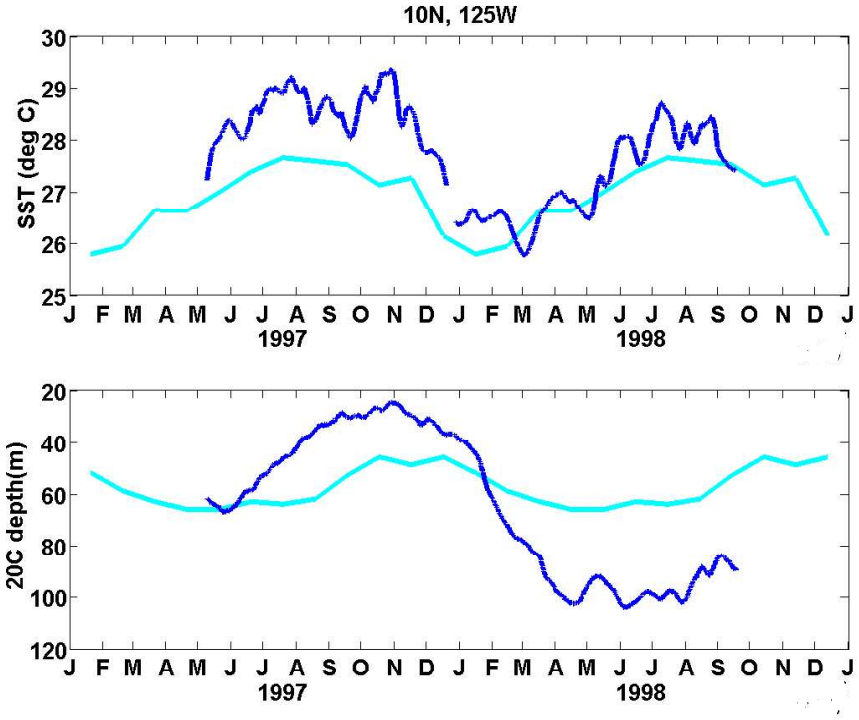

Figure 1-5: SST (top panel) and 20°C isotherm depth (bottom panel) from the PACS buoy at 10°N, 125°W in the eastern equatorial Pacific. The turquoise lines show the climatological seasonal cycle at the site (Levitus and Boyer, 1994).

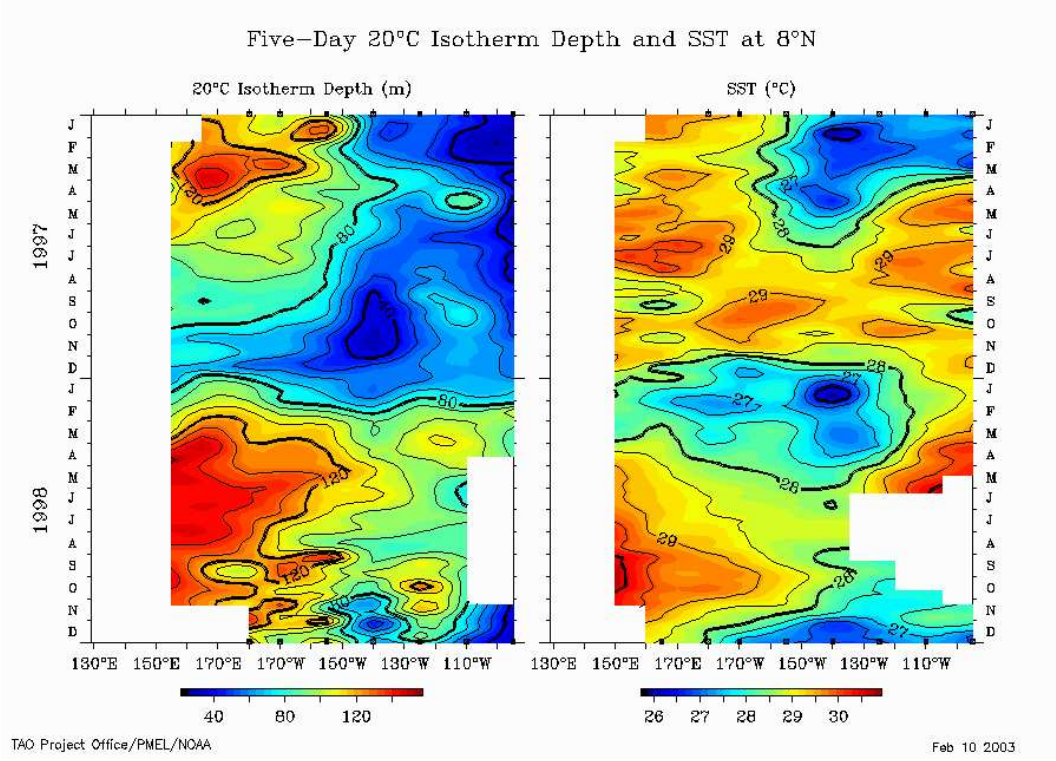

Figure 1-6: The left panel shows 20°C isotherm depth at 8°N during 1997-1998 inferred from the TAO array, and the right panel shows SST along 8°N. (Plot courtesy of TAO/PMEL.)

was almost uniformly shallow in late 1997 before beginning to deepen around the first of 1998. Figure 1-6(b) shows SST along 8°N; SST decreased as the thermocline was deepening near the first of 1998. The descent of the thermocline appears rapid and zonally coherent. We will discuss this off-equatorial deepening of the thermocline in the next section.

1.4 Motivation for Understanding the Upper Ocean Evolution at 10°N during the 1997/1998 ENSO

During late 1997 and early 1998, SST decreased and the mixed layer and thermocline deepened rapidly at 10°N. Examination of TAO data and TOPEX/Poseidon altimetry reveals that this cooling and deepening of the mixed layer were part of a larger pattern of variability, spanning much of the Pacific and extending from approximately 7-

12°N. This pattern of variability has been identified in a number of recent studies as being an inherent part of the ENSO signal (Zhang and Levitus, 1997; Perigaud et al., 2000a, b; Cassou and Perigaud, 2000; Meinen and McPhadden, 2000, 2001; Alory and Delcroix, 2002; and others). The pattern of variability is most succinctly described and quantified through empirical orthogonal function (EOF) analysis of thermocline depth or sea surface height (e.g. Zhang and Levitus, 1997; Meinen and McPhadden, 2000, 2001; Alory and Delcroix, 2002). Through the EOF analysis, a pattern of variability emerges in which the motion of the off-equatorial thermocline occurs 180° out of phase with that at the equator.

Numerous investigators have argued that off-equatorial variability may play an important role in the ENSO cycle (Wyrtki, 1977, 1985; Cane and Zebiak, 1985; Cane, 1992; Jin, 1997a,b; Perigaud et al., 2000a, 2000b; Cassou and Perigaud, 2000; Meinen and McPhadden, 2000, 2001; Alory and Delcroix, 2002; Picaut et al., 2002). In particular, recharge and discharge of warm water to and from the equatorial band is thought by some to be an important element of the ENSO cycle. The leading paradigm for ENSO, the 'recharge oscillator', relies heavily on the transport of warm water in the upper ocean between off-equatorial latitudes and the equator (Jin, 1997a,b). Considerable support for the notion that the off-equatorial ocean plays an important role in ENSO has been presented based on both observations (Meinen and McPhaden, 2000) and models (Perigaud et al., 2000a, b; Cassou and Perigaud, 2000). However, there has been debate on the subject and competing theories exist. Based on *in situ* temperature observations, Kessler has pointed out that while SST and tropical Pacific warm water volume obey the phase relationships predicted by the recharge oscillator theory, the recharge and discharge phases of the 'oscillation' are asymmetric and it is not clear that ENSO ought to be interpreted as an oscillatory phenomenon (Kessler, 2002).

The PACS data set taken at 10°N is of special interest because it is well suited for examination of a particular aspect of ENSO that has become known as the 'meridional tilting mode' based upon empirical orthogonal function (EOF) analysis of both in situ temperature data and sea surface height in the tropical Pacific (Zhang and Levitus,

1997; Meinen and McPhadden, 2000; Alory and Delcroix, 2002). In independent studies using different data sets, Alory and Delcroix (using sea surface height, 2002) and Meinen and McPhadden (using in situ temperature data, 2000) identified two principal modes of interannual climate variability in the tropical Pacific through EOF analysis. The principal mode is a zonal tilting mode along the equator; this mode is a manifestation of the classic equatorial El Niño signal where the equatorial thermocline becomes depressed in the east and elevated in the west. In the analysis of Alory and Delcroix, the temporal function of this mode has a high correlation with the Southern Oscillation Index ($R_o = -0.86$ at zero lag). This result is not surprising, since both the Southern Oscillation Index (SOI) and the zonal tilting mode are expressions of the dominant El Niño signal. A secondary mode which explains nearly as much of the interannual variance is one which tilts meridionally with a fulcrum at 5°N and anti-phased extrema near 0 and 10°N[2]. Alory and Delcroix found that the temporal function of the meridional tilting mode leads the SOI by five months with a correlation coefficient of $R_o = -0.67$. That the meridional tilting mode has a reasonably high correlation with the SOI at a five month lead is significant, because this is comparable to the skill of state-of-the-art forecast models for ENSO. In a study of 15 dynamical and statistical ENSO forecast models, Barnston et al. (1999) found that the average median model correlation skill was 0.6 for forecasts 3 to 9 months in advance of the 1997-1998 El Niño/La Niña episode.

Expressions of this meridional tilting mode are not hard to find. The mode involves out of phase movement of SSH (or, the thermocline) at the equator and 10°N. This anti-phased motion of the thermocline is visible in the TAO data presented in the previous section. Figure 1-7 is a time-latitude plot of TOPEX/Poseidon sea surface height (SSH) anomaly during 1997-98. (More detail about the particular version of the TOPEX/Poseidon SSH product used here will be given later.) We can clearly see the expected phase relationship in figure 1-7(a), with extremes occurring near

[2]Recall the anti-phasing of the thermocline at 0°N, 125°W and 10°N, 125°W in figures 1-2 and 1-5 during the El Niño and La Niña events. For example, during the El Niño of 1997-98, the thermocline was anomalously deep in the eastern equatorial Pacific, while the thermocline was anomalously shallow at 8°N in the eastern Pacific.

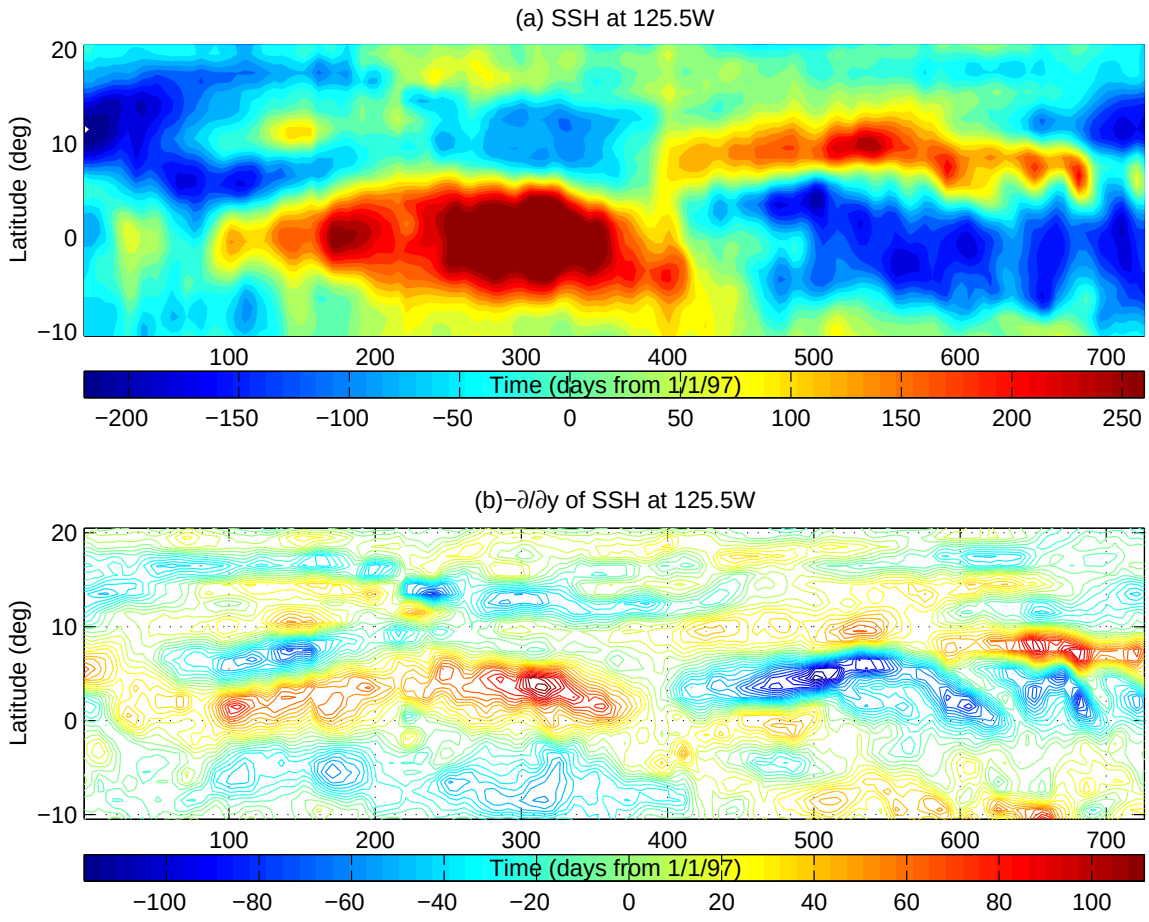

..

Figure 1-7: (a) TOPEX/Posoidon sea surface height anomaly (mm) along 125.5W during 1997 and 1998. (b) North-south derivative of sea surface height anomaly (mm/deg).

day 300 (Nov 1, 1997) and day 550 (July 1, 1998). The north-south slope of SSH anomaly is roughly proportional to (minus) the zonal geostrophic velocity, though the proportionality also depends on latitude. The opposite of north-south slope of SSH anomaly is shown in figure 1-7(b) so that the sign of the quantity plotted in 1-7(b) is the same as the sign of the zonal geostrophic velocity. We can see that the NECC (found between 3 and 8°N) reversed direction as the eastern Pacific transitioned from El Niño to La Niña states in late 1997 and early 1998. This weakening or reversal of the NECC has long been associated with the transition from El Niño to La Niña (e.g. Wyrtki, 1977, 1979) and it is another direct expression of the meridional tilting mode.

The meridional tilting mode has also come up in studies of the tropical Pacific thermocline. Meinen and McPhaden (2000) performed an EOF analysis on a 20-year gridded time series of 20°C isotherm depth in the tropical Pacific. They found zonal and meridional tilting modes accounting for 28% and 21% of the interannual thermocline variance, respectively. Meinen and McPhaden noted that the temporal function of the meridional mode is "well approximated by" the volume of water above the thermocline between 5°N and 5°S in the Pacific (hereafter, warm water volume or WWV). Because the temporal behavior of the meridional tilting mode closely resembles the time series of WWV, Meinen and McPhaden also refer to the meridional mode as a recharge/discharge mode. Consistent with the subsequent results of Alory and Delcroix (2002), Meinen and McPhaden found that WWV is significantly correlated ($R_o = 0.70$) with the Nino-3 SST index when WWV leads by 7 months.

As is true of any empirical orthogonal function, the meridional tilting mode does not necessarily correspond to a dynamical mode of the ocean. There is no *a priori* reason to expect that a single physical process is responsible for this pattern of variability. Various processes may be important in different regions at different times. Meinen and McPhaden (2000) pointed out that the meridional tilting mode is related to the recharge and discharge of water to and from the equatorial Pacific and argued that this recharge mode is important to the evolution of ENSO. In a later study, Meinen and McPhaden (2001) examined the pathways of WWV transport in the tropical Pa-

cific (again, on 8°S-8°N). They found that variations in tropical Pacific WWV (and, by extension, the existence of the meridional tilting mode) are due to variations in the relative contributions of meridional geostrophic transport, Ekman transport, and vertical water mass transformations. During the El Niño of 1997-98, when the zonal slope of the equatorial thermocline was nearly zero, Ekman transport was reponsible for nearly all of the northward transport across 8°N (Meinen and McPhaden, 2001). On the basis of numerical simulations using a linear shallow water model, Alory and Delcroix (2002) have argued that both the zonal and meridional modes are caused by anomalous zonal wind patterns and the associated Ekman pumping. While not working within the EOF context, other studies have also suggested that the zonally coherent off-equatorial variability during ENSO is associated with anomalous wind patterns (Perigaud et al., 2000a, b; Cassou and Perigaud, 2000). Based on the PACS observations at 10°N, we will argue that Ekman pumping was indeed responsible for much of the rapid thermocline deepening that occurred in early 1998, but vertical mixing also made substantial contributions to this deepening.

The meridional tilting mode has proven to be a robust feature of tropical Pacific variability, and it seems to be intimately related to the volume of water above the near-equatorial thermocline and to ENSO. The meridional tilting of the thermocline about 5°N seems to be a reliable precursor to ENSO transitions; this suggests that there may be a causal link between this mode of variability and ENSO. However, to understand this causal link, we must first understand the physical processes that produce this mode of variability. The heavily instrumented PACS mooring at 10°N, 125°W was ideally located (in time and space) to allow a detailed examination of the processes responsible for the northern end of the meridional tilting pattern. By understanding the processes that controlled the thermocline depth at 10°N, we can gain insight into the processes that give rise to the northern end of the meridional tilting mode.

1.5 Thesis Outline

This thesis uses the PACS data set, along with other data sets, to assess the processes that were important in determining the upper ocean thermal evolution at 10°N, 125°W during 1997 and 1998. Particular attention is given to determination of the processes responsible for the rapid descent of the thermocline during early 1998 which was a precursor to the end of the 1997-98 El Niño event. This off-equatorial deepening of the thermocline has been shown to have a statistical relationship (if not a causal one) with ENSO, having significant correlation with ENSO transitions at a lead of several months.

We will argue that the most important influences on the upper ocean thermal evolution (including thermocline and mixed layer depth) were surface heat fluxes, Ekman pumping, and vertical mixing associated with Kelvin-Helmholtz instabilities. We have been unable to identify any significant influence on the thermal evolution by long Rossby waves at the site, and, as we will discuss, we expect long wavelength Rossby waves to have more prominent effects on thermocline depth. We have identified intermediate wavelength baroclinic Rossby waves in the data, but their most important effect on the thermal structure was through their horizontal velocity signal rather than their vertical velocity signal.

The evolution of the surface and subsurface conditions at the mooring site can be conveniently classified using a distinction between ITCZ and non-ITCZ conditions. Figure 1-8 shows a schematic summary of the observations and the thesis presented here. This thesis deals with a complex sequence of events, and we implore the reader to refer back to this figure as necessary; it summarizes the relationship between the various important physical processes. During ITCZ conditions (shaded in figure 1-8), there were large heat and freshwater fluxes into the ocean, but the wind stress was relatively weak. The Ekman pumping was upward while the ITCZ was over the mooring. These conditions contributed to the formation of a stable, shallow mixed layer. Near the end of the ITCZ season of 1997, the thermocline was very shallow (near 30 m depth), the wind stress increased, and the buoyancy flux decreased. These

factors contributed to deepening of the mixed layer and an increase in surface density as the ITCZ season came to a close.

As the ITCZ moved completely south of the mooring, the wind stress continued to increase, as did evaporative heat and freshwater loss. During the early part of the non-ITCZ season, the mixed layer was only marginally statically stable, and a train of baroclinic Rossby waves contributed a persistent 'background shear' at the mixed layer base. The combined effect of the weakly stratified mixed layer base, reduced buoyancy flux, increased wind stress, and background shear imposed by the large scale pressure gradient led to frequently low Richardson numbers at the mixed layer base and further entrainment of cooler and saltier water from the upper thermocline; consequently, the mixed layer base became even more weakly stratified. A combination of this vertical mixing and downward Ekman pumping caused the thermocline to deepen by about 60 m over the first 3 months of 1998. Eventually, the rains and large surface heat fluxes returned as the ITCZ moved back into the region, helping to stabilize the mixed layer.

In this thesis, we seek to demonstrate that the above description of the upper ocean thermal evolution at the site is accurate. To do so, we use a combination of data analysis and model experiments. First, it is necessary to characterize the local surface forcing at the mooring site. The overall approach taken toward analysis of the oceanographic observations is to distinguish between local and large-scale influences on the observed variability. Important steps in this process involve identifying the physical processes contributing to horizontal and vertical advection, and computation of a heat budget. The high vertical resolution of moored instrumentation also allows an examination of the role of vertical mixing associated with the vertical shear and stratification. After identifying potentially important influences on the thermal and velocity structure at the mooring site, we use a series of numerical experiments to assess the importance of these influences.

The thesis is organized as follows. Chapter 2 describes the collection and processing of the subsurface and surface data collected at 10°N, 125°W. Chapter 3 describes the large-scale climatological surface meteorology and air-sea flux fields an overview of

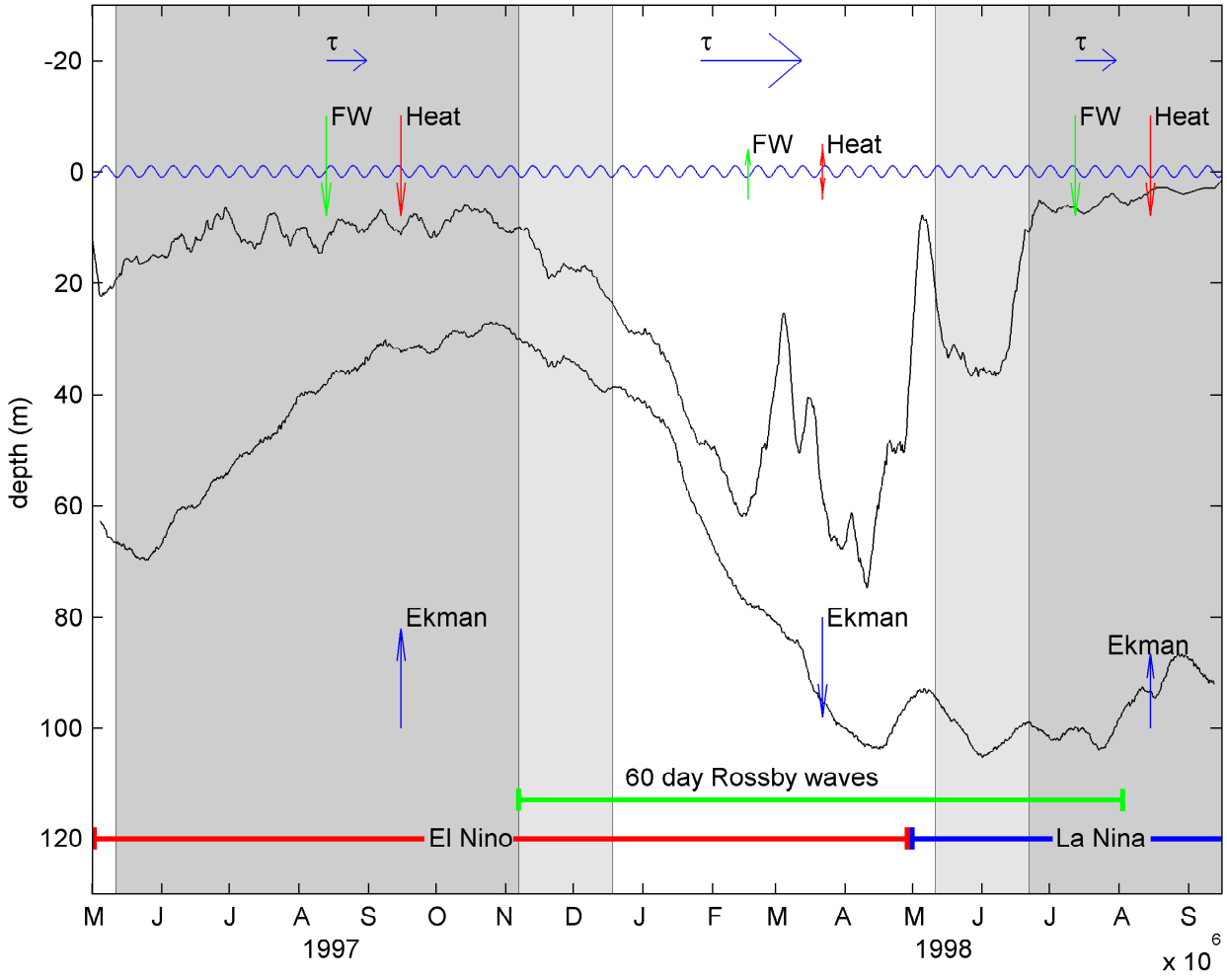

Figure 1-8: A schematic summarizing the observed meteorology, air-sea fluxes, and upper ocean thermal evolution at 10°N, 125°W. Times when the ITCZ was over the mooring are shaded. Light shading indicates the transition between ITCZ and non-ITCZ conditions. The lower black line indicates the 19°C isotherm and the upper black line indicates the mixed layer depth. The arrows labeled τ, FW, Heat, and Ekman represent the wind stress magnitude, freshwater flux, net heat flux, and Ekman pumping velocity, respectively. Notice that the thermocline began to deepen about 6 months before the termination of El Niño. masterfigN.m

the observed meteorology and air-sea fluxes. The focus of that chapter is to highlight the contrast between ITCZ and non-ITCZ conditions at the mooring site. Chapter 4 deals with the oceanographic observations taken at the mooring site. First, we present an overview of the observed upper ocean evolution. Subsequent sections of Chapter 4 examine the remote and local influences that may have contributed to the observed variability. Chapter 5 presents a numerical model and a series of numerical experiments to facilitate identification of the important physical processes that affected SST and thermocline depth at the mooring site and to quantify the relative roles of these processes. Chapter 6 summarizes the evidence that thermocline depth and SST were affected primarily by surface fluxes of buoyancy and momentum, Ekman pumping, and shear-driven vertical mixing. We discuss some aspects of the large scale oceanic behavior in light of this study before offering some concluding remarks[3].

[3]Three appendices are also included. The first contains supplementary figures that may be of interest to the reader. Two potentially important figures in appendix A are intended to allow easy conversion between the various time units used in this thesis. Appendix C contains selected aspects of an empirical orthogonal function analysis of the observed velocity signal. Appendix C contains some corroborating evidence for the thesis.

Chapter 2

PACS Data and Processing

While this thesis utilizes several data sets, an essential element of this study is the high quality time series of upper ocean and surface meteorological properties that were collected as part of the NOAA-funded Pan American Climate Study (PACS) field project. This chapter will address the collection and processing of the mooring data. The first two sections of this chapter describe the data collection, and the final two sections address the data processing. The surface meteorological data and air-sea fluxes will be presented and discussed in chapter 3, and the upper ocean data will be presented and discussed in chapter 4.

2.1 Mooring Deployment

From April 1997 through September 1998 a mooring was deployed at 10°N, 125°W by the WHOI Upper Ocean Processes Group (UOP) as part of the PACS field project. This mooring location was chosen because of its proximity to the climatological position of the Inter-tropical Convergence Zone (ITCZ). The annual migration of the ITCZ will be discussed in chapter 3. Another PACS mooring was in place at 3°S, 125°W, but this data is not used in this thesis and will be discussed elsewhere. The instrumentation on these moorings was selected to provide accurate time series of air-sea fluxes, surface meteorology, and upper ocean temperature, velocity, and salinity.

The initial deployment cruise was conducted under the leadership of chief scientist

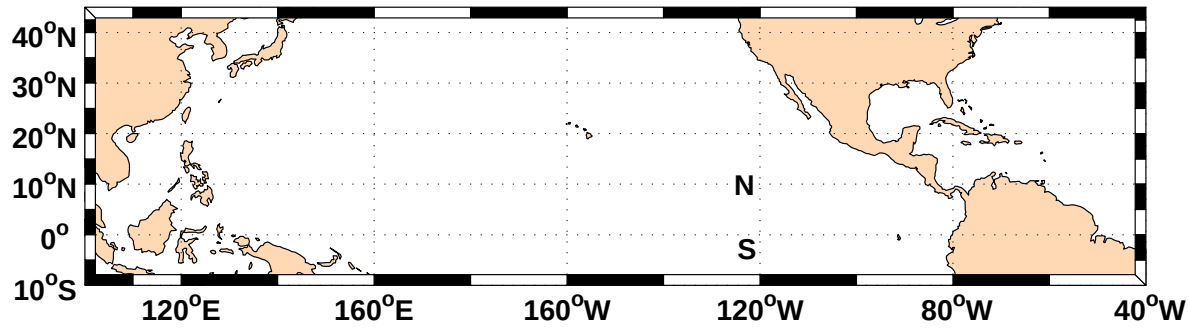

Figure 2-1: Location of the mooring used for this study (denoted by an "N" at 10°N, 125°W).

Robert Weller aboard the *R/V Roger Revelle* from April 9 to May 5, 1997 (Way et al., 1998). A mid-term cruise was undertaken aboard the *R/V Thomas Thompson* to recover, service, and re-deploy the moorings between November 28 and December 26, 1997 (Trask et al., 1998). Finally, the moorings were recovered from the *R/V Melville* during September 6 to September 30, 1998 (Ostrom et al., 1999).

CTD casts were periodically conducted by the scientific staff while underway on the mooring cruises. One CTD cast was conducted during each visit to the mooring site (three total). Figure 2-3 shows the temperature, salinity, and density structure inferred from CTDs taken at the beginning (4/30/1997) and middle (12/19/97) of the field program, and figure 2-4 shows the same for the upper 400 m of the water column. Note that there were slight changes in temperature and salinity below 150 m depth. Both temperature and salinity contribute to the stable density stratification in the upper 100 m. The thermocline, halocline, and pychnocline were well defined and were found in the upper 100 m during both cruises. Between the thermocline and 600 m, both temperature and salinity decrease with depth. The negative contribution of the salinity profile to static stability combines with the stabilizing temperature

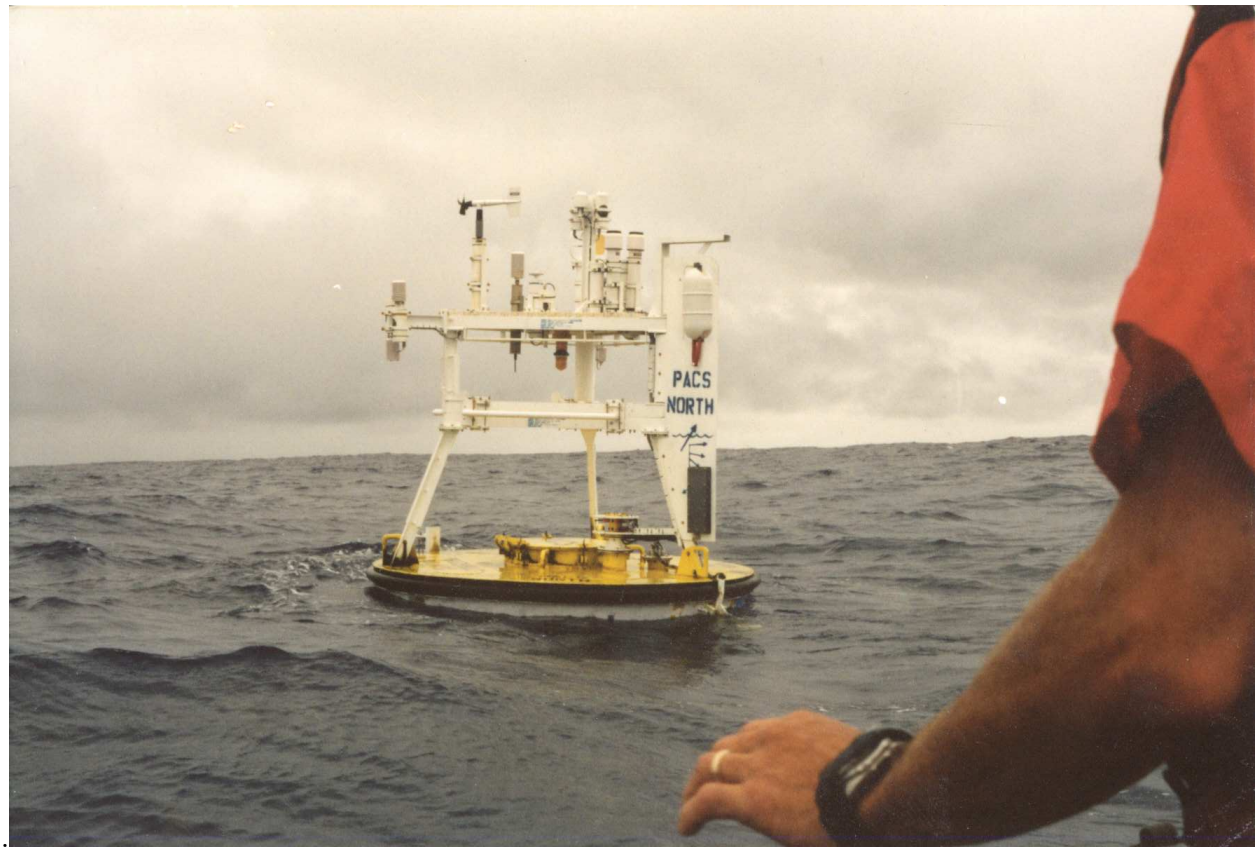

Figure 2-2: The PACS North buoy after deployment.

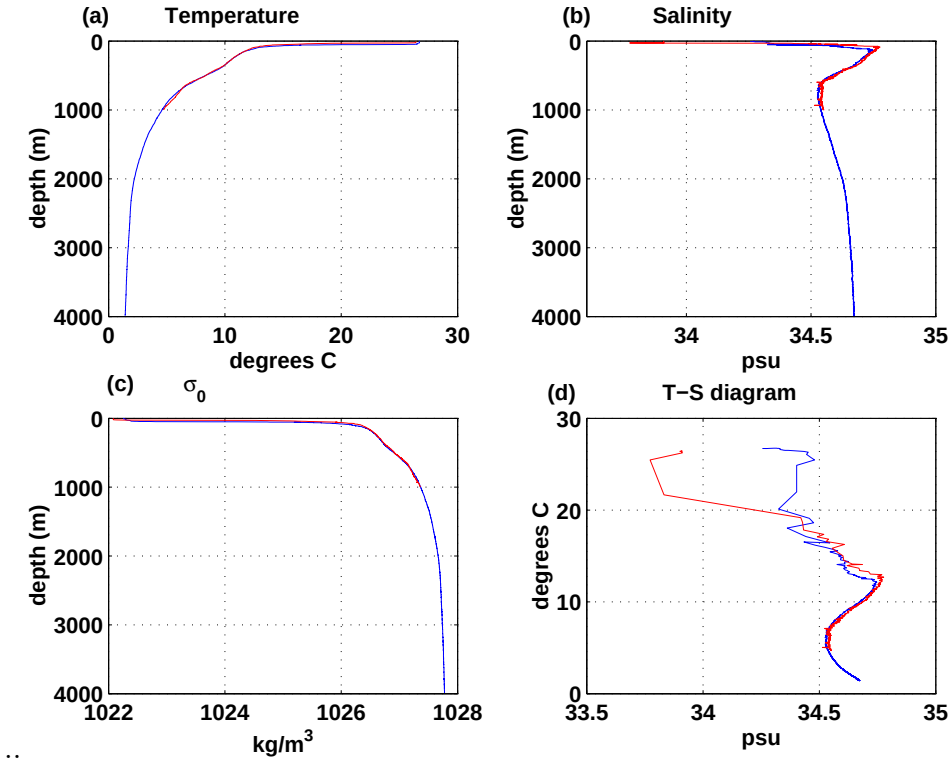

Figure 2-3: (a) Temperature, (b) salinity, (c) potential density relative to the surface, and (d) T-S relationship measured at the beginning (4/30/1997, blue lines) and middle (12/19/97, red lines) of the field program.

stratification to produce a weak pychnostad near 500 m. Below 600 m, salinity increases with depth.

2.2 Instrumentation

The PACS moorings were heavily instrumented, often redundantly, both above and below the sea surface. On the buoy, an IMET (Improved METeorological) package provided measurements of wind velocity, air temperature, barometric pressure, relative humidity, precipitation, incoming short-wave radiation, and incoming long-wave radiation. Redundantly, a Vector Averaging Wind Recorder (VAWR) measured the same quantities. Below the surface, but mounted to the buoy in the upper 3 m of the ocean (figure 2-5), there were seven independent temperature sensors and a SEACAT conductivity/temperature sensor. In addition, sea surface temperature was measured

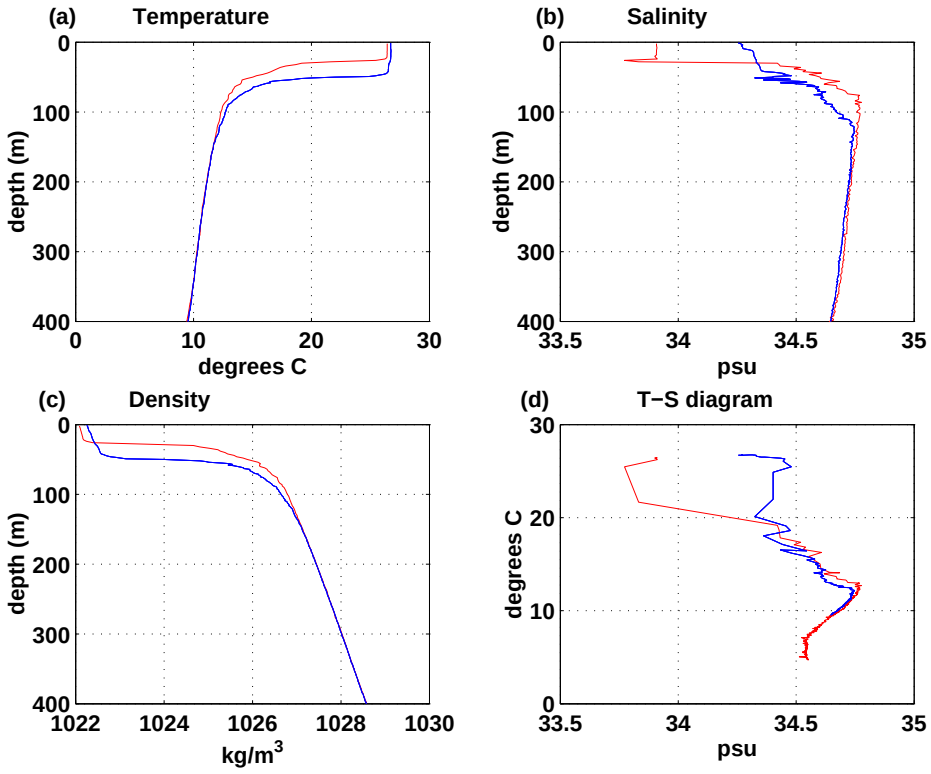

..

Figure 2-4: Same as in figure 2-3, except only the upper 400 m are shown. Upper ocean (a) temperature, (b) salinity, (c) density, and (d) T-S relationship measured at the beginning (4/30/1997, blue lines) and middle (12/19/97, red lines) of the field program.

using a floating temperature sensor. In the second phase of the field program, there were also stand-alone instruments to provide independent measurements of precipitation, relative humidity, and air temperature. Table 2.2 gives some details about the specific types of sensors used, their accuracy, and the averaging interval for the measurements.

The mooring was also heavily instrumented. Generally, there were temperature sensors down to 200 m depth, Vector Measuring Current Meters (VMCMs; Weller and Davis, 1980) down to 110 m, and SEACAT conductivity sensors down to 80 m. For all sensors, vertical resolution was weighted toward the surface. The temperature sensors had the best vertical resolution, with about 30 sensors on the upper 200 m. At deployment, salinity and velocity measurements had comparable resolution, with 8-10 sensors. Figure 2-6 depicts a typical mooring configuration for the PACS field program; there were slight differences in the sensor locations in the two deployments. Rather than burdening the reader with the details of the instrument locations here, we will instead indicate the measurement depths on the figures that display the data (chapter 4).

2.3 Data Processing and Data Return

Details of the quality control and data processing can be found in Anderson et al. (2000), but some relevant aspects are presented here. The surface meteorological and current meter measurements were processed using software developed by the WHOI UOP Group and pre-deployment calibrations were applied to each instrument. When redundant measurements were available, inter-sensor comparisons were carried out, and efforts were made to determine which record was more reliable. Post-deployment calibrations were used when they produced better agreement in comparisons between redundant instrumentation. All compass readings (surface and subsurface) were rotated by 9.46 degrees to correct for local magnetic deviation from true north. The processed data were visually inspected for sensor failure or gross errors. Sampling intervals for all instruments (including the meteorological packages) were 15 minutes

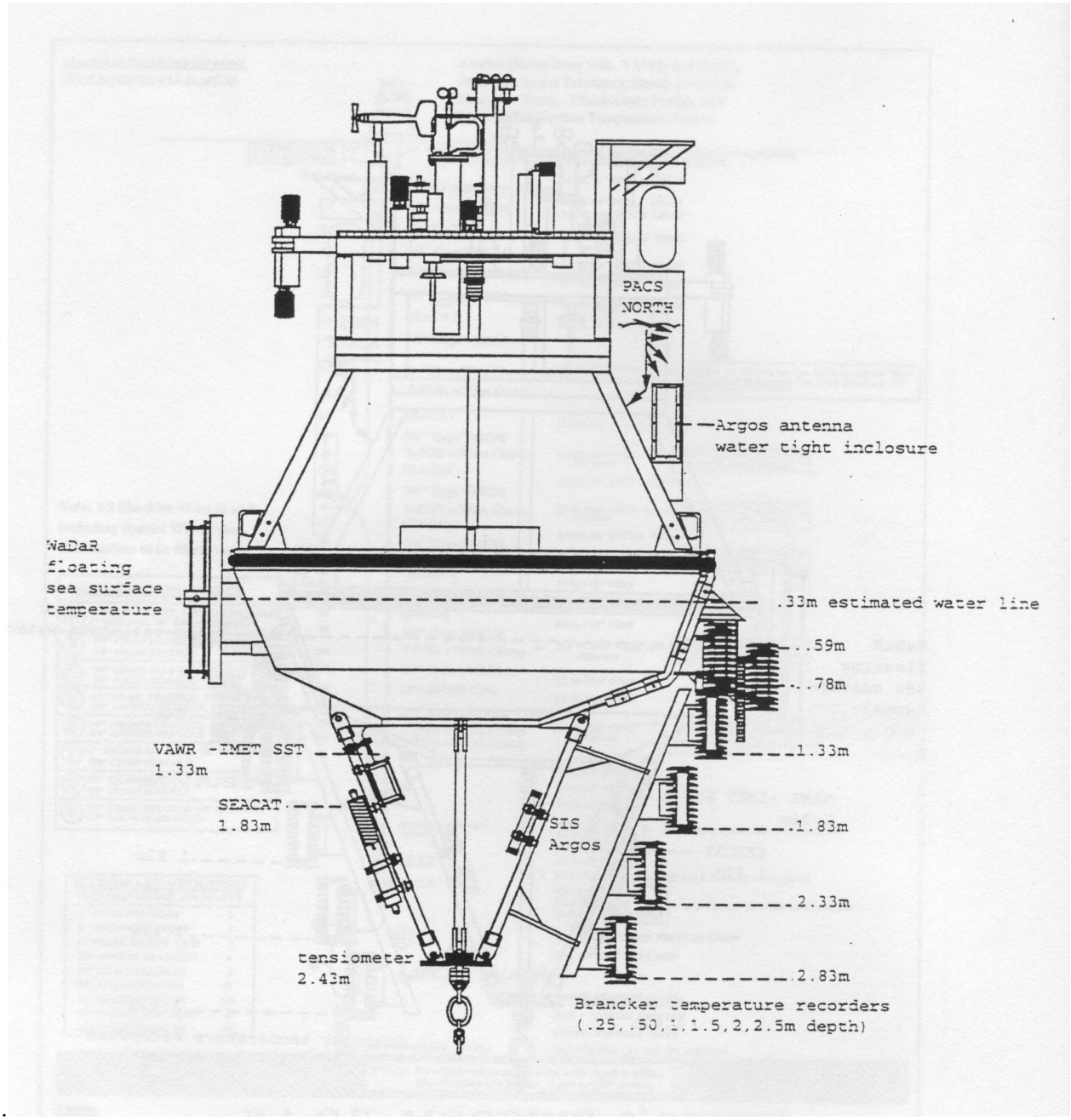

..

Figure 2-5: Schematic showing the near surface instrumentation for the second phase of the field program (from Anderson, et al., 2000).

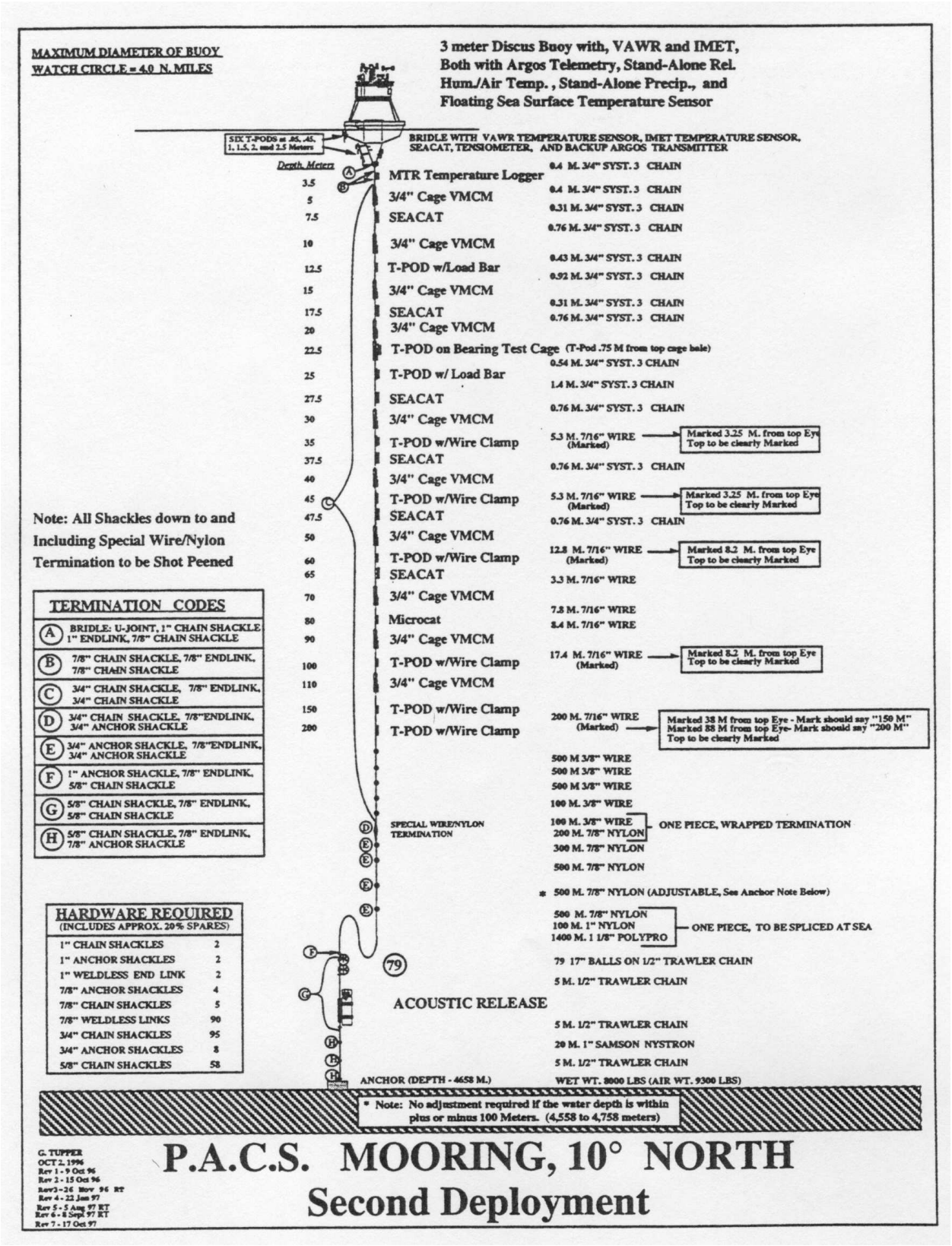

Figure 2-6: Schematic showing the mooring configuration for the second phase of the field program (from Anderson, et al., 2000).

Parameter	Sensor type	Nominal accuracy	Averaging interval
Wind speed	3-cup Anemometer^{+}	$\pm$2%	15 min
	R.M. Young 3-cup^{+}	$\pm$5%	15 min
Wind direction	Integral vane w/ vane follower^{+}	$\pm$ 1 bit (5.6 deg)	15 min
Insolation	pyranometer^{+}	$\pm$ 3%	15 min
Incoming long-wave radiation	pyrgeometer^{+}	$\pm$ 10%	15 min
Relative humidity	Variable dielectric conductor^{+}	$\pm$ 2%	15 min
	stand-alone/ASIMET*	$\pm$ 3%/$\pm$ 2%	3.75 min
Barometric pressure	Quartz crystal^{+}	$\pm$ 0.2 mbar when wind $\leq$ 20 m/s	15 min
SST	Thermistor^{+}	$\pm$ 0.005°C	15 min
Air temperature	Thermistor (unaspirated)$^{+}$	$\pm$ 0.2°C for wind $\geq$ 5 m/s	15 min
	stand-alone/ASIMET*	0.05 deg C	3.75 min
Subsurface temperature	SEACAT	0.005°C$^{@}$	7.5 min
	MicroCAT	0.005°C$^{@}$	3.75 min
	Brancker	0.005°C$^{@}$	30 min
	VMCM	0.005°C$^{@}$	7.5 min
Conductivity	SEACAT	0.01 psu	7.5 min
	MicroCAT	0.01 psu	3.75 min
Vector current	VMCM	1 cm/s	7.5 min
Precipitation	RM Young rain guage	0.1 mm/hr	3.75 min

Table 2.1: Table of measurement accuracies. $^{+}$Part of VAWR package. *The stand-alone unit was deployed during phase 1 of the field study, while the ASIMET package was deployed during phase 2. $^{@}$In the laboratory, the accuracy is considerably higher, but this is the nominal accuracy that we estimate for field measurements.

or less. All of the data was averaged to a common 15 minute time base, although this study uses only the 1 hour averages.

Many of the surface measurements were performed redundantly. Redundant deployment was a wise choice, because the IMET package failed to produce data after late April, 1998. So the VAWR record was used. The IMET package intermittently experienced additional problems associated with the Argos telemetry. When both meteorological packages were functioning properly, the agreement between the two was generally acceptable.

Two of the VMCMs ceased to produce meaningful data when the rotors failed on October 14, 1997 (20 and 40 m). The near simultaneous failure combined with the 20 m vertical separation between the two current meters suggests that a fishing vessel near the buoy ensnared the mooring with its lines. The problem was solved during the recovery and redeployment cruise on December 19, 1997 when the mooring was replaced.

Two of the Sea-bird SEACAT temperature and conductivity sensors also failed to produce data during the first phase of the field study (22.5 and 32.5 m). One was lost at sea, and the other was severely damaged. These two sensors were located between the two damaged current meters, and it seems likely that all four sensors were damaged by the same fishing vessel.

The floating SST sensor was also damaged during the first phase of the field program. The sensor was designed to follow the sea surface by floating up and down along stainless steel rods. Upon recovery, one of the rods was bent, causing the sensor to remain out of the water. We believe that the rod was bent when a fishing vessel tied up the buoy, possibly in order to pull the buoy to one side in order to catch fish that congregate around the mooring. The float functioned properly immediately after deployment and for the duration of the second leg of the field study.

2.4 Estimation of Air-sea Fluxes

The WHOI-UOP Group used the surface meteorological and near-surface oceanographic measurements to determine the air-sea fluxes according to the TOGA COARE[1] bulk flux algorithm of Fairall et al. (1996). Although the algorithm includes corrections for 'cool skin' and 'warm layer' effects (cooling of the upper few millimeters and warming of the upper few meters of the ocean due to heat exchange), only the cool skin correction was employed in the flux calculations. The wind speed relative to the sea surface was calculated as the difference between the measured vector winds and the near surface current meter record. Full details of the air-sea flux calculations are given in Anderson et al. (2000).

The outgoing long-wave radiation (O($10\mu m$)) was estimated using the Stephan-Boltzmann law, which can be expressed as $\frac{power}{area} = \epsilon\sigma T^4$, where ϵ is the sea surface emissivity ($\epsilon = 0.97$), σ is the Stefan-Boltzmann constant, and T is the sea surface skin temperature in degrees Kelvin. The skin temperature is used because long-wave radiation depends on the interfacial temperature, which is slightly less than the temperature found about a millimeter below the surface (Saunders, 1967).

The precipitation rate was estimated by first-differencing measured accumulation in time. The R.M. Young rain gauge measures accumulated precipitation using a capacitance technique to determine the amount of water in a collection chamber. Due to limited sample volume, the gauge siphons off the accumulated precipitation when the chamber is full. This process leads to spurious negative spikes in the precipitation rate, and these spikes were identified and replaced with zeros. Some additional noise in the precipitation rate was identified, and we believe that this noise is produced by electro-magnetic interference with nearby sensors (perhaps the Argos telemetry?). The first-difference derivative may have also contributed to this noise. The noise appears to be about 0.1 mm/hr based on the noise about 0.0 mm/hr during times when the precipitation rate was known to be zero. Consequently, we rejected signals in the precipitation rate that were smaller than the estimated noise by setting precipitation

[1]TOGA COARE stands for the Coupled Ocean-Atmosphere Response Experiment of the Tropical Ocean-Global Atmosphere research program.

rates less than 0.1 mm/hr to zero. The accumulated precipitation was then estimated as the time integral of the corrected precipitation rate.

The accuracy and applicability of the TOGA COARE bulk flux algorithm has been demonstrated in many contexts. The algorithm development involved simultaneous measurements from land stations, buoys, six research vessels, and 267 low-level airplane fly-overs (Weller et al., in press/submitted). As a result of this intensive inter-comparison and inter-calibration campaign, measurement techniques and the bulk flux formulae were substantially improved, allowing the TOGA COARE Flux group to meet their goal of closing the ocean heat and freshwater budgets to within 10 W/m^2 and 20%, respectively (Weller et al., in press/submitted). Since the TOGA COARE program, the Flux group has continued the coordinated effort to refine the bulk formulae and measurement techniques. Now, IMET surface fluxes, computed using the COARE flux algorithm, are being used for validation of other flux products (e.g. Shinoda et al., 1998; Shinoda and Hendon, 1998). Combined with accurate measurements of bulk surface meteorological properties, the TOGA COARE algorithm is the benchmark for calculation of air-sea fluxes of heat, freshwater and momentum.

The PACS surface meteorological and mooring measurements constitute an accurate and highly resolved time series of great utility for air-sea interaction studies in the eastern tropical Pacific. The high spatial resolution of the subsurface measurements allows a detailed view of the behavior of the upper ocean. The complete set of meteorological measurements facilitate understanding of how the ocean responds to atmospheric forcing on a wide range of spatial and temporal scales and how this oceanic response may force the atmosphere in turn. The meteorological data will be presented in chapter 3, and the oceanic behavior will be presented and analyzed in chapter 4.

Chapter 3

PACS Meteorology and Air-Sea Fluxes

In this chapter, we present and discuss the observed surface meteorology at the mooring site and discuss how these observations compare to climatological conditions. In the first section, we review the large scale climatological meteorology at the site. In the second section, we review some aspects of the large scale surface meteorology during the measurement period, and in the third section we present the measurements at 10°N, 125°W.

3.1 Large Scale Climatology and the ITCZ

The north-south migration of the Inter-Tropical Convergence Zone (ITCZ) plays a crucial role in modulating air-sea fluxes of heat, momentum, and freshwater. Located between the northeasterly and southeasterly trade winds, the ITCZ is a nearly zonally oriented band of convergent surface wind associated with deep convection. The frequent convection in the ITCZ tends to produce high precipitation rates and reduced short wave radiation. Furthermore, surface winds are usually light in the ITCZ; early sailors labelled this region the doldrums and carefully avoided it.

A straightforward measure of the location of the ITCZ is given by the surface wind divergence field estimated from the European Remote Sensing (ERS) satellite

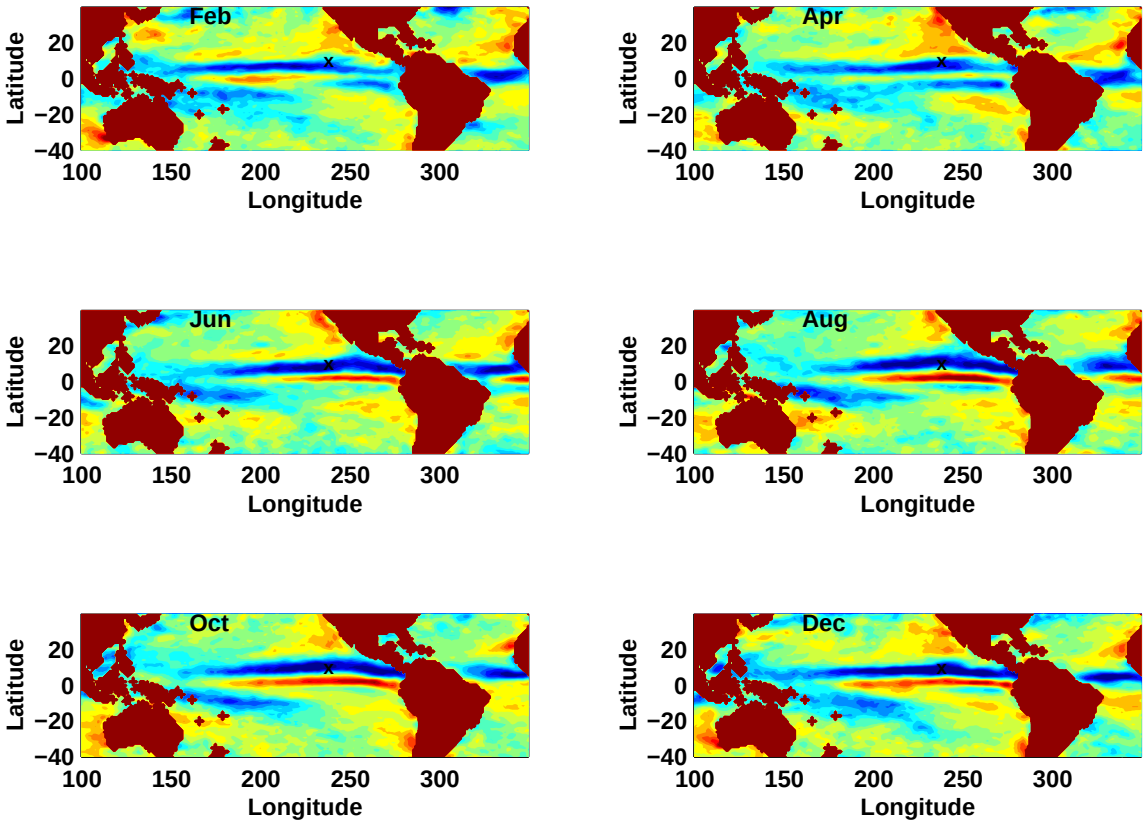

..

Figure 3-1: Climatology of surface wind divergence (IFREMER ERS scatterometer wind product). The color scale ranges $\pm 8 \times 10^{-6}$ m/s; blue is convergence and red is divergence. The band of wind convergence (i.e. negative divergence) is a rough measure of the location of the ITCZ. The mooring at 10°N, 125°W is marked by an 'x'.

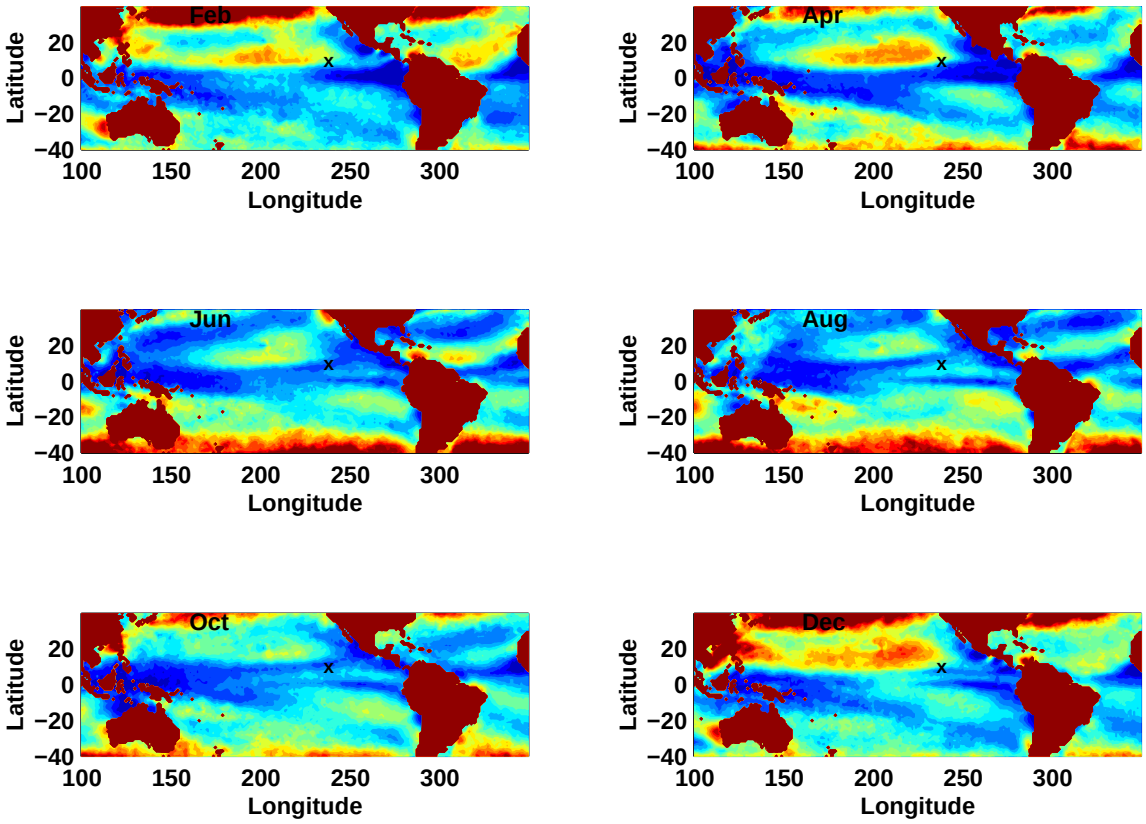

..

Figure 3-2: Climatology of wind stress magnitude (IFREMER ERS scatterometer wind product). The color scale ranges from zero to 0.16 N/m^2; blue is weak stress and red is strong. The mooring at 10°N, 125°W is marked by an 'x'.

(more detail about the ERS scatterometer data is given in chapter 4). Climatological fields of surface wind divergence from the IFREMER/ERS wind product are shown at two month intervals in figure 3-1. In the figure, the ITCZ approximately coincides with the blue band of convergent surface winds. The ITCZ undergoes an annual north-south migration following the sun and the warm surface water. The ITCZ is farthest north late during the Northern Hemisphere summer (August/September), and it is farthest south during January/February. To the extent that surface air may be considered incompressible, the regions of convergent surface flow indicate ascending air and regions of divergent flow indicate descending air. Ascending air promotes convective instability by pushing warm, moist surface air upward where it can expand and release latent heat, thus promoting further ascent and the formation of clouds. Air descending from the upper troposphere is generally cooler and drier than the surface air. In fact, the patterns of surface wind convergence and divergence are largely driven by the ascent and descent of air to and from the upper troposphere; convergence tends to occur over warm water which promotes convection.

The seasonal cycle in surface meteorology and air-sea fluxes at the mooring site can be understood in terms of the annual migration of the ITCZ. The IFREMER/ERS climatology of wind stress magnitude is shown in figure 3-2. Note that there is a band of low wind stress magnitude that approximately coincides with the position of the ITCZ, and there is a large region of high stress that extends from the northern edge of the ITCZ to near 20°N and is associated with the NE Trade Wind. Even in this spatially and temporally smoothed climatology, a remarkable gradient in wind stress magnitude stands out near the mooring site. This gradient in wind stress magnitude that occurs between the ITCZ and the region to its north is the strongest gradient found in the tropics, and the gradient is largest during the boreal winter months as the ITCZ moves closer to the equator. We might expect that the north-south migration of the ITCZ and the associated gradient in wind stress magnitude may have profound dynamical consequences for the seasonal cycle in the ocean. In section 3.3 we will present the observed surface meteorology and surface fluxes, and we will show that the surface and subsurface properties at the mooring site contrast

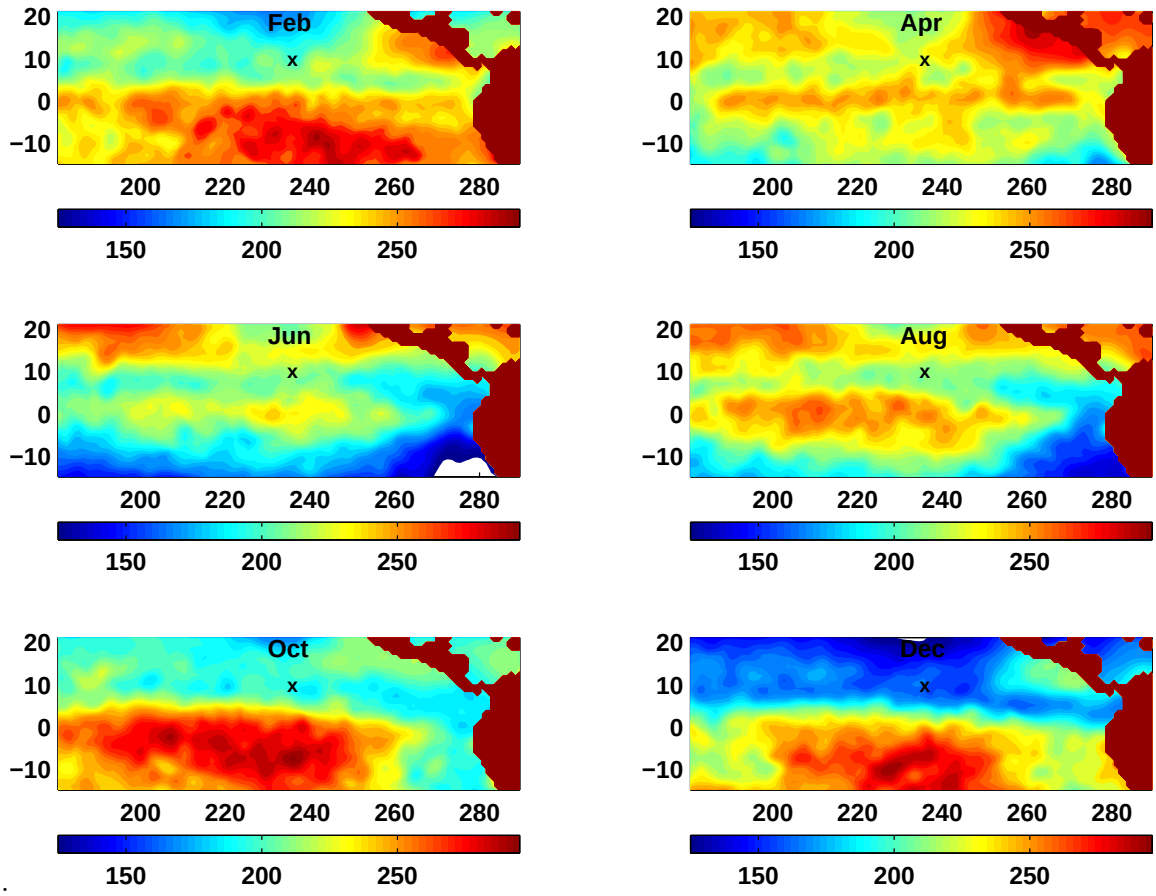

..

Figure 3-3: SOC Climatology of short wave radiative heat flux into the ocean. The color scale is in W/m^2. The mooring at 10°N, 125°W is marked by an 'x'.

dramatically depending on whether the ITCZ is south of or over the mooring site.

Surface heat and freshwater flux measurements in the tropical Pacific are inadequate to determine the climatological seasonal cycle in surface heat flux with great precision. Most of the existing heat flux climatologies are derived largely from ship based observations of wind speed, temperature, humidity, and cloud cover fraction. Here, we use the flux climatology of the Southampton Oceanography Centre (SOC) to present the qualitative aspects of the seasonal cycle of surface heat and freshwater fluxes. Figure 3-3 illustrates the climatological seasonal cycle of short wave radiative heat flux for the central and eastern tropical Pacific Ocean. The tendency of the ITCZ to block incoming short wave radiation can be clearly seen when the figure is compared with figure 3-1. Another prominent feature is the seasonal signal in insola-

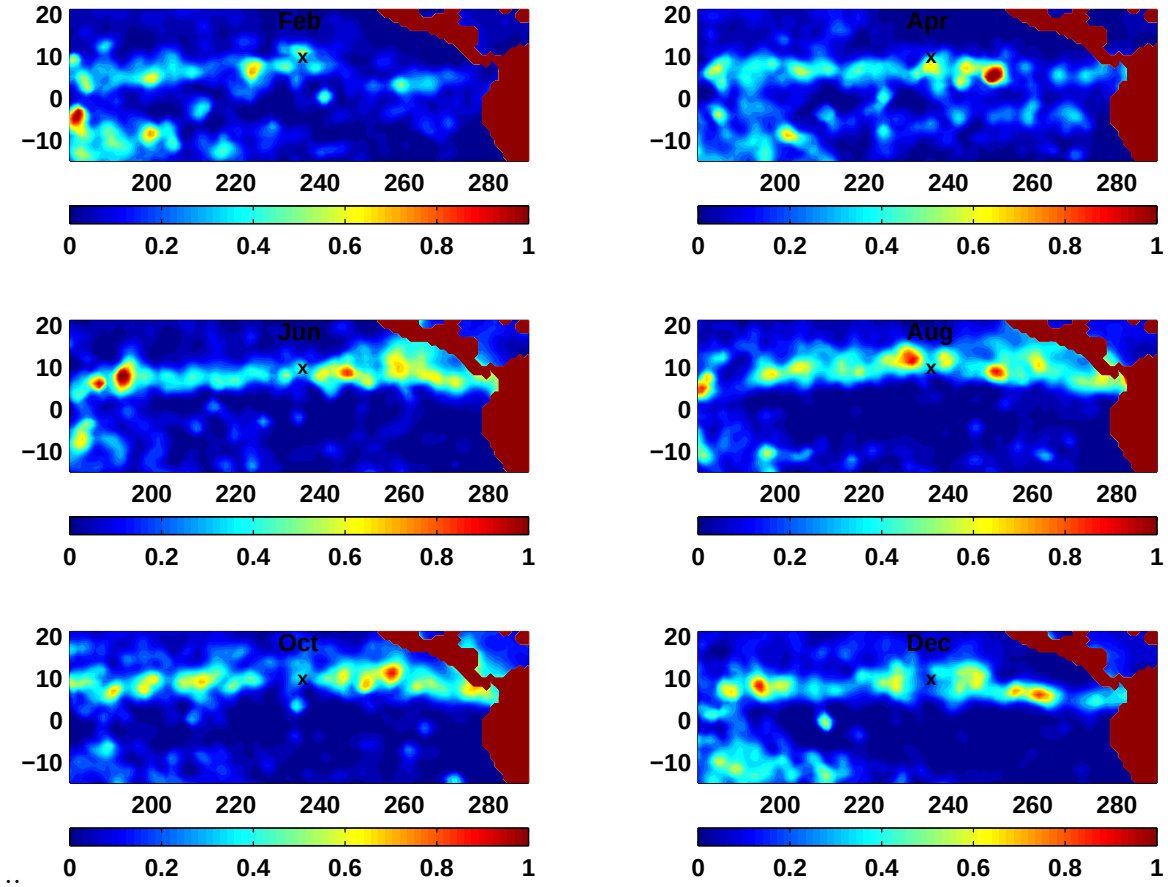

Figure 3-4: SOC Climatology of precipitation. The color scale is in mm/hr.

tion, with maximum short wave heating in the northern hemisphere during the boreal summer.

The seasonal cycle of other air-sea fluxes can also be understood in terms of the annual migration of the ITCZ. The SOC climatologies of precipitation and latent heat flux are shown in figures 3-4 and 3-5. Not surprisingly, the annual cycle of precipitation involves a north-south migration of a band of high precipitation under the ITCZ. Consistent with this and the annual cycle of wind stress magnitude is the fact that latent heat flux is high outside of the ITCZ as air rushes in to the convergence zone, picking up latent heat and water vapor to feed the convection occurring in the ITCZ. Another prominent feature of the latent heat flux climatology is the band of high latent heat flux near the equator; this can be understood in conjunction with the surface wind divergence (figure 3-1) which indicates subsidence of dry air from

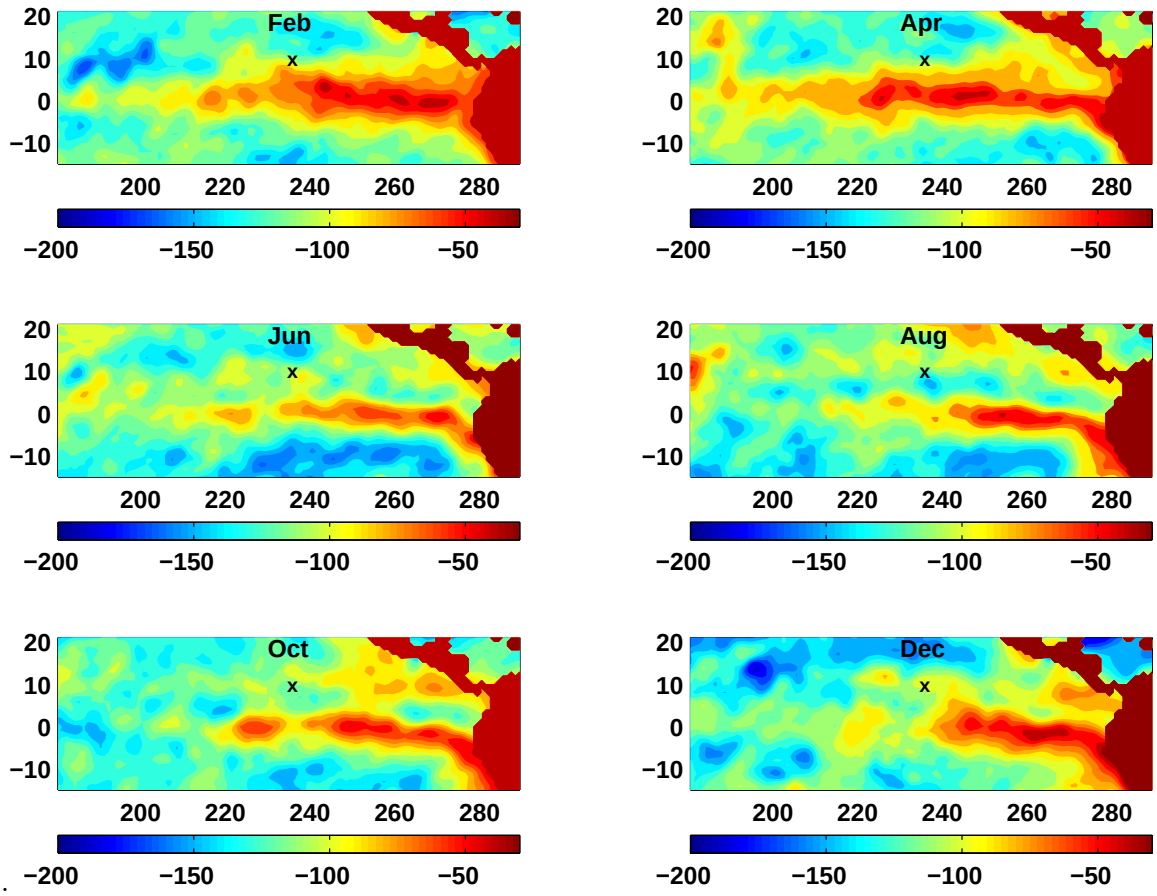

Figure 3-5: SOC Climatology of latent heat flux into the ocean. The color scale is in W/m^2.

the upper troposphere. The persistent supply of dry air promotes latent heat flux in this region by ensuring that the surface air maintains a low relative humidity.

The climatological flux fields presented in this section have high uncertainties, and they are only intended to give a qualitative picture of the seasonal cycle of and relationship between the large scale air-sea flux fields. The ERS climatology is computed using only 8 years of data (which included the strong ENSO event of 1997-98), and the SOC heat flux climatology is believed to have substantial errors (although it is arguably the best existing climatology– for example, see Weller et al., 1998). For example, the global heat budget of the SOC climatology suffers from a 29 W/m^2 imbalance, and the specific areas where the heat flux has been overestimated have not been identified. One underlying goal of the PACS field program was to

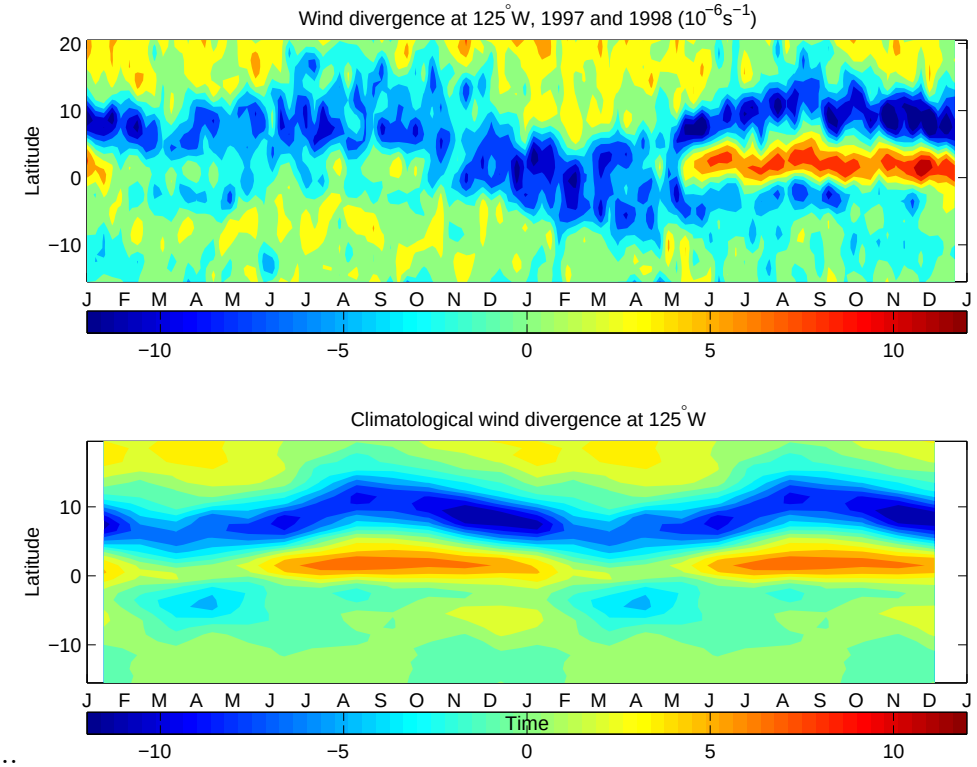

Figure 3-6: Latitude-time plot of wind divergence at 125°W estimated from the IFREMER ERS scatterometer wind product. Upper panel: 1997 and 1998. Lower panel: climatology. The band of wind convergence (i.e. negative divergence) is a rough measure of the location of the ITCZ.

obtain an accurate time series of surface heat and freshwater fluxes to improve our understanding of the processes that influence these fluxes in the eastern tropical Pacific and the way in which the ocean responds to these fluxes.

3.2 Large Scale Surface Fluxes During PACS

One of the strongest ENSO events on record occurred during the PACS field program, and there were substantial deviations from climatological meteorological conditions during the measurement period. To illustrate this, we show a comparison of surface wind divergence during the measurement period to a climatology computed from 8 years of ERS satellite scatterometer data in figure 3-6. Note that the climatology was computed over a period that includes the strong ENSO event of 1997-1998, so differences between the observed and climatological fields are probably underestimated.

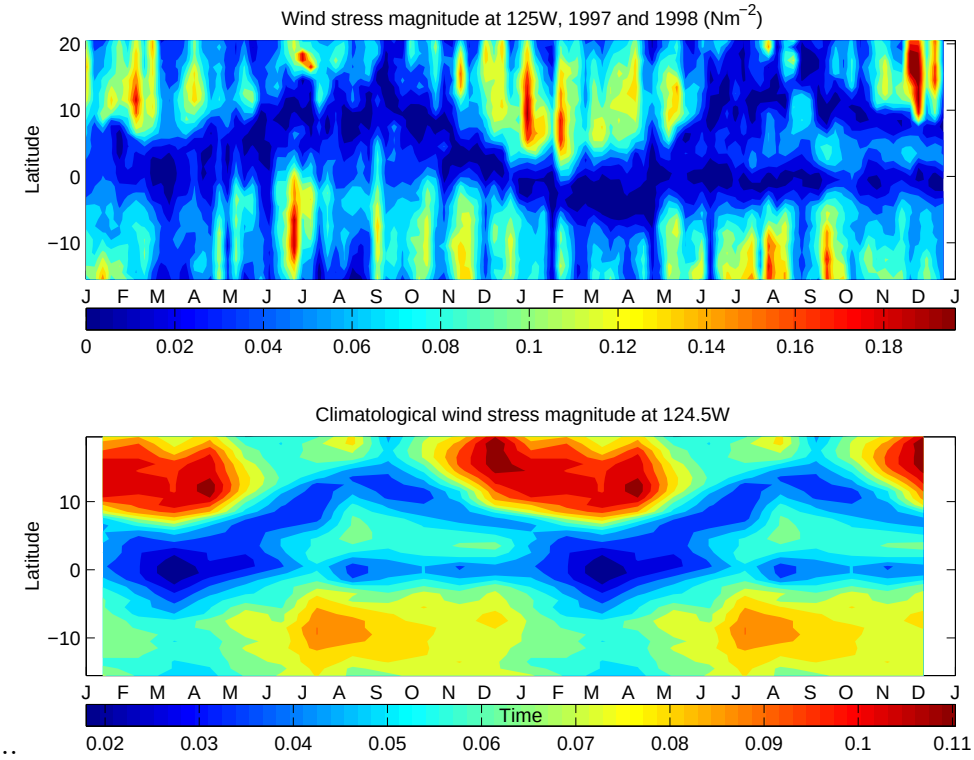

Figure 3-7: Latitude-time plot of wind stress magnitude (N/m^2) from the IFREMER ERS scatterometer wind product. Upper panel: 1997 and 1998. Lower panel: climatology.

Still, we see substantial deviations from the climatological surface wind divergence at the mooring site. Again, taking the surface wind convergence to be an indication of the location of the ITCZ, we can see that the ITCZ reached an anomalously low latitude during the height of El Niño (early 1998) when the equatorial sea surface temperature was anomalously high. Also, the ITCZ had an unusually large meridional extent, spanning more than 10 degrees of latitude during late 1997 and early 1998. A strong "double ITCZ" occurred when the equatorial cold tongue split the large convective zone, and it persisted several months longer than usual. The double ITCZ sometimes occurs in the eastern tropical Pacific when zonal bands of convection appear on both sides of the equator during the boreal spring, and it frequently occurs in association with El Niño. A nice analysis and discussion of the double ITCZ phenomenon is given by Lietzke, et al. (2001).

As we saw in section 3.1, the air-sea flux fields tend to be correlated with the

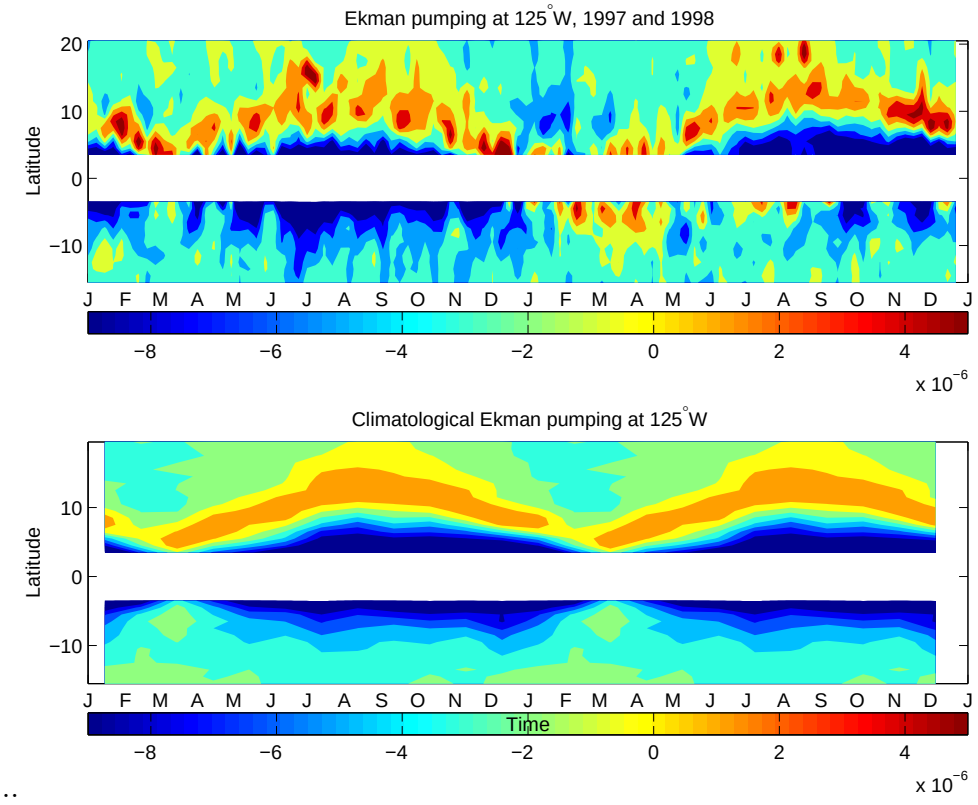

Figure 3-8: Latitude-time plot of Ekman pumping at 125°W estimated from the IFREMER ERS scatterometer wind product. Upper panel: 1997 and 1998. Lower panel: climatology. Values are not shown within 3.5° of the equator.

motion of the ITCZ, and this holds true even during the ENSO event of 1997-98. Figure 3-7 shows a comparison of wind stress magnitude along 125°W during 1997-98 to climatological conditions. The wind stress magnitude is lower under the ITCZ because of the large scale convergence that is feeding convection in the ITCZ. As has already been discussed, the wind stress is usually larger to the north of the ITCZ during the northern hemisphere winter and spring, and we can see that this area of high stress penetrated as far south as 2 or 3°N during February of 1998.

These early 1998 wind anomalies led to substantial Ekman pumping anomalies along 125°W between 5 and 10°N. Figure 3-8 shows a comparison of Ekman pumping along 125°W during 1997-98 to climatological conditions[1]. Note that the Ekman pumping is typically upward under the ITCZ, while it is usually downward outside of the ITCZ. Also note the substantial downward Ekman pumping anomalies between 3 and 10°N during the first two months of 1998. As we will see in chapters 4 and 5, this anomalous Ekman pumping had important effects on the evolution of thermocline depth at the mooring site.

3.3 Observed Surface Fluxes at 10°N, 125°W

The observed precipitation rate and accumulated precipitation at the mooring are shown in figure 3-9, along with the ERS wind divergence. There is a clear seasonal signal in the precipitation rate which corresponds to the presence of the ITCZ (compare figure 3-9 (a) and (b)). September 1997 saw the most accumulation, and the rains began to decrease in frequency and intensity by November and they ended completely by January 1998. There were a few isolated precipitation events in May and June 1998, but the rainy season resumed in earnest around the first of July.

Time series of surface meteorological parameters and air-sea fluxes observed at the mooring site are shown in figures 3-10 and 3-11. The time series have been subjected to a seven day running average to emphasize the low frequency variability.

[1]The Ekman pumping was calculated using the IFREMER ERS scatterometer wind product. This computation will be further described in section 4.2.1.

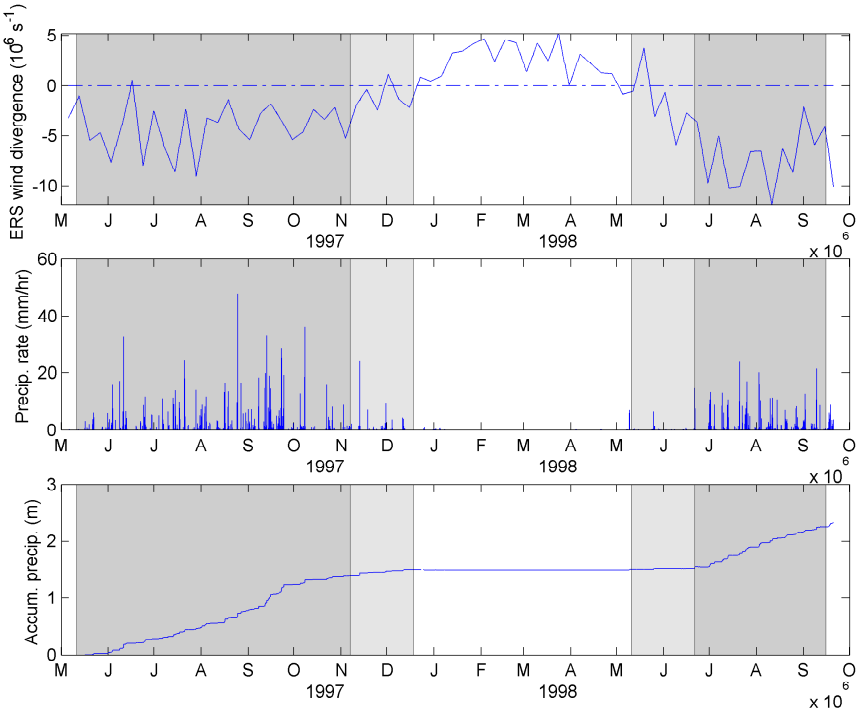

Figure 3-9: Time series of ERS wind divergence (top panel), observed precipitation rate in mm/hr (middle panel), and accumulated precipitation in m (bottom panel) at 10°N, 125°W.

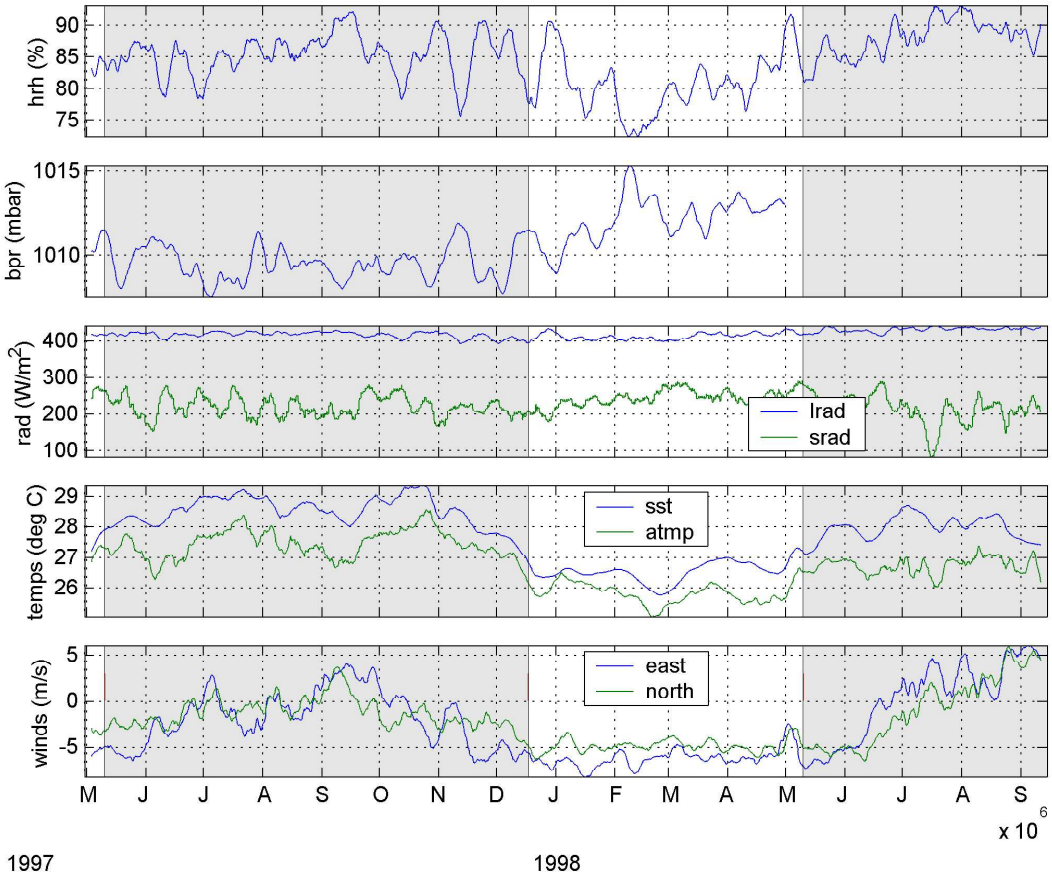

Figure 3-10: Timeseries of observed meteorology at 10°N, 125°W. Times when the ITCZ was over the mooring are shaded.

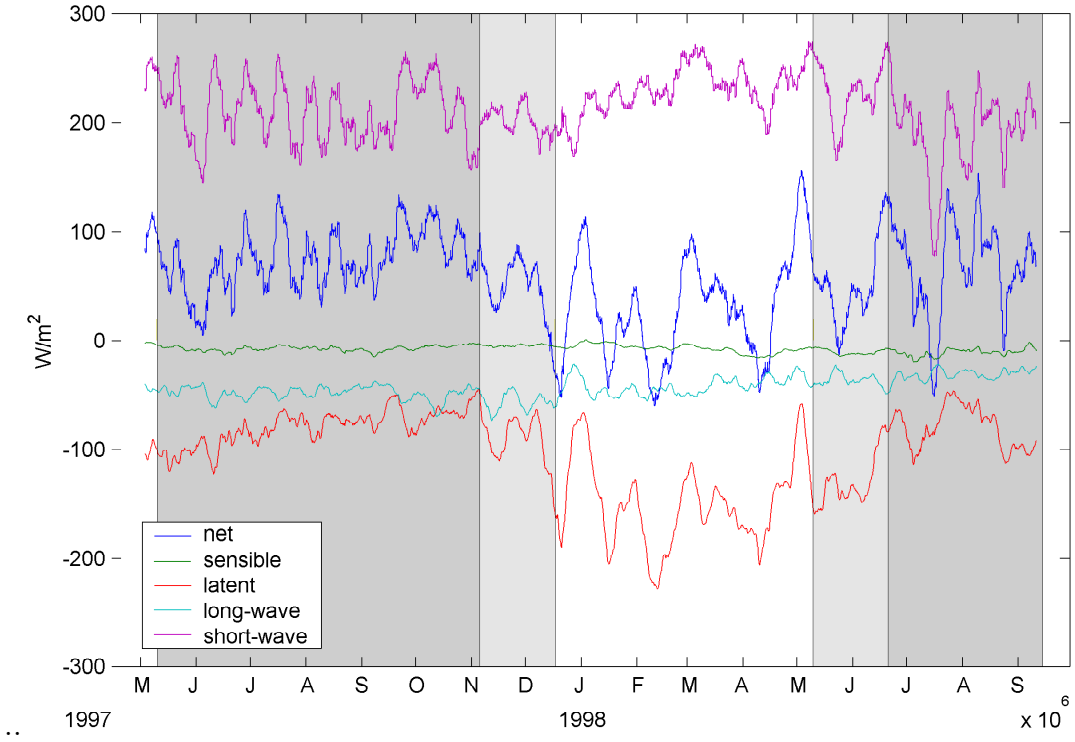

Figure 3-11: Timeseries of estimated heat fluxes at 10°N, 125°W. Times when the ITCZ was over the mooring are shaded.

As in sections 3.1 and 3.2, it is again useful to draw a gross distinction between times when the ITCZ was and was not over the mooring site. Here, we make this distinction based on the measured precipitation rate, which was near zero at the site during the first few weeks of the observation period and again during about the first six months of 1998. Note that these periods both correspond to times when the region of maximum wind stress convergence (figure 3-6) was south of the mooring site. Throughout this study, we will draw heavily on the distinction between ITCZ and non-ITCZ conditions in interpreting the surface and subsurface observations at the mooring site. Indeed, the contrasting oceanic response observed during ITCZ and non-ITCZ conditions constitutes a major theme of this thesis.

During the rainy season of 1997, there was more than 1.5 m of accumulated precipitation. This was a substantial buoyancy flux, but it was not as large as the buoyancy flux due to heating. The surface buoyancy flux into the ocean is given by

(e.g. Gill, 1982, p. 36),

$$B = B_{heat} + B_{freshwater} = c_w^{-1} g\alpha Q + g\beta(P - E)s, \tag{3.1}$$

where Q is the surface heat flux into the ocean (W/m^2), E the evaporation rate (m/s), P the precipitation rate(m/s), c_w the specific heat of water ($Jkg^{-1\circ}K^{-1}$), s the surface salinity, α the thermal expansion coefficient at the surface($^\circ K^{-1}$), and β is the saline expansion coefficient (psu^{-1}). The upper panel of figure 3-12 shows the buoyancy flux (7-day running average). During ITCZ conditions, the weekly-averaged buoyancy flux into the ocean was almost always larger than $5 \times 10^{-5}\ W/m^2$. However, by mid-December 1997 the rains had almost completely ceased and the wind speed had increased; from then through June 1998, the buoyancy flux was highly variable and intermittently fell below zero for periods of a week or more. During the ITCZ conditions of 1998, the buoyancy flux was more variable than in the previous ITCZ season, but the buoyancy flux was generally larger than during non-ITCZ conditions. The middle panel of figure 3-12 shows the contributions to the buoyancy flux by heat flux (blue line) and freshwater flux (green line). Clearly, the contribution to the surface buoyancy flux by heat flux was usually larger than that from freshwater flux. Note that both terms decrease during non-ITCZ conditions (roughly December through May). The bottom panel of figure 3-12 shows the (unsmoothed) surface density at the mooring. We expect the surface buoyancy flux to affect the surface density, but there are many other factors that may cause changes in the surface density. We will further discuss the surface density and the factors affecting it in chapter 4, but, for now, note that the surface density does appear to reflect the surface buoyancy flux on a seasonal timescale.

3.3.1 Seasonal scale variability

Inspection of figures 3-10 and 3-11 suggests that much of the seasonal signal of the observed air-sea fluxes and meteorological variability correlates with the presence of the ITCZ. Surface air and sea temperatures and relative humidity all decrease as the

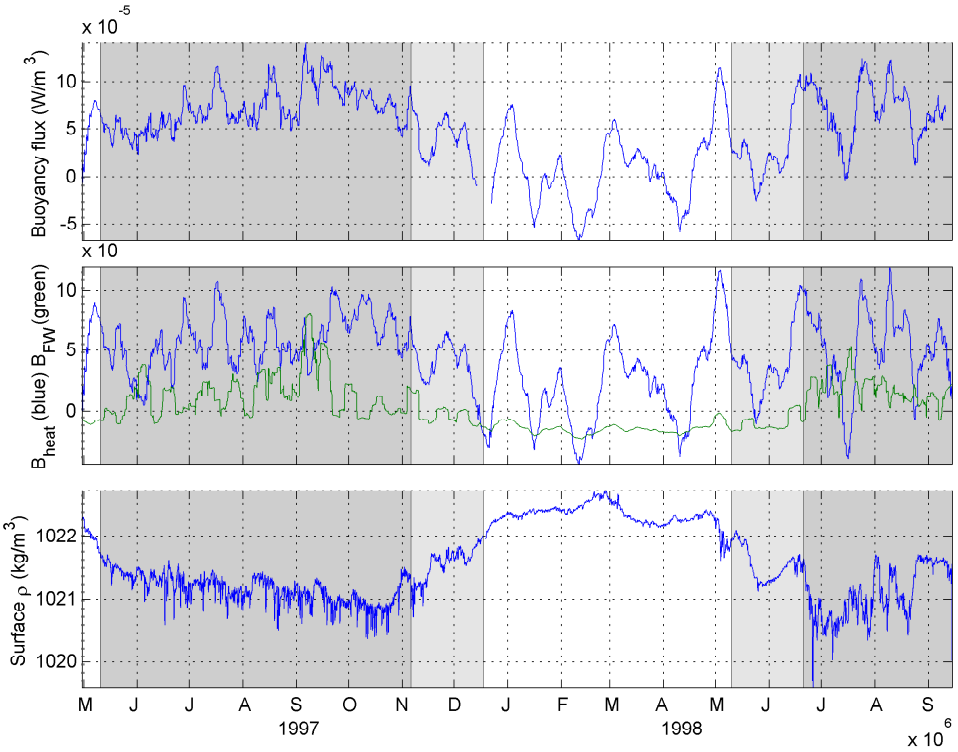

..

Figure 3-12: Upper panel: 7 day running average of observed buoyancy flux (W/m^2). Middle panel: buoyancy fluxes due to heat flux (blue line) and freshwater flux (green line). Lower panel: surface density. Times when the ITCZ was over the mooring are shaded.

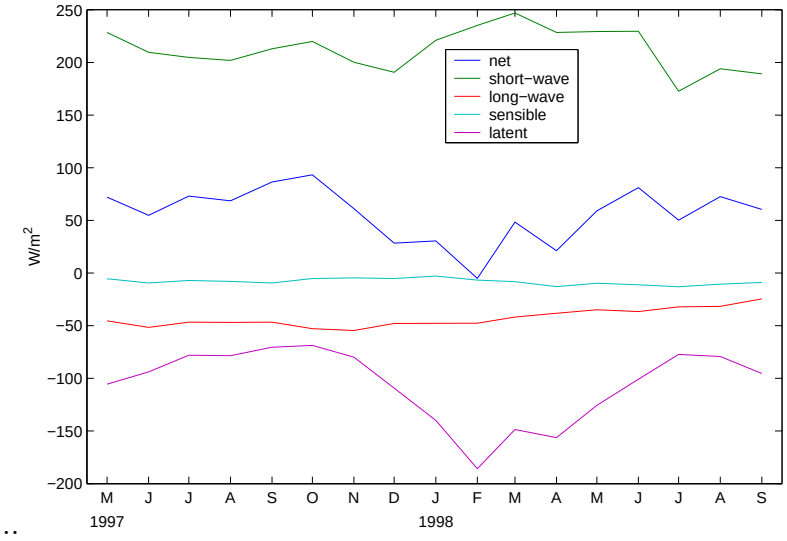

Figure 3-13: Monthly mean heat fluxes at 10°N, 125°W.

ITCZ moves south of the measurement area, while incoming short wave radiation, wind stress magnitude, and barometric pressure increase as the ITCZ moves south. However, some caution is warranted in this interpretation because the time when the ITCZ moves south from the region occurs as the tropical Pacific is beginning to undergo a transition from El Niño to La Niña states, and some of the shifts in meteorological parameters are potentially associated with this transition. Moreover, the southward migration of the ITCZ is likely to depend on oceanic processes through the sea surface temperature, so we should not view the seasonal variation of surface properties as being entirely determined by the motion of the ITCZ. Nonetheless, a basic classification of ITCZ and non-ITCZ conditions is useful for characterizing and discussing the surface variability.

The monthly mean heat fluxes at the mooring site are shown in figure 3-13. The short-wave and latent heat fluxes are the largest contributors to the net heat flux, as the long-wave and sensible heat fluxes both exhibit relatively small magnitude and variation. The short-wave heat flux increased as the ITCZ moved south of the mooring, but at the same time the magnitude of the winds and latent flux also increased from low levels. This substantial increase in evaporative heat flux was enough to counteract the relatively slight increase in solar heat flux so that the net

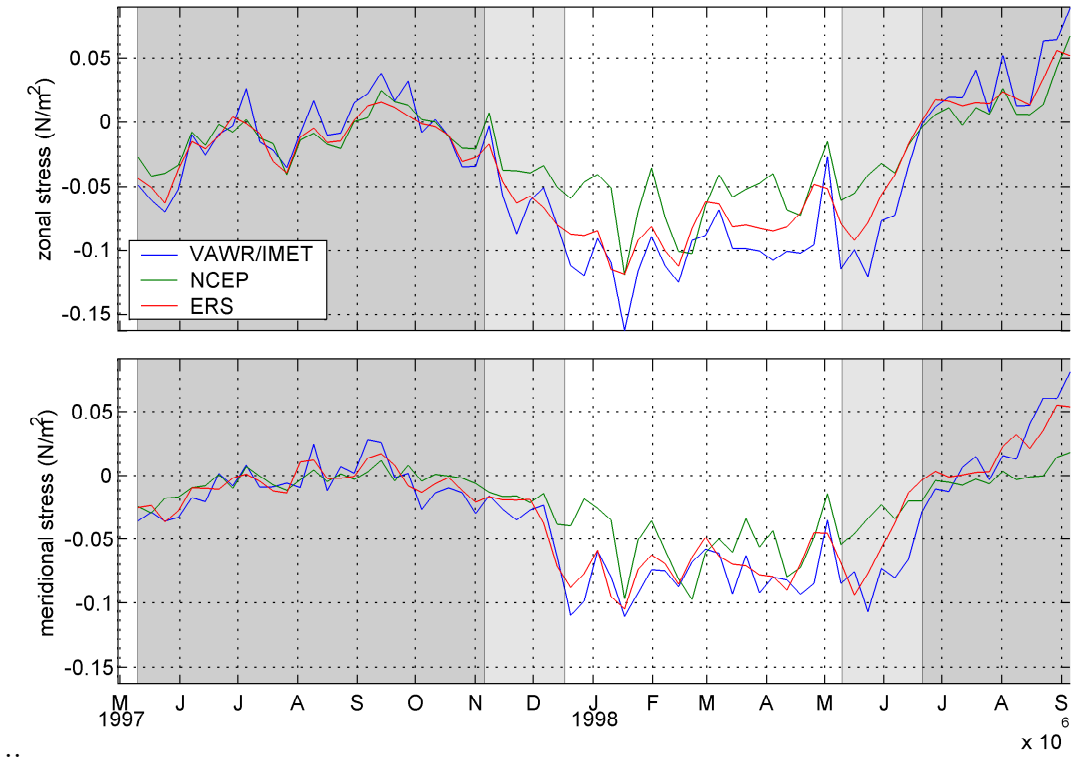

Figure 3-14: Comparison of the ERS scatterometer and NCEP reanalysis wind stress (N/m^2) to that estimated from observations at 10°N, 125°W. Upper panel: zonal stress. Lower panel: meridional stress.

heat flux was actually lower during the relatively clear skies of the non-ITCZ season. In the next subsection, we will quantify the relative roles of short-wave and latent heat flux in determining the net heat flux during ITCZ and non-ITCZ conditions.

The weekly averaged zonal and meridional wind stress components are shown in figure 3-14. For comparison, the weekly averaged NCEP reanalysis and ERS wind stresses are also shown. The zonal and meridional components of the wind stress were generally comparable. Aside from bursts of high stress in August and September 1998, the wind stress was generally smaller during ITCZ conditions. The return of the northeast trade winds occurs when the zonal and meridional stresses rapidly increase during the first few weeks of December 1997. The ERS wind stress compares favorably to that measured at the buoy. The NCEP reanalysis stresses are very close to the observed stresses during the ITCZ season of 1997, but they exhibit a substantial bias (0.01 to 0.07 N/m^2) toward smaller values during non-ITCZ conditions.

3.3.2 Intermediate frequency variability

Inspection of figure 3-11 suggests that the short-wave heat flux exerted more influence on the variation of the net heat flux while the ITCZ was over the mooring, while the latent heat flux appears to be more important to the net heat flux during non-ITCZ conditions. Fourier and wavelet time series analysis supports this conclusion. Based on the measured presipitation rate, the record was divided into separate time series for ITCZ and non-ITCZ conditions. We then computed the coherence amplitude and phase of the net heat flux with the various heat flux components as a function of frequency using a Fourier transform method. We estimated the level of no significance at 95% using Monte Carlo simulations against white noise in order to identify statistically significant coherence. We also computed the wavelet coherence and phase using the full record following Torrence (1999). The two methods produced similar results.

Strictly speaking, a high correlation between two variables does not imply that one variable controls the other. However, in this case, we know all of the terms that contribute to the net heat flux, and we have seen that the dominant contributions are from the latent and short-wave heat flux. When only one of these contributions is coherent with the net heat flux on a given time scale, we can say with confidence that this contribution is controlling the variability of the net heat flux on that time scale.

The relationship of the latent and short-wave heat flux to the net heat flux can be conveniently illustrated using the wavelet coherence and phase (Torrence, 1999), which can give the the coherence as a function of frequency and time. Figure 3-15 shows the coherence of the short-wave heat flux with the net heat flux, while figure 3-16 shows the coherence of the latent heat flux with the net heat flux. Clearly, the short-wave heat flux is more highly correlated with the net heat flux on 2 to 30 day time scales during ITCZ conditions than during non-ITCZ conditions. Conversely, the latent heat flux is more highly correlated with the net heat flux during non-ITCZ conditions. In fact, the presence of the ITCZ at the mooring can be inferred

directly from the coherence amplitudes shown in figures 3-15 and 3-16; the statistical transition from ITCZ to non-ITCZ conditions is apparent. The solid black curves in the lower corners of each panel mark the region where edge effects limit the reliability of the coherence estimate (also called the 'cone of influence'). In a sense, this is the response of the wavelet transform to a delta function or a discontinuity. We see this shape, for example, in the transition from ITCZ to non-ITCZ conditions (i.e. around December) in figure 3-15. This suggests that the transition from ITCZ to non-ITCZ conditions occurred rather abruptly around December 1997.

Time-series analysis of the estimated heat fluxes suggests that short-wave heat flux dominates the variability of the net heat flux on time scales from 2h to 20 days while the ITCZ is overhead (mid-May to December, 1997). However, during non-ITCZ conditions (January to June, 1998), latent heat flux plays a more significant role than short-wave heat flux in determining the variability of the net heat flux on 2 to 15 day timescales. This result is not counterintuitive; the decreased winds and increased cloudiness associated with the ITCZ serve to reduce evaporation and increase variation in insolation, while the high winds of the dry season increase the importance of evaporative cooling. During this period of lower relative humidity and higher winds, evaporation, rather than short-wave radiation, controlled the variability of the net heat flux. Then, in mid-June, the rains and clouds of the ITCZ returned, and short-wave heat flux once again dominated variability of the net heat flux on timescales from 2 hours to 16 days.

3.4 Summary

Buoyancy and momentum fluxes at the site contrasted dramatically between ITCZ and non-ITCZ conditions. Mean buoyancy fluxes were lower (or even negative) and momentum fluxes were higher during non-ITCZ conditions. While the ITCZ was over the mooring site, the monthly mean net heat flux into the ocean was 50-90 W/m^2 and the wind stress was weak. When the ITCZ was south of the mooring, the wind stress was stronger and evaporation played an important role in modulating the net heat

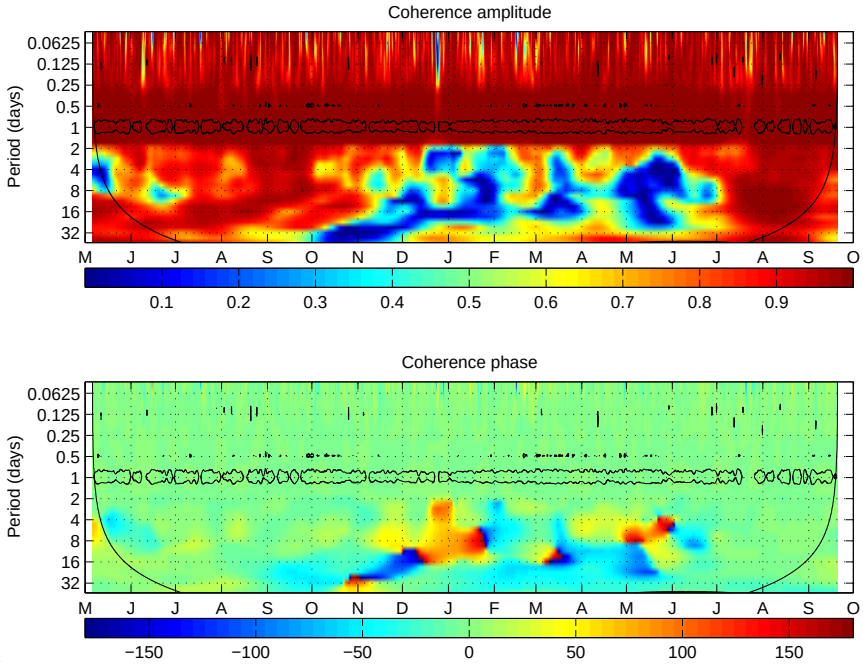

Figure 3-15: Wavelet coherence of short-wave heat flux with net heat flux. (a) Coherence amplitude. (b) Coherence phase (degrees).

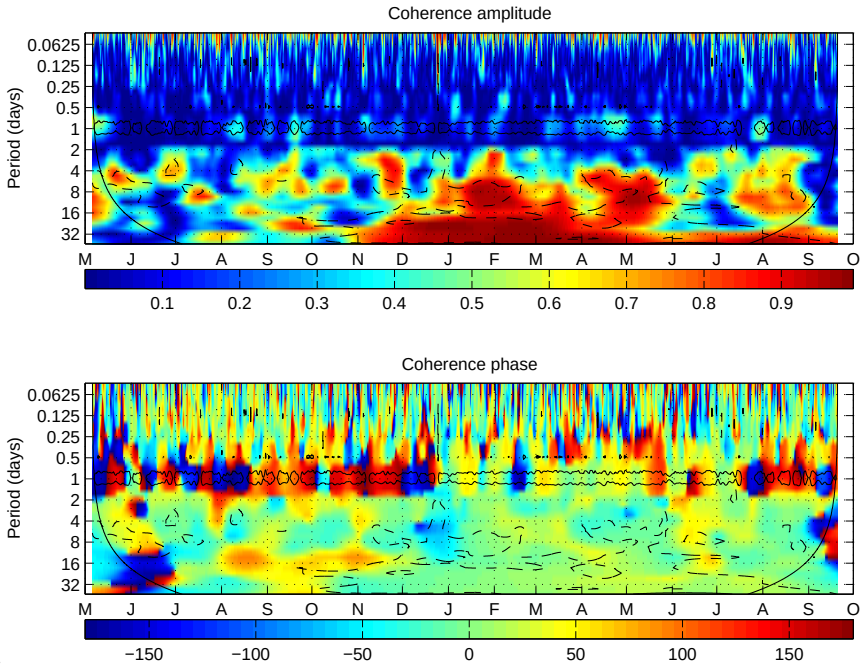

Figure 3-16: Wavelet coherence of latent heat flux with net heat flux. (a) Coherence amplitude. (b) Coherence phase (degrees).

flux, causing the monthly mean heat flux to be between 0 and 50 W/m^2. Precipitation only occurred when the ITCZ was over the mooring, and evaporation was enhanced when the ITCZ was south of the mooring. So, the net buoyancy flux was larger when the ITCZ was over the mooring, but the momentum flux was significantly smaller.

Chapter 4

Oceanic Response at 10°N, 125°W

In this chapter, we present and discuss the observed upper ocean evolution and examine the mechanisms contributing to its variability. Section 4.1 describes the observed behavior at the moorings, sections 4.2 and 4.3 analyze the remote and local physical mechanisms contributing to the variability in the observations. Chapter 5 will address the relationship between the observed forcing and the local oceanic response using a one-dimensional model of the upper ocean. We will ultimately conclude that the dominant mechanisms affecting the mixed layer and main thermocline at the mooring site are Ekman pumping, surface heat flux, and vertical mixing.

4.1 Overview of Observed variability

This section summarizes the variability of the observed surface properties and upper ocean temperature and velocity structure. The first subsection presents the observed surface behavior, the second subsection presents the observed subsurface temperature and salinity structure, and the final subsection presents the observed velocity.

4.1.1 Variability of surface properties

Figure 4-1 shows the observed sea surface temperature (SST) and sea surface salinity, along with the corresponding sea surface density. In chapter 3, it was shown that the

net surface heat flux was larger during the rainy season (relative to the dry season) because the lower winds led to lower evaporative heat loss from the sea surface. This seasonal variation in surface heat flux is partially reflected in the variation of SST during the observing period, though the SST at the site was also affected by entrainment and advection. As will be discussed in section 4.3 and chapter 5, much of the cooling that occurs late in 1997 can be attributed to mixing processes which entrain cooler water from depth. The maximum recorded SST value of 30.79°C was reached around local solar noon on June 18, 1997.

The sea surface salinity also shows a clear seasonal signal, but just as the surface temperature cannot be entirely explained by the surface heat flux, this seasonal signal cannot be explained in terms of the surface flux of freshwater alone. The surface salinity tends to decrease from May 1997 to September 1997, reflecting the frequent rains and low evaporation of the rainy season. However, the surface salinity begins a long term (seasonal) increasing trend around October/November of 1997 despite the fact that it rained frequently until December.

The surface density was computed using the UNESCO equation of state[1] (Fofonoff and Millard, 1983) from the observed surface temperature and salinity. On a seasonal timescale, the anti-correlation of SST and surface salinity led to a large seasonal cycle in surface density, since increasing temperature and decreasing salinity both serve to decrease density. While SST is important to atmospheric dynamics, surface density is more important to oceanic dynamics, and the observed surface density range of about 2 $\frac{kg}{m^3}$ is remarkably large given that the potential density difference from the surface to 4000 m depth at this location is less than 6 $\frac{kg}{m^3}$.

Surface salinity and SST are generally more highly variable during ITCZ conditions; the diurnal cycle in SST typically exceeds 0.5°C, and surface salinity can vary by more than 0.5 psu over a day in association with precipitation events. As was discussed in chapter 3, the wind stress was typically smaller during ITCZ conditions, and we expect that the low winds and large positive buoyancy flux will contribute to

[1]The computer program used to carry out the calculation was provided by Phil Morgan and the (Austrailian) Commonwealth Science and Industrial Research Organization (CSIRO) as part of the 'seawater toolbox' for Matlab.

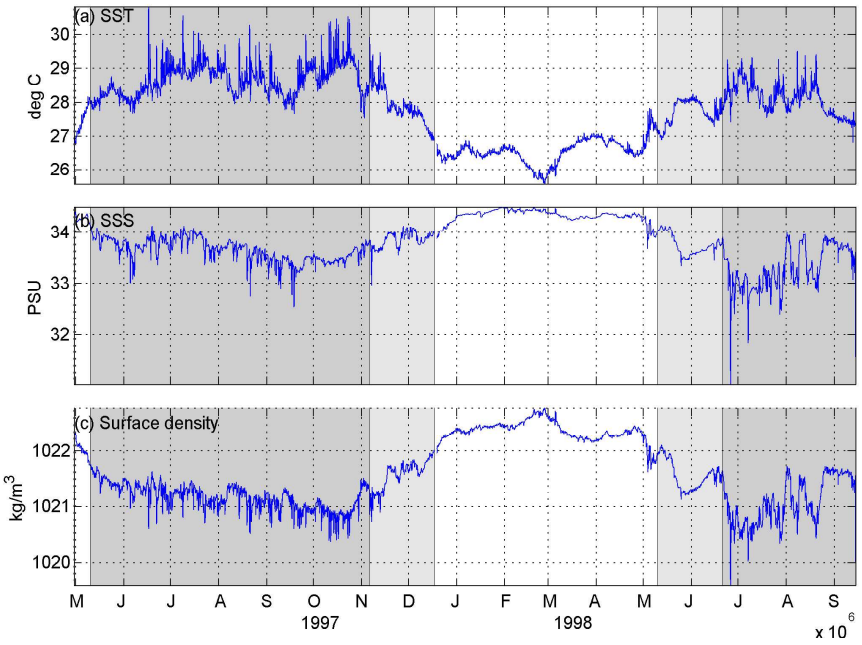

..

Figure 4-1: (a) Observed sea surface temperature, (b) observed sea surface salinity, and (c) sea surface density at 10°N, 125°W. ITCZ conditions are marked by dark shading, and light shading indicates the transition between ITCZ and non-ITCZ seasons.

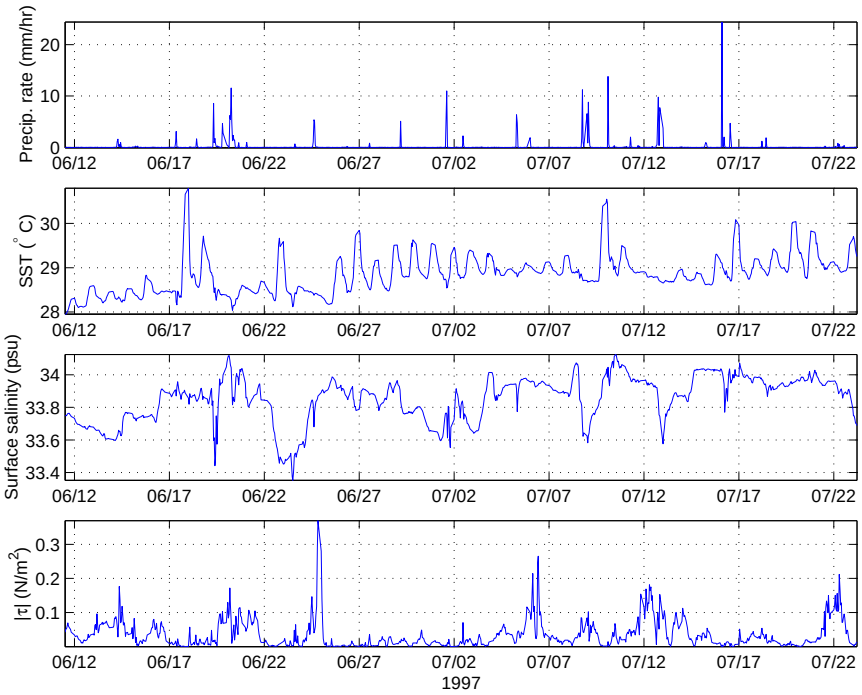

Figure 4-2: ITCZ conditions: (a) Observed precipitation rate, (b) observed SST, and (c) sea surface salinity, and (d) wind stress magnitude at 10°N, 125°W.

a shallow, stable mixed layer. Figure 4-2 gives a detailed depiction of precipitation rate, SST, surface salinity, and wind stress magnitude over a 40 day period while the ITCZ was over the mooring. The record-maximum SST was reached on June 18, 1997 as the SST increased by more than 2°C during the morning. Although precipitation can produce a thin buoyant layer of water at the surface which can inhibit mixed layer entrainment and facilitate a rapid surface warming (Anderson et al., 1996), the times of large diurnal cycling of SST appear to correspond more closely to periods of low winds than to precipitation events. Similarly, periods of relatively high winds tend to exhibit relatively small daily SST cycles.

Figure 4-3 shows SST, surface salinity, and wind stress magnitude over a 40 day period during non-ITCZ conditions. In contrast to ITCZ conditions, the diurnal cycle in SST during non-ITCZ conditions was much smaller, having a typical value of 0.1°C (note that the scale for SST is about three times smaller in figure 4-3 than in 4-2). In part, this is related to the much larger mixed layer depth during the relatively dry, windy, and cool non-ITCZ season. Since active mixing serves to distribute most of

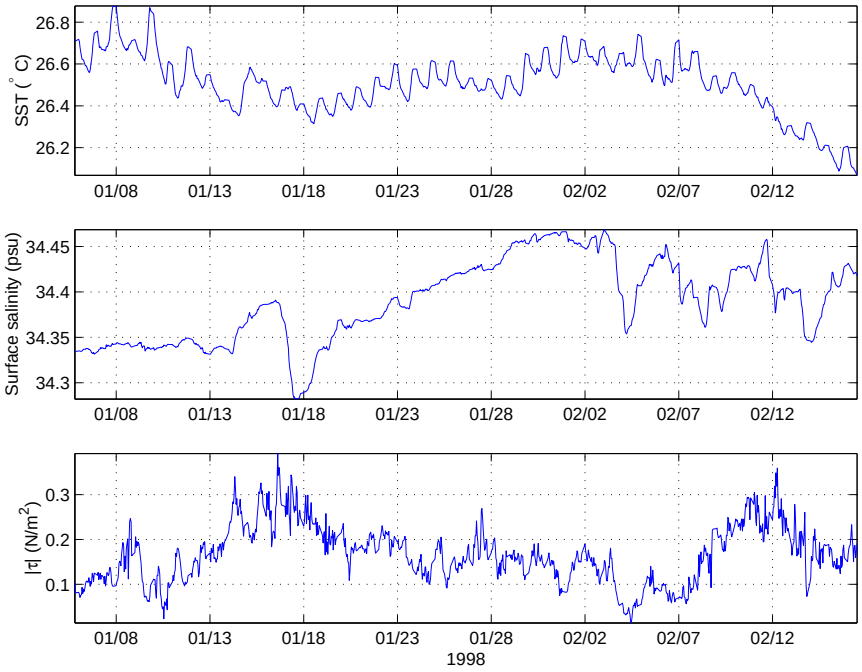

Figure 4-3: Non-ITCZ conditions: (a) Observed SST, (b) sea surface salinity, and (c) wind stress magnitude at 10°N, 125°W. The precipitation rate was zero during the time period shown.

the surface heat flux uniformly over the mixed layer, a given surface heat flux will produce a smaller temperature change in a deeper mixed layer.

4.1.2 Variability of temperature and salinity structure

Figure 4-4 shows a time series of observed isotherm and mixed layer depth (determined by a potential density criterion of $\Delta\sigma_0 = 0.05\ kg/m^3$). The time series has been subjected to a seven-day running average to emphasize the long term variability. The isotherms in the figure were chosen to be representative of the thermocline. The 20°C isotherm depth is thought to be a good proxy for thermocline depth in the tropical Pacific (Kessler and Taft, 1987). The most outstanding feature in the temperature record is the rapid drop-off of the thermocline that occurs between mid-January and mid-February of 1998. During this month-long period, the thermocline fell from near 45 m to near 75 m, descending at a rate of about $1.16 \times 10^{-5} \frac{m}{s}$ (i.e. $1\ m/d$). The physical mechanisms that could be responsible for this change in thermocline depth

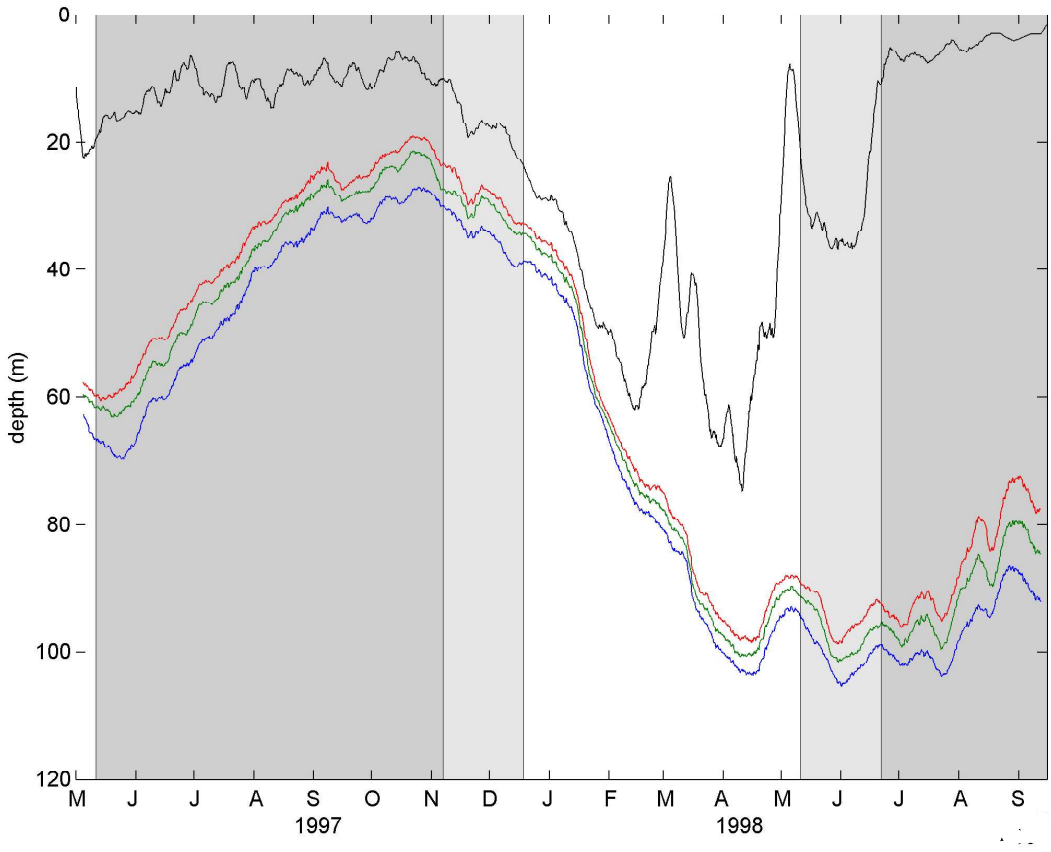

Figure 4-4: Isotherm depth and 7-day averaged mixed layer depth time series at 10°N, 125°W. The blue, green, and red lines represent the 19, 22, and 24 degree isotherms, respectively. Dark shading denotes ITCZ conditions, and light shading indicates transition between ITCZ and non-ITCZ seasons.

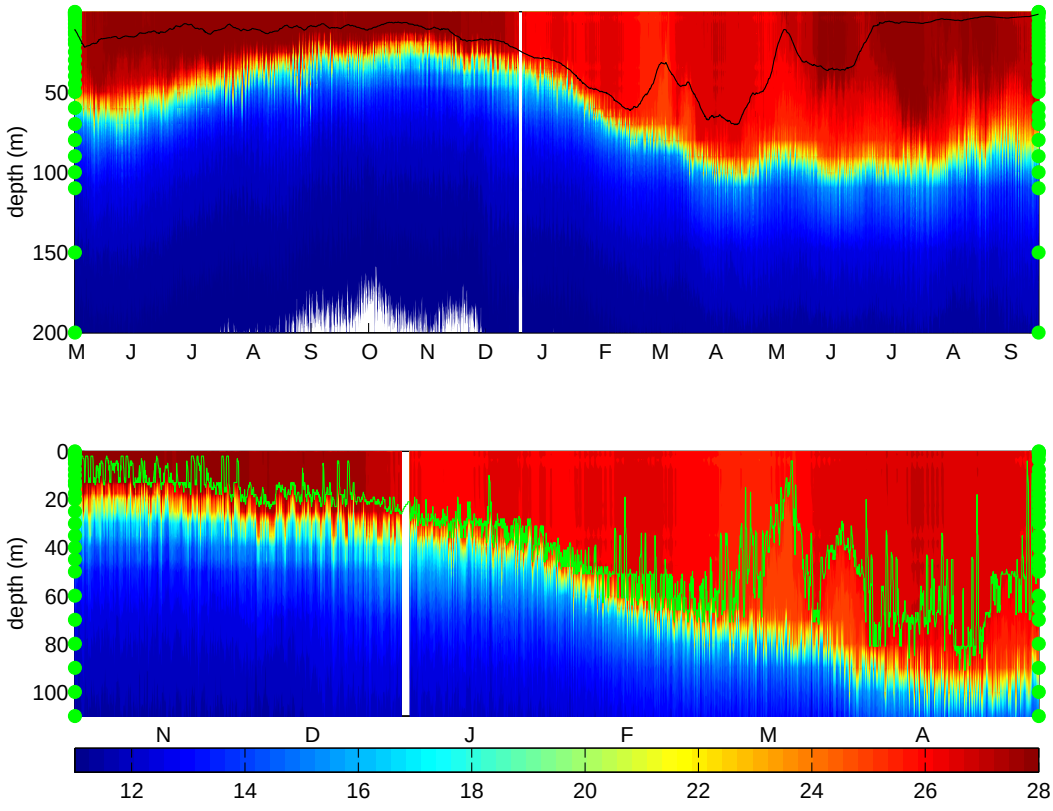

Figure 4-5: Upper panel: Observed temperature evolution as a function of depth and time at 10°N, 125°W. The 10-day averaged mixed layer depth is also shown (black line). Lower panel: A close-up of temperature evolution and mixed layer depth time series (no smoothing; green line) during the time of most rapid thermocline deepening. In both panels, the white line marks the mid-study mooring recovery and redeployment.

can be broadly classified as surface heat flux, advection, or turbulent heat flux due to mixing. An important goal of this thesis is to specifically identify the processes that caused this rapid descent of the thermocline and the nearly coincident changes in SST and sea surface salinity. The surface heat fluxes were presented in chapter 3. After presenting the the subsurface salinity and velocity observations, we will address the role of advection and turbulent heat flux in sections 4.2 and 4.3. As with the SST and surface salinity, it will be argued that local mixing processes play an important role in this rapid change in the depth of the thermocline.

A more detailed view of the temperature evolution at the site is shown in figure 4-5. The 10-day running averaged mixed layer depth[2]is also shown. Note that, much like

[2]Again, mixed layer depth was determined by a potential density criterion of $\Delta\sigma_0 = 0.05\ kg/m^3$.

the SST, the mixed layer temperature is typically higher during ITCZ conditions. However, the mixed layer temperature does begin to decrease as the mixed layer deepens during the last 1-2 months of the ITCZ period (i.e. November/December 1997). Also, the base of the mixed layer lies nearer to the thermocline during the deepening period.

In the lower panel of figure 4-5, we focus on the oceanic transition from ITCZ to non-ITCZ conditions. The mixed layer depth (at hourly resolution) is also shown (green line). The choice of a mixed layer depth criterion of $\Delta\sigma_0 = 0.05\ kg/m^3$ is slightly larger than ideal, but it is mandated by imperfect inter-sensor calibration; consequently, this criterion does not adequately represent the diurnal cycle of the depth of the actively mixing layer (e.g. Brainerd and Gregg, 1995). This criterion can capture very strong diurnal stratification cycles, but during times of weak diurnal cycling the criterion gives something closer to a maximum daily mixed layer depth. The period of most rapid deepening of the thermocline was during January 1998. It is noteworthy that, aside from the fairly steady deepening of the mixed layer, the mixed layer depth was less variable during the period of rapid thermocline deepening. This suggests that the diurnal cycle of re-stratification was weak during the period of rapid thermocline deepening. Furthermore, the mixed layer was almost always within 10 m of the thermocline during this period. While there are various conceivable mechanisms that might cause this coincident deepening of the mixed layer and thermocline, the cooling of the mixed layer and its near proximity to the cooler thermocline suggest that entrainment may have played an important role in both the deepening of the thermocline and the cooling of the mixed layer.

The salinity structure at the site is illustrated in figure 4-6. Note that the near surface salinity values qualitatively reflect the presence of the ITCZ with lower salinity during the rainy season. As was discussed in chapter 2, two of the Sea-Bird SEACAT instruments failed to return data during the first leg of the field program, so the gross vertical salinity structure was not resolved during the first seven months of the observing period. During the second phase of the field program, there were eight

Unless otherwise stated, this is how the mixed layer depth is computed throughout this thesis.

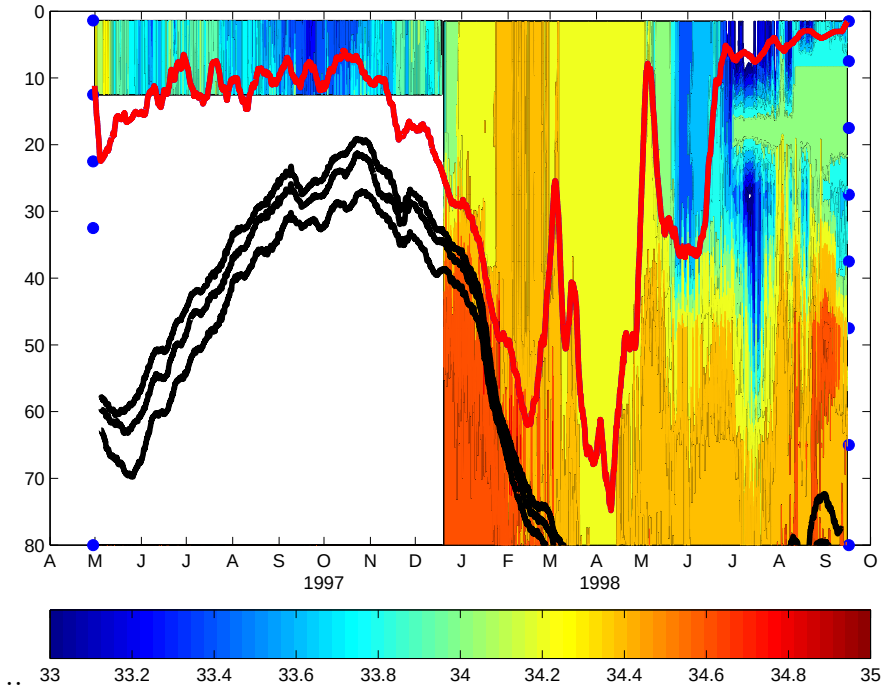

Figure 4-6: Observed salinity structure at 10°N, 125°W. The 19, 22, and 24 degree isotherms (black lines) and estimated mixed layer depth (red line) from figure 4-4 are over-plotted for reference. Sensor locations during the two phases are indicated by blue dots on the left and right edges of the figure, and the color scale is in psu.

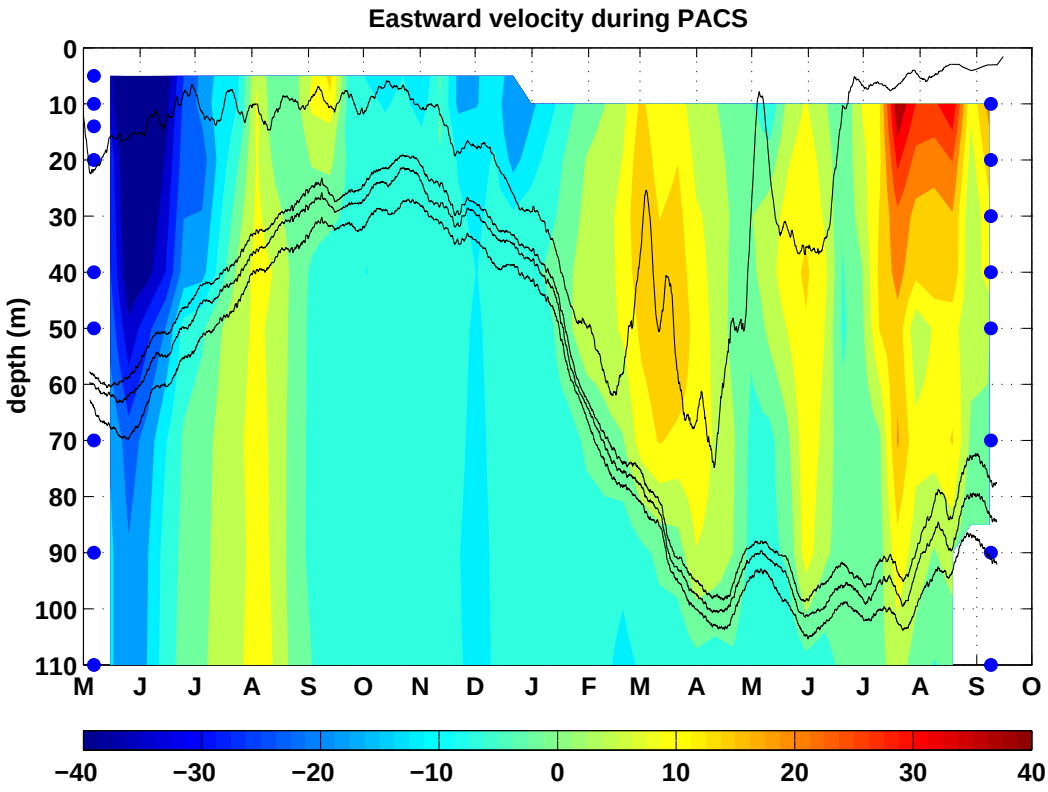

Figure 4-7: Depth-time plot of 10-day averaged zonal velocity at 10°N, 125°W. Current meter locations during the two phases are indicated by blue dots on the left and right edges of the figure. The 19, 22, and 24 degree isotherms and estimated mixed layer depth are indicated by black lines.

functioning conductivity sensors in the upper 80 m. Temperature and salinity are well correlated, and there is an increase in halocline depth coinciding with the rapid change in thermocline depth. Notice that the salinity is higher below the thermocline and that the mixed layer salinity increases abruptly in late January as the mixed layer and thermocline deepen.

4.1.3 Variability of velocity structure

There were ten vector measuring current meters (VMCMs) in place between 5 m and 110 m depth during the first phase of the field study, and there were nine VMCMs in place between 10 m and 110 m during the second phase. Figures 4-7 and 4-8 show ten-day averages of the measured velocity components at the mooring site. The ten day averaging period was chosen to emphasize the sub-inertial variability, as the

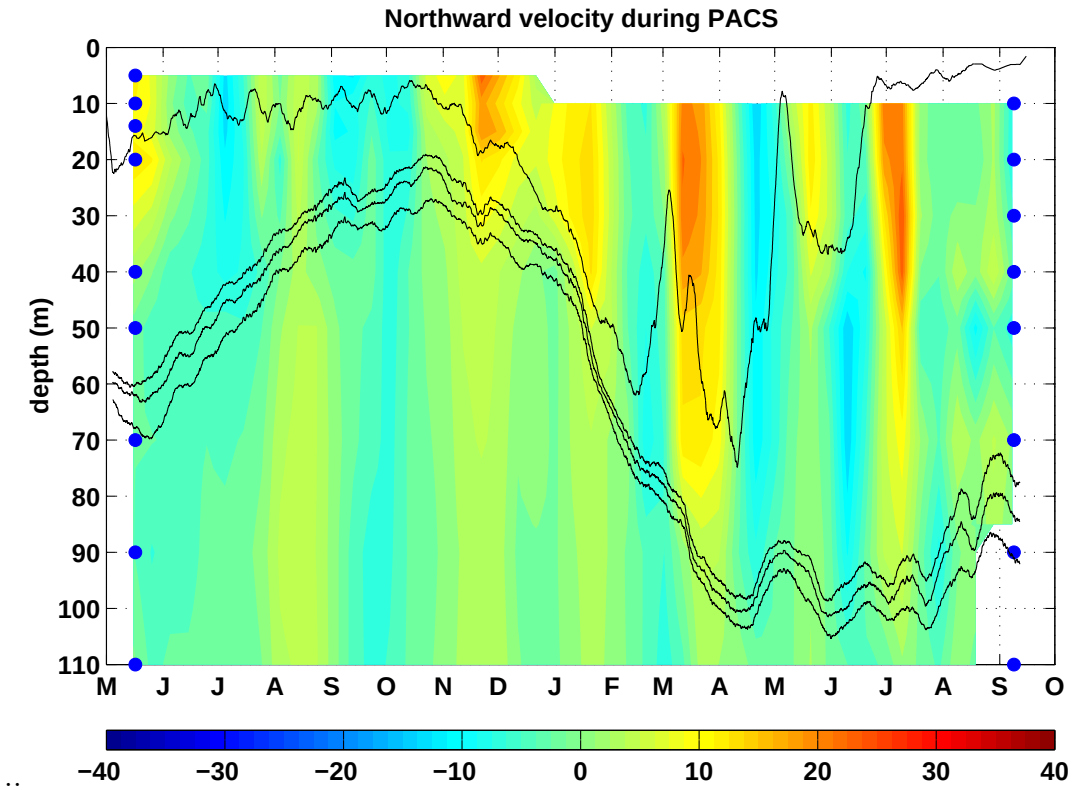

Figure 4-8: Depth-time plot of 10-day averaged meridional velocity at 10°N, 125°W. Current meter locations during the two phases are indicated by blue dots on the left and right edges of the figure.

inertial period is about 2.8 days at 10°N. The current meter depths for the respective measurement periods are shown on the left and right sides of the velocity plots (figures 4-7 and 4-8).

Some fairly intense low frequency zonal flows (approaching speeds of $40 cms^{-1}$) were registered at the mooring during May and June, 1997 and during July and August, 1998 (figure 4-7). The strong flow in the early summer of 1997 was westward and it was at almost full strength from the surface to 50 m depth. However, the strong flow in the summer of 1998 was eastward, and the strength of the signal attenuated rapidly between the surface and 20 m depth, even though the thermocline was much deeper during 1998. The meridional velocity (figure 4-8) exhibits a remarkable oscillatory pattern that appears to have a period of about two months. This signal looks like it might be due to a baroclinic Rossby wave; this possibility will be addressed in section 4.2.2. Aside from the two periods of strong zonal currents discussed earlier, the low frequency meridional currents are comparable in size to the zonal currents; both are typically 10 to $20 cms^{-1}$.

The velocity record is rich with near inertial wave activity, as can be seen in figure 4-9, which shows a few weeks of the velocity record (with no smoothing in time). Quantitative verification that this inertial frequency variability is due to near-inertial waves is given by the rotary auto-spectra of velocity. Figure 4-10 shows the rotary component auto-spectra of the velocity as a function of depth computed over an 85 day period starting around Feb 1, 1998. The velocity record exhibits a clear predominance of clockwise rotating velocities with near-inertial frequency. The reasonably dense sampling of velocity in time and depth allows for an analysis of shear as a function of depth and frequency; this will be presented in section 4.3. Another noteworthy feature of figure 4-10 is that the M_2 tidal power decreases below the thermocline, which implies that some of the observed M_2 tidal motions are baroclinic.

Further insight into the evolution of the the frequencies contributing to the velocity record can be obtained using a wavelet spectral analysis. Estimation of the wavelet power spectrum (WPS) yields information about the power in a given frequency band as a function of time (by decomposing the time series into time-frequency space). The

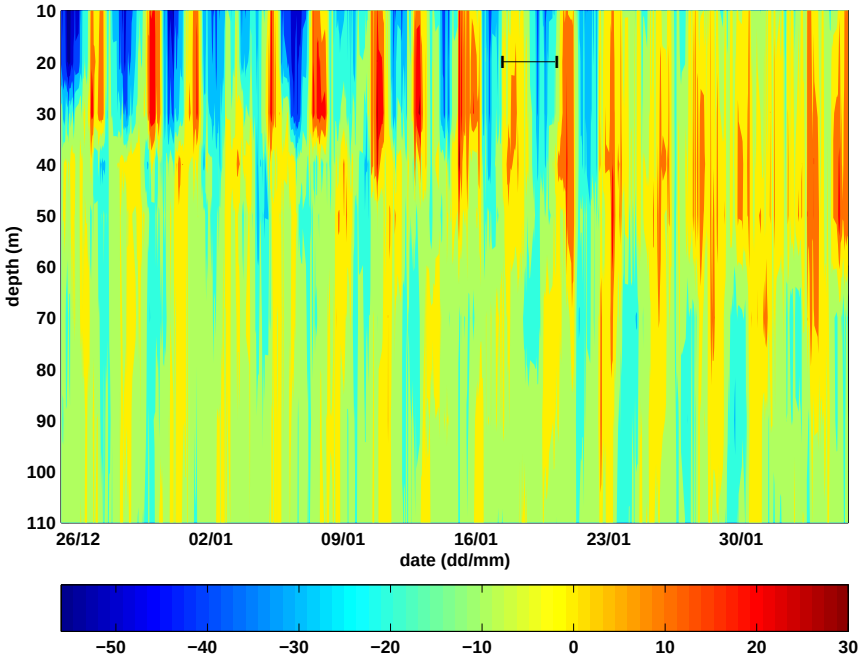

Figure 4-9: Depth-time plot of observed meridional velocity for a 42 day period beginning December 19, 1997. The inertial period is about 67 hours and is indicated by a horizontal bar.

same result could be achieved using conventional Fourier analysis, but the evolution of the power spectrum through time is an automatic result of the wavelet analysis. So, the wavelet spectrum constitutes a convenient vehicle for examination of the non-stationary velocity time series. Estimation of the WPS and levels of no significance has been performed using the continuous wavelet transform following Torrence and Compo (1998)[3]. Briefly, the continuous wavelet transform is the convolution of the time series with the wavelet function, and the level of no significance is estimated by Monte Carlo simulation using a theoretically derived red-noise wavelet spectrum. In addition, we attempted to reduce spurious edge effects by padding the edges of the time series with zeros (until its length is a power of two) and taking account of the so-called 'cone of influence' (the $t(\omega)$ for which edge effects are important). We used a Morlet wavelet for the calculations presented here because its wavelike pattern makes it appropriate for examination of wavelike behavior; the well defined period of

[3]Wavelet software was provided by C. Torrence and G. Compo, and is available online at "URL: http://paos.colorado.edu/research/wavelets/".

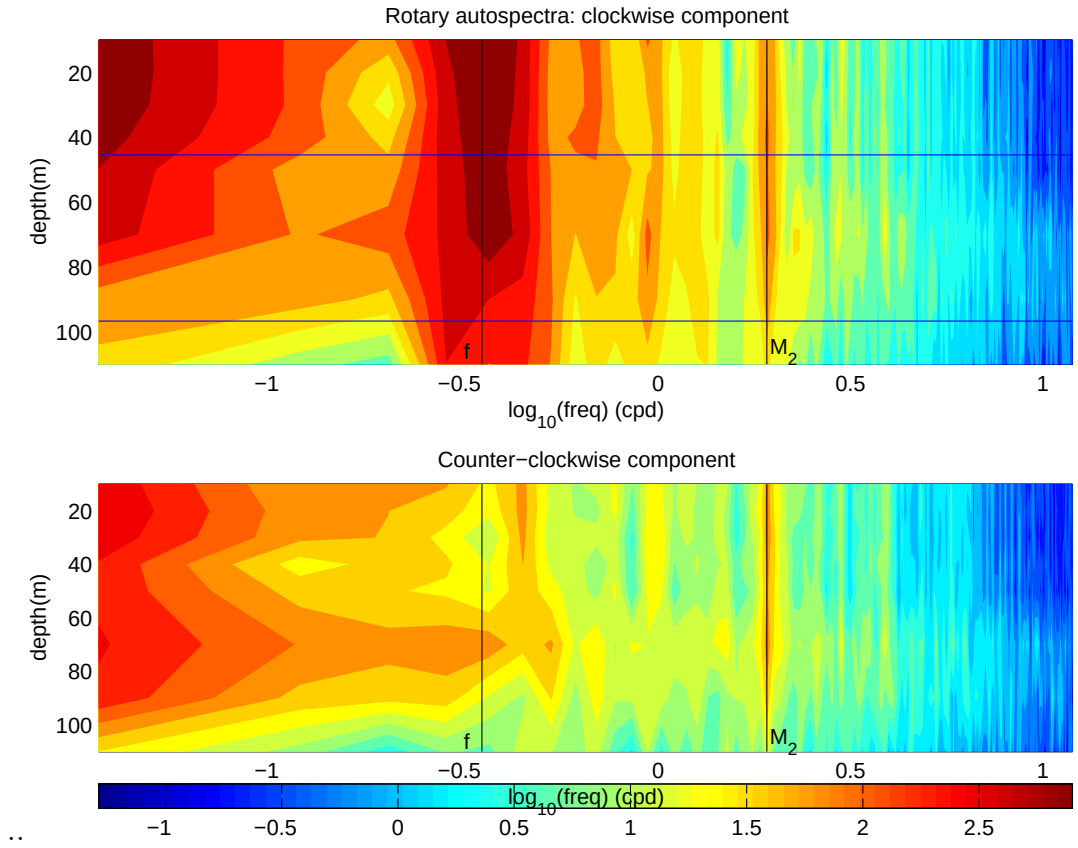

Figure 4-10: Frequency-depth plot of the rotary component auto-spectra of observed velocity; the color scale is in units of log_{10} of power density. The top panel shows the clockwise component, and the bottom panel shows the counter-clockwise component. In the top panel, the average mixed layer depth (upper blue line) and the average 19°C isotherm depth (lower blue line) are shown for reference. The spectra were computed over the 85 day period spanning Jan, 29 to May 12, 1998 . The inertial and M_2 tidal frequencies are marked by vertical lines.

this wavelet facilitates unambiguous interpretation of periods in the wavelet power spectrum (Torrence and Compo, 1998).

Figure 4-11 shows the wavelet power spectra (WPS) for the meridional velocity component at 40 m. The normalized northward velocity at 40 m is shown in figure 4-11(a). We can see in figure 4-11(b) that there was statistically significant power in the near inertial band much of the time. Also, there is statistically significant power in the 30-130 day range, with a distinct maximum that transitions from about 60 days in mid-December to about 50 days by mid-June, corresponding to the apparent periodic 50-60 day signal that appears in figures 4-8 and 4-11(a). The global wavelet spectrum (4-11(c)) shows that the time average power of the meridional velocity peaks near 60 days. Figure 4-11(d) provides a more graphical illustration of the time evolution of the power in the two dominant frequency bands in the meridional velocity record; here, we can see that the power in both the near-inertial (2.5 to 3 day) and intraseasonal (50 to 70 day) frequency bands becomes elevated in late 1997 and early 1998[4].

Variability near 10°N with a 60 day period has been identified in a handful of observational studies (Miller et al., 1985; Perigaud, 1990; Giese et al., 1994). All of these studies used satellite altimetry data, except the analysis of Miller et al., which used 14 months of inverted echo sounder data to compute dynamic height. These studies noted a seasonality to the variability much like that seen in the current meter record (figure 4-8). Specifically, these studies found more prominent 60 day variability during roughly the first half of the year[5]. The fact that this 60 day variability has been observed in dynamic height and sea surface height indicates that the observed velocity

[4]We also computed the WPS for zonal velocity (shown in appendix A, figure A-4). The evolution of near-inertial power in zonal velocity is similar to that in meridional velocity. Otherwise, the spectrum of zonal velocity is dominated by broad-band, low frequency flow.

[5]Miller et al. (1985) reported that 60-80 day variability at 9°N was most prominent between February and August 1981. Perigaud (1990) noted prominent 60 day variability at 12°N between February and July 1987 and November 1987 to March 1988. Giese et al. show large amplitude 60 day variability at 11°N between March and August 1993 (their figure 3b). In the present study, we have found statistically significant variability from November 1997 to August 1998. It is worth noting that the seasonality of the 60 day variability contrasts with the seasonality in tropical instability waves found farther south; tropical instability waves are more apparent beginning in the early summer, as the equatorial cold tongue and the NECC/SEC shear strengthen (Perigaud, 1990; Giese et al. 1994).

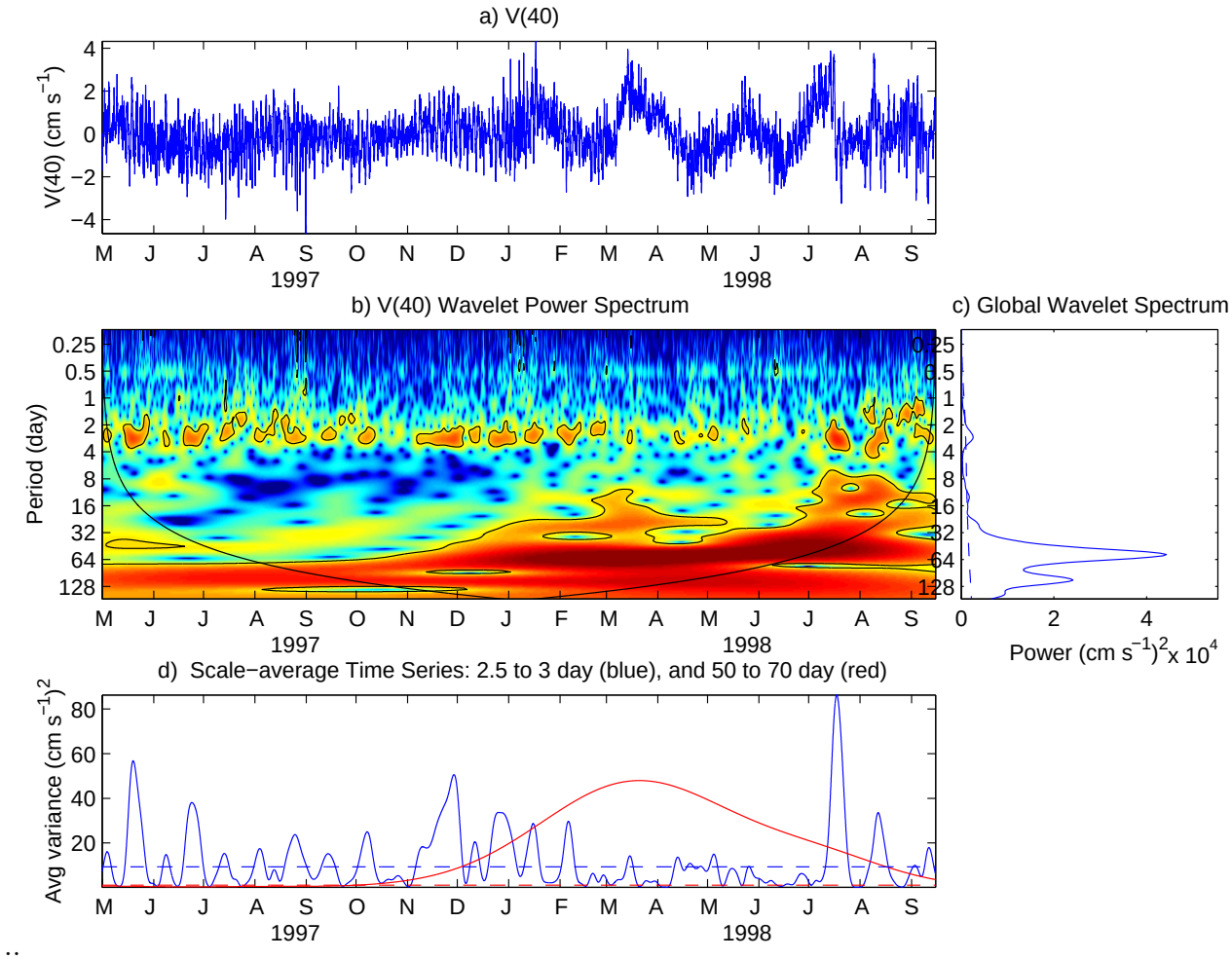

Figure 4-11: Wavelet analysis of spectral power in the meridional velocity at 40 m. (a) The velocity time series, divided by its standard deviation and with the mean removed; (b) the WPS, with period in days on the vertical axis and time on the horizontal axis; (c) the global wavelet spectrum, a time average of the WPS and analog to the more traditional Fourier power spectrum; (d) the average power in two different frequency bands, one having a period of 2.5 to 3 days (near-inertial) and the other 50 to 70 days (intraseasonal). The black parabolic curve in (b) shows the region of time-frequency space where edge effects potentially contaminate the results. In (b), statistically significant power is surrounded by a black line. In (c) and (d), dashed lines indicate the significance threshold.

variability is likely due to large-scale pressure gradients, rather than being a locally wind driven signal[6]. Although the 60 day variability along 10°N has been recognized for some time, there is no consensus on its cause. After using the sea surface slope to estimate the wave number and frequency of this prominent variability (section 4.2.2), we will briefly discuss some potential generating mechanisms.

4.2 Remote and Large Scale Influences Contributing to Variability

Discerning between the local and remote influences that determine the hydrographic structure of the eastern tropical Pacific is an important (but difficult) task. The approach taken here is to identify large-scale processes that may contribute to the variability observed at the site and to assess what role these processes played. In the present section, we will first address the role of Ekman pumping and Rossby waves. Then, the local heat budget will be examined, and the role of advection will be inferred from the residual of the local heat budget.

4.2.1 Vertical Advection and Ekman pumping

While Ekman pumping may be considered a local process, it results from spatial variations in the large scale wind field. The large scale wind field was not measured for this field study, but a number of wind products exist for 1997 to 1998. Satellite wind stress estimates have also become increasingly available, and we use a gridded satellite scatterometer wind stress product produced by a joint effort between the Institut Francais pour l'Exploitation de la Mer (IFREMER) and the University of Hawaii and distributed as part of the WOCE program (WOCE Product, 2001). We chose this wind stress product over other alternatives (e.g. NCEP reanalysis) because it compares most favorably with the measurements at the buoy. Furthermore, scatterometer

[6]We have performed an empirical orthogonal function analysis that supports the notion that the bulk of the low frequency signal is not due to locally forced Ekman transport. This analysis is included in appendix B

wind stress products are known to provide a better representation of the time-mean Ekman pumping than reanalysis products (Kessler, 2002b). The stress fields are produced by objective interpolation based on raw scatterometer data provided by the European Space Agency from the European Remote Sensing (ERS) satellites. The estimation of surface meteorolgical properties is based on measurements from the on-board altimeter, scatterometer, and Synthetic Aperture Radar (SAR) wave mode instrument. After the wind speed and direction is determined, the wind stress is estimated using the bulk formula,

$$\vec{\tau} = (\tau_x, \tau_y) = \rho C_D |\vec{u}| \vec{u}, \tag{4.1}$$

where $|\vec{u}|$ and $\vec{u}$ are the wind speed and wind vector, respectively. The neutral stability drag coefficient (C_D) at 10 m was determined following Smith (1988), and the surface air density (ρ) was taken to be $1.22 \frac{kg}{m^3}$. The satellite typically made three measurements per week over the PACS mooring, but the objective interpolation scheme incorporates measurements from nearby locations. The gridded stress fields are provided with a time resolution of one week and a spatial grid of 1×1 degree.

Ekman pumping is thought to be an important dynamical influence on the seasonal cycle of thermocline depth at 10°N in the eastern Pacific (e.g., Meyers, 1979; Kessler, 1990), and it is believed to be an important mechanism in producing the meridional tilting mode of ENSO (recall chapter 1; Perigaud et al., 2000a, 2000b; Cassou and Perigaud, 2000; Alory and Delcroix, 2002). The Ekman pumping is given by,

$$w_{ek} = \nabla \times (\frac{\vec{\tau}}{\rho f}) = \frac{1}{\rho f} \nabla \times \vec{\tau} + \frac{\beta \tau^x}{\rho f^2}, \tag{4.2}$$

where f and β are the Coriolis parameter and its meridional derivative, and ρ is density of seawater, which is assumed constant for this calculation. Outside of the tropics, the β-term in equation 4.2 is usually negligible, but at 10°N the β-term is comparable to the curl term and must be included to produce an accurate estimate of the Ekman pumping. The IFREMER wind stress product includes an estimate of the wind stress curl, produced by a fourth-order finite difference of the gridded stress

field. The Ekman pumping was estimated by adding the IFREMER curl estimate to the beta-term in equation 4.2. The implied Ekman pumping displacement is given by the time integral of the Ekman puming velocity. The Ekman puming velocity and the Ekman pumping displacement are shown in figure 4-12. There is a striking seasonal signal in Ekman pumping at the site associated with the movement of the ITCZ; the Ekman pumping is upward during ITCZ conditions and downward during non-ITCZ conditions. The Ekman pumping displacement is highly correlated with the observed thermocline depth at the mooring site; the correlation coefficient between the Ekman pumping displacement and the (low-pass filtered) 19° isotherm depth during the observation period is 0.83. In other words, Ekman pumping can account for about 69% of the low frequency variance of the thermocline during the observation period. It should be noted that the Ekman pumping velocity computed using NCEP reanalysis stress was almost always positive, lacking the seasonal sign reversal. As we have noted, based on comparison to the buoy winds and previous studies, we believe that the NCEP wind stresses are less reliable than the ERS wind stresses.

4.2.2 Rossby waves

Many authors have argued that first baroclinic mode Rossby waves are an important mechanism in the adjustment of the oceans, both in the tropics and at higher latitudes. Rossby waves play a major role in the formation of western boundary currents such as the Gulf Stream and the Kuroshio Current (Anderson and Gill, 1975), and they have been shown to be especially important for the transient adjustment of the tropical oceans away from western boundaries (e.g. White, 1977; McCreary, 1977; Meyers, 1979; Kessler, 1990). In a breakthrough study, Chelton and Schlax used data from the TOPEX/Poseidon satellite altimeter to demonstrate the ubiquitous presence of long Rossby waves in the world oceans (1996). Furthermore, they used the extensive data set to show that the theory of long Rossby waves developed by Carl Gustav Rossby (1939, 1940) provides a first order explanation of these observations, although apparent discrepancies were found between theoretical and observed phase speeds outside of ± 15°N. This result spurred a number of studies which sought to explain

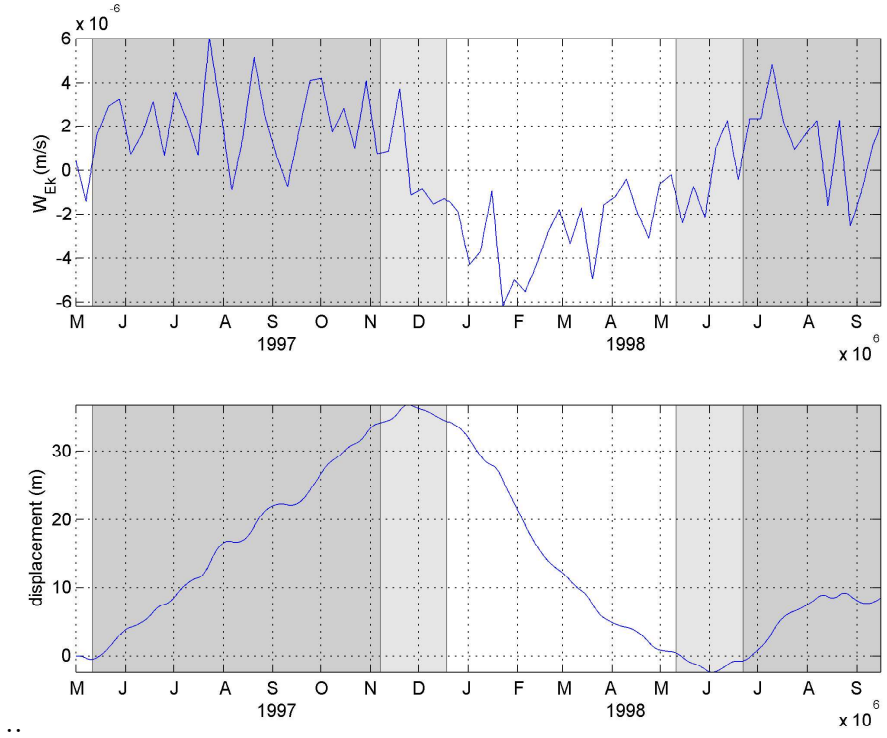

Figure 4-12: Upper panel: Ekman pumping velocity estimated at 10°N, 125°W from the ERS satellite scatterometer wind stress. Lower panel: estimated Ekman pumping displacement (time integral of w_{Ek}). ITCZ conditions are marked by dark shading and transitional periods are marked by light shading.

the discrepancy. In a subsequent study, Zang and Wunsch (1999) argued that the apparent deviation from theoretical phase speeds is a consequence of the superposition of Rossby waves with other processes, since a significant amount of power in sea surface height is consistent with the Rossby wave dispersion relation, while some power is apparently due to other processes.

Under the quasi-geostrophic (QG) approximation, the behavior of wind-forced, linear Rossby waves can be clearly understood. Another useful simplification that will be employed here is that the ocean can be approximated as a thin, active layer of warm fluid overlying an infinitely deep, motionless abyss. That is, we will employ the $1\frac{1}{2}$ layer approximation. For this qualitative discussion, we will also treat the wind stress as a body force acting on the upper layer. The linearized QG vorticity equation for a $1\frac{1}{2}$ layer system is derived by taking the curl of the linearized horizontal momentum equation. The linearized QG vorticity equation for a $1\frac{1}{2}$ layer system can then be written as,

$$\frac{-g'}{f_o}\frac{\partial}{\partial t}(\nabla^2 h) - f_o w_z + \beta v = \nabla \times (\frac{\vec{\tau}}{\rho(H+h)}), \tag{4.3}$$

where $H+h$ is the thickness of the active layer, H is the mean thickness, $f = f_o + \beta y$, and g' is the reduced gravity. Under assumptions that the leading order contributions to v are geostrophic and Ekman transport, that the vertical velocity at the sea surface is zero, and that variations in the depth of the thermocline are negligible in the curl term, we can rewrite equation 4.3 as,

$$L_D^2\frac{\partial}{\partial t}(\nabla^2 h) - h_t + \beta L_D^2 h_x = \nabla \times (\frac{\vec{\tau}}{\rho f_o}), \tag{4.4}$$

where the deformation radius is $L_D^2 = \frac{g'H}{f_o^2}$. The dispersion relation for free Rossby waves can be obtained by setting the right hand side of equation 4.4 to zero and substituting a sinusoidal function for h to obtain,

$$\omega = \frac{-\beta k}{k^2 + l^2 + L_D^{-2}} \tag{4.5}$$

where ω is the angular frequency, (k, l) is the wave number vector, and L_D is the Rossby deformation radius. The value of the first baroclinic Rossby radius of deformation is about 1 degree of longitude at 10°N (Chelton et al., 1998). For long wavelengths ($2\pi L_D \ll \lambda$), we expect Rossby waves to propagate non-dispersively westward at a phase speed of,

$$c_p \approx -\beta L_D^2 \approx \frac{-\beta g' h}{f^2}. \tag{4.6}$$

For wavelengths of 20° or larger along 10°N, the westward phase speed of a first-mode baroclinic Rossby wave should be at least 90% of the long wave phase speed, which is about 24 cm/s. In the short wave limit ($2\pi L_D \gg \lambda$),

$$c_p \approx \frac{-\beta}{k^2 + l^2}. \tag{4.7}$$

In the short-wave regime, Rossby waves are highly dispersive and propagate much more slowly than long waves.

It is also instructive to consider how the ratio of kinetic to potential energy density of a Rossby wave varies with wavelength. Under the QG approximation, the ratio of kinetic to potential density over a wave cycle is given by (Gill et al., 1974; Gill, 1982, p.502):

$$\frac{\langle KE \rangle}{\langle PE \rangle} = \frac{\frac{\rho H}{2}\langle u_g^2 + v_g^2 \rangle}{\frac{\rho g'}{2}\langle h^2 \rangle} = (k^2 + l^2) L_D^2. \tag{4.8}$$

In the long wave limit, the energy is mostly in potential form; we expect long waves to have a more prominent height signal (i.e. change in density structure due to vertical velocity) than horizontal velocity signal. Conversely, short waves have a more prominent horizontal velocity signal than height signal. We will make use of this fact in our investigation of Rossby waves along 10°N by using sea surface height data to examine the role of long Rossby waves and using sea surface slope to examine the role of shorter Rossby waves.

Long Rossby waves

In a series of papers in the late 1970's, Gary Meyers and Warren White pioneered the study of long Rossby waves in the interior tropical Pacific by examining XBT and mechanical bathythermograph (MBT) records, and William Kessler extended these efforts using a larger XBT/MBT database in 1990. These studies have convincingly demonstrated that long Rossby waves are one of the most important factors in the time dependent behavior of the tropical Pacific thermocline, although the region between 8 and 12°N has historically been a region of relatively poor agreement between observations of thermocline depth and predictions using a long Rossby wave model (e.g. Meyers, 1979; Kessler, 1990). Given the results of these previous studies, it is reasonable to expect that the behavior of the thermocline that was observed at the PACS mooring could be the direct result of long Rossby waves propagating past the site. However, given the persistently poorer performance of the long Rossby wave model near 10°N, the previous studies have also indicated that other dynamical mechanisms may also play an important role in the observed behavior. The goal of this subsection is to assess the role of long Rossby waves in contributing to the variations in thermocline depth observed at the mooring site.

Figure 4-13 is a longitude-time plot of sea surface height (SSH) anomaly estimated from TOPEX/Poseidon satellite altimetry data. After geopotential, tidal, steric, and inverted barometer effects on the SSH have been accounted for, the SSH field is approximately proportional to thermocline depth. The SSH field largely reflects changes in thermocline depth associated with the first baroclinic wave mode (Wunsch, 1997). In figure 4-13, the solid blue line indicates westward propagation at a speed of 0.24 m/s. There are some long-wavelength disturbances that appear to propagate westward at approximately the long wave phase speed. However, the rapid change in thermocline depth that occurred at the mooring in January and February 1998 does not appear to have propagated to the mooring from the east. Instead, the deepening of the thermocline occurred almost simultaneously (i.e. within a few weeks) between 140° and 115°W (i.e. 220°E to 245°E). An analogous deepening of the thermocline

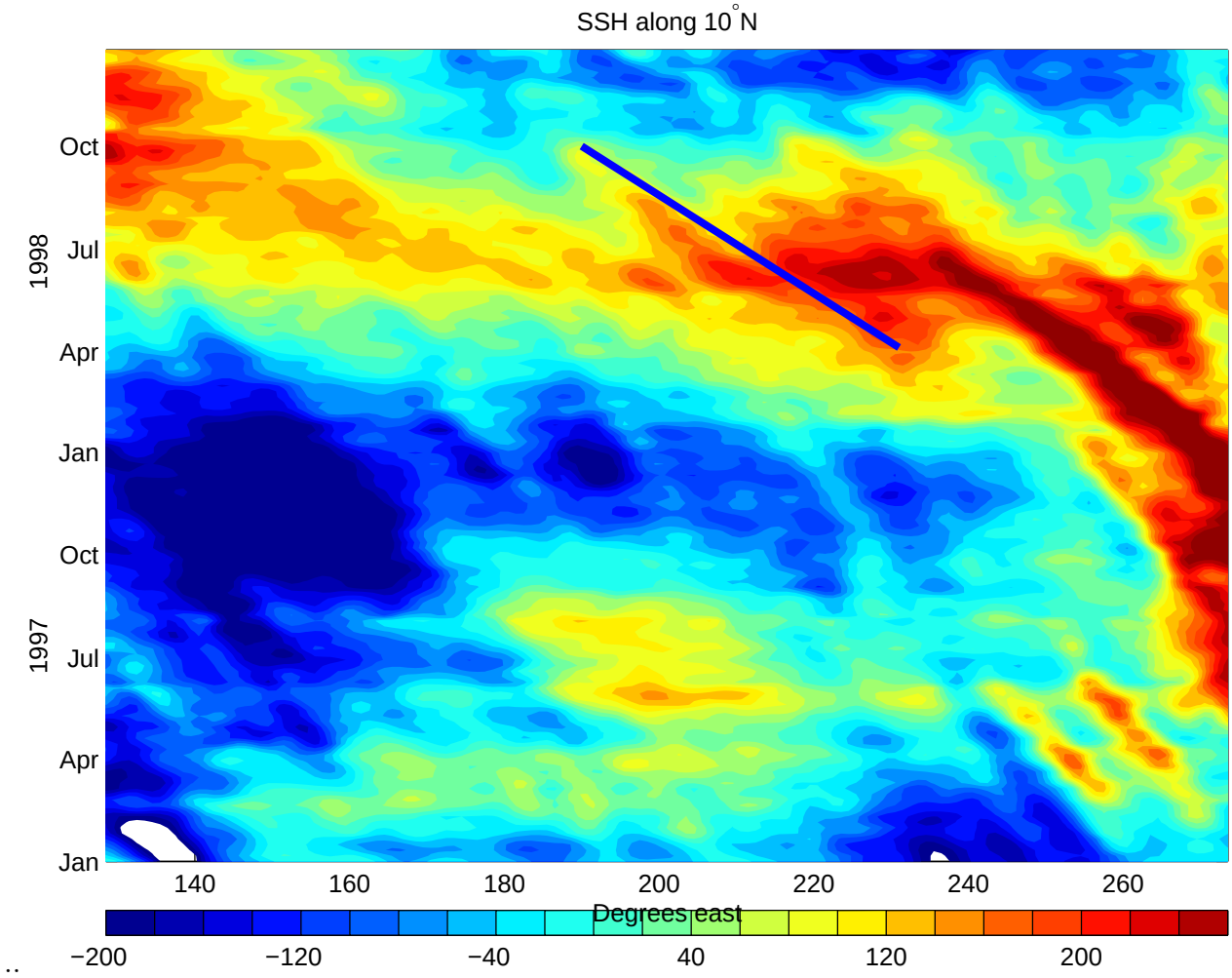

Figure 4-13: Longitude-time plot of Topex sea surface height anomaly. The mooring was located at 235°E (i.e. 125°W). Red and blue represent positive and negative displacements, respectively. Positive SSH anomalies correspond to negative thermocline depth anomalies. The expected long Rossby wave phase speed is indicated by a blue line.

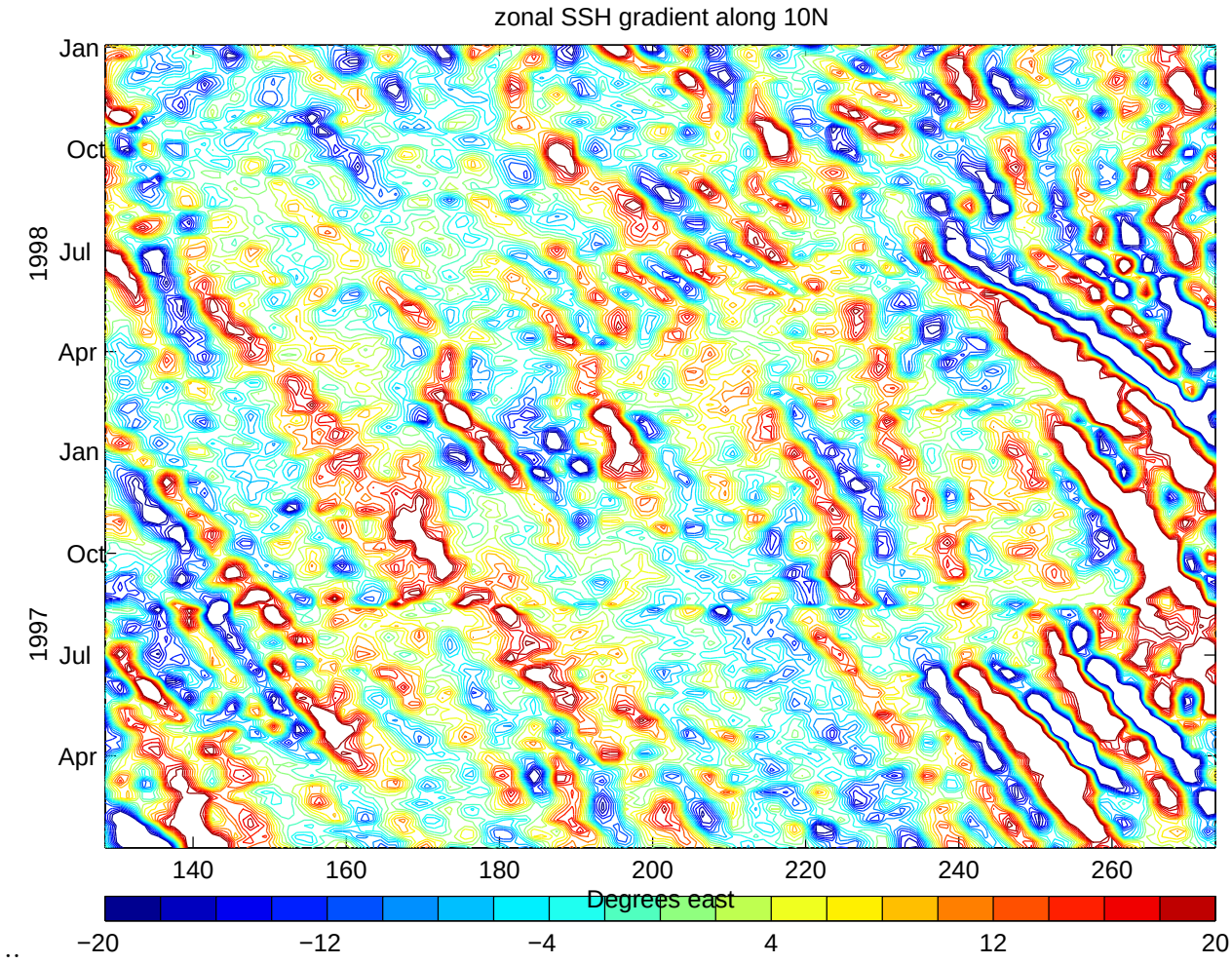

Figure 4-14: Zonal sea surface anomaly slope along 10°N in mm/deg. The mooring was located at 235°E (i.e. 125°W).

occurred over almost the whole width of the Pacific basin. Although the deepening does appear to propagate westward, it does so at a speed of roughly 1 m/s, which is far too fast to be due to free long baroclinic Rossby waves at this latitude[7]. There is discernable westward propagation at the mooring site that appears markedly slower than the long wave phase speed; in the next subsection we will look at the variability associated with shorter Rossby waves by turning our attention to the slope of the SSH.

Finite wavelength Rossby waves

By looking at the zonal gradient of the SSH anomaly, we can gain further insight into the role of Rossby waves at the mooring site. While computation of the discretized derivative introduces some additional noise, this procedure serves two useful purposes. First, it removes zonally coherent signals that obscure the westward propagation of SSH anomalies over time (e.g. zonally coherent seasonal changes in Ekman pumping or seasonal steric effects). Second, the zonal derivative of SSH should be proportional to the meridional geostrophic velocity, and Rossby waves involve meridional velocity fluctuations and should be detectable by the signal in SSH gradient. This operation is similar in character to one of the filters applied by Chelton and Schlax to the SSH anomaly data in their analysis of long Rossby wave propagation in the Pacific Ocean (1996). Chelton and Schlax applied one filter to remove zonally coherent changes and another filter to remove disturbances of less than 10 degrees of longitude. Here, we have elected not to filter smaller scales, but the zonal derivative effectively filters all changes in SSH that do not depend on longitude. This operation also tends to emphasize the scales and frequencies that make energetic contributions to the geostrophic velocity.

Along 10°N (and throughout the near-equatorial band), most of the westward propagating energy in SSH is at very low frequencies (less than two cycles per year) and very long wavelengths (the width of the basin or larger) (Zang et al., 2002). We expect the spectrum of westward propagating energy in the zonal derivative of the height-field to be proportional to the that of the height-field times the zonal wave number squared (i.e. $(\frac{\partial h}{\partial x})^2 = k^2 h^2$). Thus, it is not surprising that the zonal gradient in SSH may have energy at scales and wavelengths that are very different from those that make energetic contributions to SSH. Furthermore, QG theory (e.g. equation 4.8) leads us to expect that shorter waves will have more energy in the geostrophic velocity signal than in the height signal, and thus they should be more easily detectable in the sea surface slope. Figure 4-14 shows an estimate of the zonal gradient in SSH anomaly along 10°N estimated using a fourth-order accurate finite

[7]Note that 1 $m/s \approx 0.95$ deg/day.

difference scheme. The presence of westward propagating signals can be clearly seen.

We can take advantage of the broad spatial and temporal coverage of the TOPEX/ Poseidon SSH data set to obtain a quantitative estimate of the dominant frequencies and wave numbers along 10°N. Inspection of figure 4-14 suggests the presence of a quasi-periodic signal with a wavelength of 5 to 10 degrees, a period between 40 and 80 days, and a peak-to-peak amplitude of about $\pm 15 mm/deg$. Given the stated 40 mm accuracy of the 1 by 1 degree gridded TOPEX/Poseidon product used here and the peak-to-peak signal amplitude of 3-8 cm (before differentiation), the signal-to-noise ratio is about 0.75 to 2.0. This signal-to-noise ratio is not especially good, and the problem is exacerbated by the discretized spatial derivative.

While the marginal signal-to-noise ratio precludes direct comparison of sea surface slope to measured velocity, we can use the long data record from the TOPEX/Poseidon mission to draw reliable inferences about the characteristic frequencies and wave numbers along 10°N. The 2D wave number frequency spectrum was estimated using a method similar to the one described in Zang et al. (2002) using a two-dimensional Fast Fourier Transform (2DFFT). We calculated the zonal slope of the sea surface for the period of 1997-98 using a fourth-order accurate finite difference scheme. The mean was removed from the sea surface slope before computing the 2DFFT. Then, non-overlapping averaging was carried out across two adjacent frequency bands and 3 wave number bands to improve the statistical stability of the spectral estimate. This leads to a total of $2 \times 2 \times 3 - 1 = 11$ degrees of freedom (the -1 is a result of removing the mean before processing) and a chi-square error estimate of 0.8 decibels.

Figure 4-15 shows the estimated wave number-frequency spectrum of zonal sea surface slope along 10.5°N. In the figure, westward propagating signals have negative wave numbers. As might be expected, most of the energy is associated with westward propagating signals. The solid blue line in the figure shows the Rossby wave dispersion relation where we have used the value for the first baroclinic deformation radius given by Chelton et al. (1998) of about one degree of longitude. For these dispersion curves, we have assumed a plane wave structure (i.e. meridional wave number near zero); non-zero values of the meridional wave number would cause the dispersion curve

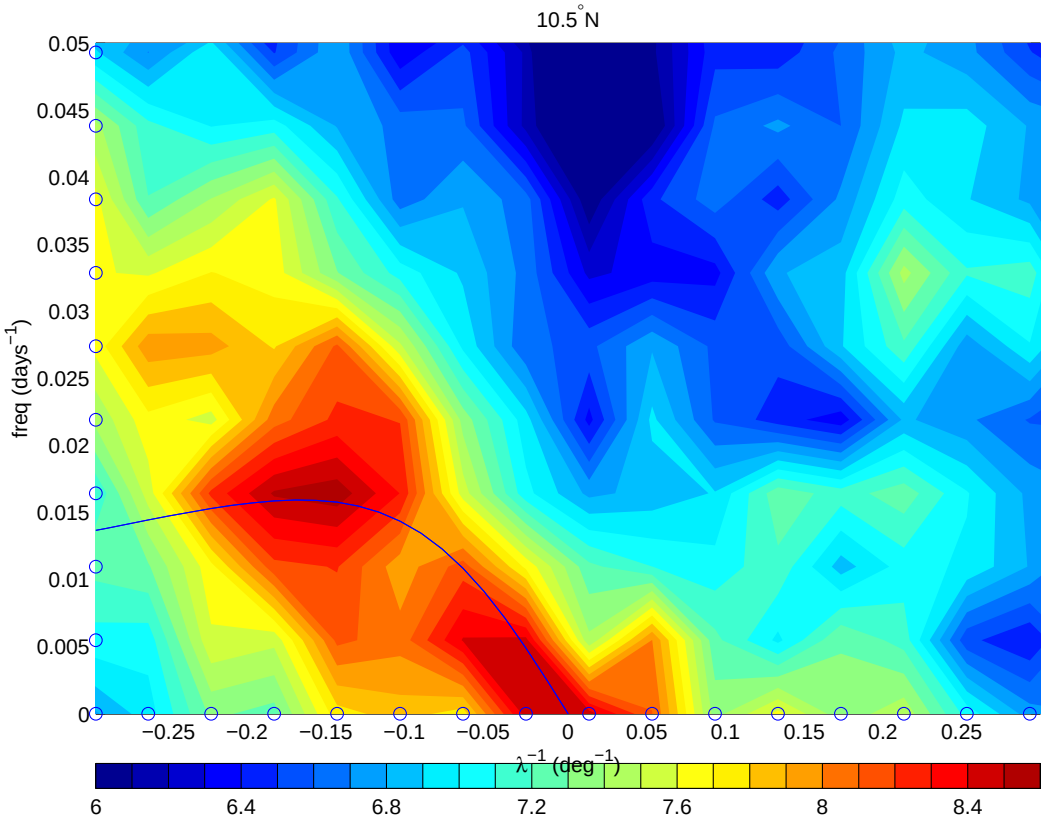

Figure 4-15: 2D FFT estimate of wavenumber-frequency spectrum of zonal sea surface slope along 10.5°N. The solid blue line shows the Rossby wave dispersion relation assuming $l = 0$ and a first baroclinic Rossby radius of 103 km. The color-bar has a log_{10} scale, and the error bar is about 0.8 units on the log scale. The blue circles indicate the discrete values of frequency and wavenumber for the estimate.

to lie at lower frequencies for the same values of the zonal wave number. All of the statistically significant power in the zonal sea surface slope lies near the first baroclinic mode Rossby wave dispersion curve, which indicates that the quasi-periodic features in figure 4-14 are probably first-mode baroclinic Rossby waves. There is a distinct peak corresponding to a frequency of about 60 days (ω = .015) with a wavelength of about 7 degrees (k=0.15 deg^{-1}). This wavelength is very nearly 2π times the deformation radius[8].

The wavenumber-frequency spectrum of the TOPEX/Poseidon data suggests that Rossby waves with a period of about 60 days and a zonal wavelength of about 7 degrees were a prominent and persistent part of the velocity variability along 10°N during 1997 and 1998. This strongly suggests that the observed meridional velocity signal, with a period near 60 days and a vertical structure consistent with interpretation as baroclinic motion, is associated with these waves.

Variability near 10°N with a 60 day period has been identified in a handful of observational studies (Miller et al., 1985; Perigaud, 1990; Giese et al., 1994), and variability with either a period near 60 days or a wavelength near 7 degrees is evident in others (e.g. Lagerloef et al., 1999, figure 9b). All of these studies used satellite altimetry data, except the analysis of Miller et al., which used 14 months of inverted echo sounder data to compute dynamic height. As we have noted, the studies that directly addressed this 60 day variability (Miller et al., 1985; Perigaud, 1990; Giese et al., 1994) found a seasonality to the variability much like that seen in the current meter record (figure 4-8). Generating mechanisms for this variability have been proposed, but no consensus has been reached. Perigaud hypothesized that the 60 day variability near 10°N is generated by a shear instability associated with the NEC/NECC shear, in a manner analogous to the generation of tropical instability waves farther south. However, she noted that the shear strength does not coincide well in space and time

[8]A similar spectral peak has been been observed in the SSH of the Pacific near 12°N (Zang and Wunsch, 1999). In the analysis of along-track TOPEX/Poseidon conducted by Zang and Wunsch, a statistically significant peak was found along 12°N lying on the first baroclinic mode Rossby wave dispersion curve and having a frequency of about 100 days. In that study, the peak corresponded to a wave number of about 11 degrees longitude, which is roughly twice 2π times the deformation Radius at that latitude.

with the observed wave growth. Giese et al. seized upon this discrepancy and sought to show that the 60 day variability is forced by the strong wind stress curl signal associated with the passage of the trades through the Central American mountain gaps of Tehuantepec and Papagayo, based on the relative timing of 7 wind events and 5 visible eddies over a 17 month period (1994). We would also like to point out that Philander (1976) suggested that the NEC may be baroclinically unstable, and he suggested that the resulting waves would have a period of 30 days and a wavelength of 7 degrees. We have found here that the dominant wavelength of sea surface slope is about 7 degrees, but the dominant period differs from Philander's prediction by a factor of two. Perhaps this is a small difference in the context of the 2-layer model used by Philander.

Another potential generating mechanism for this 60 day variability is radiation of Rossby waves from the eastern boundary associated with coastal Kelvin waves. On the equator, prominent baroclinic Kelvin wave activity has been observed with a period of 60-75 days (Kessler et al., 1995; Zang et al., 2002). A first baroclinic mode Kelvin wave with a wavelength equal to the width of the Pacific should have a period of about 70 days (Zang et al., 2002). In figure 4-14, we can see that the intraseasonal waves are strongest near the eastern boundary, so it is conceivable that these waves might be radiating from the eastern boundary as a consequence of coastal Kelvin waves propagating from the equator. In any case, it is not the goal of this thesis to settle the question of how this 60 day variability near 10°N is generated.

This study differs from previous studies that have identified 60 day variability near 10°N in some important respects. The PACS observations represent the first detailed *in situ* observations of the velocity signal associated with this variability. Also, in our experience, neither the sea surface height nor the sea surface slope provide a clean enough signal to allow visual identification and tracking of an individual wave crest or eddy, except in cases where the amplitude of the signal is unusually large. However, this was the approach used by Giese et al. (1994), but we have seen that there is a clear velocity signal despite the fact that the signal is not obvious in the sea surface height (or slope). This fact may explain the depiction of the variability by Giese et

al. as episodic eddies. We observed a truly oscillatory behavior in the velocity signal at the mooring site, and it may be the case that the approach of Giese et al. was only capable of identifying signals that were large enough to be visually apparent despite the noise.

Rossby wave summary

In this subsection, we have arrived at two important intermediate conclusions: (1) There is no clear sign that the rapid thermocline depth change at the mooring is associated with long Rossby waves, and (2) the TOPEX data reveals the presence of first-mode baroclinic Rossby waves with inverse wavenumber equal the deformation radius and a period of about 60 days; this is probably the origin of the low frequency meridional velocity signal observed at the mooring.

4.2.3 Assessing the role of advection using a heat budget

While it is generally difficult to distinguish between specific local and remote influences in an observational record from an isolated mooring, computation of a one-dimensional heat budget can be a powerful approach for determining times when the ocean is responding primarily to local forcing (especially when the surface heat flux is known with some precision). If a one-dimensional heat budget can be approximately closed, then it is plausible that the effect of horizontal advection is small. Of course, the 1D heat budget can appear to be closed when 3D processes are actually important, such as when vertical entrainment into the control volume balances horizontal advection out of the volume. The equation for conservation of heat can be written as,

$$\rho c_p[\frac{\partial T}{\partial t} + \vec{u} \cdot \nabla T] = \frac{\partial}{\partial z}(q - r), \tag{4.9}$$

where T is the temperature, q is the penetrating solar heat flux, and r is the turbulent heat flux. Here it has been assumed that horizontal turbulent heat fluxes are negligible. Equation 4.9 expresses the fact that the temperature at a point can change due to advection of temperature gradients and divergence of solar and turbulent fluxes.

By integrating equation 4.9 from the surface to some depth where turbulent fluxes are assumed negligible, we obtain,

$$\rho c_p \int_{-z}^{0} [\frac{\partial T}{\partial t} + \vec{u} \cdot \nabla T] = Q + R, \tag{4.10}$$

where Q is the net surface heat flux and R is a residual term that represents neglected processes and errors in the the other terms. Since both the upper ocean heat content and the surface heat flux both have a large diurnal signal, long-term comparisons are facilitated by integrating in time. By selectively excluding all or part of the advective term in equation 4.10, we can get some measure of the importance of the advective term in the heat budget. Ideally, we would like separate estimates of the components of (u, v, w) and ∇T, but the vertical velocity was not measured and there are no coincident measurements from which we can accurately estimate $\nabla_H T$. Instead, we use the estimated Ekman pumping velocity (section 4.2.1) as an estimate of the actual vertical velocity. In order to incorporate the vertical velocity into the heat budget, we must choose a vertical profile of the vertical velocity. The vertical velocity is most consequential to the heat budget near large temperature gradients, and it is utterly inconsequential to the heat budget where the vertical temperature gradient is zero. With the understanding that the temperature gradient is small above and below the thermocline and that, consequentially, only the vertical velocity in the thermocline can exert a profound influence on upper ocean heat content, we have chosen a vertical profile of vertical velocity which is constant in the upper 150 m, except for a linear interpolation to zero in the upper few meters. Since there is insufficient data to accurately determine the horizontal temperature gradient as a function of time and depth, we are compelled to lump the horizontal advection term into the residual term (R). Since the temperature, its vertical derivative, and the surface heat flux are estimated to a high degree of accuracy from measurements, any imbalance in the heat budget is ascribed to horizontal advection, errors in the vertical velocity estimate, or non-negligible vertical or horizontal turbulent heat flux at the boundaries of the control volume.

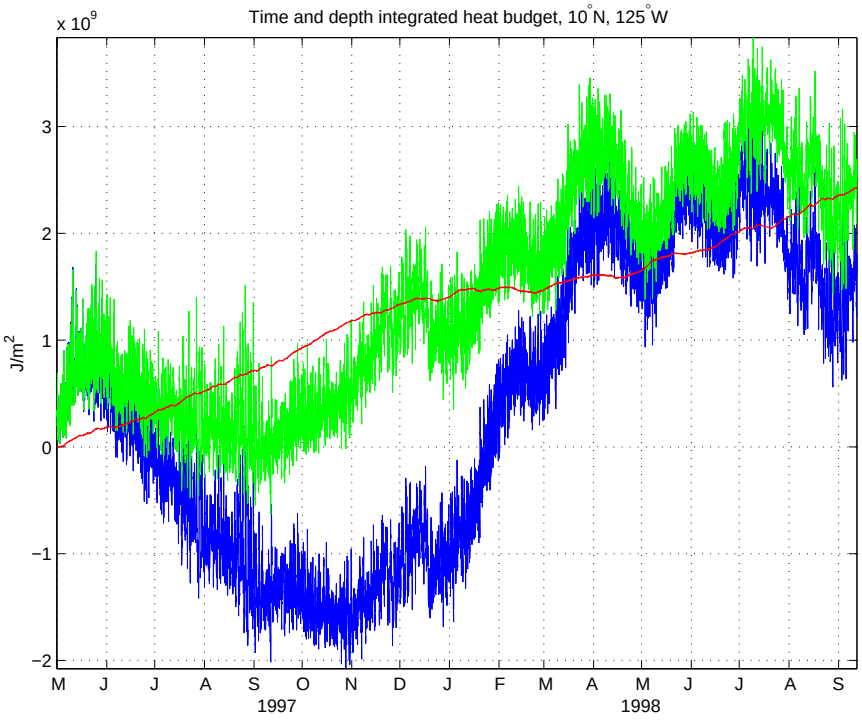

Figure 4-16: Time and depth integrated heat equation. The vertical axis reflects the change in upper ocean heat content in J/m^2. The depth integration was carried out to 150 m. The red line is the integrated surface heat flux. The blue line is $\rho c_p \int\int \frac{\partial T}{\partial t} dtdz$ and the green line is $\rho c_p \int\int [\frac{\partial T}{\partial t} + w\frac{\partial T}{\partial z}] dtdz$. In other words, the blue line is the evolution of actual upper ocean heat content per m^2 through time, and the green line is actual heat content plus the contribution of vertical advection by Ekman pumping. Hours 2000, 6000, and 8000 are during late July, early January, and early April, respectively.

Figure 4-16 shows a comparison between a heat budget computed by ignoring vertical advection (blue line) and one computed using an estimate of vertical advection (green line). The depth integration was carried out to 150 m, which is well below the main thermocline during the entire record, so turbulent heat flux through the bottom of the control volume should be small. Both heat budget estimates ignore the contribution from horizontal advection. In the figure, the measure of the closure of the heat budget at a given time is the extent to which the slope of the integrated net surface heat flux matches that of the oceanic heat content. (The slope, rather than the magnitude, is important because an integration constant arises from the integration). Including vertical advection in the heat budget markedly improves the balance between surface heat flux and upper ocean heat content, especially at time scales longer than a couple of months. This indicates that much of the observed behavior of the upper ocean thermal structure may be explained by surface heat flux, turbulent mixing, and vertical advection. In appendix C, we re-address the role of horizontal advection by performing a similar budget in a data-assimilated general circulation model (GCM) that does a fair job of reproducing the observed behavior at the mooring site. There, it is argued that the contribution of horizontal advection in the heat equation is of secondary importance. Furthermore, in chapter 5 we will show that incorporation of Ekman pumping and shear driven turbulent vertical mixing into a 1D numerical model can account for most of the observed thermal evolution.

Summary of large-scale influence

The mechanisms that can affect upper ocean thermal structure are advection, mixing, and surface heat flux. At seasonal timescales, the primary contributions to vertical advection are thought to be Ekman pumping and Rossby waves. In this section we examined the contribution to vertical advection by Ekman pumping and Rossby waves, which are thought to be the primary large-scale contributions to vertical advection in the region (Meyers, 1979; Kessler, 1990). We found that advection by Ekman pumping can explain much of the observed motion of the thermocline, but long Rossby waves do not appear to have had an important role in bringing about

the rapid deepening of the thermocline in early 1998. In addition, we identified the dominant large-scale frequencies and zonal wave-numbers present in sea surface slope along 10°N and found that a large amount of the variability is consistent with interpretation as 60-day period Rossby waves. We suggest that this is the same 60-day variability observed in the meridional velocity record. Finally, we presented a heat budget for the upper ocean and showed that incorporation of Ekman pumping and surface fluxes can account for the seasonal changes in upper ocean heat content. We take this as evidence that horizontal advection and other contributions to vertical velocity are of secondary importance in the evolution of upper ocean heat content. However, the observed motion of the isotherms is not entirely explained by vertical advection by Ekman pumping, particularly during the rapid mixed layer and thermocline deepening of early 1998. This fact, in conjunction with the vertically integrated heat budget, suggests that mixing processes may have been important in bringing about the rapid deepening of the thermocline in early 1998.

4.3 Local Influences Contributing to Variability

In section 4.2.3, it was argued (on the basis of a 1D heat budget) that local processes may explain much of the observed evolution of the upper ocean thermal structure. The heat budget alone has little explanatory power, though, because in its computation, we integrated over the region of interest (in depth). A primary goal of this study is to determine the physical mechanisms that caused the rapid descent of the thermocline at the mooring site during the first few months of 1998, and the heat budget of the preceding section indicates that much of the observed thermal evolution is due to some combination of (1) vertical advection, (2) surface heat flux, and (3) turbulent heat flux. The previous section argued that the vertical advection plays a substantial role in the depth integrated heat budget, but adiabatic advection does not entirely account for the observed motion of the isotherms (for example, compare the Ekman pumping displacement in figure 4-12 to the observed isotherm time series in figure 4-4).

This section has two goals: (1) to assess the presence of turbulence associated with vertical shear instability, and (2) to determine whether there is enhanced shear in a particular frequency band. The high spatial resolution of velocity measurements allows us to estimate the vertical shear of horizontal velocity components. In this section, we first present estimates of the shear and gradient Richardson number as a function of time and depth in order to identify times and depths where shear driven mixing was likely to have been important to the evolution of the velocity and thermal structure. Then, we will present spectral analysis of shear to determine whether there is enhanced vertical shear in a particular frequency band. We have seen that the velocity record contains a significant amount of inertial power; we will show that much of the shear is associated with these near inertial motions.

4.3.1 Shear and Richardson number

A low gradient Richardson number (Ri_g) is thought to be a reliable indicator of favorable conditions for vertical shear instabilities[9]. Vertical shear instability is thought to be an important mechanism of diapycnal mixing throughout the world oceans in the mixed layer base (Dillon and Caldwell, 1978; D'Asaro, 1985b; Price et al., 1986; others), the main thermocline (Gregg, 1987; Kundu and Beardsley, 1991; D'Asaro, 1991), and the stratified deep ocean (Garrett, 1979; Munk, 1981; Toole and Schmitt, 1987; Kunze, 1990; Polzin, 1996, and many others). A necessary condition for shear instability in a stratified, parallel shear flow is that the gradient Richardson number be less than 1/4 (Miles, 1961; Howard, 1961). The gradient Richardson number is defined as,

$$Ri_g \equiv \frac{N^2}{S^2}, \tag{4.11}$$

[9]We use the term 'vertical shear instability' to refer instabilities occurring as a result of vertical shear in a stratified fluid. This term is meant to refer primarily to Kelvin-Helmholtz instability, but also to associated instabilities, such as Holmboe waves, which have been shown to occur in similar parameter ranges (e.g. Strang and Fernando, 2001; Smyth and Winters, 2003). Despite the fact that unstable Holmboe waves have a slower linear growth rate than Kelvin-Helmholtz waves, Holmboe waves may cause as much mixing in the ocean as Kelvin-Helmholtz waves (Smyth and Winters, 2003), and they can cause substantially enhanced mixing when they co-exist with Kelvin-Helmholtz waves (Strang and Fernando, 2001).

where N is the buoyancy frequency and S is the vertical shear of the horizontal velocity vector. Since the 1970's, laboratory study of shear instability in stratified flows has been an active field of research (Thorpe, 1968, 1973; Koop and Browand, 1979; Scinocca, 1995; Strang and Fernando, 2001). These studies generally confirm that $Ri_g < 1/4$ is a reliable indicator of the onset of turbulence in a vertically sheared, stratified fluid, though nonlinearities may cause turbulence to persist until $Ri_g \sim 1$ (Abarbanel et al., 1986; also, Stull, 1988, p. 176-177). While the gradient Richardson number is thought to be a reliable indicator of mixing and turbulence, it is generally difficult to estimate Ri_g accurately from moored instruments because the vertical resolution of instrumentation limits the accuracy of gradient estimates.

The vertical shear of horizontal velocities was estimated by first differences between adjacent current meters. This provides an estimate of each component of the vertical shear at the midpoints between current meters. While the discretization error associated with the use of first differences is a significant source of error in calculation of vertical derivatives from the data, it is not clear that a higher order differencing scheme would be an improvement. Shears on vertical scales less than the separation between current meters are not resolved; consequently, the shear estimates are likely to be too low. Since the vertical separation of current meters varies from 5 m to 20 m, the shear estimates are expected to be more accurate near the surface (where vertical resolution was better).

The zonal and meridional components of vertical shear are shown in figure 4-17, and the current meter depths are indicated by blue dots for the respective measurement periods. There are occasionally substantial shears in and above the thermocline throughout much of the measurement period. During January 1998, the shear in the thermocline reached values of $0.04 s^{-1}$, corresponding to a velocity difference of $40 cm/s$ over the $10 m$ depth interval between current meters. The largest shears occur below the mixed layer base between August 1997 and January 1998; this corresponds to the latter 65% of the ITCZ season and the first two months of the non-ITCZ season. The low frequency components of the vertical shear are shown in figure 4-18. the low frequency shear is much less than the total shear; note that the contour range

is about 8 time smaller than that for the total shear.

Estimation of the gradient Richardson number requires estimates of shear and the buoyancy frequency (N). Unfortunately, only a few of the conductivity sensors returned data during the first part of the field study. This complicates estimation of the vertical density gradient. While variations in salinity are undoubtedly important to the density stratification, the temperature field dominates the density structure. Because the record shows large surface freshwater fluxes (both positive and negative), we expect salinity variations to be most important near the surface. At some times associated with heavy precipitation, salinity obviously controls the stratification within the top 15 m of the water column, as we observe temperature inversions here that persist for several days. However, based on CTD profiles at the buoy, we argue that temperature generally controls the density structure, especially at depths greater that 20 m. For example, the density structure inferred from the temperature and salinity profiles from a CTD cast on December 19, 1997 differs little from the density profile estimated from observed temperature profile and a value of salinity that is constant in depth. Here, we use a constant salinity value and the highly resolved temperature measurements to estimate the density profile during the first phase of the field program[10]. This estimate of buoyancy frequency will tend to be too low due to the neglect of the stabilizing salinity stratification, and thus may produce artificially low Ri_g values. However, even a 50% error in N^2 is not unacceptably large considering that Ri_g varies over several orders of magnitude. In summary, we estimated the buoyancy frequency during the second part of the field study as a function of time and depth based on the temperature and salinity data; we estimated the buoyancy frequency during the first part of the field program based on the temperature data alone by assuming a constant salinity.

Since the temperature and salinity measurements had a high vertical resolution, we elected to linearly interpolate temperature and salinity before calculating N^2 in

[10]On the basis of CTD profiles taken at the beginning, middle, and end of the field program, we estimate the maximum error in $\frac{\partial \rho}{\partial z}$ that will result from this treatment to be about 30%. This maximum error is a result of a small error in the position of the pychnocline (a few meters). However, throughout most of the water column, the error is much smaller than this. The RMS error is estimated to be about 6%.

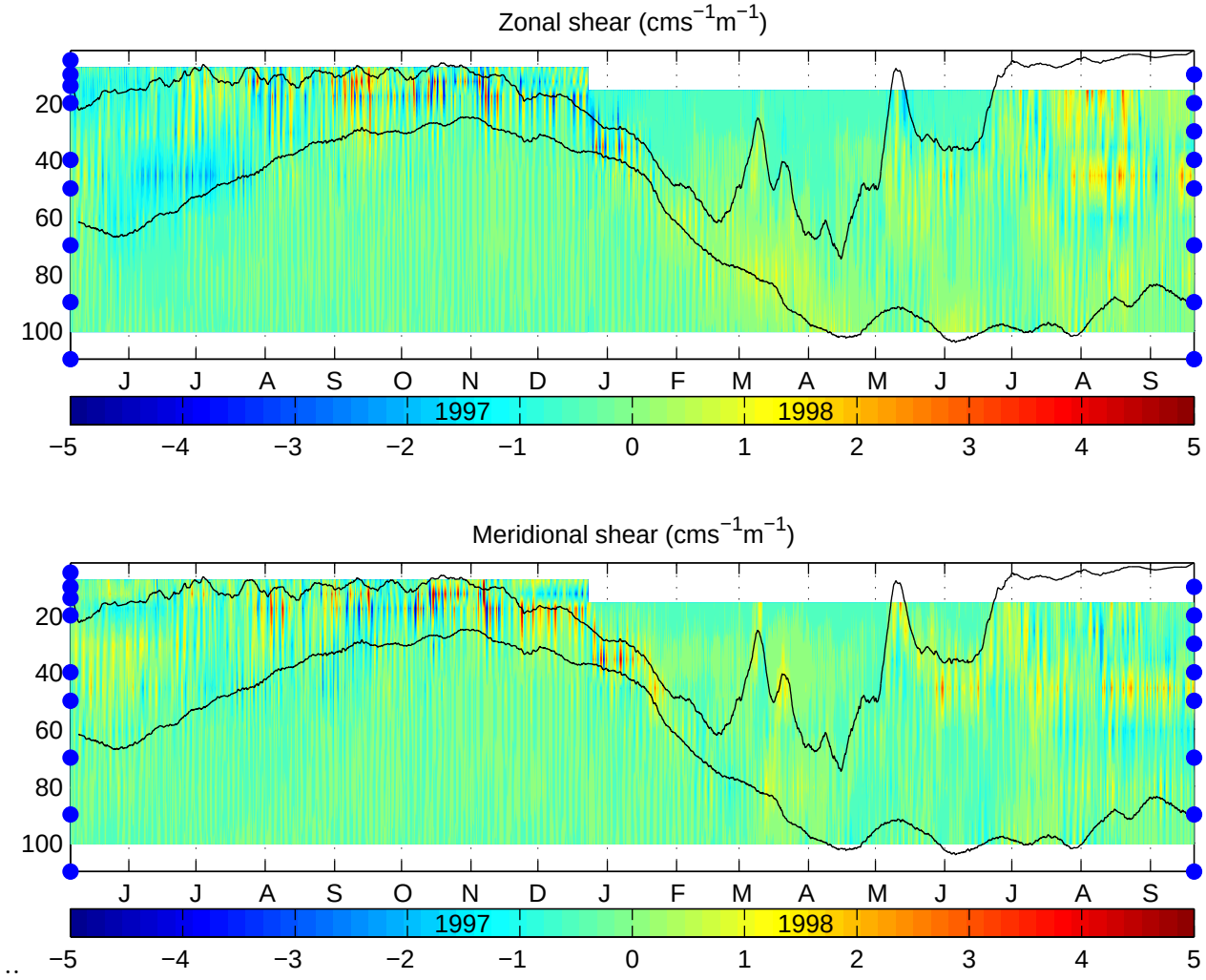

Figure 4-17: Estimated vertical shear. The current meter depths are indicated by blue dots for the respective measurement periods. The current meter depths are indicated by blue dots for the respective measurement periods. The two black lines are the 19°C isotherm depth (lower line) and mixed layer depth (upper line).

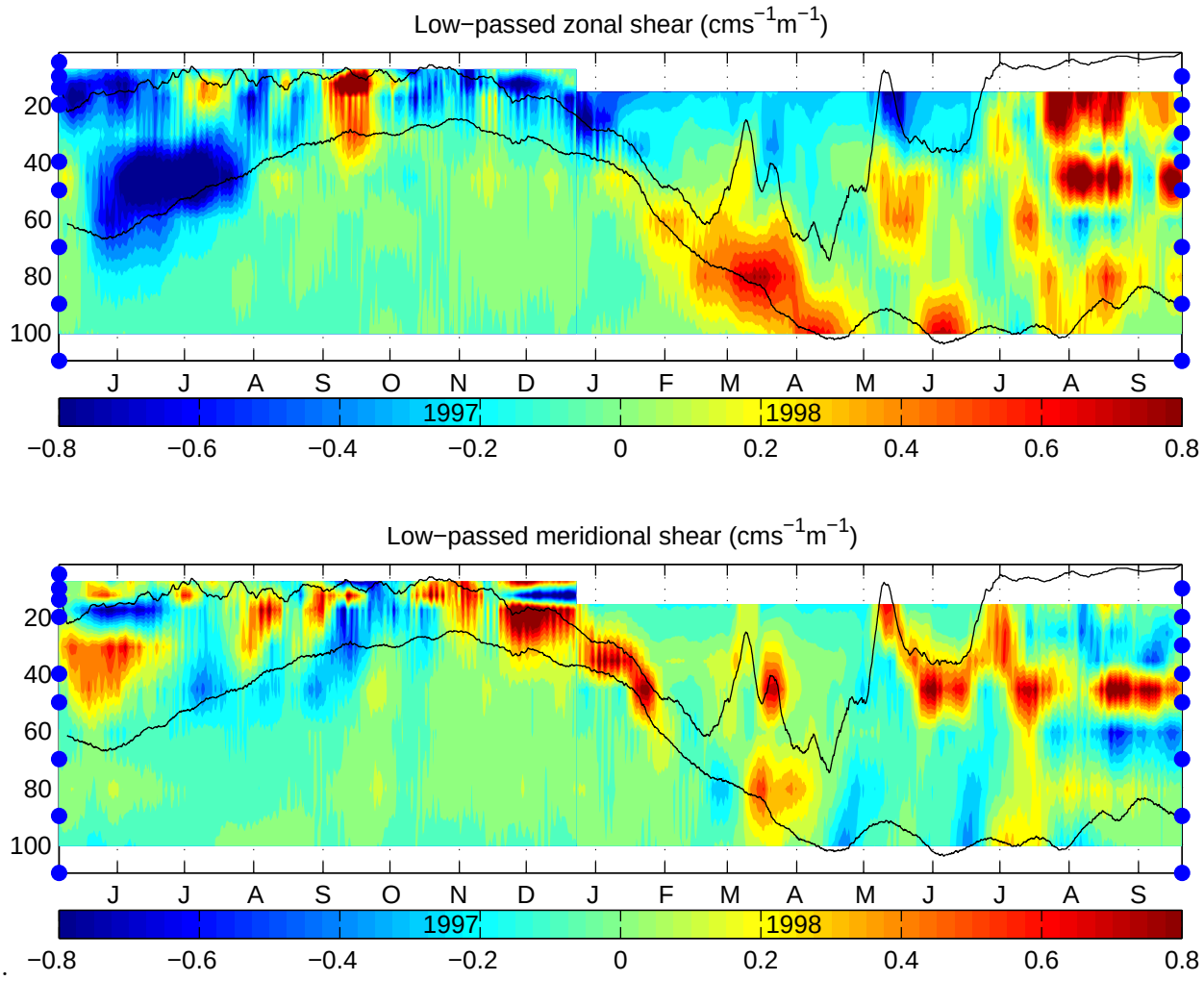

Figure 4-18: Estimated vertical shear of the low frequency flow. The top and bottom panels show the meridional and zonal components, respectively. The current meter depths are indicated by blue dots for the respective measurement periods. The two black lines are the 19°C isotherm depth (lower line) and mixed layer depth (upper line).

order to produce estimates of the Ri_g at the midpoints between current meters. Figure 4-19 shows the estimated squared buoyancy frequency (N^2). Note the apparent dependence of the N^2 estimate on the vertical separation of instrumentation. For example, the N^2 estimate in the thermocline varies by about a factor of two in early 1998 as the thermocline descends past clusters of temperature sensors near 50 m. Of course, the dependence of the N^2 estimate on instrument resolution is most pronounced near sharp gradients such as the thermocline.

An estimate of the gradient Richardson number is shown in figure 4-20. Throughout most of the measurement domain, the Richardson number is well above critical, having values between 10 and 1000. There are rapid order of magnitude changes in Ri_g that may not be apparent in figure 4-20 because the 17 month contour plot can not fully reflect the true one hour time resolution of the measurements. Still, the figure is worthwhile because it helps us to identify times and depths where the Richardson number was generally high or low. Some critical Richardson numbers occur in the top 20 m during the first phase of the field program, which was also during the period when the ITCZ was over the mooring. These near-surface critical values should be viewed with caution because they may simply reflect the fact that the near surface stratification was weak and they may also be the consequence of our neglect of salinity variations in estimating the density profile during the first phase of the field program. A significant amount of the observational domain contains Richardson numbers of about 1, which may indicate past remnants of turbulence or turbulence associated with nonlinear instabilities (Abarbanel et al., 1986; Stull, 1988), or this may also constitute unresolved critical Richardson numbers. In the remainder of this study, values of the Richardson number near 1 will be referred to as near-critical Richardson numbers. It is noteworthy that near-critical Richardson numbers occur in the main thermocline at the mooring. The 19°C isotherm and mixed layer depth are plotted over the Ri_g contours in figure 4-20. Figure 4-21 shows only those Richardson numbers that are in the thermocline (i.e. between 15 and 25.5°C) and have a value less than one. Periods when near-critical Richardson numbers are frequently present in the thermocline occur in the last five months of 1997 and the first three months of

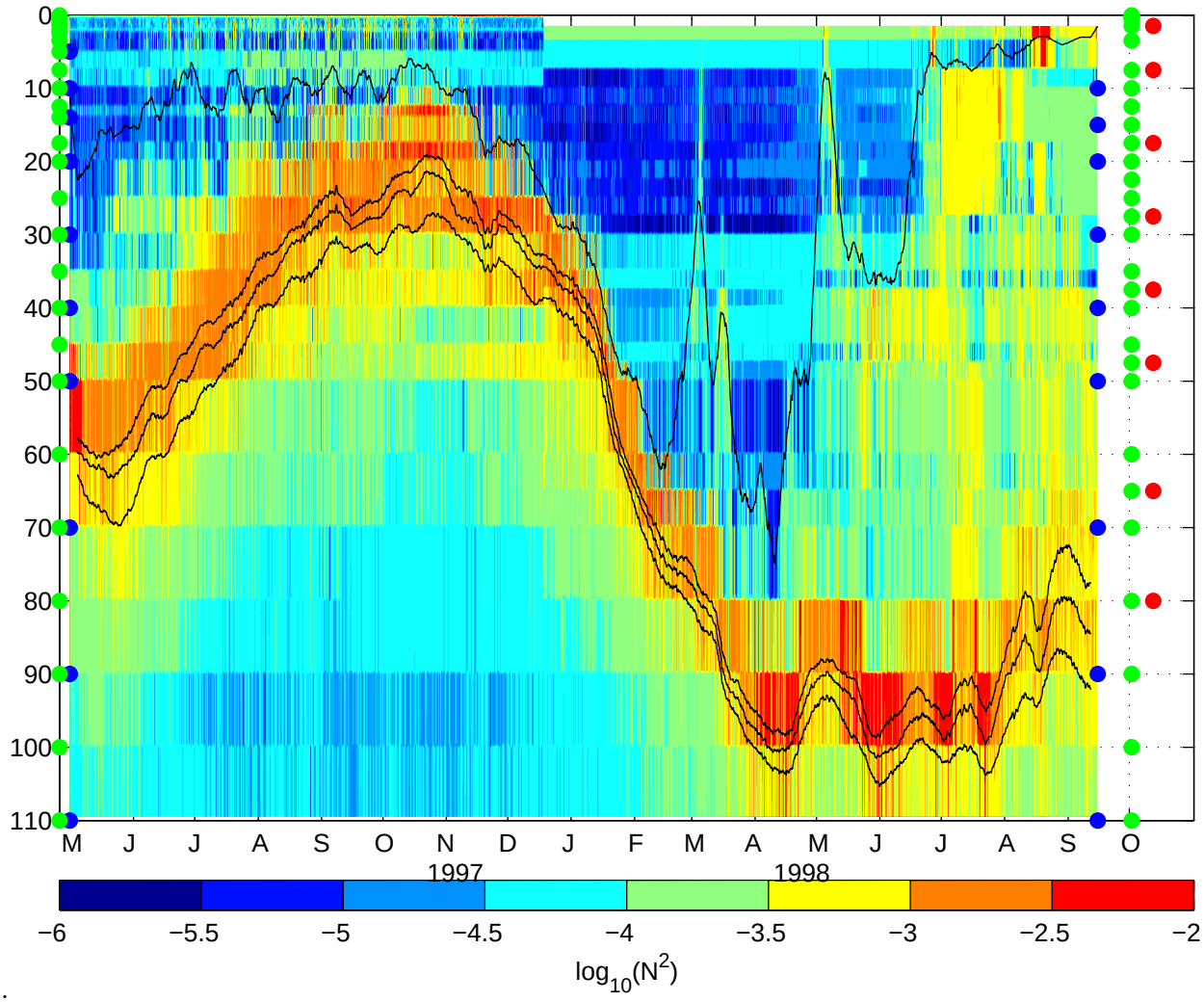

..

Figure 4-19: Estimated buoyancy frequency squared (s^{-2}). The color bar has a log_{10} scale, and the isotherms (19°, 22°, and 24°C) and mixed layer depth from figure 4-4 are plotted for reference. Current meters are indicated by blue dots for respective measurement periods, temperature sensors by green dots, and conductivity sensors by red dots.

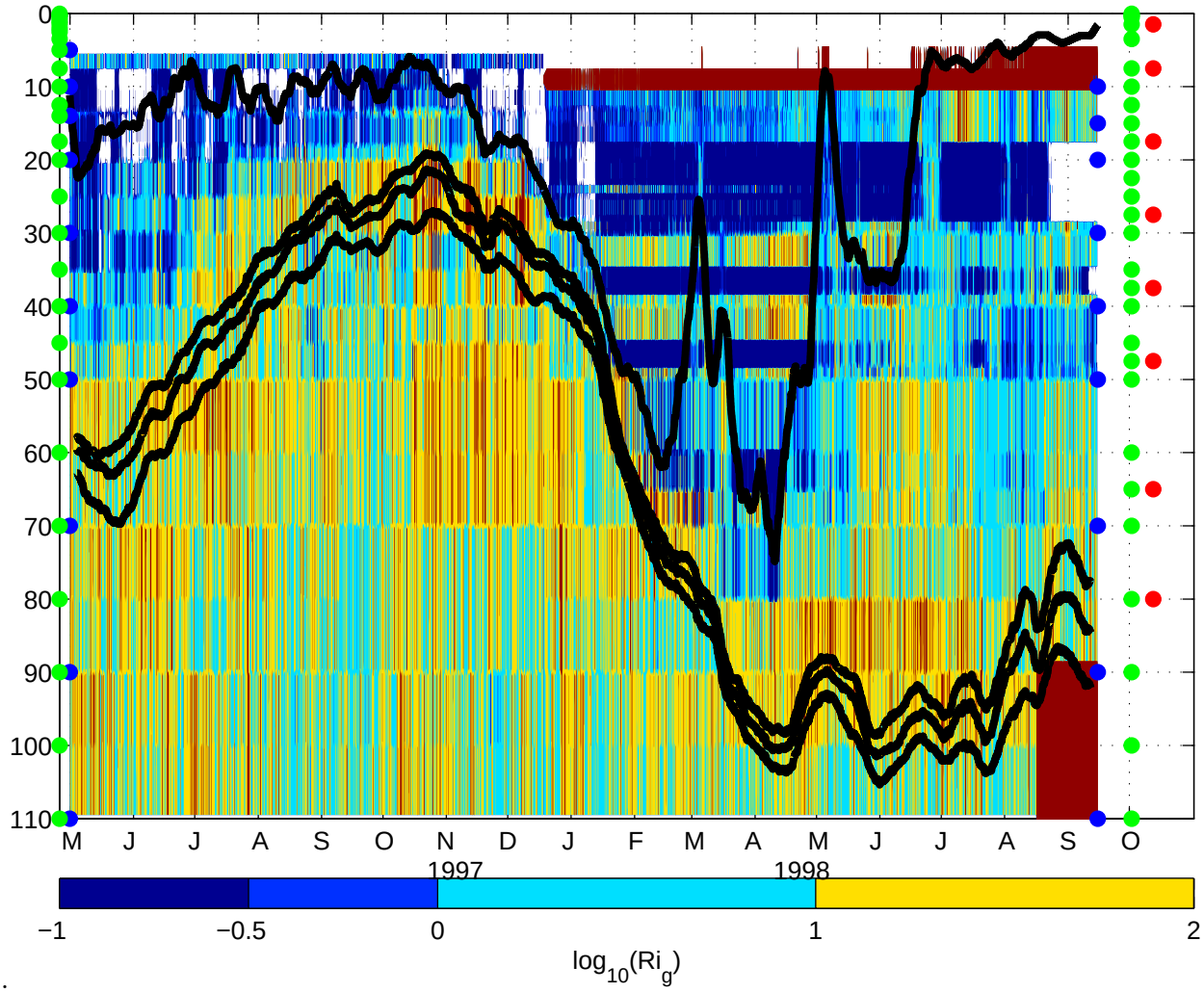

..

Figure 4-20: Estimated Ri_g. Current meters are indicated by blue dots for respective measurement periods, temperature sensors by green dots, and conductivity sensors by red dots. The color bar has a log_{10} scale, and the 19°, 22°, and 24°C isotherms and mixed layer depth (upper black line) from figure 4-4 are plotted for reference.

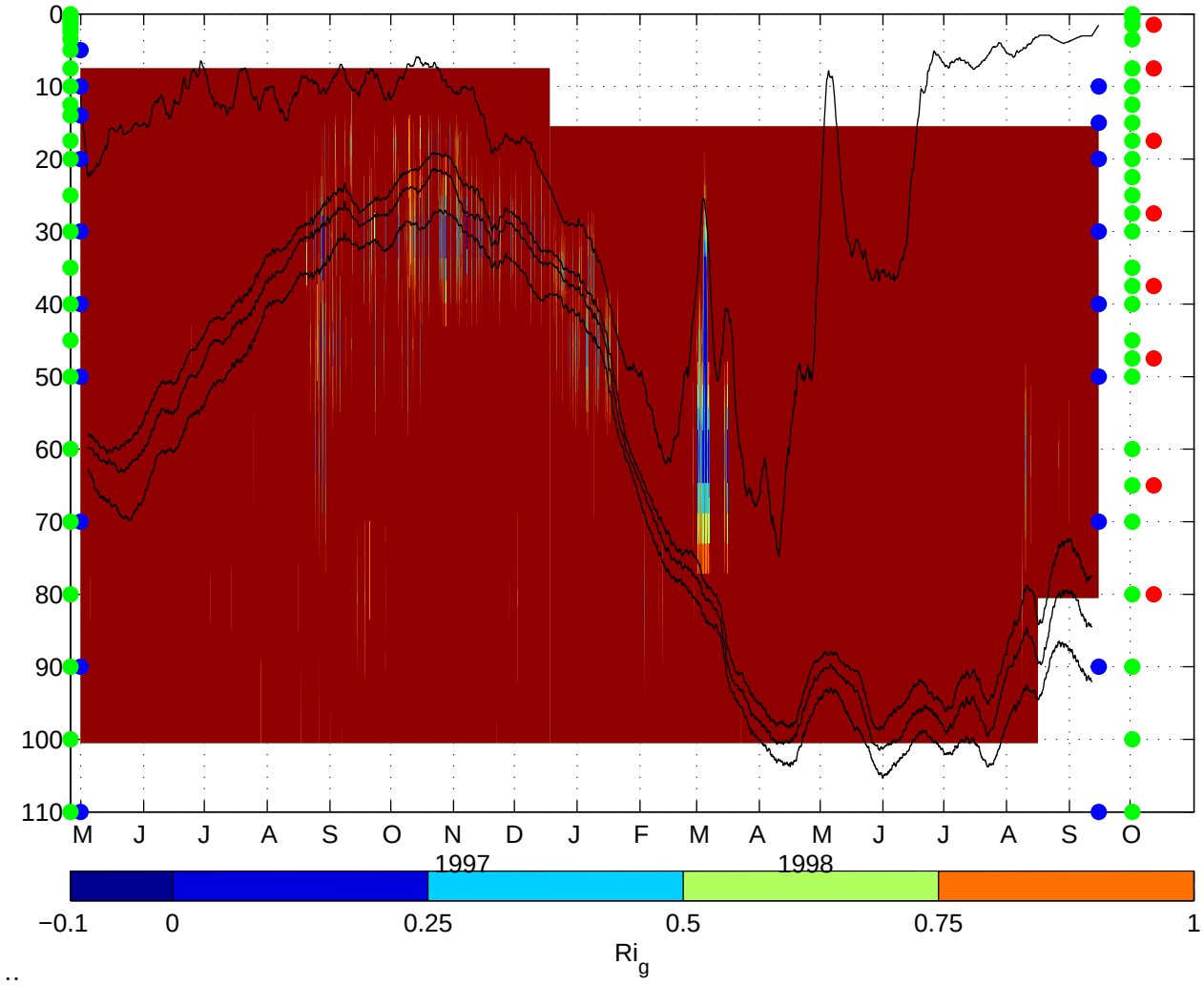

..

Figure 4-21: Estimated Ri_g less than 1.0 that occurs in water between 15 and 25.5 degrees (in the thermocline). Current meters are indicated by blue dots for respective measurement periods, and conductivity sensors are indicated by red dots. The color bar has a linear scale, and the 19, 22°, and 24°C isotherms and mixed layer depth from figure 4-4 are plotted for reference.

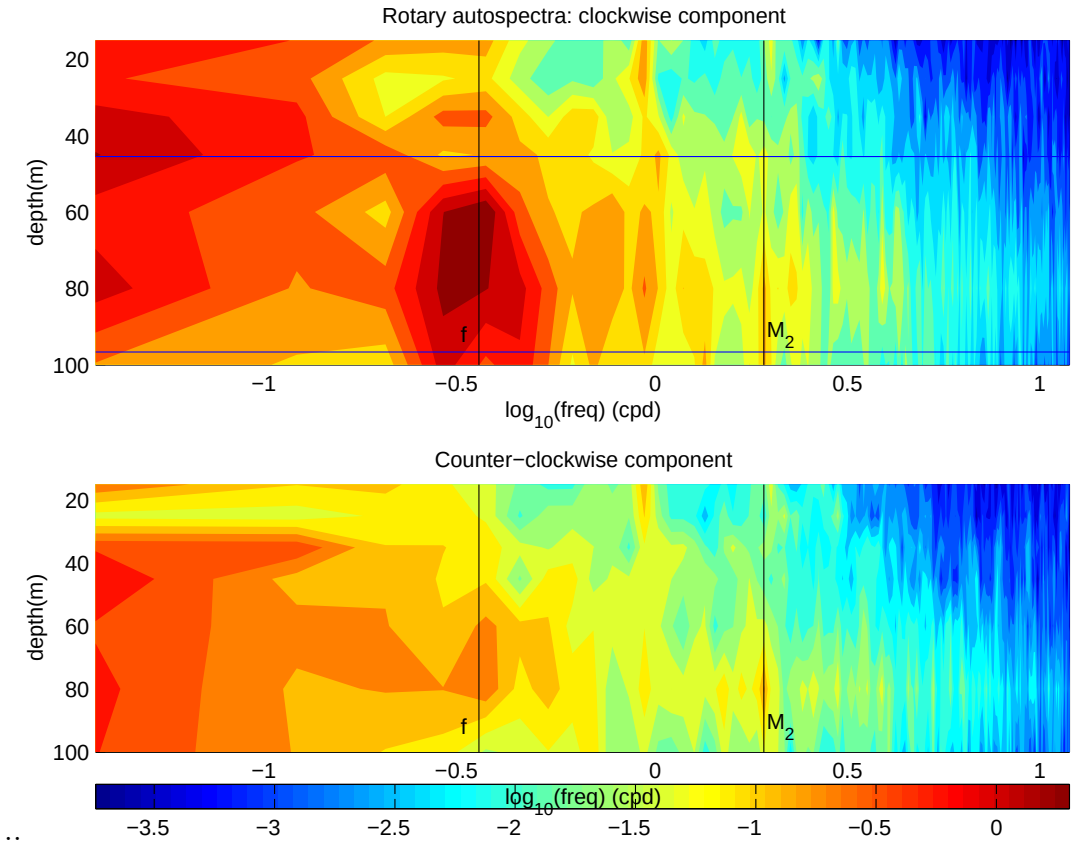

Figure 4-22: Frequency-depth plot of the rotary component auto-spectra of observed vertical shear; the color scale is in units of log_{10} of power density. The top panel shows the clockwise component, and the bottom panel shows the counter-clockwise component. In the top panel, the average mixed layer depth (upper blue line) and the average 19°C isotherm depth (lower blue line) are shown for reference. The spectra were computed over the 85 day period spanning Jan, 29 to May 12, 1998. The inertial and M_2 tidal frequencies are marked by vertical lines.

1998. In the next subsection, we will investigate the frequency spectra of the shear estimate that was presented in this section.

4.3.2 Frequencies contributing to shear

Power spectra of the shear components were computed using a fast fourier transform and a 16-hour Hanning window (not shown). During both phases of the field program there was statistically significant enhanced energy in the near-inertial band at all depths below 17 m. The Fourier spectra do not reveal any other statistically significant spectral peaks in vertically resolved shear. This indicates that a significant

amount of the shear is associated with near-inertial motions, and is consistent with the general prevalence of near-inertial motions in the velocity record (for example, see figure 4-9). The lack of enhanced energy at other frequencies may not reflect a true lack of shear, but rather that the shear at other frequencies is more intermittent (i.e. the shear is not statistically stationary).

To gain some understanding of the relationship between shear and stratification at the site, we also computed rotary auto-spectra of the shear components during times when the hydrographic structure was relatively stationary. Figure 4-22 shows the rotary auto-spectra of the shear components computed over the 85 day period spanning Jan, 29 to May 12, 1998 (as in figure 4-10 which is analogous except that it showed velocity rather than shear). Here, we can see that most of the shear at periods less than 30 days occurs between the mixed layer and the thermocline; the largest signal is near-inertial and clockwise-rotating. This is not surprising since we do not expect much shear in the nearly uniform mixed layer and we have seen that near inertial motions are perhaps the most prominent feature of the velocity record. It is interesting that at all of the frequency bands considered, the largest shear power occurs in the upper thermocline (10-20 m above the 19°C isotherm). This is also not surprising given the strong stratification in the thermocline, which allows a substantial vertical shear to be sustained.

Further insight into the frequencies contributing to shear can be gained through use of the wavelet transform. Estimation of the wavelet power spectrum (WPS) yields information about the power in a given frequency band as a function of time. By estimating the WPS at each depth for which we have a shear estimate, we can determine the time and depth dependence of the power in a particular frequency band. The wavelet power spectra discussed here are computed as in section 4.1.

Figure 4-23 shows the wavelet power spectra (WPS) for vertical shear of the meridional velocity component[11]at 30 m. The normalized vertical shear of the northward velocity at 30 m is shown in figure 4-23(a). The vertical shear at 30 m reached its

[11]We also computed the WPS for the vertical shear of the zonal velocity component at 30 m, but it is not shown here because it does not add much to our discussion of the shear. It is shown in appendix A, figure A-5.

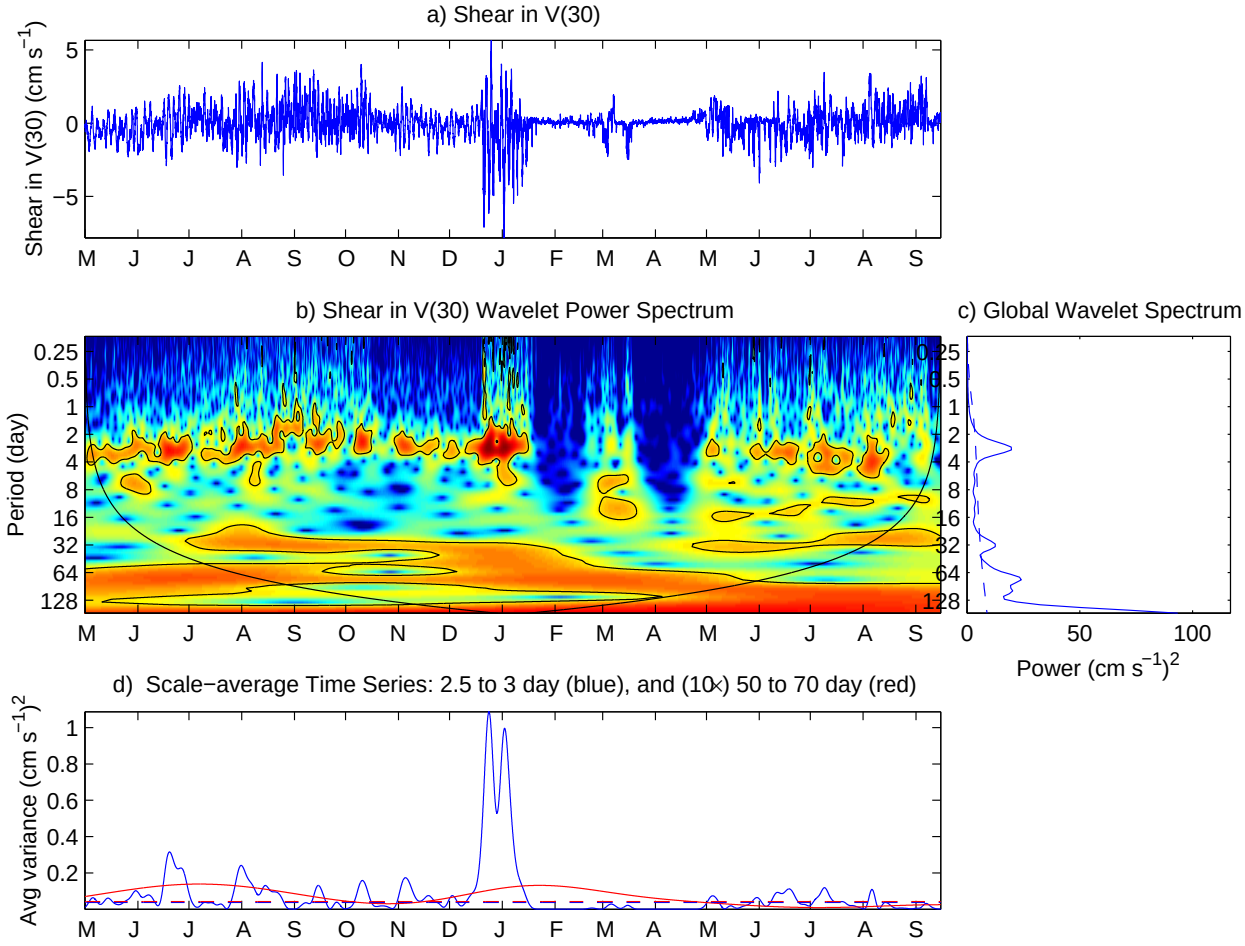

..

Figure 4-23: Wavelet analysis of vertical shear of meridional velocity at 30 m. (a) The shear time series, divided by its standard deviation and with the mean removed; (b) the WPS, with period in days on the vertical axis and time in days on the horizontal axis; (c) the global wavelet spectrum, a time average of the WPS and analog to the more traditional Fourier power spectrum; (d) the average power in two different frequency bands, one having a period of 2.5 to 3 days (near-inertial; blue line) and the other 50 to 70 days (intraseasonal; red line, magnified by a factor of 10).

largest amplitude between mid-December and mid-January, and we can see in figure 4-23(b) that most of the power during this time was at periods of 2-4 days (near-inertial) or 30 to 90 days. The near inertial shear power increased from already high background values near mid-December, but it decreased to become near zero just after mid-January when the vertically uniform mixed layer descended below 30 m. However, even when the current meters used to compute the shear at 30 m were inside the mixed layer, the shear at 60 day periods was statistically significant.

Figure 4-24 shows the band averaged near-inertial and intraseasonal power in vertical shear of meridional velocity[12]. These quantities were calculated by computing the wavelet power spectrum and levels of no significance at each depth (as was done to produce figures 4-23 and A-5). Then, we computed the band averaged power as a function of time at each depth. The meridional shear power in the 60 to 72 hour frequency band is shown in the upper panel of figure 4-24[13]. This frequency band is roughly $f \pm 10\%$ and was chosen to represent near-inertial motions. The level of no significance at 95% varies with depth, and these levels are indicated on the right edge of the figure. We can see that there is usually statistically significant near-inertial shear power in and above the main thermocline. Near-inertial shear power in the thermocline was above background levels (at a given depth) between late December, 1997 and April, 1998.

The lower panel of figure 4-24 shows the average shear power in the 54 to 71 day frequency band. In this band, statistically significant shear power was registered above the thermocline throughout much of the record. Particularly, statistically significant shear power was found near the thermocline from December, 1997 through August, 1998. It is important to note that, even if there were always shear at a 60 day period just above the thermocline, we would be unable to detect it by this method during the period of most rapid thermocline deepening because our wavelet analysis,

[12]Essentially, figure 4-24 conveys the same information as the bottom panel of 4-23, except as a function of time *and* depth.

[13]We also computed the band averaged near-inertial and intraseasonal power in vertical shear of *zonal* velocity (not shown), but the near-inertial power was qualitatively identical. In the intraseasonal band, there was statistically significant power just below the mixed layer from June to January and along the thermocline from March through August.

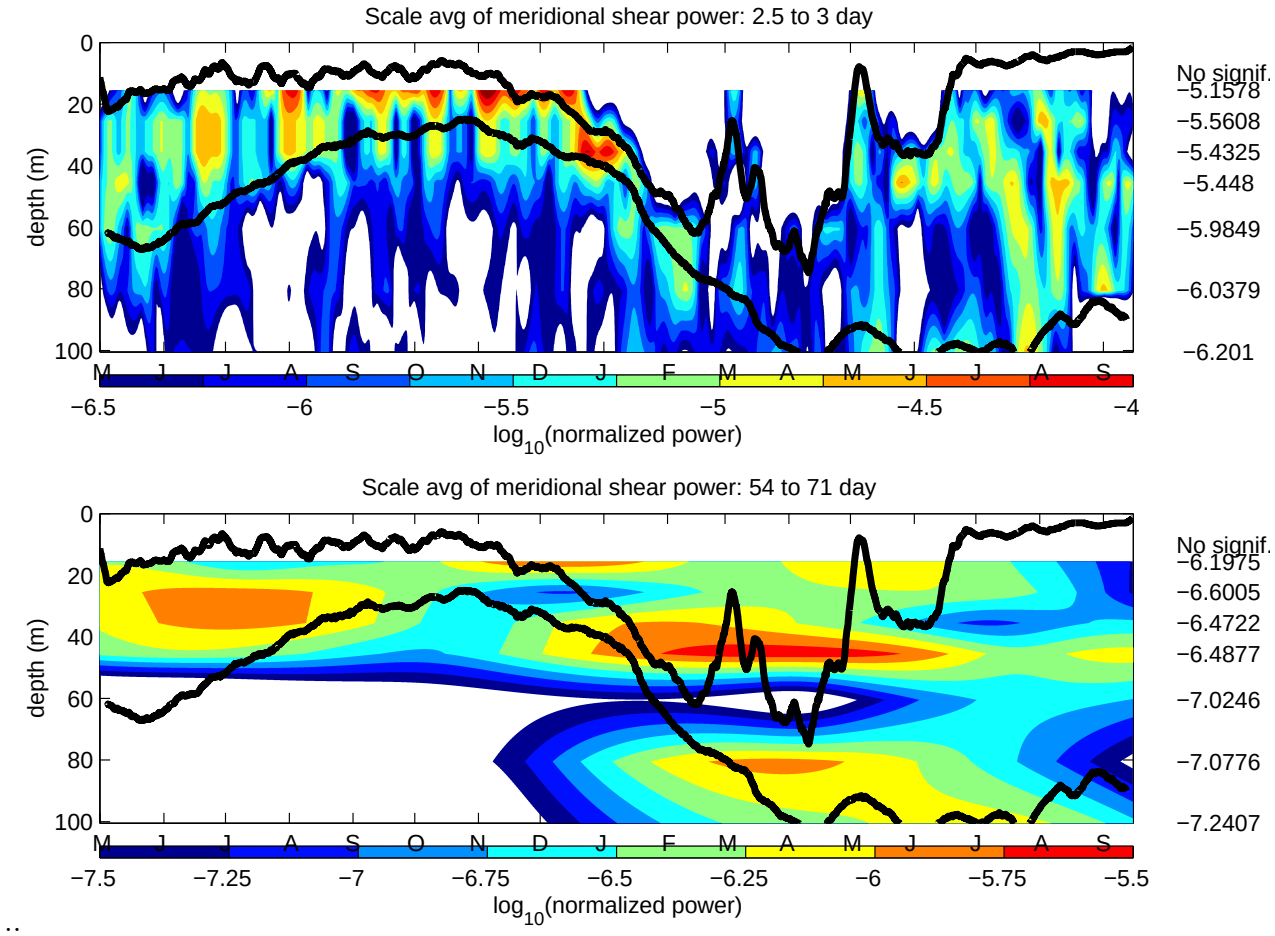

..

Figure 4-24: Band averaged (normalized) power in vertical shear of meridional velocity (log_{10} color scale). The solid black lines indicate the running 7-day average mixed layer depth (upper line) and 19°C isotherm depth (lower line). The level of no significance (in decibels) for each depth is indicated on the right hand side of each panel; contour values that are less than the level of no significance at a particular depth are not statistically significant. For example, in the upper panel at the uppermost depth (17.5 m), contours in yellow and red represent statistically significant power. Upper panel: (normalized) power in vertical shear of meridional velocity in the near-inertial band. Lower panel: (normalized) power in vertical shear of meridional velocity in the 54 to 71 day band.

computed at each depth, requires that shear be present at a given depth for at least 60 days; the thermocline fell by 40 m over about a month, and we can only expect to detect 60 day shear near the thermocline before and after this rapid deepening. So, it is noteworthy that the intraseasonal shear power in the thermocline is elevated just before and just after the rapid descent of the thermocline.

4.4 Summary and Discussion

During ITCZ conditions (mid-May to mid-December 1997 and July 1998 onward) there were large positive buoyancy fluxes, winds were calm, the thermocline and mixed layer were shallow, and SST had a large diurnal cycle. A couple of months before the end of the ITCZ season (i.e. mid-October), the winds began to increase, the Ekman pumping remained upward, the thermocline and mixed layer began to deepen, and SST began to decrease. The ITCZ moved completely south of the mooring by late December, a few weeks after the Ekman pumping became negative. By the time the ITCZ had moved south, SST was near the record low. Within the first three months of 1998 the thermocline would plummet from 40 to 100 m depth. This rapid descent of the thermocline is an expression of the so-called 'meridional tilting mode' (section 1.4), and it was one of the earliest signs of the termination of El Niño and the beginning of La Niña[14]. Especially during the first three months of 1998, the mixed layer also steadily deepened. The thermocline and mixed layer both began to shoal around July 1998 as the ITCZ moved back into the region, the Ekman pumping became once again positive, winds decreased, and the buoyancy flux increased.

We expect adiabatic motions of the thermocline to be caused by a combination of horizontal advection and vertical advection. In section 4.2, we sought to identify large scale influences on the thermal and velocity structure at the mooring; in particular, we examined the potential influence of Ekman pumping and Rossby waves. At this

[14]The transition from El Niño to La Niña is commonly held to have been around May 1998 (e.g. Wang and Weisberg, 2000); recall that the meridional tilting mode temporal function is coherent with ENSO indices with a lead of 5-7 months (Meinen and McPhaden, 2000; Alory and Delcroix, 2002).

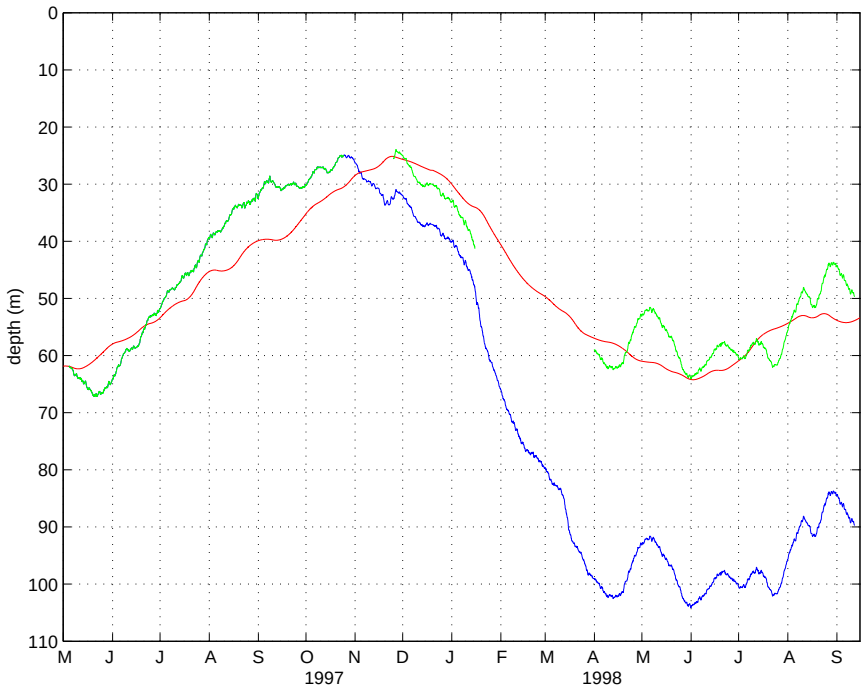

Figure 4-25: Comparison of observed thermocline depth (blue line) to expected Ekman pumping displacement (red line). The green line is intended to highlight times when the agreement between the two is reasonable.

latitude and outside of the internal gravity wave band, vertical advection is thought to be due to a superposition of the locally forced Ekman response and remotely forced, propagating Rossby waves (White, 1977; Meyers 1977; Kessler, 1990). We have argued that high-frequency Rossby waves were present at the mooring site (particularly during 1998), and some of the more rapid motions of the thermocline (i.e. 60 day time-scale) are undoubtedly associated with these waves. In the TOPEX/Poseidon SSH data, the rapid descent of the thermocline in early 1998 appears to have been zonally coherent and we were unable to detect any sign that the rapid drop-off of the thermocline was directly associated with long Rossby waves propagating past the mooring site.

Figure 4-25 shows a comparison between the observed evolution of the 19°C isotherm and the displacement that we would expect from vertical advection by Ekman pumping; here, we can see that the two nearly co-evolve (on a seasonal time-scale) except during the time of most rapid deepening during early 1998. To aid in

this comparison, the observed 19°C isotherm depth has been displaced (green lines) to highlight this co-evolution.

The evolution of total upper ocean heat content through time can be largely accounted for by vertical advection and surface heat flux. This suggests that horizontal advection was of secondary importance in determining the thermal structure at the mooring site. However, the evolution of thermocline depth is not well described by vertical advection alone, especially during the period of rapid deepening in early 1998. This suggests that vertical redistribution of heat by mixing processes may have been important in producing the observed changes in upper ocean thermal structure. In the next chapter, we will investigate this possibility using a one-dimensional model of the upper ocean.

Chapter 5

Modelling the Oceanic Response

Based on a heat budget using an Ekman pumping estimate of the vertical velocity, we have argued that the vertical velocity is important to the evolution of the upper ocean thermal structure. While the inclusion of the Ekman pumping helps in closing the vertically integrated heat budget, the Ekman pumping does not explain the rapid descent of the thermocline that was observed in January and February of 1998. If Ekman pumping were the only mechanism affecting the thermocline depth, then the thermocline would have fallen by only 20 m during January and February. In fact, the thermocline fell more than 40 m during January and February, indicating that other mechanisms were important. However, the near closure of the heat budget when using an Ekman pumping based estimate of the vertical velocity suggests that the Ekman pumping estimate is close to the true vertical velocity and that horizontal advection is of secondary importance. If this is the case, then it is unlikely that any other adiabatic processes are responsible for the observed descent of the thermocline, and it is plausible that local mixing processes are responsible for much of the observed variation in thermocline depth.

There are various conceivable approaches by which we could attempt to model the observed oceanic response, which exhibited shoaling of the thermocline and high SST during ITCZ conditions and a rapid deepening of the thermocline and SST cooling as the ITCZ moved south of the measurement region. One approach that is commonly employed is use of a general circulation model (GCM). This requires specification of

the large scale air-sea fluxes and a spin-up time of at least a few years. Unfortunately, the temporal and spatial resolution of the large scale air-sea flux database is so coarse that the use of measured forcing fields is not possible. Instead, GCMs are typically forced with re-analysis fields from operational weather prediction models, such as those from the National Center for Environmental Prediction (NCEP) or the European Center for Medium-range Weather Forecasting (ECMWF). Figure 5-1 shows the isotherm structure for 10°N, 125°W during the PACS field study in the Massachusetts Institute of Technology GCM when forced by NCEP re-analysis flux fields. The primitive equation model has 21 vertical levels and $\frac{1}{3}$ degree meridional resolution in the tropics. This particular GCM run has been used in a number of studies and is described in more detail in McKinley et al (2000). The model clearly fails to reproduce the observed behavior of the thermocline at the mooring site, exhibiting less than a 25 m change in thermocline depth during the entire observation period. We will not attempt to determine the source of this discrepancy from the observed temperature evolution here, but it should be noted that the NCEP wind stress magnitude had a large low bias during non-ITCZ conditions during the PACS observation period (figures 3-14). Also, the Ekman pumping velocity calculated using the NCEP wind stress field differs qualitatively from that calculated using the ERS scatterometer wind stress. This discrepancy has been noted for the mean fields by Kessler (2002b).

The failure of a complex GCM to reproduce the observed variability at the mooring site does not bode well for the prospect of using a large scale model of intermediate complexity to model the details of the oceanic response at the mooring site. A large scale model of intermediate complexity still requires large scale forcing fields, but the representation of the physics is less sophisticated. One potential advantage of using a large scale model is that this might help to clarify the generating mechanism for the observed 60 day Rossby wave activity seen at the mooring and in the TOPEX/Poseidon data. While this is an interesting and important issue that needs to be addressed, this pursuit is outside the scope of this thesis. Instead, we will take the large scale geostrophic flow as given and investigate the local evolution at the

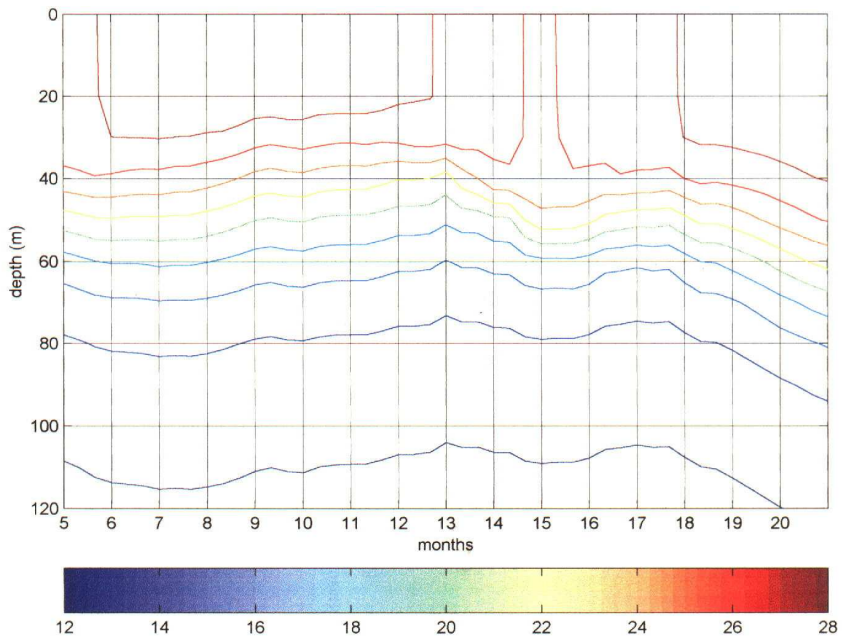

Figure 5-1: Time-depth plot of temperature at 10°N, 125°W during 1997-1998 in an MIT-GCM run with NCEP forcing as described in the text. (Model output courtesy of Galen McKinley).

mooring. That is, we will examine the local response of the upper ocean to wind and buoyancy forcing in the presence of the large scale baroclinic flow.

We have argued that vertical mixing may play an important role in redistributing heat and momentum in the upper ocean at the mooring site, and that this mixing may be one of the key factors affecting the thermocline depth during the observing period. In the previous chapter, we showed that there is elevated shear power in the near-inertial frequency band, and that this elevated power was coincident in time and depth with the rapid descent of thermocline in early 1998. Low Richardson numbers were also observed at these times and depths, although the vertical resolution of instrumentation limits our confidence in this estimate. Since most of the shear appears to be in the inertial frequency band, the wave number aspect ratio of the internal waves should be very small (i.e. the motions are nearly horizontal), and it should be possible to model the shear using a horizontally infinite, one-dimensional model.

If the evolution of the hydrographic structure at the site is indeed governed primarily by a combination of surface fluxes, vertical turbulent fluxes, and vertical ad-

vection, then it should be possible to simulate the observed temperature, salinity, and density structure using a one-dimensional mixing model of the upper ocean. In this chapter, we use a one-dimensional mixing model of the upper ocean (Price et al., 1986), forced by observed surface fluxes of heat, freshwater, and momentum to model the observed behavior of the thermocline and mixed layer. It is found that, in addition to vertical advection, the observed evolution of the thermocline depends critically on mixing associated with vertical shear driven by an interaction between inertial currents and the large scale flow. The model experiments incorporate various levels of realism to determine the factors contributing to this mixing, and we conclude that the low-frequency near-geostrophic currents couple with the inertial currents to produce significant mixing in the main thermocline. A full model run that includes a data-derived representation of the low-frequency currents and an estimate of the vertical velocity can account for 96% of the low frequency variance of the observed thermocline depth over a 6 month period when the thermocline depth ranges from 30 to 100 m. Eighty-five percent of the observed 70 m change in thermocline depth is achieved during the first three months of 1998 (see figure 4-4), and about half of the observed change can be ascribed to diapycnal vertical mixing.

We have hypothesized that the interaction between the inertial and the low frequency velocities produces high vertical shear that leads to shear instability in the thermocline. An efficient way of testing this hypothesis is to impose the large scale, low frequency velocity on a one-dimensional model capable of modelling the inertial currents and shear driven mixing. This technique was used successfully by Schudlich and Price (1992) to simulate the mixing between the mixed layer and the Equatorial Undercurrent. We use a model formulation similar to theirs. However, their study used mean upwelling and pressure gradient profiles derived field data, while the present study uses time varying estimates derived from data. Like Schudlich and Price, we have found that the details of the vertical profile of vertical velocity are of little consequence to the model results. More detail about the model formulation is given in section 5.1.

5.1 Model Formulation

The physical and numerical model that we use is based on the model of Price, Weller, and Pinkel (1986) (hereafter, PWP). The model is described in detail in Price et al. (1986), and it is further described by Schudlich and Price (1992) and others. The model described here most closely follows Schudlich and Price (1992), but there are some minor differences[1]. The model ignores horizontal advection and steps forward the one-dimensional equations for conservation of momentum, heat, and salt:

$$u_t + wu_z - fv = \frac{\tau_z^x}{\rho_o}, \tag{5.1}$$

$$v_t + wv_z + fu = \frac{\tau_z^y}{\rho_o}, \tag{5.2}$$

$$T_t + wT_z = \frac{1}{\rho_o c_p}(q_z - r_z), \tag{5.3}$$

and

$$S_t + wS_z = -a_z, \tag{5.4}$$

where (u,v) is the wind-driven velocity[2], (τ_x, τ_y) is the vertical turbulent flux of horizontal momentum, q is the penetrating solar radiation, r is the turbulent heat flux, and a is the turbulent salinity flux. Equation 5.3 is the same as the one used in section 4.2.3 to compute the heat budget (i.e. it is equation 4.9, except that horizontal advection is neglected outright here). No linear drag is applied, and all momentum damping in the model arises from mixing or wind forcing. The penetrating solar radiation, q, is imposed using a double exponential depth decay from the surface, with decay constants corresponding to clear, mid-ocean water (Jerlov, type IA). The model cannot calculate w, so this quantity is imposed. The vertical velocity, w, is estimated using the Ekman pumping. The momentum equations (5.1 and 5.2) are

[1]The most important difference is that Schudlich and Price investigated oceanic behavior at the equator (i.e. $f = 0$). Also, Shudlich and Price had an estimate of the pressure gradient; this leads to some practical differences in how the model equations are solved

[2]The term "wind-driven" is used loosely here to mean the part of the velocity signal that is not driven by pressure gradients. Of course, so long as the wind is not zero, the diurnal cycle in heat flux and mixed layer depth can force inertial oscillations (e.g. D'Asaro, 1985a), and we intend this type of velocity variability to also be included under the term wind-driven velocity.

prognostic equations for the wind driven velocity. The geostrophic velocity is included by adding it to the the wind-driven velocity before performing the stability calculations which govern the evolution of the turbulent fluxes $\vec{\tau}$, r, and a. In practice, this amounts to superimposing the locally wind driven velocity upon a weakly sheared background flow. More detail about how the geostrophic velocity and vertical velocity are estimated and imposed on the model will be given shortly.

The model uses three stability conditions as mixing criteria to implicitly determine $\vec{\tau}$, r, and a. The stability conditions are,

$$\rho_z \geq 0, \tag{5.5}$$

$$Ri_{bulk} = -\frac{g\Delta\rho h}{\rho_o \Delta \vec{u}^2_{Net}} \geq 0.65, \tag{5.6}$$

and

$$Ri_g = \frac{N^2}{(\frac{\partial}{\partial z}(\vec{u}_{Net}))^2} \geq \frac{1}{4}, \tag{5.7}$$

where Ri_{bulk} is a bulk Richardson number measured from the mixed layer to the grid cell just below, and h is the depth of the mixed layer. The first criterion is that of static stability, and the second one is meant to simulate mixed layer entrainment (Price et al., 1986). The third criterion is meant to simulate shear instability and has been discussed in section 4.3.1. In model experiments including the geostrophic flow, the geostrophic contribution to velocity is included in the stability calculations; the total velocity, $\vec{u}_{Net}$, is taken to be the wind driven velocity ($\vec{u}$) plus the pressure driven velocity ($\vec{u}_g$, estimated from observations). If any of these criteria are not met, mixing occurs in a way that conserves the total heat, salt, and momentum. In addition to mixing governed by these criteria, there is also a small 'background diffusion' ($\kappa = 10^{-5} m^2/s$, for both heat and salt) that is intended to represent mixing by internal waves and other processes that are not modelled. This is the same value of the background diffusion used in the standard configuration of the K-Profile Parameterization upper ocean model of Large et al. (1994), and it is generally smaller than the vertical eddy diffusivity used in general circulation models.

Procedurally, the numerical model works in a physically intuitive way; at each time step (1) radiative and surface heat fluxes and freshwater fluxes are applied, (2) Static stability is checked and convective mixing ensues if necessary, (3) Surface momentum fluxes are applied and the inertial velocity is rotated by a half-timestep angle, (4) the bulk Richardson number is checked and the mixed layer deepens and entrains as necessary to ensure non-criticality, (5) the gradient Richardson number is checked and iterative mixing occurs between adjacent grid cells as necessary to ensure non-criticality, (6) the inertial velocity is rotated by a final half-timestep angle, and (7) the effects of vertical advection and diffusion are calculated.

We approximate the vertical velocity at the thermocline with the Ekman pumping velocity calculated using the IFREMER ERS scatterometer wind stress product as described in section 4.2.3. The velocity is assumed to be equal to the Ekman pumping velocity at and below the 19°C isotherm, and it tapers linearly to zero at the surface. We explored the use of other vertical velocity profiles (e.g. vertically constant or maximum at the thermocline). We found that the model results are somewhat sensitive (quantitatively) to the imposed vertical velocity profile, but the qualitative relationship between the various experiments is unaffected by the particular choice of vertical velocity profile.

5.2 Model Forcing and Initialization

The model is forced using hourly averaged observations of heat flux, freshwater flux, and winds from the PACS field study. These observations were discussed in detail in chapter 3. Although the wind stress at the mooring was estimated to a high degree of accuracy from observations of surface humidity, air-sea temperature difference, and air-sea velocity difference using a state-of-the-art bulk formula (Fairall et al., 1996), this stress was not used because the air-sea velocity difference introduces an inertial frequency variation in the stress. This inertial frequency variation arises from the presence of inertial oscillations in the near-surface current meter record. A steady wind always opposes upper ocean inertial oscillations in the sense that the stress

decreases when the wind and the mixed layer velocity are in the same direction, and the stress increases when they are opposed. However, the model inertial velocity is not always perfectly in phase with the observed mixed layer velocity, and if the two become 180° out of phase the observed stress can produce a spurious resonant response in the model. To avoid this artificial resonance, we calculate the stress within the model using the difference between observed wind and modelled (net) surface velocity and the bulk formula of Large and Pond (1981). For all model experiments, the vertical resolution is 0.5 m and the time step is 1 hour.

The model temperature and salinity profiles are initialized using the running average mooring profiles because the high frequency (e.g. tidal and internal waves) variation in the hydrography sometimes produces large ($O(10m)$) vertical excursions from the mean depth. For example, at the beginning of the second phase of the field study, the 7-day running averaged depth of the thermocline changes only by about a quarter meter per day, but in a given day the thermocline depth can vary by more than 10 m. The model cannot represent these high frequency vertical motions, so if we were to initialize the model with a thermocline depth that is 10 m off of the local time mean depth, this error would propagate though time in the model producing significant model errors.

The initial value of the wind-driven component of the velocity is always taken to be zero. Of course, the (real) wind driven velocity is probably not in fact zero, but the model is fairly insensitive to this aspect of the initialization and the model inertial currents begin to resemble the observed ones within a few inertial periods. In experiments including an estimate of the low-frequency, pressure driven flow, the total initial velocity is equal to the pressure driven velocity.

5.3 Estimating and Imposing the Background Geostrophic Flow

There are various conceivable approaches to estimating and imposing the low frequency pressure-driven flow on the one-dimensional model. It is desirable to maintain some relationship between the vertical profile of the pressure driven flow in the model and the model's density structure because there is clearly such a relationship in the observations. Moreover, imposing the low frequency flow as a function of depth might artificially force the model toward the observations. Vertically coherent low frequency velocity variability was visually apparent in the vertically banded structure of the meridional velocity (e.g. figure 4-8) and in the zonal velocity (figure 4-7). The vertical EOF analysis presented in appendix B suggests that the dominant mode of low-frequency velocity variability was associated with the large scale pressure gradient rather than the local wind. One way of representing the low frequency component of this pressure-driven flow might be to use the first vertical EOF time series, but this would impose a frozen vertical structure on the model low frequency velocity. Instead, we chose to use an idealized vertical profile of velocity which compresses and stretches as the model thermocline moves up and down to mimic the observed pressure driven flow. This idealized profile increases quadratically from zero at the 19°C isotherm to full value at the surface. We experimented with various idealized profiles, but settled on this one because it most closely resembles the first vertical EOF of the observed velocity and the low-passed observed velocity below the mixed layer. We will further discuss the relationship of the idealized vertical profile to the observations after giving more detail about how the idealized profile is imposed.

To impose the low frequency currents, we first made an estimate of the low frequency currents by producing a 7-day running average of the observed velocity at 30 m. The running average effectively filters inertial and higher frequencies. We chose this depth because it is shallow enough capture the full magnitude of the low frequency flow, as the low frequency flow decays toward the thermocline. In the model, we assume a level of no motion at a depth in the lower thermocline and have the low

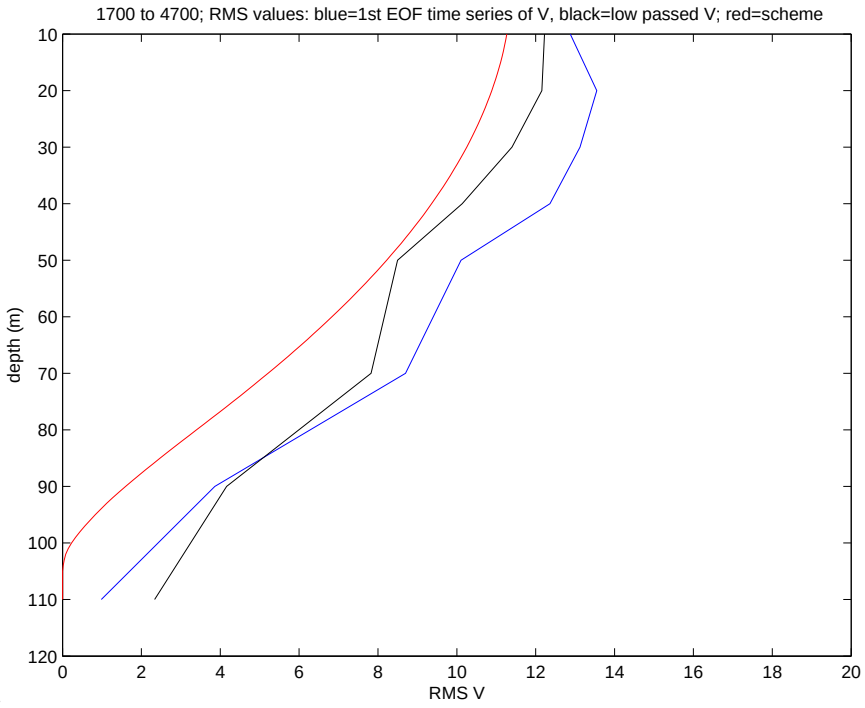

Figure 5-2: Comparison of the RMS value of observed meridional velocity (black line) to that of the first EOF reconstructed time series (blue line) and the idealized velocity profile (red line).

frequency velocity increase gradually to full speed near the surface. (The increase with depth goes like $u_g(z) = u_g(30m)(1 - \frac{z}{z_{thcl}})^2)$. The idea that the low frequency velocity becomes small at the lower thermocline is supported by the observations presented here (see figures 4-7 and 4-8). The approximation seems especially appropriate during the second phase of the field study, when the velocity at the 19°C isotherm is about 10% of its surface value.

Figures 5-2 and 5-3 show comparisons of the idealized vertical profile of the low frequency pressure-driven velocity to the first vertical EOF time series, which has been shown to be uncorrelated with the local wind stress. Figure 5-2 shows the root-mean-square (RMS) value of meridional velocity in the first vertical EOF time series (blue line) computed over an 85 day period when the thermocline depth did not change drastically (March through May, 1998, as in appendix B). Also shown is the RMS value of the idealized vertical profile of the meridional velocity (red line) and the RMS value of the low-passed meridional velocity (black line). The surface value

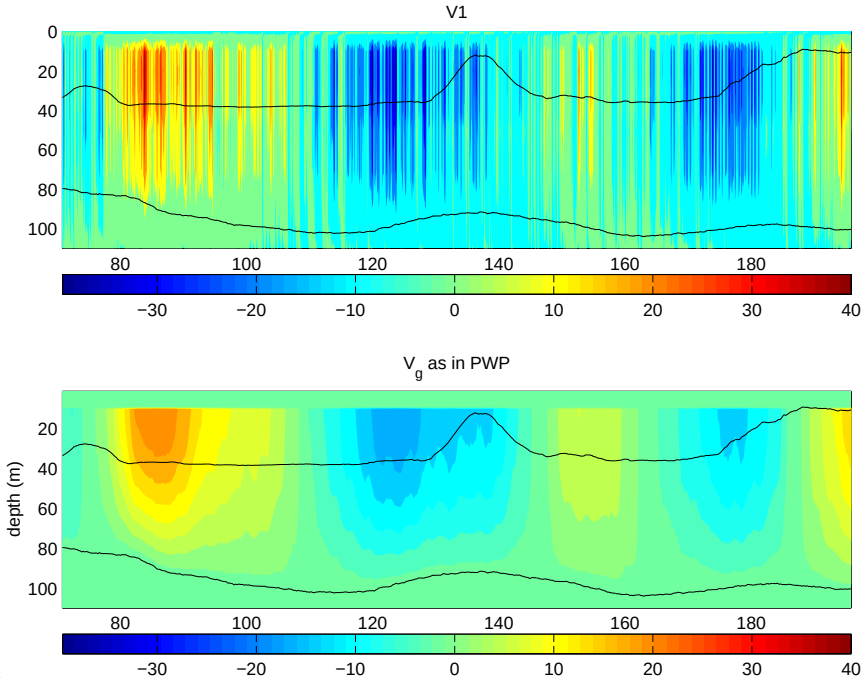

Figure 5-3: Comparison of the first EOF reconstructed time series of meridional velocity to the idealized low frequency velocity (cm/s). The 19°C isotherm and mixed layer depth are also shown. The mixed layer depth shown here is determined by a density criterion.

corresponds to the wind stress and is not important for this discussion. All three curves are similar, and in particular, they all represent similar vertical shear profiles. Figure 5-3 shows a comparison of the first vertical EOF time series to the idealized vertical profile of meridional velocity that would be imposed on the model if the model thermocline depth were the same as the observed thermocline depth. Aside from the high frequency variability in the EOF time series, there is a clear correspondence between the two. We conclude that this quadratic increase of imposed velocity from zero at the thermocline to full value at the surface is a reasonable representation of the low frequency pressure-driven flow, though we did explore several other profiles and found no serious qualitative differences in the model results.

5.4 Model experiments and results

In what we will refer to as a full model run, the vertical velocity and the low frequency horizontal velocity are imposed on the model as described in sections 5.1 and 5.3. Additional experiments are conducted to determine the relative roles of w, $\vec{u}_g$, and local forcing in the evolution of the hydrography at the site. A straightforward way of assessing these roles is to conduct model runs where one of these factors is left out of the model formulation. After demonstrating that the model does an adequate job of reproducing the observations, we will present and discuss runs which exclude w, $\vec{u}_g$, heat flux, freshwater flux, and wind forcing from the model in various combinations.

A comparison of the observed temperature structure to that of the full model run is shown in figure 5-4. The agreement of the model with the observed temperature structure is remarkably good; the model accounts for 96% of the low frequency (7-day running average) variance of the observed thermocline depth over a 9 month period. A comparison of the observed velocity structure to that of the full model run is shown in figure 5-5. In the figure, the model output has been sampled at depths corresponding to current meter depths to facilitate a visual comparison. Qualitatively, the observed velocity is well represented by the model, though there are some obvious discrepancies.

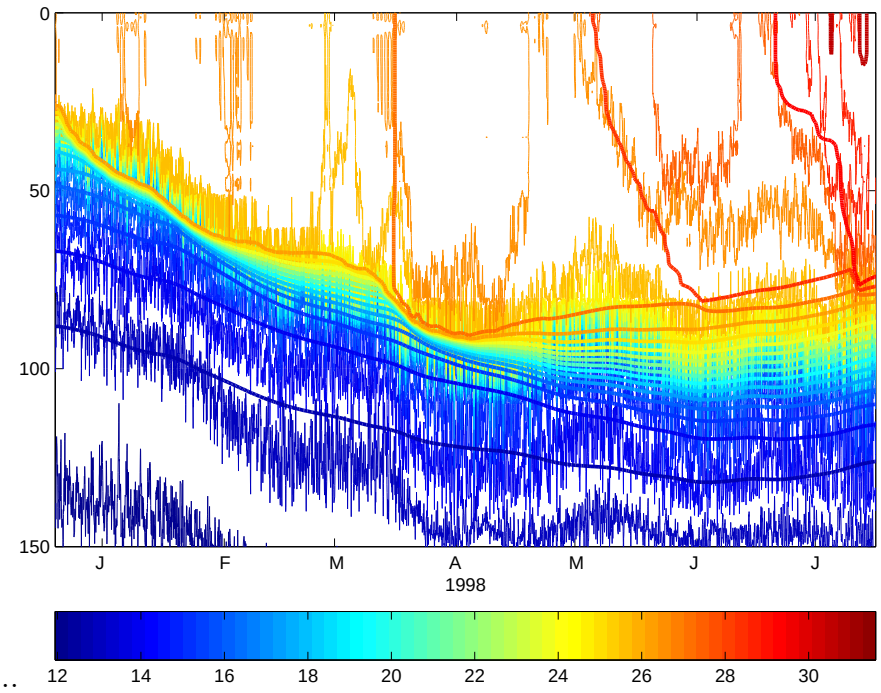

Figure 5-4: Comparison of modelled (smooth, thick contours) and observed ('noisy' contours) temperature structure. The color scale is in degrees C.

	setup	$z_{thcl}(90\ days)\ [m]$	$SST(90\ days)$	variance of $v(10\ m)$
Observed	N/A	93	26.80	0.0259
Full model	full run	88	27.26	0.0256
Experiment I	no u_g; no w	49	25.92	0.0590
Experiment II	no u_g	72	26.75	0.0483
Experiment III	no w	65	27.09	0.0292
Experiment IV	No local τ	62	27.03	0.0106

Table 5.1: Comparison of model experiments and observations. $z_{tcl}(90\ days)$ is the 19 degree isotherm depth after 90 days of simulation.

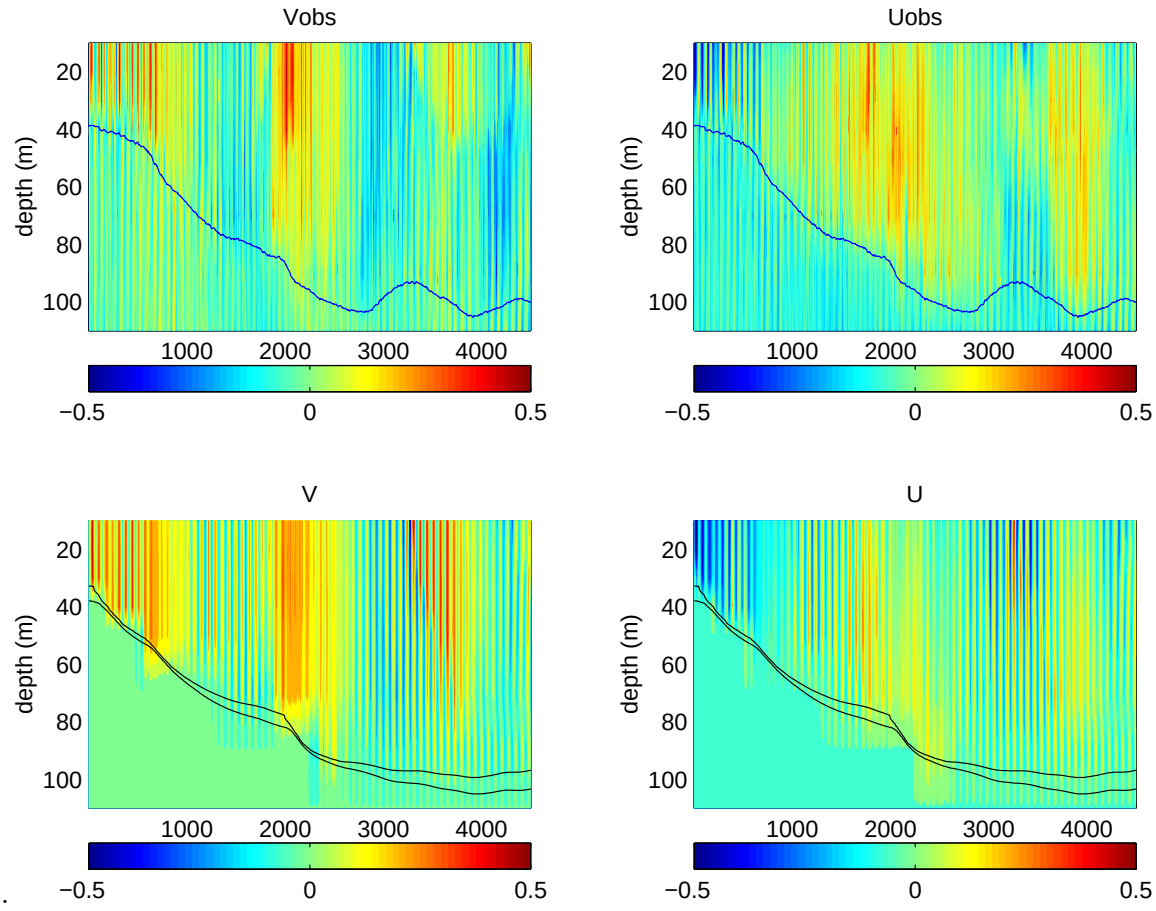

Figure 5-5: Comparison of modelled (bottom two panels) and observed (top two panels) velocity structure. The color scale is in m/s.

To understand the important mechanisms in the full model run, we conducted a series of experiments which selectively excluded the imposed vertical velocity and low frequency background flow. Table 5.1 summarizes the model experiments and shows a comparison of model experiments and observations. The depth of the thermocline, SST, and the near surface velocity are important aspects of the upper ocean hydrography, and the columns of the table are meant to be measures of these properties. The variance of the meridional velocity at 10 m was chosen as a metric of the velocity because it is a rough measure of the amplitude of near-inertial oscillations in the mixed layer. A common shortcoming of slab-type mixed layer models is the unrealistic build-up of inertial energy (D'Asaro et al., 1995). The most common 'remedy' for this problem is to introduce a linear drag in the momentum equations. None of the experiments presented here use artificial damping. The full model run produces inertial oscillations that are of the right amplitude. This is presumably because the model has an adequate representation of shear driven dissipation and mixing.

Time series plots of thermocline depth in the observations and in selected model experiments are shown in figure 5-6. In the first model experiment, we did not include any representation of the low frequency current or vertical advection. This model set-up might be deemed the 'standard configuration' of the PWP mixed layer model, since this is the way that the model is traditionally run (e.g., Price et al., 1986; Large and Crawford, 1995; Anderson et al., 1996). In this configuration, the model thermocline moves downward approximately linearly with time at a rate of about five meters per month as a result of mixing driven by the surface forcing. Overall, there is much less mixing in this model experiment[3], and as a consequence of reduced downward mixing of momentum and turbulent dissipation of kinetic energy, the model mixed layer velocity becomes unrealistically large. The generally shallower mixed layer also contributes to the unrealistically large mixed layer velocities by distributing the momentum flux from the wind over a shallower layer.

In the second model experiment (experiment II, figure 5-6d), we included an estimate of vertical velocity, but we did not include a representation of the low frequency

[3]Mixing in the model will be quantified in the next section.

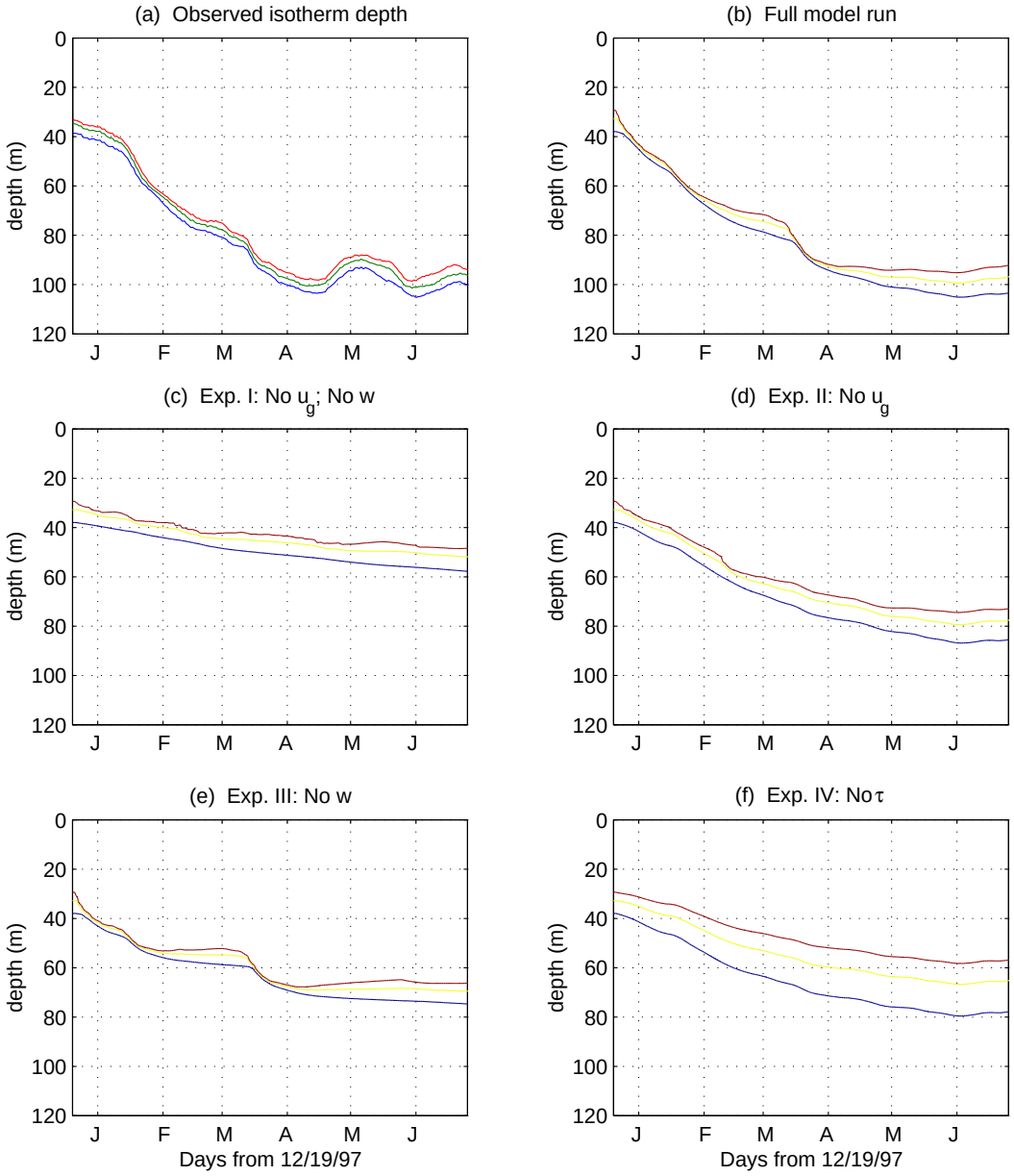

Figure 5-6: Comparison of modelled and observed thermocline depth. Each panel shows the depth of the 19, 22, and 24 degree isotherms which are meant to be representative of the upper thermocline.

velocity. Again, there is less mixing than in the full model run. Here, most of the change in thermocline depth is due to vertical advection, but some of the change is due to vertical mixing. As in the first model experiment, the mixed layer velocity becomes unrealistically large due to reduced dissipation and downward mixing of momentum caused by less frequent and less intense shear instabilities.

In the third model experiment, we included a representation of the low frequency velocity, but we did not include an estimate of vertical velocity. There was significantly more mixing in this experiment than in experiment I (no u_g; no w), and the mixing occurred at times corresponding to ones when the observed thermocline depth changed (see figure 5-6). The mixing is larger and more episodic than in experiment I, but the only difference between these two model experiments is the inclusion of the low frequency velocity. The low frequency velocity modulates the wind driven mixing by modulating the vertical shear. The precise physical mechanism by which the low frequency flow affects mixing will be discussed in the next section. In this model experiment, the mixed layer velocities were reasonable, but slightly larger than observed. This could be attributed to insufficient mixing in the model, but it is more likely due to the relatively shallow depth of the thermocline and mixed layer. The relative roles of mixing and vertical advection in determining the thermocline depth and near surface velocity will be discussed more quantitatively in section 5.5.

In the fourth model experiment, the model was configured for a full run except the wind stress forcing was set to zero. With no momentum flux from the wind, the model velocity is entirely due to the imposed low frequency velocity. Consequently, the mixed layer velocity was much smaller than in the other experiments, and there was no mixing caused by shear instability. Instead, changes in the model thermocline depth were due primarily to vertical advection. This experiment also serves as a verification that the imposed low frequency currents are not solely responsible for the mixing.

Figure 5-7 summarizes the evolution of thermocline depth in the observations and model experiments, as reflected by the motion of the 19°C isotherm. In addition to the experiments already discussed, the Ekman pumping displacement is also shown;

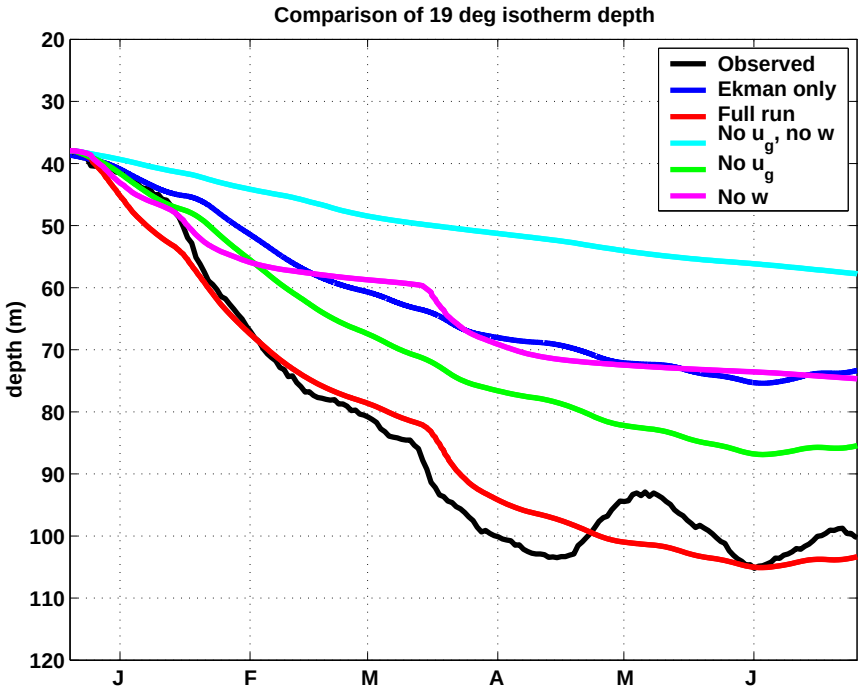

..

Figure 5-7: Comparison of modelled and observed 19 degree isotherm depth. Note that the 'Ekman only' case is not from a model run, but rather it is the displacement of the thermocline that we would expect if the only influence on thermocline depth were vertical advection by Ekman pumping. The 'no u_g' case (experiment II) includes Ekman pumping and surface buoyancy and momentum fluxes.

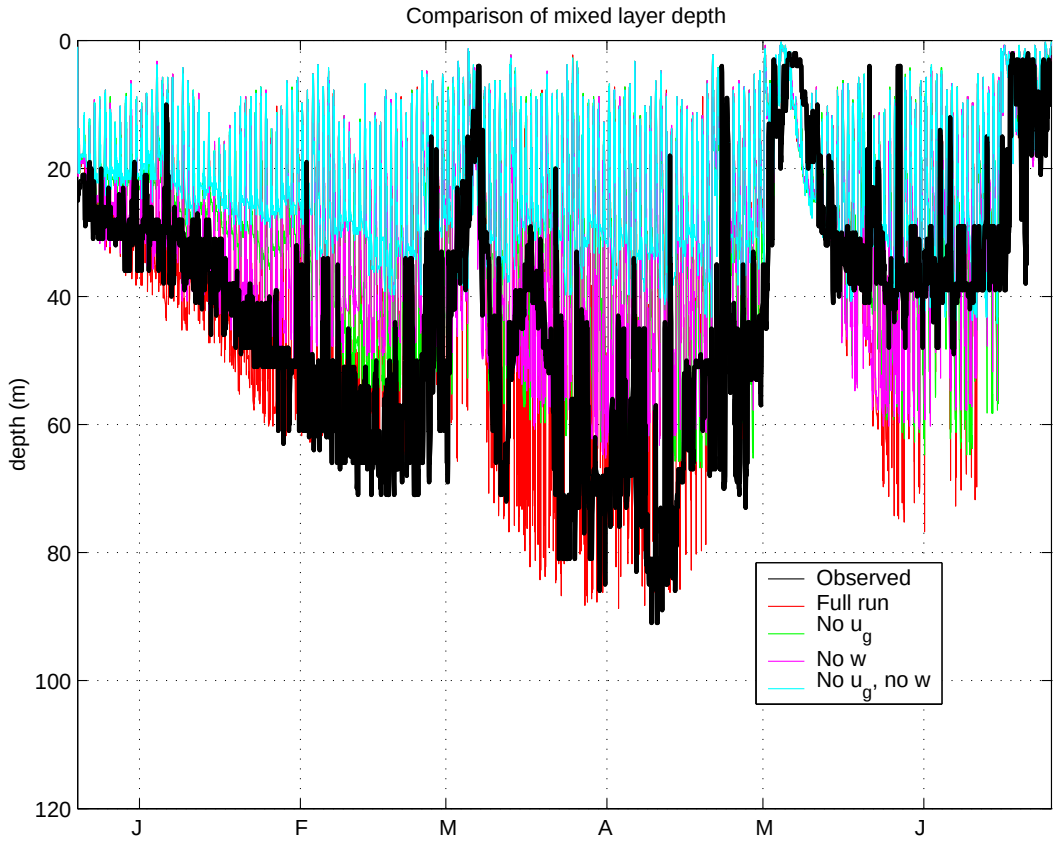

Figure 5-8: Observed and modelled mixed layer depths. Note that different a criteria were used in computation of observed and modelled mixed layer depths; the observed mixed layer depth is computed using a relatively coarse $\Delta\sigma$ criterion of 0.05 kg/m^3 mandated by sensor noise.

this was not produced using the numerical model, but, rather it is the displacement of the thermocline that we would expect if advection by Ekman pumping were the only mechanism affecting the thermocline depth. Here, we can clearly see that the full model run most accurately represents the observed motion of the thermocline. Particularly, the full model run captures the character of the rapid deepening of the thermocline that occurred in January and March.

Among the model experiments, the full run also did a good job of representing mixed layer depth. A comparison of the observed mixed layer depth and that in the various model experiments is shown in figure 5-8. Note that the criterion for determination of mixed layer depth in the observations is much coarser than that

for the model. The mixed layer depth from the model represents the depth of the unstratified, actively mixing layer, while the mixed layer depth estimated from the observations represents something closer to the daily maximum depth of the true mixed layer[4]. In figure 5-8, we can see that inclusion of Ekman pumping and the near-geostrophic flow produces a fairly realistic simulation of mixed layer depth during the first four months of 1998. It is interesting that the mixed layer appears to shoal and deepen near the same time in all of the model experiments and in the observations. This implies that the shoaling and deepening of the mixed layer are ultimately caused by the local surface forcing (because one of the experiments includes only the local surface forcing and it too exhibited this effect).

5.5 Discussion

In the full model configuration, which incorporates estimates of the vertical velocity and the low frequency horizontal velocity, the details of the evolution of the hydrographic structure are well reproduced. The physical processes represented by the model are changes in temperature, salinity, and velocity caused by surface fluxes, turbulent fluxes, and vertical advection. The model experiments reveal an interesting sensitivity of the upper ocean thermal structure to the small background shear associated with the large scale pressure gradient. In this section, we will diagnose the role of vertical mixing and examine the physical role of the background shear in bringing about the large and rapid change in thermocline depth.

Mixing in the model experiments

One way of quantifying the cross thermocline mixing in the model experiments is to diagnose the diapycnal velocity. We can decompose w into a vertical velocity associated with isopycnal motions ($\frac{dz}{dt}$) and one associated with cross-isopycnal motions

[4]This undesirably large $\Delta\sigma$ criterion is mandated by noise in the conductivity measurement which increases the noise in the potential density estimate.

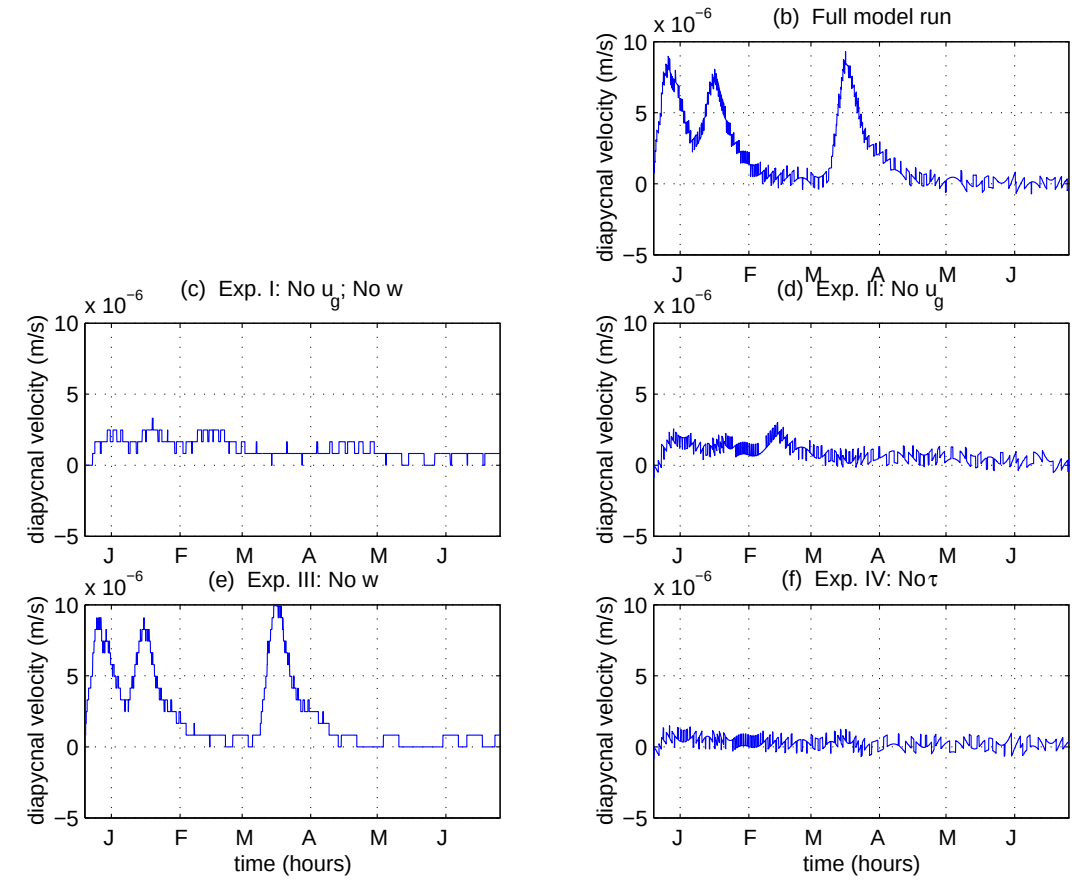

Figure 5-9: Comparison of modelled diapycnal vertical velocities (w^*) across the 20° isotherm. w^* has been smoothed using a 7 day running average.

(w^*) (e.g. Pedlosky, 1987):

$$w_{z=-h} = \frac{dz}{dt} + w^*. \tag{5.8}$$

Calculation of $\frac{dz}{dt}$ is straightforward, and there is no contribution to this term by horizontal advection in the model. The value of w is imposed on the model. Thus, the value of w^* can be known unambiguously. Alternative mixing metrics, such as diffusivity or mixing efficiency, require additional assumptions about the nature of the turbulent motions responsible for the mixing (e.g. Schudlich and Price, 1991). The diapycnal velocity is really a measure of diabatic processes so it can also be affected by penetrating solar radiation. However, the vertical divergence of penetrating solar radiation (i.e. the q_z term in equation 5.3) is less than 10% of its surface value at a depth of 3 m and less than 1% at 20 m; so, at the depth of the thermocline, the diapycnal velocity should be due almost entirely to turbulent mixing (and background diffusion). Figure 5-9 shows the diapycnal flow across an isopycnal corresponding to the 20°C isotherm for selected model experiments.

The diagnosis of w^* allows us to reinforce some of the statements made in section 5.4 about the amount of mixing in the model experiments. Clearly, there is more cross-thermocline mixing in the model experiments that include a representation of the low frequency currents. There is about the same amount of cross-thermocline mixing in the two experiments that did not include the low frequency velocity (i.e. experiments I and II), and the difference in the thermocline depth in these two experiments can be attributed to the different vertical velocities. Similarly, the two experiments that did include the low frequency velocity (i.e. the full run and experiment III) also had similar cross-thermocline velocities. In fact, there was more mixing in experiment III (no w) than in the full model run because the lack of downward Ekman pumping in experiment III left the thermocline at a relatively shallow depth, producing a shallower mixed layer and more intense inertial oscillations. To summarize, experiments which did not include the low frequency velocity exhibited steady, but small, diapycnal velocities. The experiment that included the low frequency velocity but no near inertial motions (i.e. no wind forcing) had very little diapycnal

velocity in the thermocline (almost certainly due to 'background diffusion'). Experiments that included near inertial motions and the low frequency velocity showed large bursts of diapycnal velocity that dramatically affected the thermocline depth in a manner closely resembling the observations.

In the model, diapycnal velocity is caused by turbulent fluxes of temperature and salinity. Since turbulent fluxes below the model mixed layer are the result of shear instability, we expect turbulent scalar fluxes to be accompanied by turbulent momentum fluxes in stratified regions of the water column. Put another way, a finite vertical shear is required in order to cause a critical Richardson number and a consequent turbulent scalar flux; below the mixed layer, turbulent momentum and scalar fluxes are linked in the model by the Richardson number mixing criterion. So, we expect diapycnal velocity across the pycnocline to be accompanied by a turbulent momentum flux. This is clearly the case in the model; periods of large w^* are also periods when momentum is present below the thermocline. It is noteworthy that the observed velocity also increases below the thermocline at these times (figure 5-5, e.g. near hours 900 and 2100). This corroborates the notion that vertical shear instability is the basic mechanism for thermocline deepening at these times.

An additional series of experiments

Although inclusion of the geostrophic flow has profound effects on the evolution of thermocline and mixed layer depth, we have noted that the timing of the mixing events seems to be governed by the surface forcing. All of the experiments so far that have included $\vec{u}_g$ have included both zonal and meridional components. However, the sensitivity of the upper ocean to the background flow naturally prompts the question of which component of the geostrophic flow is more important to the upper ocean evolution. To address this question, we conducted two additional experiments in which only one component of the geostrophic flow was included. To our surprise, the inclusion of the low-frequency zonal flow had almost no effect on the upper-ocean thermal evolution in the model. To understand this result and the fact that the timing of the mixing events seems connected to the surface forcing, we conducted a

experiment	U_g	V_g	Heat flux	Fresh water	$\vec{\tau}$	w^*_{max} ($10^{-}6$ m/s)
I (control)	0	fixed+	1	1	1	10@ t=300
II	fixed+	0	1	1	1	3@ t=100
III	0	fixed+	0	1	1	7@ t=300
IV	0	fixed+	1	0	1	9@ t=300
V	0	fixed+	1	1	0	3@ t=100
VI	0	fixed+	0	0	1	6@ t=300
VII	0	fixed+	1	1	offset by t-150	8@ t=160
VIII	0	fixed+	1	1	90° ccw rotation	3@ t=100
IX	0	fixed+	1	1	$\tau^x \rightarrow -\tau^x$	3@ t=100
X	0	fixed+	1	1	$\tau^y \rightarrow -\tau^y$	7@ t=300
XI	fixed-	0	1	1	1	6.5@ t=300

Table 5.2: Summary of a second round of experiments intended to gauge the importance of the various forcing terms and the dependence of the orientation of the geostrophic background flow to the wind stress. In the U_g and V_g columns, 'fixed+(-)' means that the geostrophic component was imposed as discussed in section 5.3, but the near-surface value was fixed at +(-)0.2 m/s. Table values of 1 indicate that the observed forcing was used; values of 0 indicate that the term was zero for the experiment. For all experiments, the time period was the month of February, 1998. Units of time are in hours; for example, "t=300" means 300 hours into the model run.

second series of model experiments.

The second set of experiments was designed to determine which type of surface forcing controls the timing of the mixing events and why the thermal evolution seems more sensitive to the meridional geostrophic signal than the zonal one. We conducted a total of eleven additional experiments using the observed forcing from the month of February 1998. The surface heat flux and wind velocity during the time period are shown in figure 5-10. The winds were fairly steady toward the southwest, and the mean net heat flux was nearly zero. Each experiment was initialized with the observed (running averaged) density structure and a wind-driven velocity equal to zero. Because there were so many experiments, we will not discuss them individually. With respect to the geostrophic velocity, our approach was to fix the imposed signal and to only impose one component in a given experiment. We did this in order to allow a clear interpretation of the role of the geostrophic flow and its relation to the surface forcing. The experiments are summarized in table 5.2.

To identify the surface forcing that is most important to the timing of the mix-

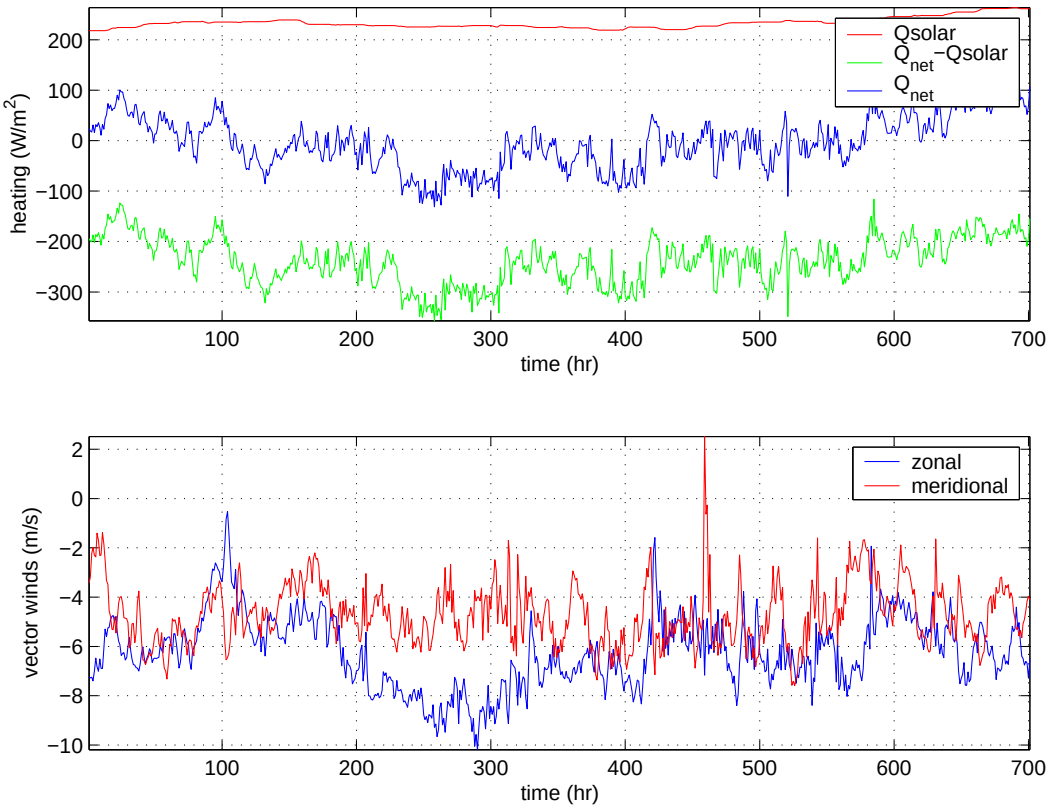

..

Figure 5-10: Surface heat flux and wind velocity during the second series of model experiments (February 1998). The solar heat flux was smoothed with a 10-day running average for display. The non-solar heat flux and the wind were not smoothed, but the smoothed solar heat flux was used in calculating the net heat flux for this figure. Smoothing was applied because the diurnal cycle in solar heat flux is up to 5 times larger than the mean, making trends difficult to detect by inspection.

ing events, we conducted a number of experiments that had a temporally constant geostrophic velocity profile, but excluded heat, freshwater, and momentum forcing individually and in various combinations (experiments I-VI of table 5.2). In these experiments (I-VI), all of the experiments except two, the one without wind stress (V) and the one with a (positive) zonal geostrophic velocity (II), exhibited peak cross-pycnocline velocities at the same time. Moreover, the maximum value of w^* was comparable, between 6 and 10×10^{-6} m/s (again with the exception of experiments II and V). The most important result of experiments I-VI is that the time of maximum mixing appears to depend on both the wind stress and the orientation of the geostrophic flow.

The fact that the timing and magnitude of the cross-pycnocline velocity seems to depend on both the wind stress and the orientation of the geostrophic velocity motivated our choice of experiments VII-XI. In these experiments, we varied aspects of the wind stress and the orientation of the geostrophic velocity. Experiment VII, which differs from the control run only in the timing of the wind stress, is consistent with the notion that, all else being equal, the wind stress controls the timing of the maximum mixing. While it does seem clear that the wind stress plays an important role in controlling the timing of the mixing, there are various properties of the stress that could be responsible. For example, the rate of rotation of the stress vector influences the generation of mixed layer inertial motions and this might be important in determining the time of maximum mixing. Also, the fact that experiments which differ only in the orientation of the geostrophic velocity exhibit different timing and magnitudes of cross-pycnocline mixing may be explained by the orientation of the mean stress with respect to the geostrophic velocity. For example, perhaps the shear of the Ekman flow, superimposed upon the geostrophic shear, can create a significant background shear which is large enough to preferentially cause mixing when the inertial velocity is aligned with the net background shear. Experiments VII-XI are intended to explore the reason why the timing of maximum mixing seems to depend on both the wind stress and the orientation of the geostrophic velocity.

While perhaps incomplete and inconclusive, the second set of model experiments

suggests that the sheared geostrophic velocity most effectively enhances vertical mixing when it is oriented to the right of the wind stress. Because the trade winds at the site are fairly steady, the second set of experiments is not properly constructed to distinguish the orientation of the geostrophic velocity with the mean stress from the orientation of the geostrophic velocity with the instantaneous stress. However, it is apparent from the experiments (especially XI) that, had the observed zonal geostrophic flow been westward (i.e. in the same direction as the zonal Ekman transport), the mixing would have been even more enhanced by the geostrophic flow. This expectation is confirmed by an additional model experiment (not shown) that is the same as the full model run except that the sign of the imposed geostrophic zonal velocity is reversed; in this experiment, the thermocline deepens more rapidly and reaches a greater depth than in the observations or in any of the model experiments. In other words, it appears that the reason that the zonal geostrophic flow had little influence on the cross-pycnocline flow is that the geostrophic flow was to the left of the meridional wind. Moreover, episodes of large mixing in the full model run occurred exclusively when the the meridional geostrophic velocity was to the right of the prevailing easterly winds (i.e. when $v_g > 0$).

The model that we have employed, where the wind driven velocity is superimposed upon the near-geostrophic velocity, implicitly assumes that the true momentum equation governing evolution of velocity at the site can be treated as approximately linear. That is, in formulating the model, we have assumed that the velocity signal can be meaningfully separated into wind and pressure driven signals. Within this linear framework, the role of the background shear is clear because the total shear is equal to the sum of the shears from the two velocity contributions.

If the size of an inertial oscillation remains constant for the duration of a cycle, then we would expect a maximum total shear when the inertial signal is oriented parallel to the relatively steady background flow. (In this context the 'background flow' should be thought of as the sum of geostrophic and Ekman flows). This leads us to expect that vertical mixing associated with the inertial shear may occur preferentially when the inertial signal is aligned with the background flow. If this is the case, then

we would also expect that, in the absence of further mixing, the background shear should be manifested in the other component of the flow after in a quarter inertial period. Figure 5-11 illustrates this scenario. For this discussion, assume that the wind stress is zero so that the we can eliminate the steady wind-driven flow from consideration. In the illustration, the velocity profile, made up of contributions from the steady and inertially rotating flows, is initially unstable. Rapid mixing (i.e. with respect to an inertial period) results, reducing the total shear. The part of the total velocity that is not in near-geostrophic balance with the large scale pressure gradient will rotate inertially into the other component. The pressure driven velocity remains in near-geostrophic balance with the large scale pressure gradient, and thus does not rotate. Because of the superposition of velocity contributions, the background baroclinic shear can only temporarily be mixed away. In the absence of further mixing, the background shear will be reflected in the inertial signal because the signal rotates about the background flow. The inertial oscillations, superimposed upon the background baroclinic flow, cause the background shear to be persistently re-manifested despite the repeated action of mixing due to vertical shear instability. In the absence of external forcing, there is still a potential for further mixing because of the background shear, whereas if there were no background shear, the velocity profile would remain stable for all time after relieving the initial shear instability[5].

The effects of the background geostrophic flow are most apparent in the observations when subsurface velocity maxima are present in one component, as in the schematic illustration (figure 5-11). Figure 5-12 illustrates the appearance of subsurface velocity maxima that result from mixing and the superposition of the wind driven flow upon the baroclinic flow in both the model and the observations. The time period shown spans March 12 to April 23 and includes an episode of rapid thermocline deepening due to mixing. Notice that in both model and observations, the

[5]The presence of surface buoyancy and momentum fluxes complicates this scenario. The mean surface buoyancy flux, when positive, will tend to counteract this process by increasing the bulk stability of the mixed layer and the stratification at the mixed layer base. (This is necessarily so because the mixed layer base must smoothly join the density (and other properties) of the mixed layer with the ocean interior). Surface momentum flux may either counteract or exacerbate the process by changing the momentum of the mixed layer and decreasing or increasing the shear at the mixed layer base.

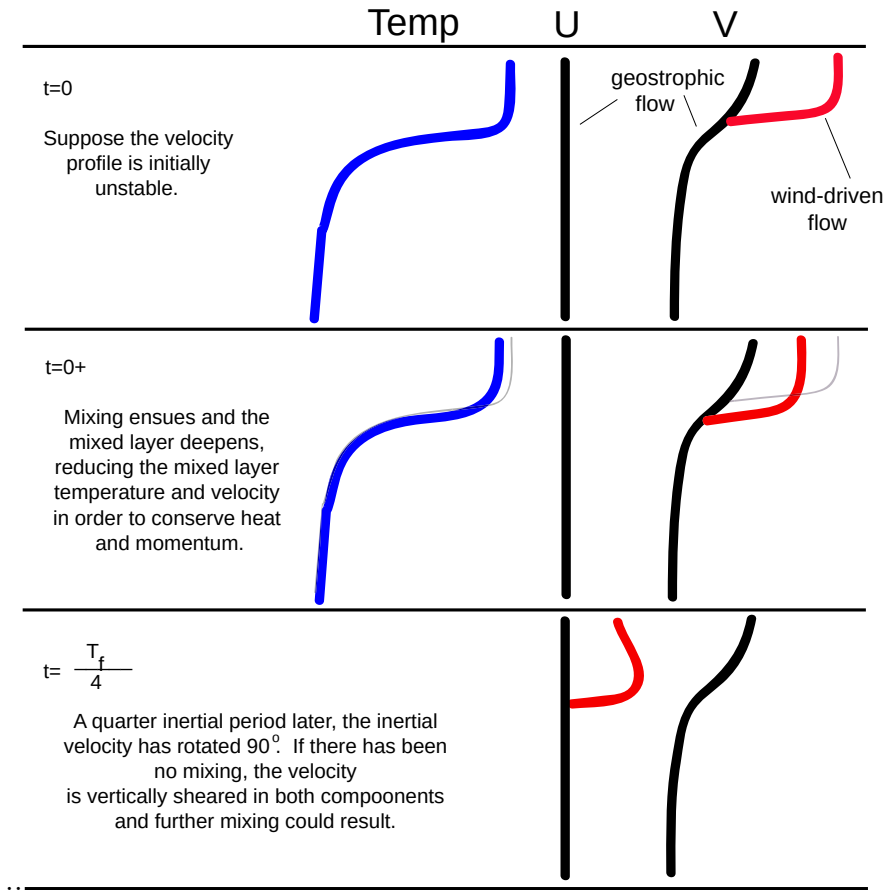

Figure 5-11: Schematic illustration of rotation of inertial oscillation about a background baroclinic flow. The mixed layer depth is marked on each vertical profile by a short horizontal line segment. At $t = 0$, the flow is unstable. A short time later, at $t = 0+$, the water column has adjusted to relieve the instability by mixing temperature and velocity in the vertical. However, a quarter inertial period later ($t = T_I/4$), the inertial component of the velocity has rotated toward a zonal orientation, and there is now vertical shear in both u and v. If the density gradient is weak enough, further mixing will ensue.

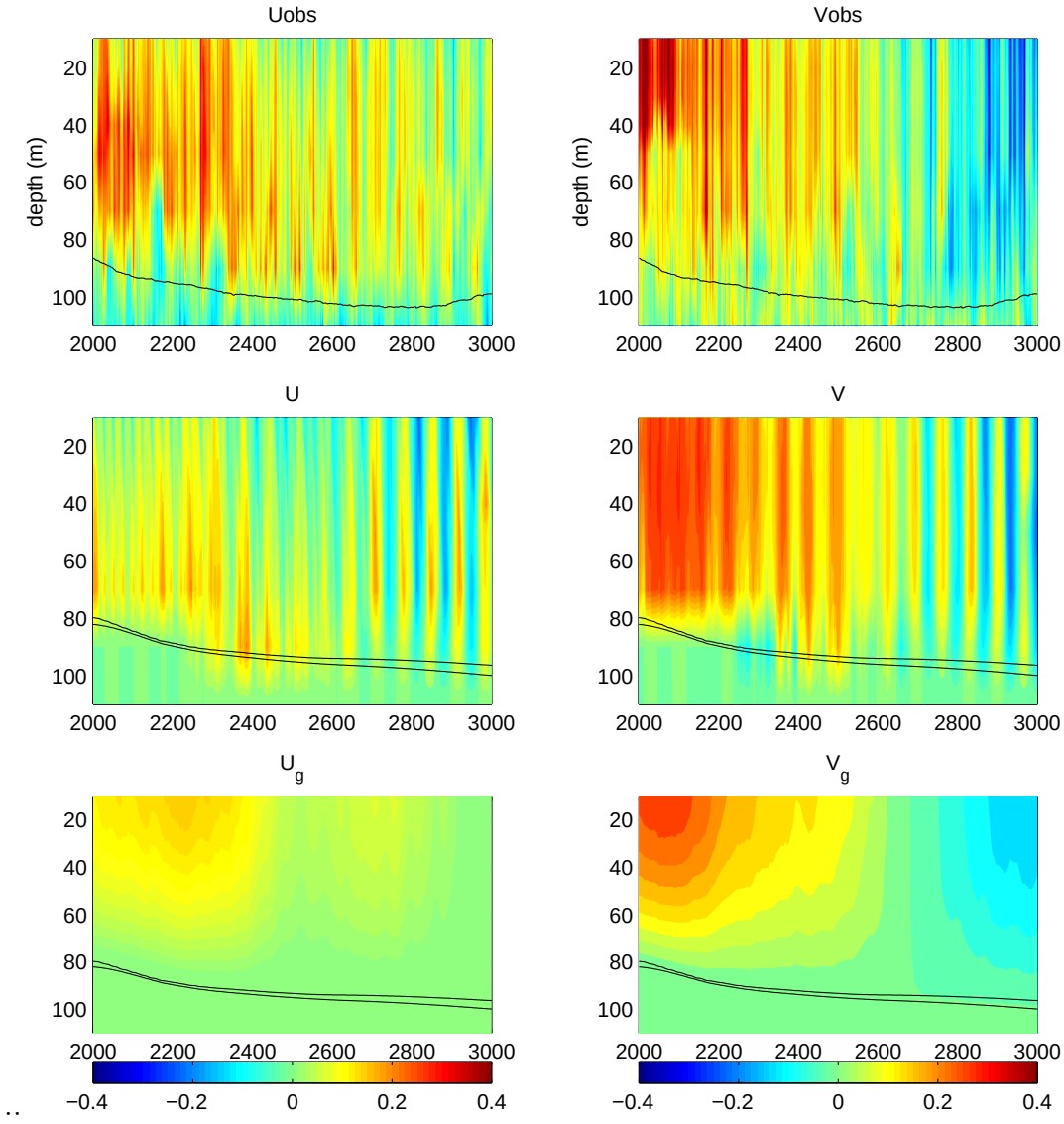

Figure 5-12: Example of generation of subsurface velocity maxima (m/s) in observations (top) and model (middle). The low-frequency velocity imposed on the model is shown in the lower two panels. The horizontal axis in each panel is time in hours; the time period shown spans March 12 to April 23. The 19°C isotherm is shown for the observations, and the 19° and 22°C isotherms are shown for the model. Notice that U (left panels) tends to have positive subsurface maxima in both the observations and model.

meridional component of velocity tends to increase toward the surface while the zonal component tends to have a subsurface maximum above the thermocline. During the period of rapid thermocline deepening (the first 250 hours shown, or March 12 to March 22), the subsurface velocity maxima appear to have a diurnal frequency. However, later in the interval as the mixing decreases, the subsurface velocity maxima occur at near-inertial periods.

Although the effects of turbulent momentum flux on the observed velocity are not easy to determine directly, we can diagnose the turbulent stress divergence in the model. This allows us to examine the role of vertical mixing and verify that the appearance of subsurface velocity maxima are the result of mixing and the rotation of the inertial velocity upon the sheared background flow. The turbulent stress is determined implicitly in the model by the stability criteria (equations 5.5 to 5.7), and we diagnosed the turbulent stress using the momentum equations (5.1 and 5.2). The vertical divergence of the turbulent stress is shown in figure 5-13 for the period of March 12 to April 24 (same time period as in the previous figure). Also shown are the model mixed layer depth (blue line) and 19° and 22°C isotherms (black lines). Note that the zonal component has larger peak values, located at the mixed layer base and associated with the diurnal cycle of mixed layer depth. The meridional component has a more prominent inertial cycle, and peak values occur in the upper thermocline during the period of rapid thermocline deepening (the first 250 hours shown, or March 12 to March 22). It is also noteworthy that the maximum daily mixed layer depth extends to the top of the thermocline and there was almost continuous active mixing just above the thermocline during the period of rapid thermocline deepening.

The most important aspect of figure 5-13, though, is that it helps to explain the occurrence of the subsurface velocity maxima. During the time of the most apparent subsurface zonal velocity maxima (hours 2200 to 2600, or March 20 to April 6), there are prominent inertial signals in the meridional turbulent stress divergence near the base of the mixed layer, just as we would expect from the scenario depicted in the upper panels of the schematic illustration (figure 5-11). In the phase of the inertial cycle where $v > 0$, there is mixing that increases the meridional momentum below

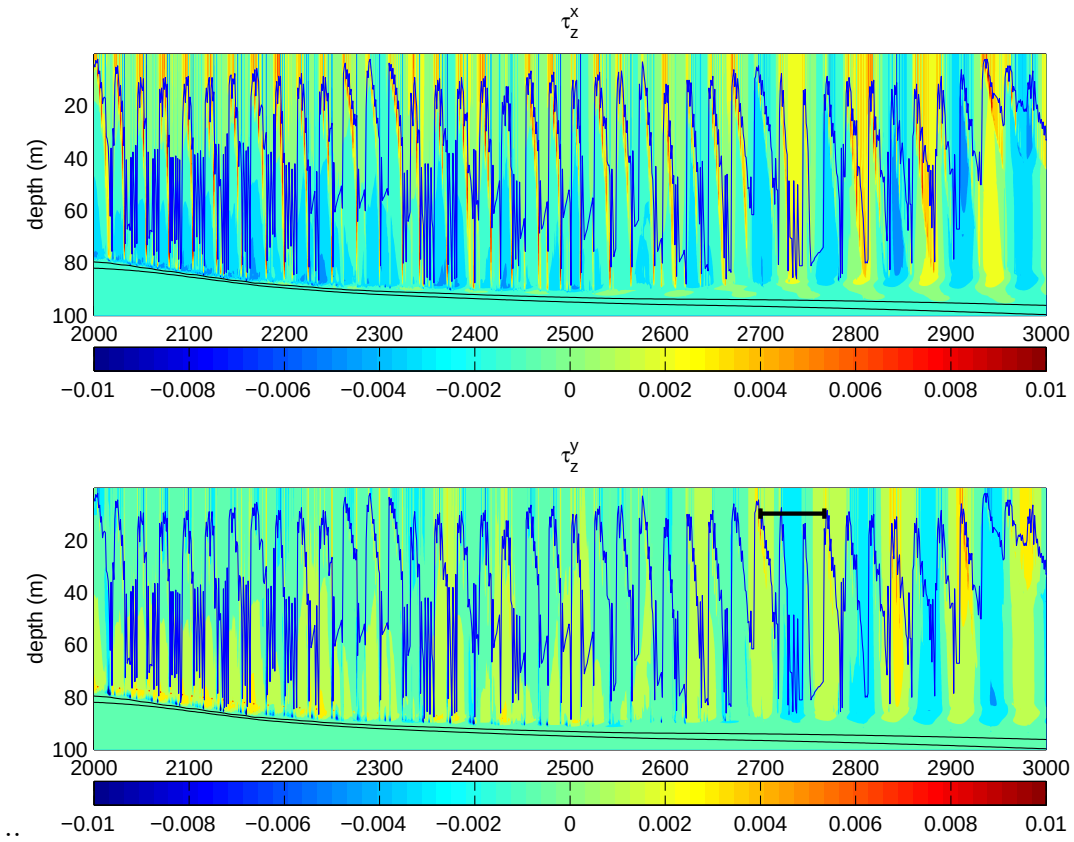

Figure 5-13: Vertical divergence of turbulent stress in the model during the time period shown in figure 5-12. Top and bottom panels are zonal and meridional components, respectively. The horizontal axis in each panel is time in hours; the time period shown spans March 12 to April 23. The 19° and 22°C isotherms are shown in black, and the model mixed layer depth is shown in blue. The mixed layer shoals during the day. The inertial period (67 hours) is indicated by a black bar near hour 2700 in the lower panel. Notice that the turbulent stress divergence is significantly larger at the mixed layer base in the zonal component and has pronounced diurnal cycle, while the meridional component of turbulent stress divergence has a more pronounced inertial cycle and attains maximum values in the upper thermocline during times of thermocline deepening.

the mixed layer (i.e. $\tau_z^y > 0$). This destroys the shear in the meridional velocity and creates a subsurface maximum in inertial momentum below the mixed layer base; this subsurface maximum becomes visible when it rotates into a zonal orientation and is no longer superimposed upon the background meridional velocity. If there is further mixing associated with the newly manifested vertical shear of zonal velocity, we would expect $\tau_z^x < 0$, and this is what we observe in the model. This may be part of the reason why the background shear has such a dramatic effect on vertical mixing; a shear instability in the component with the background flow may lead to a later shear instability in the other component of the flow[6]. If there were no sheared background flow, the first mixing event would be enough to permanently relieve the initial shear instability.

In summary, we have found that the presence of a weakly sheared, low-frequency background flow has profound consequences for vertical mixing and thermocline depth at the mooring site. We have explained these effects as being due to the fact that the wind-driven inertial velocity, which is responsible for most of the shear, is superimposed upon, and rotating about, the low-frequency baroclinic flow. During times of mixing, this may enhance the mixing by repeatedly re-manifesting the background shear only a short time after mixing has acted to reduce the total shear. The meridional component of the geostrophic flow played a more important role in the evolution of thermocline and mixed layer depth during the rapid deepening of the thermocline in early 1998. Model experiments suggest that the mixing is larger when the geostrophic velocity is oriented to the right of the wind, but further work will be required to understand the physical details of this relationship.

[6]I have devised what I believe to be the simplest model that can exhibit this effect (i.e. a two box model). The model shows that perpetual mixing can result when an inertially rotating signal is superimposed on a weak background shear. Time permitting, I intend to incorporate this into an appendix.

Chapter 6

Conclusion

In this chapter, we present a synthesis of the work contained in this thesis and discuss the evidence presented. We briefly discuss our new understanding of the rapid deepening of the thermocline associated with the 'meridional tilting mode' of ENSO. We bring the thesis to a close with some concluding remarks. We gratefully acknowledge the reader's patience in having read this far, and we will now synthesize the results of this thesis in the next section.

6.1 Synthesis

In this thesis we have endeavored to use the PACS data set, along with other data sources, to understand the physical mechanisms responsible for the evolution of upper ocean thermal structure at 10°N, 125°W during 1997-1998. We have concluded that surface heat flux and Ekman pumping were important to the evolution of net upper ocean heat content, while horizontal advection appears to have been of secondary importance. A dramatic deepening of the thermocline occurred in early 1998; this zonally coherent deepening of the thermocline near 10°N has been identified by other invesitgators as being associated with the transition from El Niño to La Niña, and Ekman pumping has been identified as an important contributor to this phenomenon (Alory and Delcroix, 2002). The temporal variation in Ekman pumping at the site is associated with the southward migration of the ITCZ from the site in late 1997.

We have argued that, at 10°N, 125°W, the rapid deepening of the thermocline was also due in part to changes in the local air-sea fluxes which were also associated with the southward migration of the ITCZ. As the ITCZ began to move south from the mooring site, increasing winds contributed to a deepening of the mixed layer and entrainment of cooler and saltier water from below the mixed layer. This entrainment served to reduce the static stability of the mixed layer, which otherwise would have been highly stable because of the large surface heat and freshwater fluxes during ITCZ conditions. Around the same time, the mean buoyancy flux began to decrease because of less frequent rains and higher evaporation (associated with higher winds); the mean buoyancy flux was intermittently negative during non-ITCZ conditions. These effects combined to reduce the static stability of the mixed layer.

The reduced static stability of the mixed layer reduced the vertical shear that could be supported at the mixed layer base, making the mixed layer quite sensitive to the presence of background shear associated with the large scale flow. A train of intermediate wavelength baroclinic Rossby waves propagated past the mooring site; these waves had an inverse wavelength of about the deformation radius and a substantial meridional velocity signal. These waves contributed to substantial diapycnal mixing by providing a small but persistent background shear at a time when only a very small vertical shear could be supported at the base of the mixed layer.

6.2 Overview of Supporting Evidence

In arriving at the conclusion presented in the previous section, we have relied on a series of intermediate results based on data analysis and model experiments. Below, we summarize the relevant evidence for the thesis that we have presented:

1. Buoyancy and momentum fluxes at the site contrasted dramatically between ITCZ and non-ITCZ conditions. Mean buoyancy fluxes were lower (or even negative) and momentum fluxes were higher during non-ITCZ conditions.

2. We observed a long-term decrease of surface density (due to changes in surface

temperature and salinity) from late October 1997 to early March 1998.

3. The thermocline deepened rapidly in early 1998. This was part of a larger, zonally coherent pattern of variability and was a precursor to the transition of the tropical Pacific from El Niño to La Niña states (Meinen and McPhaden, 2000; Alory and Delcroix, 2002). The rapid deepening of the thermocline coincided with a rapid deepening of the mixed layer, and the mixed layer base was closer than usual to the upper thermocline during this period.

4. The Ekman pumping displacement estimated from the ERS scatterometer wind stress agrees well with the observed displacement of the thermocline, but the Ekman pumping cannot account for all of the observed displacement of the thermocline, especially during the period of most rapid deepening during January 1998.

5. We identified baroclinic signals in the velocity record. That is, through an EOF analysis, we identified a statistical vertical mode that was uncorrelated with the local wind stress. This mode captured nearly all of the baroclinic M_2 tidal energy and the 60 day meridional velocity signal. The notion that the 60 day meridional velocity signal is a baroclinic, nearly geostrophic signal is corroborated by the fact that previous investigators have identified 60 day variability in dynamic height (Miller et al., 1985) and sea surface height (Perigaud, 1990; Giese et al.,1994).

6. Based on spectral analysis of TOPEX/Poseidon SSH data from 1997 and 1998, we identified the dominant wave numbers and frequencies in zonal sea surface slope along 10°. These wave numbers and frequencies were found to agree well with the dispersion relation for first mode baroclinic Rossby waves, and the dominant frequency was very close to the dominant frequency of the meridional velocity observed at the mooring.

7. We found no evidence that the rapid descent of the thermocline at the mooring site was directly associated with free, long Rossby waves propagating to the

mooring site from the east.

8. A heat budget computed from the observations suggests that an efficient account of the evolution of the upper ocean heat content at the site may be given by surface heat flux and vertical advection by Ekman pumping. Evaluation of the budget is made possible by vertical integration, which removes the vertical turbulent heat flux from the budget. However, turbulent heat flux may still move heat around within the sample volume, which in this case was the upper 150 m of the water column.

9. Most of the vertical shear at the site was associated with near-inertial motions. Statistically significant inertial shear power was identified between the mixed layer base and the thermocline. A much smaller vertical shear signal was associated with the low frequency, baroclinic flow; this signal had a magnitude roughly eight times smaller than the total shear signal.

10. Estimates of the gradient Richardson number were presented as a function of time and depth. The base of the mixed layer was almost always critical, or nearly critical, to vertical shear instability (i.e. Kelvin-Helmholtz type instability). Near critical gradient Richardson numbers were also registered in the main thermocline, most notably between September 1997 and March 1998.

11. A physical and numerical model of the upper ocean as a high frequency, wind-driven flow superimposed upon a vertically sheared, low frequency background flow with shear-driven vertical mixing and vertical advection by Ekman pumping did an adequate job of reproducing the observed upper ocean thermal evolution. Subsequent numerical experiments with this model showed that the background shear, while relatively weak, exerted a profound influence on the thermal evolution of the upper ocean. This was also partly due to the reduced buoyancy flux associated with non-ITCZ conditions and the consequent marginal static stability of the mixed layer base. A second series of experiments indicates that the effect of the baroclinic flow on the upper ocean thermal evo-

lution is largest when the geostrophic flow is oriented to the right of the wind. Consequently, the eastward zonal flow (which was to the left of the meridional wind) was less important than the meridional geostrophic flow (which changed signs about once per month) in causing the rapid deepening of the mixed layer and thermocline in early 1998.

Taken together, these intermediate results support the notion that the rapid deepening of the thermocline at the site in early 1998 was due to a combination of vertical advection by Ekman pumping, surface buoyancy and momentum fluxes, and vertical turbulent heat flux related to the superposition of inertial oscillations upon the large scale baroclinic flow.

6.3 The Meridional Tilting mode of ENSO

In the introductory chapter, we discussed the so-called 'meridional tilting mode' associated with ENSO. In this thesis, we have reached a conclusion about this phenomenon consistent with the work of other investigators; namely, the northern end of the meridional tilting mode is largely due to anomalous Ekman pumping patterns associated with large scale wind anomalies. However, the detailed view of the upper ocean evolution and coincident air-sea fluxes made possible by the high quality PACS data set has allowed us to further identify diapycnal mixing as an important contributor to the rapid descent of the thermocline during early 1998, just before the tropical Pacific underwent a transition from El Niño to La Niña states. In the numerical simulation presented here, vertical mixing was responsible for 29 m of the 56 m descent of the thermocline during the first three months of 1998. This diapycnal mixing was associated with enhancement of the vertical shear by the large scale baroclinic flow and the local air-sea fluxes of heat, freshwater, and momentum at the mooring site.

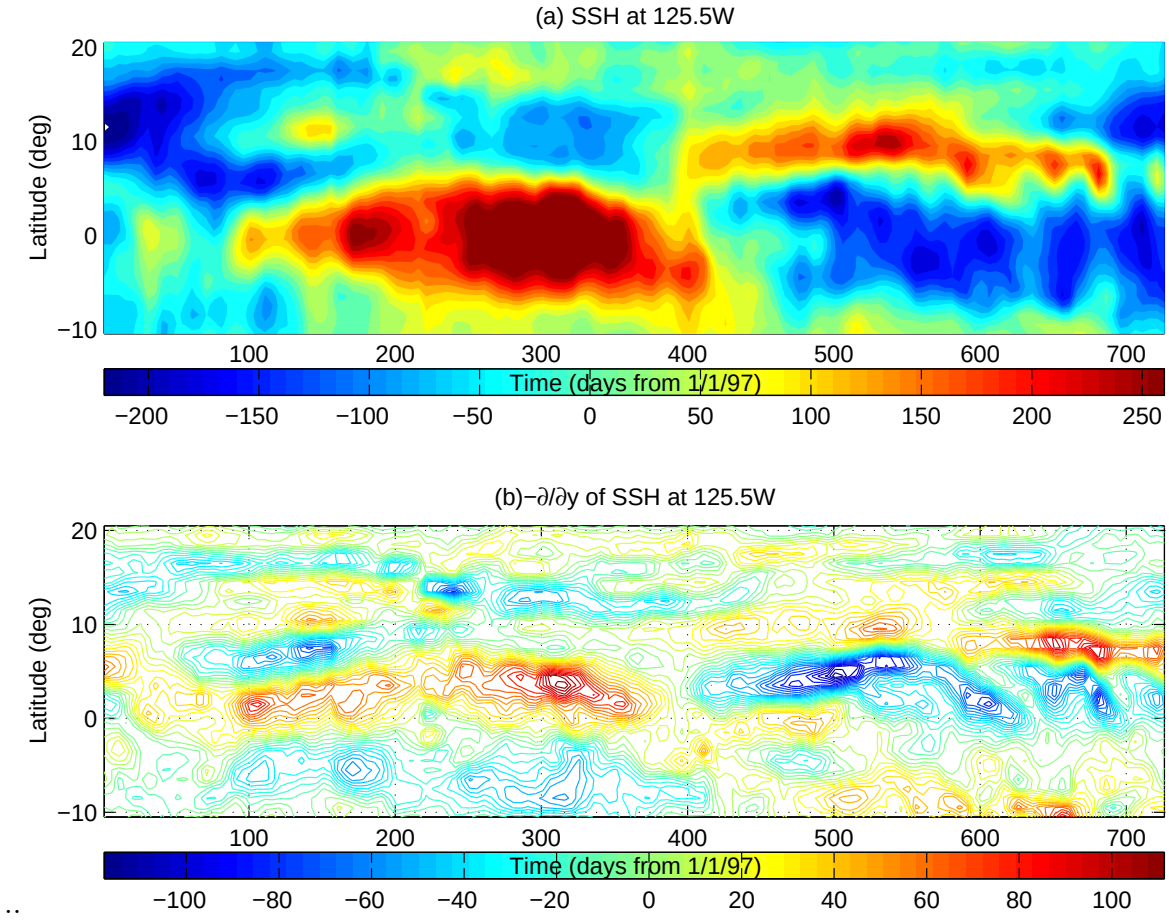

Figure 6-1: (a) TOPEX/Posoidon sea surface height anomaly (mm) along 125.5W during 1997 and 1998. (b) North-south derivative of sea surface height anomaly (mm/deg).

6.4 Concluding Remarks

From a local perspective, we have gained some understanding of the factors governing thermocline depth and upper ocean heat content at the PACS mooring. Measurement of coincident air-sea fluxes and upper ocean temperature, salinity, and velocity were pivotal in arriving at this understanding. We identified an interesting and simple mechanism by which the large scale pressure driven flow played a role in the rapid deepening of the thermocline in early 1998. We have argued that the rapid deepening of the thermocline was also associated with the north-south migration of the ITCZ through its effect on Ekman pumping and surface fluxes of buoyancy and momentum.

The Ekman transport, which converged near 10°N during early 1998, was such as

to remove warm surface water from the eastern equatorial Pacific, before the equatorial Pacific began to transition from El Niño to La Niña states. The role that the large scale zonal flow may have played in draining warm surface water from the eastern equatorial Pacific is less obvious, though. We expect the zonally coherent deepening of the thermocline to affect the meridional pressure gradient and the corresponding large scale zonal flow. Consistent with this expectation is the observed change of the low frequency zonal flow as the thermocline deepened in early 1998. The low frequency zonal flow at the mooring increased from near zero to about $+20\ cm/s$ as the thermocline deepened. In the introductory chapter, we mentioned that a slackening or reversal of the NECC is a characteristic feature of the transition from El Niño to La Niña states. During the 1997-98 event, the NECC actually changed direction. To facilitate this closing discussion, we have repeated figure 1-7 here (figure 6-1). In inspection of this figure, the reader may have noticed that the NEC also appears to have reversed direction in association with the meridional seesaw action of the SSH (or thermocline) in early 1998 (look along 10°N near day 400). The reversals of the NEC and NECC occur nearly simultaneously, a few months before the equatorial Pacific transitions from El Niño to La Niña states. This raises the question of whether the reversal of these off-equatorial geostrophic currents played a role in removing warm water from the eastern equatorial Pacific. The westward flow of the "counter-current" just before and during La Niña was in the right direction to remove warm water from the eastern Pacific. The reversed NEC, flowing eastward near 10°N, might be thought to be counteracting the flow of the reversed NECC. On the other hand, we have seen that the rapid deepening of the thermocline was partly due to entrainment, which helped to restore climatological SST conditions, even before the meridional tilting began in earnest. So, this may have diminished the tendency of the reversed NEC to increase the amount of warm water in the eastern Pacific.

Given our new understanding of the processes responsible for the deepening phase of the northern end of the meridional tilting mode (i.e. the rapid descent of the thermocline at 10°), we may be able to make further progress in understanding the causal relationship (if one exists) between the meridional tilting of the thermocline

and the transition from El Niño to La Niña states.

Appendix A

Supplementary Figures

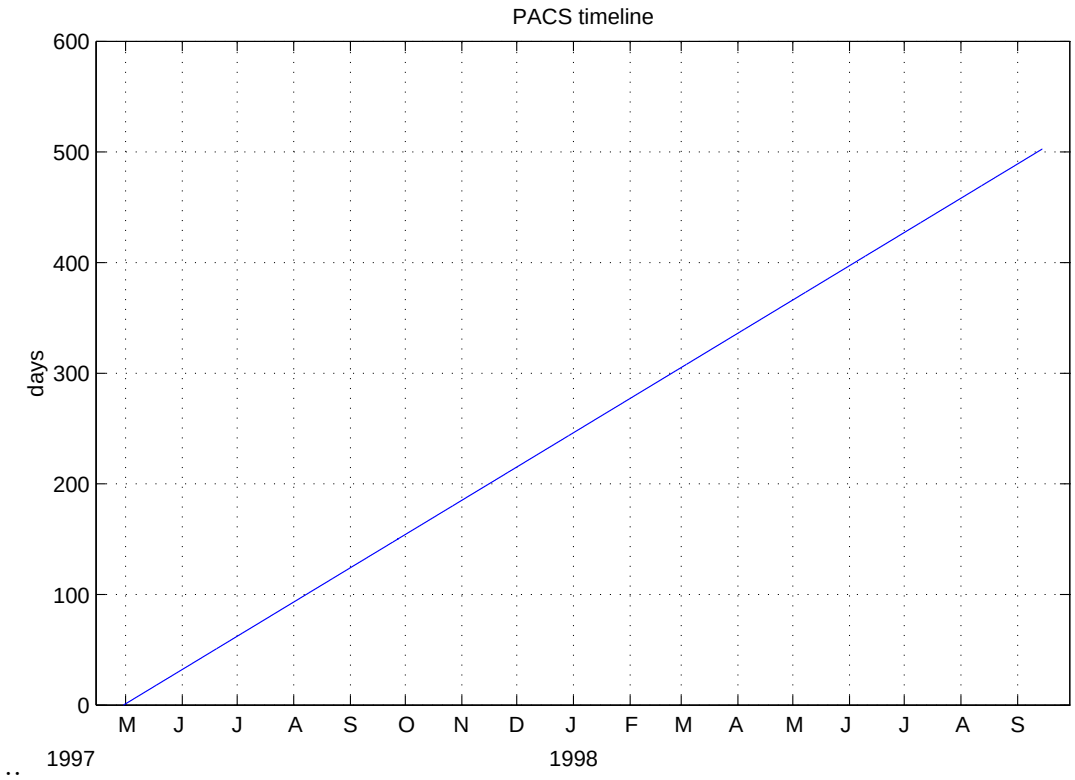

Figure A-1: Time conversion chart for PACS.

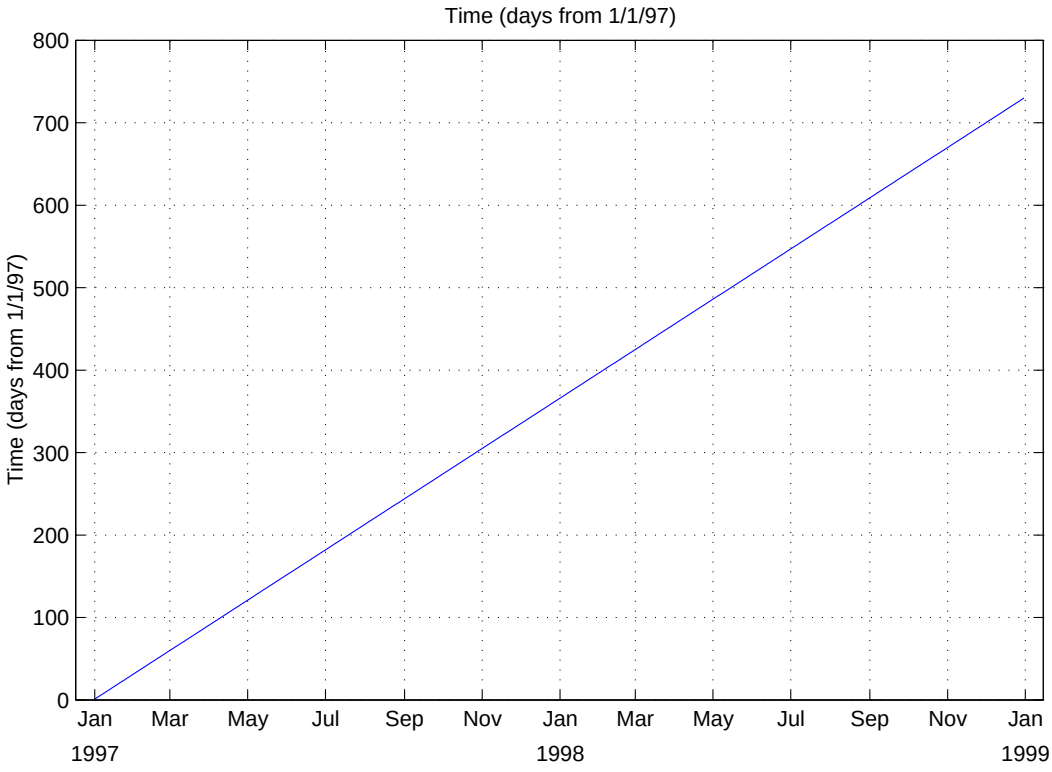

..

Figure A-2: Time conversion chart for plots with a time axis labeled 'Time (days from 1/1/97)'.

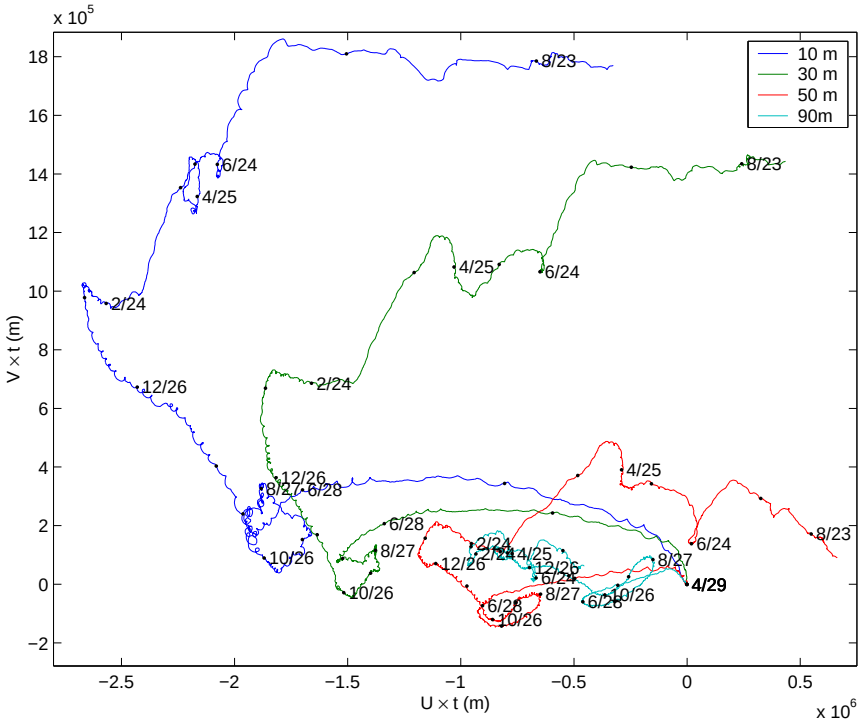

Figure A-3: Progressive vector diagrams of velocity at various depths. KEinertialN.m then pvd.m

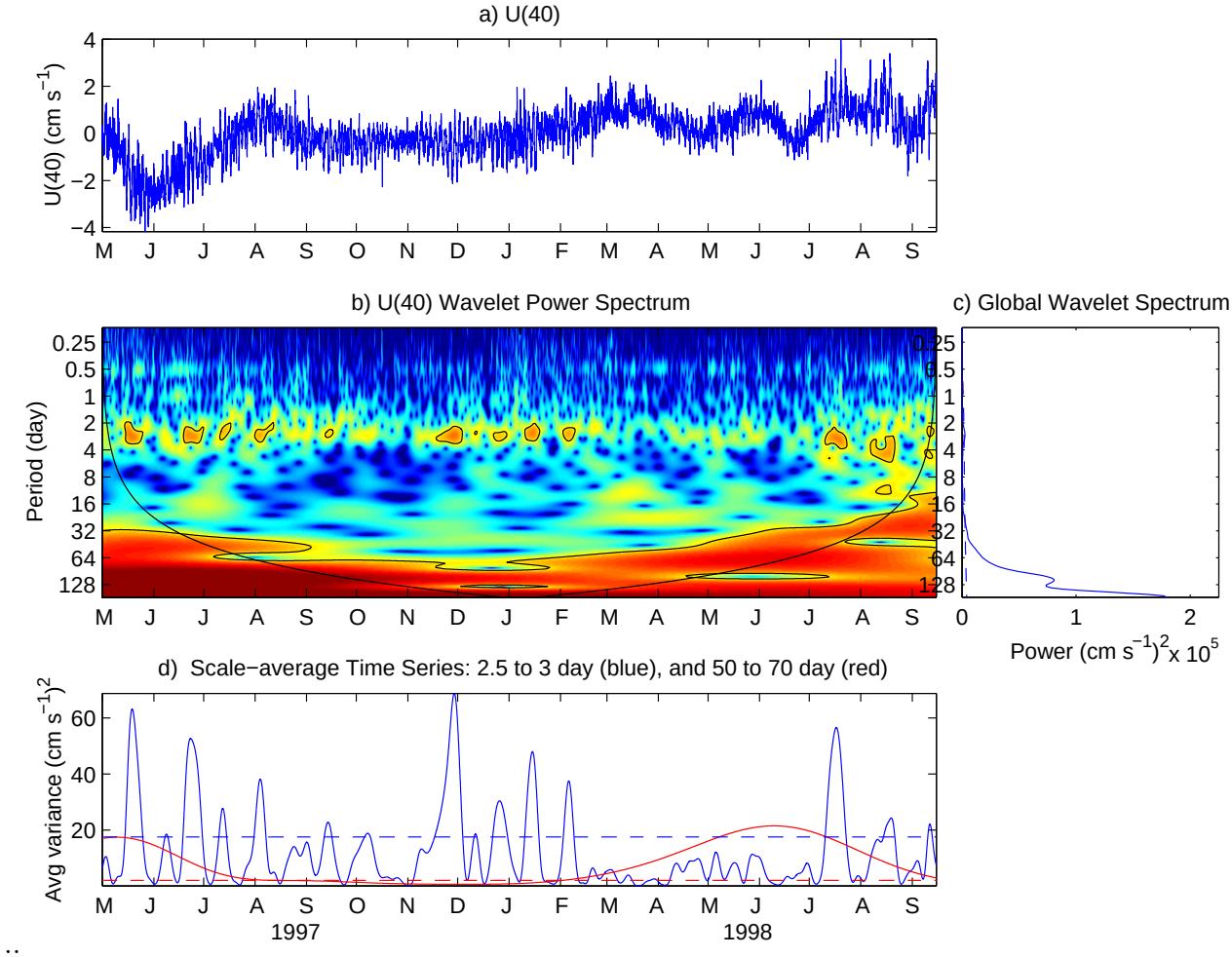

Figure A-4: Wavelet analysis of spectral power in the zonal velocity at 40 m. (a) The velocity time series, divided by its standard deviation and with the mean removed; (b) the WPS, with period in days on the vertical axis and time on the horizontal axis; (c) the global wavelet spectrum, a time average of the WPS and analog to the more traditional Fourier power spectrum; (d) the average power in two different frequency bands, one having a period of 2.5 to 3 days (near-inertial) and the other 50 to 70 days (intraseasonal). In (b), statistically significant power is surrounded by a black line. In (c) and (d), dashed lines indicate the significance threshold.

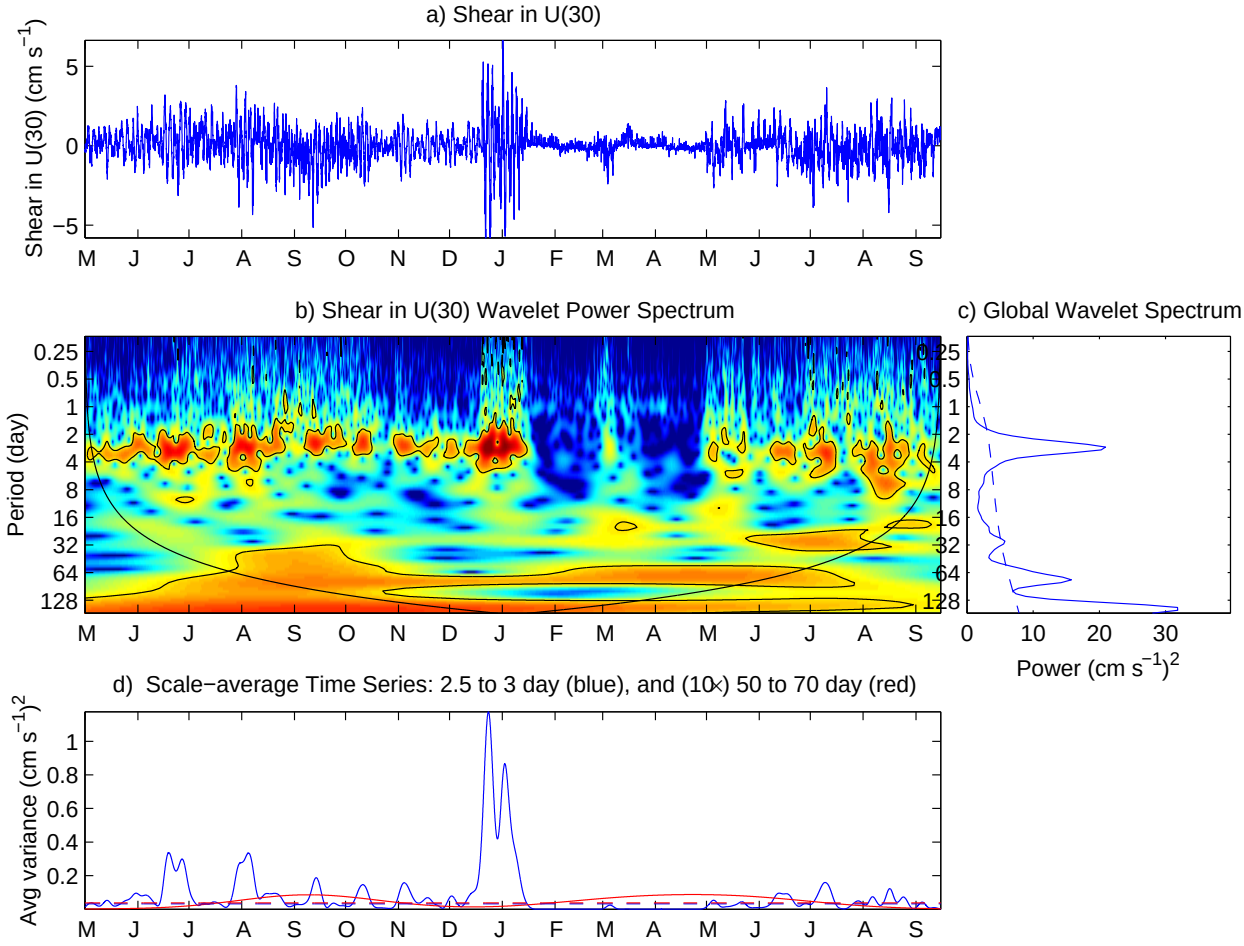

..

Figure A-5: Wavelet analysis of vertical shear of zonal velocity at 30 m. (a) The shear time series, divided by its standard deviation and with the mean removed; (b) the WPS, with period in days on the vertical axis and time in days on the horizontal axis; (c) the global wavelet spectrum, a time average of the WPS and analog to the more traditional Fourier power spectrum; (d) the average power in two different frequency bands, one having a period of 2.5 to 3 days (near-inertial; blue line) and the other 50 to 70 days (intraseasonal; red line, magnified by a factor of 10).(wavelet-shearN.m)

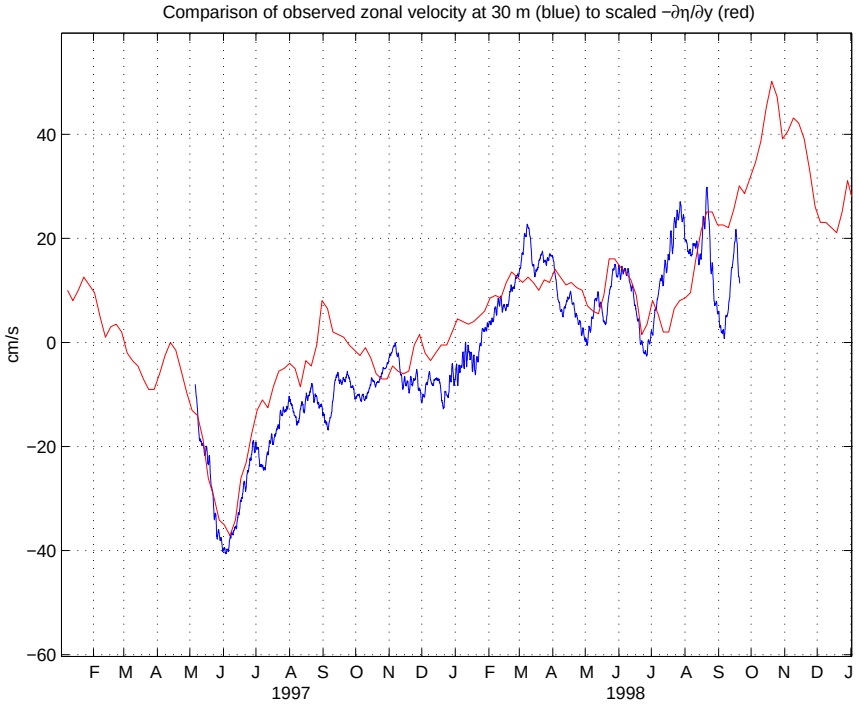

Figure A-6: Comparison of observed low frequency velocity at 30 m (blue line) to (the opposite of) meridional SSH slope. Note that the sea surface slope has been arbitrarily scaled for the comparison.

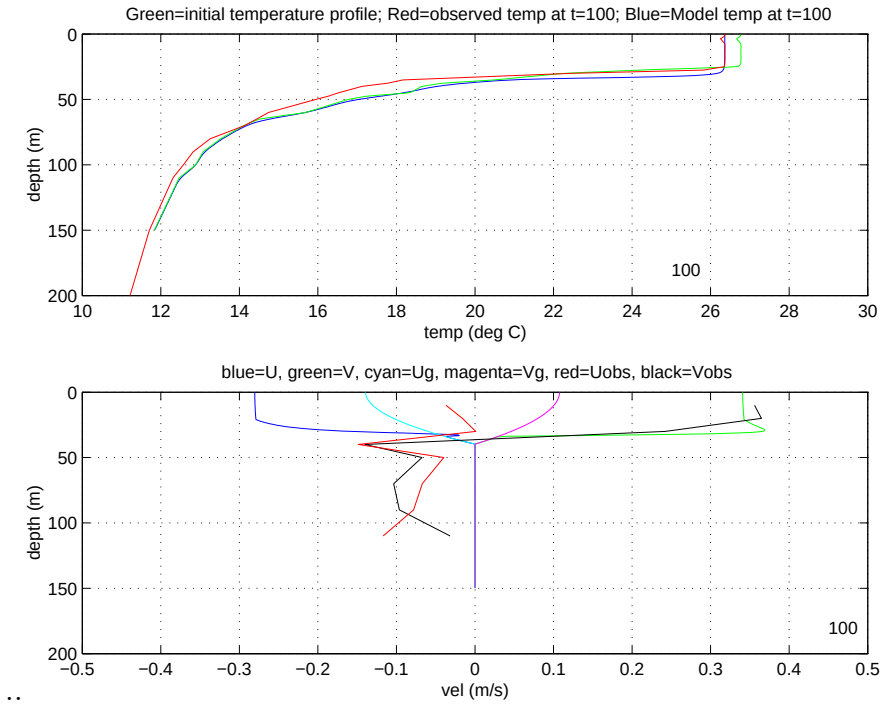

Figure A-7: Example of modelled and observed temperature and velocity profiles 100 hours into a model run. (a) Temperature profiles (red=observed, blue=modelled, green=initialization). The sizable displacement of the thermocline four days after initialization reflects high frequency processes not represented in the model. (b) Velocity profiles. Red and black lines are observed zonal and meridional velocities, respectively. The cyan and magenta lines are the imposed pressure-driven velocities at this particular time. The blue and green lines are the modelled velocity profiles; the mismatch of modelled and observed V (blue and red lines) is due to high frequency motions that are not represented in the model.

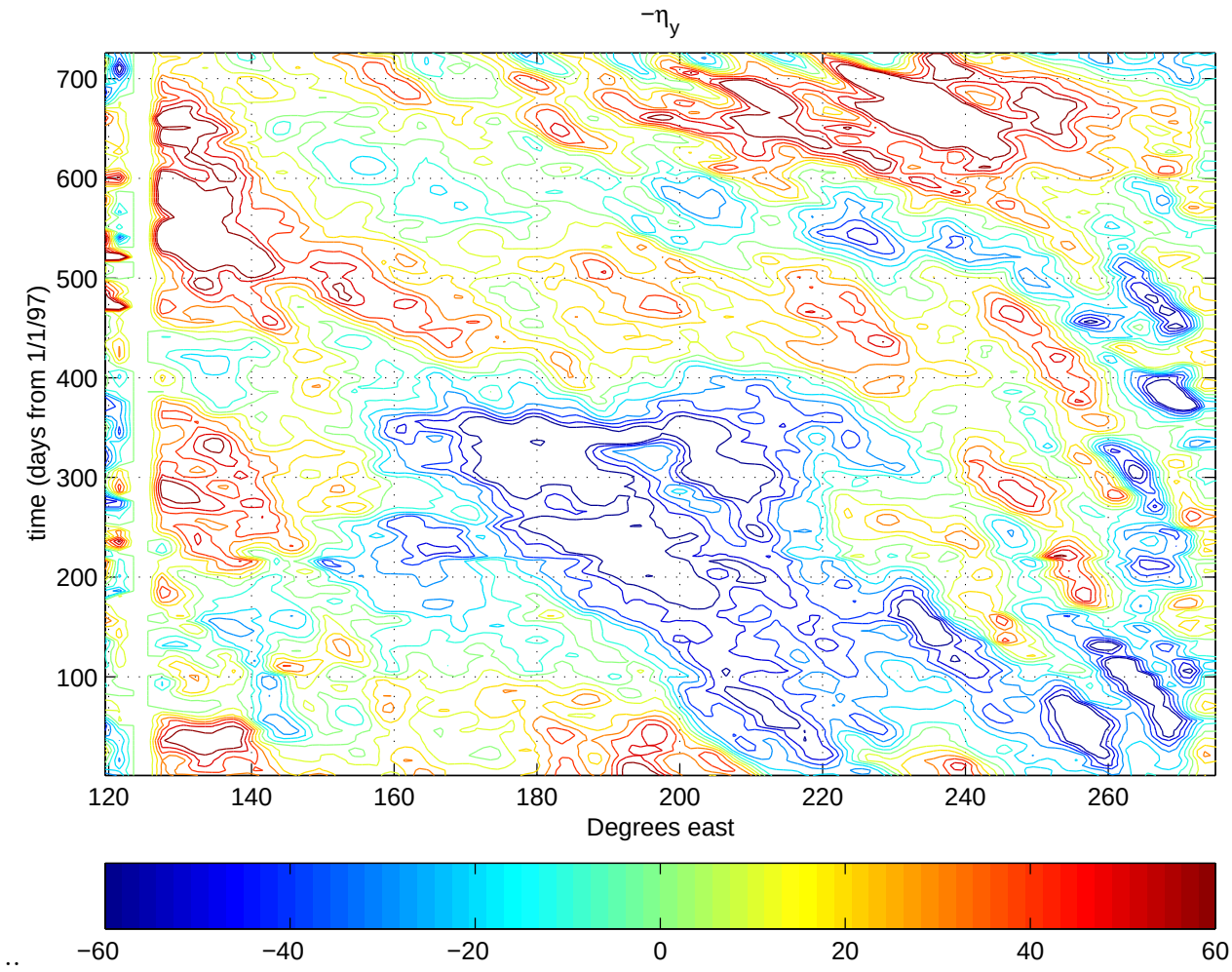

Figure A-8: Longitude-time plot of meridional SSH slope.

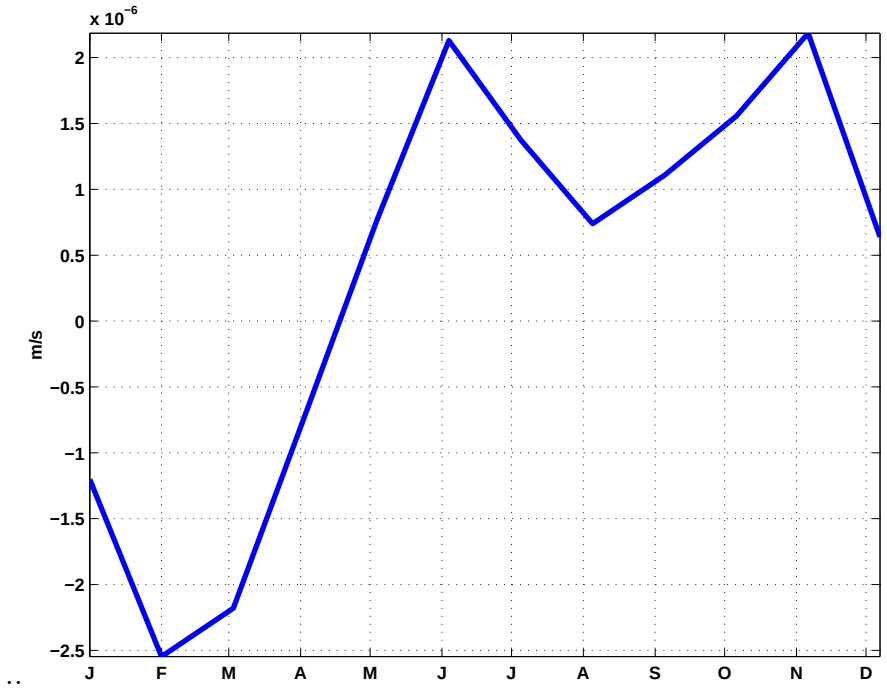

Figure A-9: Climatological Ekman pumping at 10°N, 125°W.

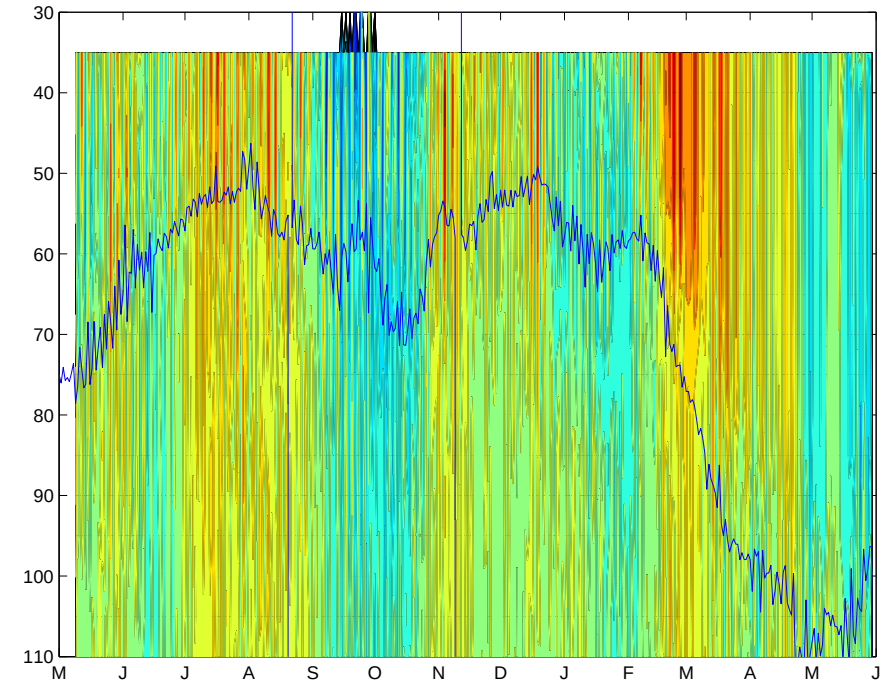

Figure A-10: Meridional velocity at 8n, 125W. The depth of the 20 degree isotherm is shown in blue. (tao8n.m)

Appendix B

Supplementary Analysis

In the thesis, we occasionally made reference to an empirical orthogonal function (EOF) analysis of the observed velocity. In order to avoid disrupting the flow of the thesis with the details of this analysis, we have chosen to include some details of the EOF analysis here rather than in the main body of the text.

Through an empirical orthogonal function (EOF) analysis, we can attempt to statistically separate vertically coherent patterns of variability and identify patterns of variability in the velocity that are not correlated with the wind stress. We computed the complex vertical EOFs of the observed velocity and wind stress using a method similar to that used by Weller and Plueddemann (1996). First we formed a complex matrix from the wind stress and each velocity time series after scaling each time series to have unit variance and removing the mean of each series. Then, the 2D complex EOFs were calculated; we performed the calculation for up to 8 vertical EOFs, but the first few EOFs were relatively unchanged, regardless of the number of EOFs computed. Since the vertical structure of the velocity varies markedly in time, we performed this computation over various time intervals. The first vertical EOF (computed over March through June, 1998)[1]has a relatively small component associated with the wind stress, accounts for 53% of the variance, is fairly unidirectional, and gradually increases from a low value at the thermocline to a maximum value at 20 m depth. The first vertical EOF is shown in figure B-1. The time series

[1]Our intent with this procedure is to identify coherent vertical structure in the velocity record

of wind stress reconstructed using the first EOF is not significantly correlated with the observed wind stress. The corresponding reconstructed time series of velocity are significantly correlated with the observed velocity. For example, the reconstructed time series of meridional velocity at 30 m correlates with the observed signal, having a correlation coefficient of 0.94. Nearly all of the M_2 tidal energy is represented by the first EOF time series. Although EOFs do not necessarily represent physical modes of variability, the vertical structure of the first EOF is consistent with that of a baroclinic signal, having a minimum velocity in the thermocline and increasing toward the surface. Interpretation of the tidal signal as a baroclinic wave is also supported by the rotary autospectra of velocity shown in figure 4-10, in which the power at the M_2 tidal frequency is significantly higher than background levels above the thermocline, but it is not significantly above background levels below the thermocline.

The first EOF time series also has a prominent low frequency signal resembling the observed low frequency signal. For example, the first EOF time series of the meridional velocity correlates with the low-passed meridional velocity with a correlation coefficient of $R_o = 0.84$. Figure B-2 shows the first EOF reconstructed time series of meridional velocity along with the low-pass filtered observed velocity. The low-passed velocity shown has had the mean at each depth removed to facilitate comparison since the mean was removed in computation of the EOFs. One class of low frequency motions that we expect in the upper ocean is Ekman transport, which is forced by the local wind stress and has a depth integrated transport that is to the right of the wind (Ekman, 1905; Weller, 1981; Price et al., 1987). Although the vertical structure of the Ekman flow depends on turbulent processes and is often difficult to determine, we expect a high correlation of the Ekman transport with the local wind stress. Since the first EOF reconstructed time series is vertically unidirectional and not correlated with the local wind stress we surmise that the Ekman transport is not represented

and decide whether this structure is associated with the wind or other forcing. Since the EOF is a statistical tool, we cannot expect physically meaningful results if the time series are not somewhat statistically stationary. This particular time period was chosen because it is a time when the mixed layer and thermocline depths were relatively constant. This choice was motivated by the desire to avoid the abrupt change in velocity characteristics that would be expected if the thermocline moved past a current meter during the time period.

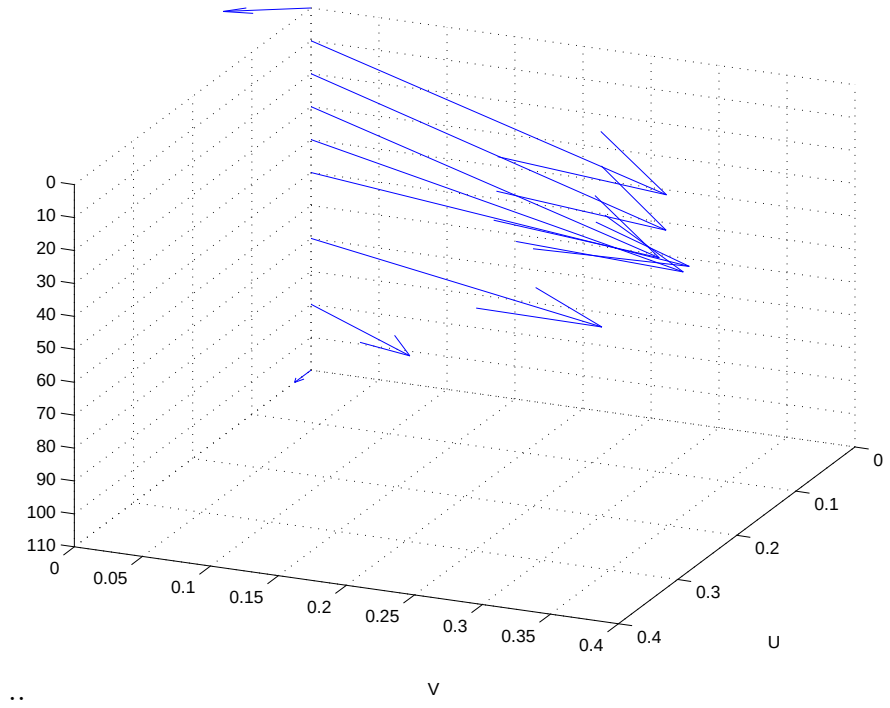

Figure B-1: First complex vertical EOF of velocity. The vertical axis is depth (m). The top arrow represents the wind stress, and lower arrows correspond to current meter depths.

by the first EOF.

All of this suggests that the low frequency velocity signal in the observations and in the first EOF time series is not locally forced by the wind. The vertical structure is consistent with that of a first baroclinic mode wave, and it is reasonable to assume that this low frequency velocity signal that is not correlated with the wind is a large scale, pressure-driven flow. The maximum frequency of low frequency pressure-driven flows is given by $\omega = \beta L_D/2$, where ω is the angular frequency and L_D is the deformation radius (e.g. Gill, 1982, p. 493). Along 10°N, using a first baroclinic deformation radius of about one degree longitude (Chelton et al., 1998), this frequency corresponds to a period of about 59 days for first mode baroclinic motions. This frequency is close to the observed 60 day signal seen in the first EOF and in the observed velocity. The frequency of the observed low frequency signal is consistent with the interpretation of this signal as being a result of the large scale pressure field, though the wavelet spectrum shows that the period drifts toward a

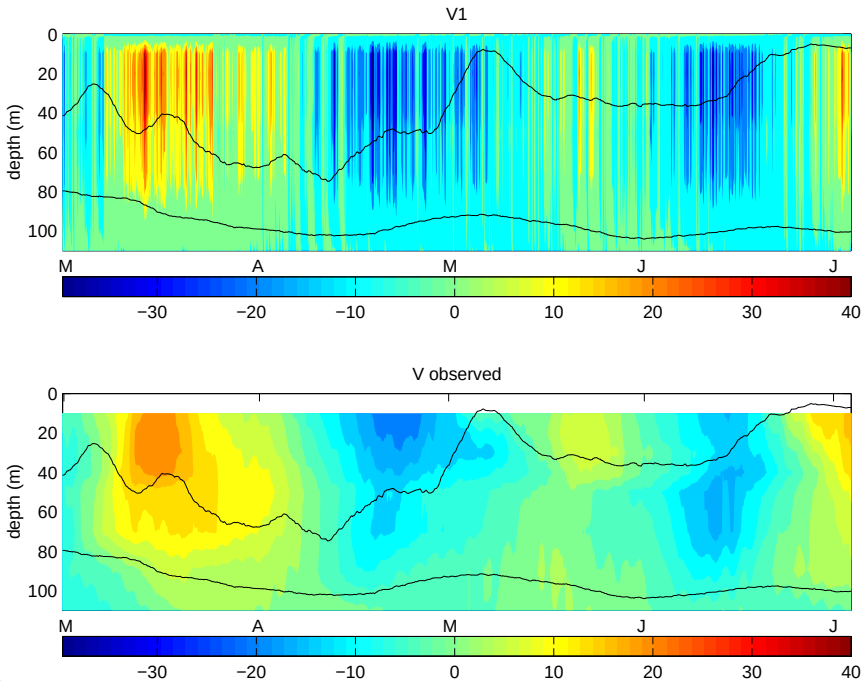

Figure B-2: Top panel: first EOF reconstructed time series. Bottom panel: low-pass filtered observed meridional velocity.

value that is somewhat lower (i.e. 50 days) than we might expect for a first mode baroclinic wave. Still, the thermocline was anomalously deep during this time, and if the deformation radius were about 25% larger than the value given by Chelton et al. (1998), then the minimum period for low frequency first baroclinic mode motions is about 47 days at this latitude.

Appendix C

Additional Evidence

There is additional evidence for some of the conclusions presented in this thesis, but this evidence was not presented in the main body of the thesis because we found it less amenable to unambiguous interpretation. Here, we present some of this evidence.

In section 4.2.2, we argued that the dominant variability in zonal sea surface slope at the site was consistent with the dispersion relation of first mode baroclinic Rossby waves. From spectral analysis of the sea surface slope, we estimated the dominant period to be about 60 days and the dominant (zonal) wavelength to be about 7 degrees of longitude. The signal-to-noise ratio of the sea surface slope was too low to allow direct comparison of the observed meridional velocity signal to the sea surface slope, but we argued that the low frequency meridional velocity signal should be attributed to the dominant Rossby waves because the frequency of the observed velocity signal was very close to the dominant frequency in zonal sea surface slope. Some signs of these waves are detectable in satellite SST fields, particularly during the early months of 1998 when the velocity signal at the mooring site was strong, and these allow an independent, if rough, estimate of the wavelength of the signal seen at the mooring. However, as we have seen, the SST field can be affected by many factors; for example, during a period of low winds, the SST signal associated with the waves may be overwhelmed by the local heating. The various competing influences on SST complicate inferences about the Rossby waves from the SST field. Moreover, the specific reasons that the wave signal can be detected at all in the SST field are not

obvious. Some possible reasons for this signal are north-south advection across the eastern Pacific warm pool boundary by the waves or vertical mixing associated with the vertical shear caused by the waves. Both probably contribute to the wavelike signal that we see in the SST field; we have argued that the vertical turbulent heat flux is important, and we saw in the heat budget that there are (relatively small) deviations from a balanced budget associated with the oscillating meridional velocity signal. Regardless, a wavelike signal can be seen near the mooring site during the first half of 1998, and this signal has a wavelength between 5 and 10 degrees of longitude. Another interesting corroboration of the wavenumber-frequency estimate presented in section 4.2.2 involves the meridional wave number. We did not find any evidence that the meridional wave number was different from zero. In other words, the observed signal (both in velocity and sea surface slope) seemed consistent with interpretation as a plane wave. The fact that the wave-like deformation of the SST front appears coherent over a latitudinal span of 10° or more is also consistent with this interpretation (e.g. compare the blue-light blue interface with the light blue-yellow interface west of the mooring during, say, January).

In the upper ocean heat budget presented in section 4.2.3, we mentioned that a data-assimilating GCM which did a good job of reproducing the observed motion of the thermocline also lent support to the notion that horizontal advection is of secondary importance at the mooring site. The data-assimilating GCM that we were referring to is a Kalman filter assimilating model developed at NASA's Jet Propulsion Laboratory (JPL). The assimilation scheme uses SSH and available *in situ* temperature, salinity, and velocity measurements to constrain and refine errors in the forcing fields. (The PACS data was not included in the assimilation.) The physical and numerical model used is an adaptation of the MIT-GCM discussed briefly in chapter 5. In effect, the assimilation scheme adjusts the forcing fields (primarily wind at this point) to allow the model to evolve in a way that is consistent with both the model physics and the assimilated observations. The model uses NCEP reanalysis forcing fields (like the unconstrained model run shown in chapter 5), and we have seen that the NCEP wind stress does not compare very well with the actual wind stress at

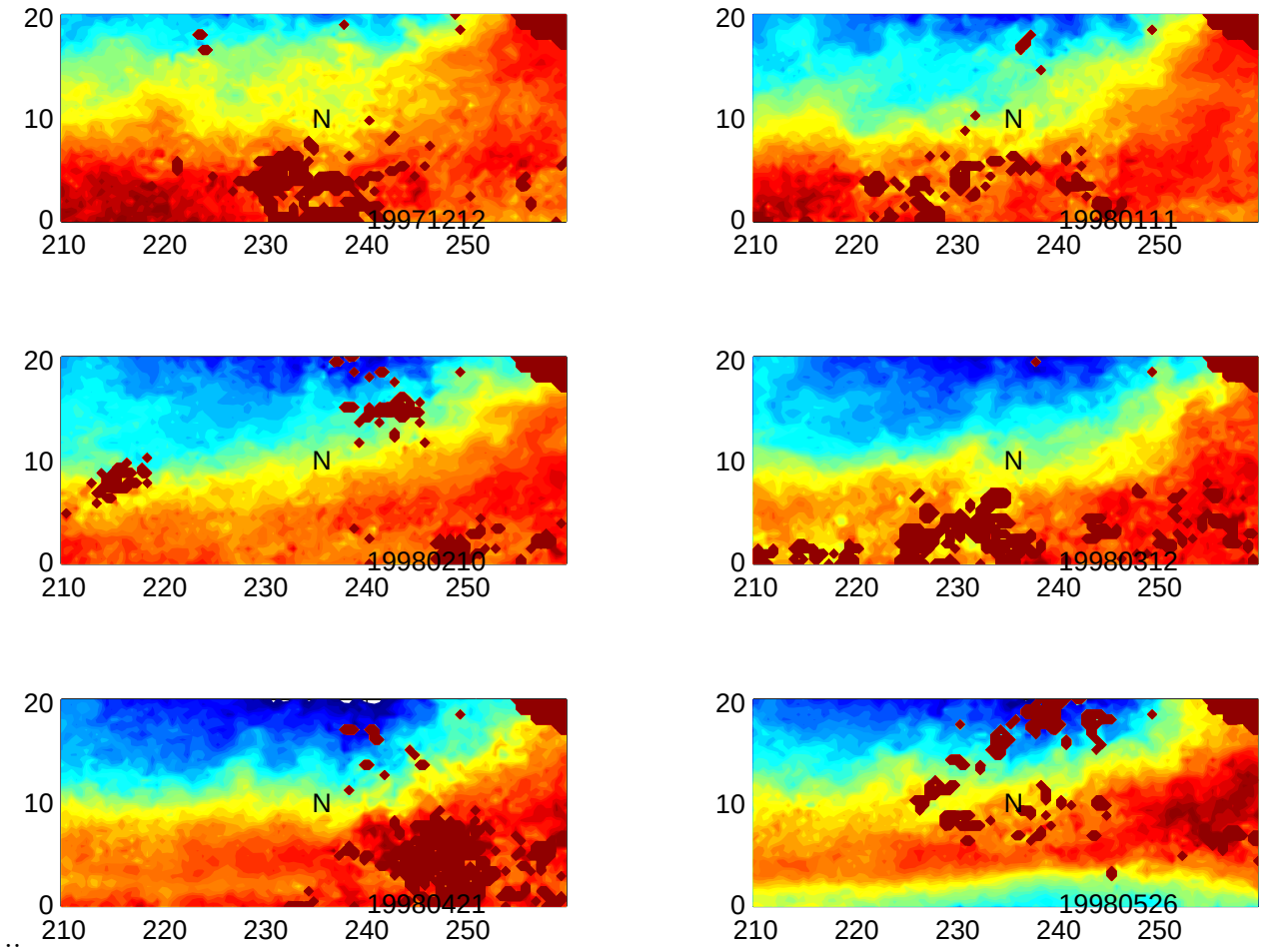

Figure C-1: WOCE satellite SST at times about a month apart during late 1997 and early 1998. Note the cooling between December and January and the presence of disturbances with $\lambda \approx 7^\circ$ on/near the SST front. The patches of dark red mark land or areas that were obscured by clouds during the measurement period.

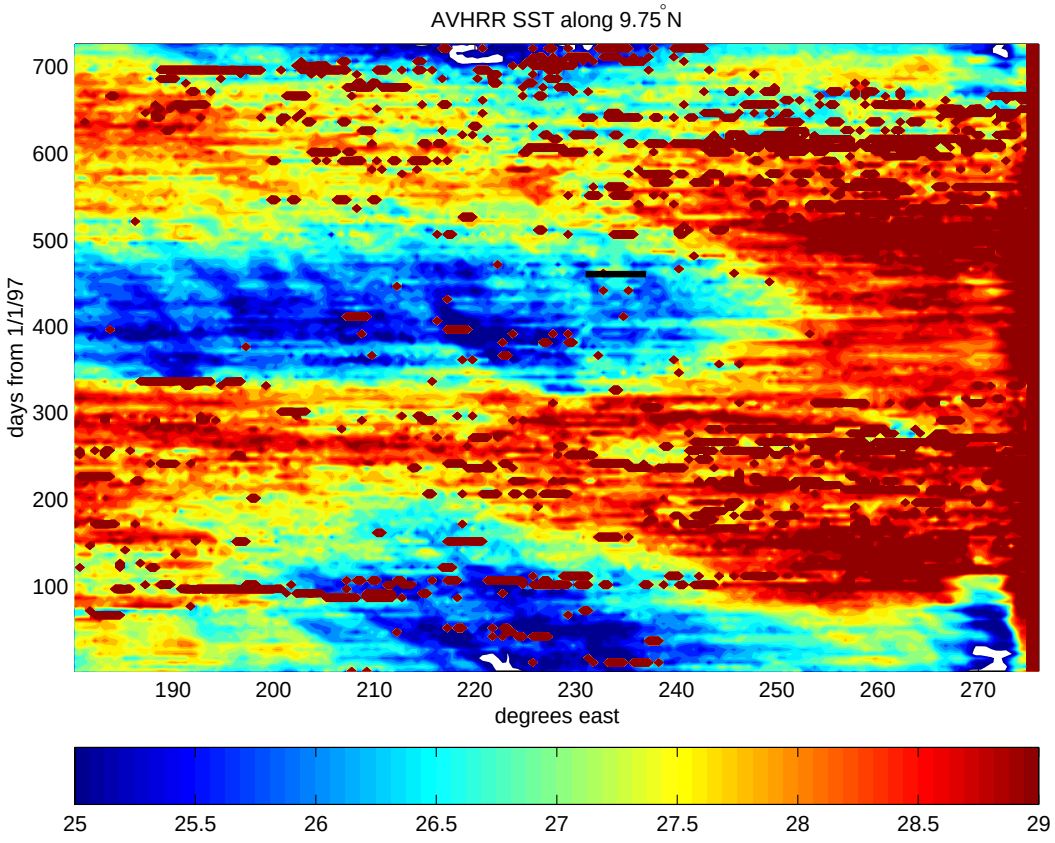

Figure C-2: Longitude-time plot of WOCE satellite SST during 1997 and 1998. The horizontal black line roughly marks the mooring location ($235°E = 125°W$) and has a horizontal extent of 7°. Note the zonally coherent cooling near the end of December and the presence of westward propagating disturbances with $\lambda \approx 7°$ in early 1998.

the buoy. So, it does seem reasonable that the assimilation scheme should assign a high uncertainty to the forcing, as these fields are probably less reliable than the SSH and *in situ* measurements. The top panel of figure C-3 shows the upper ocean temperature in the JPL Kalman filter assimilation at 10°N, 125°W during the 1997 and 1998. Here, we can see that the assimilated model represents the observed thermal evolution at the site much more realistically than the unconstrained model (figure 5-1). The lower panel shows the time and depth integrated heat budget computed by direct diagnosis of the model output for three different treatments: (1) full 3D advection, (2) horizontal advection only, and (3) vertical advection only. Clearly, the assimilated model supports the notion that horizontal heat flux played a secondary role in the thermal evolution at the mooring site.

While it is possible that the JPL assimilated model exhibited the proper thermal structure for the wrong reasons, it is interesting to note that the JPL model gave large positive diapycnal vertical velocities (i.e. w^*) at the time of the most rapid deepening of the thermocline. The peak value of w^* in the JPL model is quantitatively consistent with the peak value presented in section 5.5. Peak values of w^* in the two models are within 10^{-8} m/s of 7.55×10^{-6} m/s and the two peaks occur simultaneously as far as can be determined from the 10-day GCM output interval. Figure C-4 shows the diapycnal vertical velocity across an isopycnal roughly corresponding to the 19°C isotherm, diagnosed as in section 5.5 (except that horizontal advection was included here). We can see that the model showed a substantial diapycnal velocity beginning near the first of 1998. The direction of this diapycnal velocity (i.e. positive) is such as to deepen the thermocline. Another interesting feature of the cross-isopycnal velocity longitude-time plot is the apparent presence of westward propagating signals. Based on the analysis presented in the present study, we might expect a westward propagating signal similar to the Rossby wave signal that makes the dominant contribution to the low frequency meridional velocity field. However, it is not clear that we could assign a specific wavelength to the propagating signals in figure C-4; if anything, they look as if they might have a wavelength slightly longer than the expected 6 or 7 degrees, perhaps double that. Nonetheless, the apparent propagation speed of

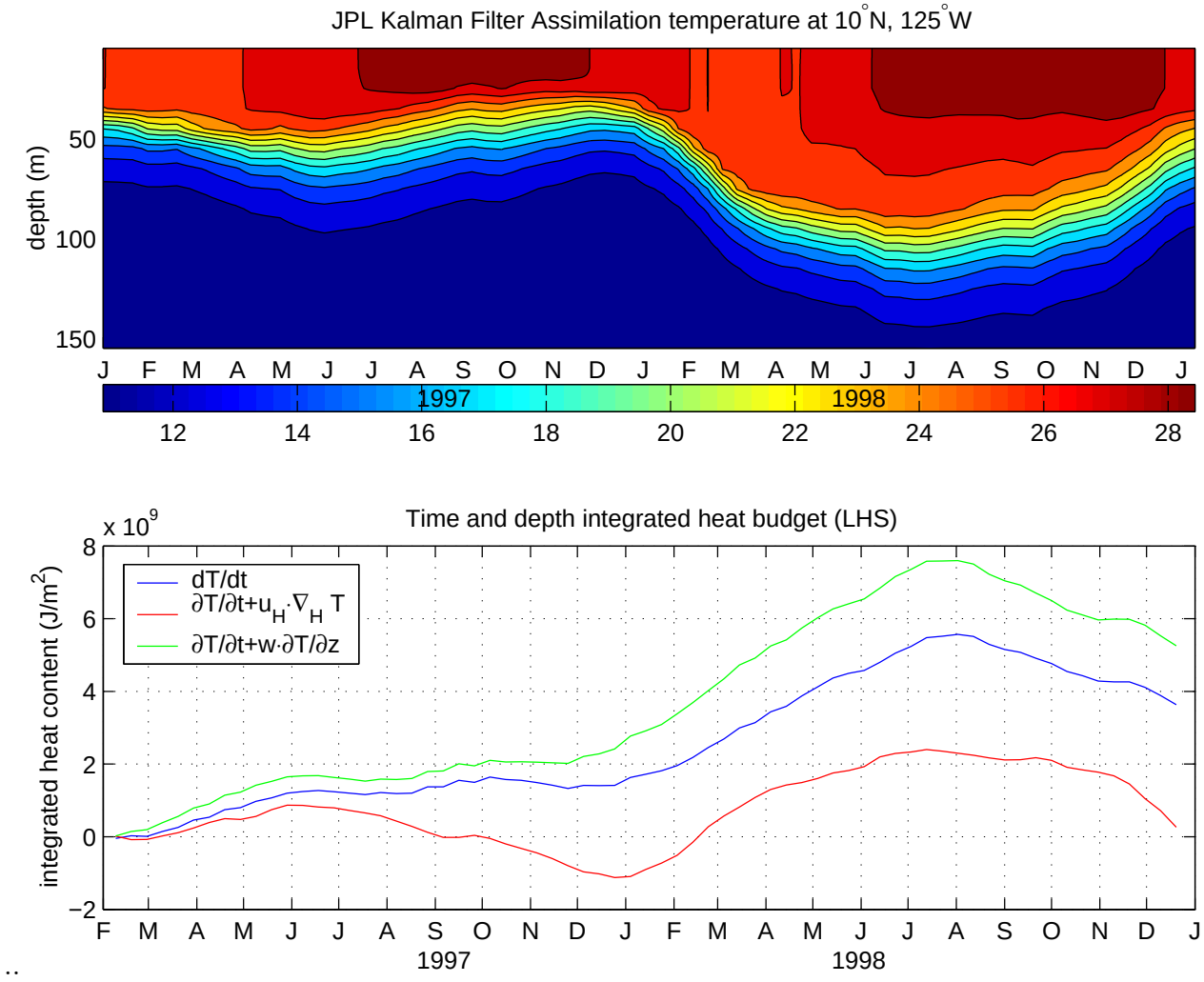

Figure C-3: Upper panel: Temperature structure at 10°N, 125°W in the JPL Kalman Filter data assimilating model. Note that the temperature evolution agrees fairly well with the observations. Lower panel: Terms in the time and depth integrated heat budget; complete heat budget (blue line), budget computed using only horizontal advection (red line), and budget computed using only vertical advection (green line). Here, note that the budget that incorporates only vertical advection is closer to the full budget than the one that uses only horizontal advection; this corroborates our claim that horizontal advection is of secondary importance.

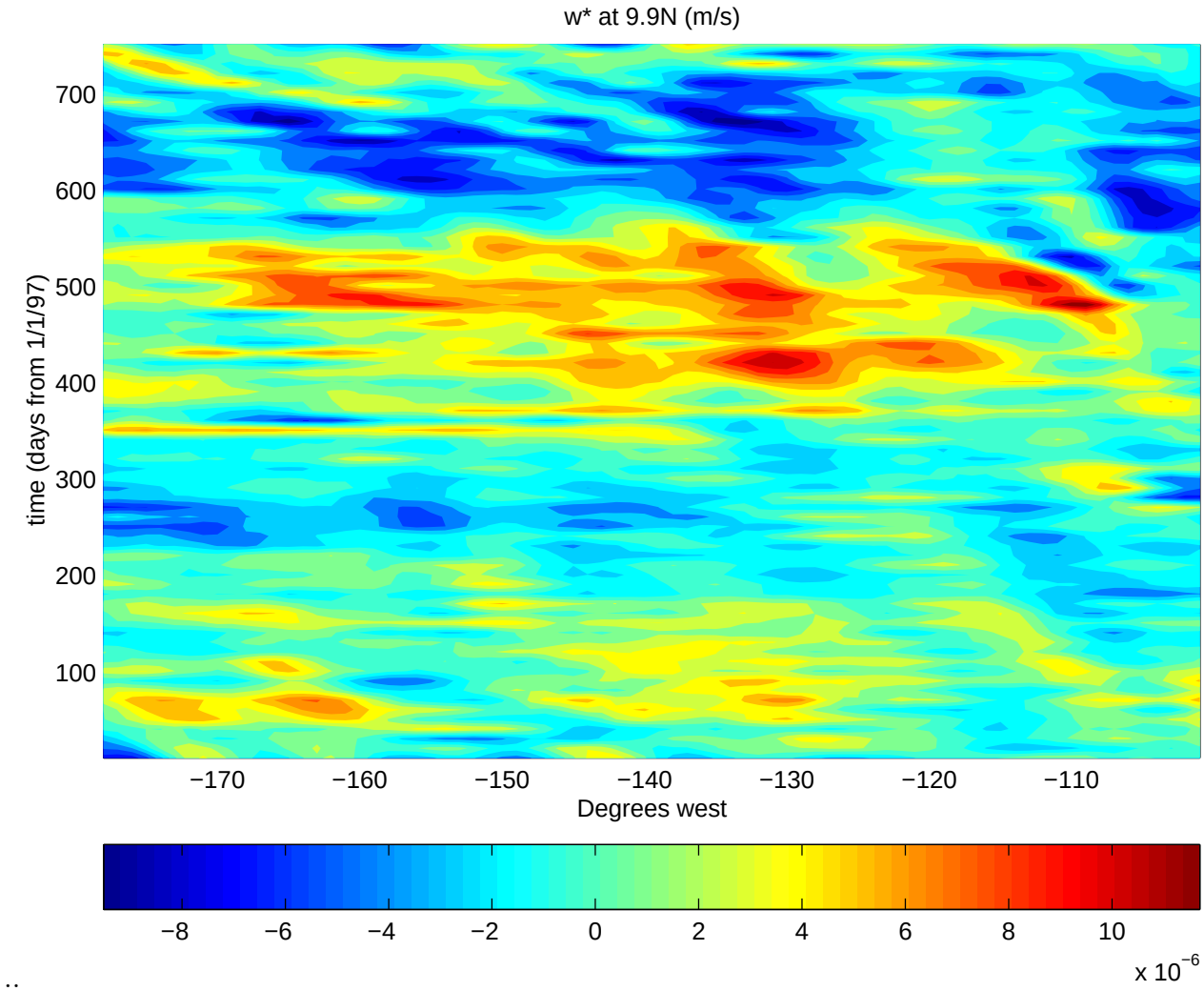

..

Figure C-4: Cross isopycnal velocity diagnosed from the JPL KF GCM.

these signals is slower than the long wave phase speed, and the wavelengths do not appear to approach the long wave limit. (Recall that wavelengths longer than 20° are effectively in the long wave limit). This suggests that these signals may be associated with intermediate wavelength (i.e. high frequency) baroclinic Rossby waves, which have a relatively large velocity signal.

Bibliography

[1] H.D.I. Abarbanel, D.D. Holm, L.E. Marsden, and T.S. Ratiu. Nonlinear stability analysis of stratified fluid equillibria. *Phil. Trans. Roy. Soc. London.*, pages 349–409, 1986.

[2] G. Alory and T. Delcroix. Interannual sea level changes and associated mass transports in the tropical Pacific from TOPEX/Poseidon data and linear model results (1964-1999). *J. Geophys. Res.*, 100:doi:10.1029/2001JC001067, 2002.

[3] D.L.T. Anderson and A.E. Gill. Spin-up of a stratified ocean, with apllications to upwelling. *Deep Sea Res.*, 22:583–596, 1975.

[4] S.P. Anderson, K. Huang, N.J. Brink, M.F. Baumgartner, and R.A. Weller. Pan American Climate Study data report. Technical report, Woods Hole Oceanographic Institution, Technical Report 2000-03, Woods Hole, MA, 2000.

[5] S.P. Anderson, R.A. Weller, and R.B. Lukas. Surface buoyancy forcing of the mixed layer of the Western Pacific Warm Pool: Observations and 1D model results. *J. Climate*, 9:3056–3085, 1996.

[6] A.G. Barnston, M.H. Glantz, and Y. He. Predictive skill of statistical and dynamical climate models in SST forecasts during the 1997-98 El Niño episode and the 1998 La Niña onset. *Bull. Amer. Meteor. Soc.*, 80:217–243, 1999.

[7] K.E. Brainerd and M.C. Gregg. Surface mixed and mixing layer depths. *Deep Sea Res.*, 42:1521–1543, 1995.

[8] M.A. Cane. A role for the tropical Pacific. *Science*, 282:59–60, 1998.

[9] C. Cassou and C. Perigaud. ENSO simulated by intermediate coupled models and evaluated with observations over 1970-98. Part II: role of off-equatorial ocean and meridional winds. *J. Climate*, 13:1635–1663, 2000.

[10] P. Chang and S.G. Philander. A coupled ocean-atmosphere instability of relevance to the seasonal cycle. *J. Atmos. Sci.*, 51:3627–3648, 1994.

[11] D.B. Chelton, R.A. DeSzoeke, M.G. Schlax, K. El Naggar, and N. Siwertz. Geographical variability of the first baroclinic Rossby radius of deformation. *J. Phys. Oceanogr.*, 28:433–460, 1998.

[12] D.B. Chelton and M.G. Schlax. Global observations of oceanic Rossby waves. *Science*, 272:234–238, 1996.

[13] E. A. D'Asaro and J. H. Morison. Internal waves and mixing in the arctic ocean. *Deep-Sea Res.*, 39:S459–S484, 1992.

[14] E.A. D'Asaro. The energy flux from the wind to near inertial motions in the surface mixed layer. *J. Phys. Oceanogr.*, 15:1043–1059, 1985.

[15] E.A. D'Asaro. Upper ocean temperature structure, inertial currents, and Richardson numbers observed during strong meteorological forcing. *J. Phys. Oceanogr.*, 15:943–962, 1985.

[16] E.A. D'Asaro, C.C. Eriksen, M.A. Levine, P. Niiler, C.A. Paulson, and P. van Meurs. Upper ocean inertial currents forced by a strong storm, part I: Data and comparisons with linear theory. *J. Phys. Oceanogr.*, 25:2909–2936, 1995.

[17] V.W. Ekman. On the influence of the earth's rotation on ocean-currents. *Arkiv for Matematik, Astronomi och Fisik*, 2:1–52, 1905.

[18] K.A. Emanuel. An air-sea interaction model of intraseasonal oscillations in the tropics. *J. Atmos. Sci.*, 44:2324–2340, 1987.

[19] C.W. Fairall, E.F. Bradley, D.P. Rogers, J.B. Edson, and G.S. Young. Bulk parameterization of air-sea fluxes during TOGA COARE. *J. Geophys. Res.*, 101:3747–3764, 1996.

[20] B.S. Giese, J.A. Carton, and L.J. Holl. Sea level variability in the eastern tropical Pacific as observed by TOPEX and the Tropical Ocean-Global Atmosphere Tropical Atmosphere-Ocean Experiment. *J. Geophys. Res.*, 99:24,739–24,748, 1994.

[21] A. E. Gill. *Atmosphere - Ocean Dynamics*. Academic Press, San Diego, California, 1982.

[22] A.E. Gill, J.S.A. Green, and A.J. Simmons. Energy partition in the large-scale ocean circulation of mid-ocean eddies. *Deep-Sea Res.*, 21:499–528, 1974.

[23] N.E. Graham and T.P. Barnett. Sea surface temperature, surface wind divergence, and convection over tropical oceans. *Science*, 238:657–659, 1987.

[24] W.M. Gray and R.W. Jacobson. Diurnal variation of deep cumulus convection. *Mon. Wea. Rev.*, 105:1171–1188, 1977.

[25] M.C. Gregg. Diapycnal mixing in the thermocline: a review. *J. Geophys. Res.*, 92:5249–5286, 1987.

[26] G. Gu and C. Zhang. Westward-propagating synoptic scale disturbances and the ITCZ. *J. Atmos. Sci.*, 59:1062–1075, 2002.

[27] L. Howard. Note on a paper of John W. Miles. *J. Fluid Mech.*, 10:509–512, 1961.

[28] W.S. Kessler. Observations of long Rossby waves in the northern tropical Pacific. *J. Geophys. Res.*, 95:5183–5217, 1990.

[29] W.S. Kessler. EOF representations of the Madden-Julian Oscillation and its connection with ENSO. *J. Clim*, 14:3055–3061, 2001.

[30] W.S. Kessler. Is ENSO a cycle or series of events? *Geophys. Res. Lett.*, 29:doi:10.1029/2002GL015924, 2002.

[31] W.S. Kessler. Mean three-dimensional circulation in the northeast tropical Pacific. *J. Phys. Oceanogr.*, 32:2457–2471, 2002.

[32] W.S. Kessler, M.J. McPhaden, and K.M. Weickmann. Forcing of intraseasonal Kelvin waves in the equatorial Pacific. *J. Geophys. Res.*, 100:10613–10631, 1995.

[33] W.S. Kessler and B.A. Taft. Dynamic heights and zonal geostrophic transports in the central tropical Pacific during 1979-84. *J. Phys. Oceanogr.*, 17:97–122, 1987.

[34] G.N. Kiladis. Observations of Rossby waves linked to convection over the eastern tropical Pacific. *J. Atmos. Sci.*, 55:321–339, 1998.

[35] G.N. Kiladis and K.M. Weickmann. Circulation anomalies associated with tropical convection during northern winter. *Mon. Wea. Rev.*, 120:1900–1923, 1992.

[36] G.N. Kiladis and K.M. Weickmann. Extratropical forcing of tropical Pacific convection during northern winter. *Mon. Wea. Rev.*, 120:1924–1938, 1992.

[37] C. Koop and F. Browand. Instability and turbulence in a stratified layer with shear. *J. Fluid Mech.*, 93:135–159, 1979.

[38] P.K. Kundu and R.C. Beardsley. Evidence of a critical Richardson number in moored measurements during the upwelling season off northern California. *J. Geophys. Res.*, 96:4855–4868, 1991.

[39] W.G. Large and G.B. Crawford. Observations and simulations of upper-ocean response to wind events during the Ocean Storms Experiment. *J. Phys. Oceanogr.*, 25:2831–2852, 1995.

[40] W.G. Large, J.C. McWilliams, and S.C. Doney. Oceanic vertical mixing: a review and a model with a nonlocal boundary layer parameterization. *Reviews of Geophysics*, 32:363–403, 1994.

[41] W.G. Large and S. Pond. Open ocean momentum flux measurements in moderate to strong winds. *J. Phys. Oceanogr.*, 11:324–336, 1981.

[42] S. Levitus and T. Boyer. Temperature. In *World Ocean Atlas 1994 Volume 4*. NOAA Atlas NESDIS 4, U.S. Department of Commerce, Washington, D.C., 1994.

[43] T. Li. Air-sea interactions of relevance to the ITCZ: Analysis of coupled instabilities and experiments in a hybrid coupled GCM. *J. Atmos. Sci.*, 54:134–147, 1997.

[44] C.E. Lietzke, C. Deser, and T.H. Vonder Haar. Evolutionary structure of the eastern Pacific double ITCZ based on satellite moisture profile retrievals. *J. Climate*, 14:743–751, 2001.

[45] R.E. Livezey, M. Masutani, A. Leetmaa, H. Rui, M. Ji, and A. Kumar. Teleconnective response of the Pacific-North American region atmosphere to large central equatorial Pacific SST anomalies. *J. Climate*, 10:1787–1820, 1997.

[46] R.E. Livezey and T.M. Smith. Covariability of aspects of North American climate with global sea surface temperatures on interannual to interdecadal timescales. *J. Climate*, 12:289–302, 1999.

[47] V. Magaña, J.A. Amador, and S. Medina. The midsummer drought over Mexico and Central America. *J. Climate*, 12:1577–1588, 1999.

[48] G.O. Marmorino and C.L. Trump. 'Turbulent mixing' induced by upgoing near-inertial waves in the seasonal thermocline of the Norwegian Sea. *J. Geophys. Res.*, 96:7137–7143, 1991.

[49] G. McKinley, Follows M.J., and J. Marshall. Interannual variability of the air-sea flux of oxygen in the North Atlantic. *Geophys. Res. Lett.*, 27:2933–2936, 2000.

[50] M.J. McPhaden. The child prodigy of 1997-98. *Nature*, 398:559–562, 1999.

[51] M.J. McPhaden. Climate oscillations- Genisis and evolution of the 1997-98 El Niño. *Science*, 283:950–954, 1999.

[52] M.J. McPhaden and coauthors. Tropical Ocean Global Atmosphere (TOGA) observing system: a decade of progress. *J. Geophys. Res.*, 103:14169–14240, 1998.

[53] C.S. Meinen and M.J. McPhaden. Observations of warm water volume changes in the equatorial Pacific and their relationship to El Niño and La Niña. *J. Climate.*, 13:3551–3559, 2000.

[54] C.S. Meinen and M.J. McPhaden. Interannual variabilty in warm water volume transports in the equatorial Pacific during 1993-99. *J. Phys. Oceanogr.*, 31:1324–1345, 2001.

[55] G. Meyers. On the annual Rossby wave in the tropical North Pacific Ocean. *J. Phys. Oceanogr.*, 9:663–674, 1979.

[56] J. Miles. On the stability of heterogeneous shear flows. *J. Fluid Mech.*, 10:496–508, 1961.

[57] L. Miller, D.R. Watts, and M. Wimbush. Oscillations of dynamic topography in the eastern Pacific. *J. Phys. Oceanogr.*, 15:1759–1770, 1985.

[58] T.P. Mitchell and J.M. Wallace. The annual cycle in equatorial convection and sea surface temperature. *J. Climate*, 5:1140–1156, 1992.

[59] D.L. Montroy. Linear relationship of central and eastern North American precipitation to tropical Pacific sea surface temperature anomalies. *J. Climate.*, 10:541–558, 1997.

[60] W.M. Ostrom, B.S. Way, S.P. Anderson, B. Jones, E. Key, and G. Yuras. Pan American Climate Study, Mooring Recovery Cruise Report, *R/V Melville*, cruise number PACS03MV. Technical report, Woods Hole Oceanographic Institution, Technical Report 99-01, Woods Hole, MA, 1999.

[61] J. Pedlosky. *Geophysical Fluid Dynamics*. Springer-Verlag, New York, NY, 1987.

[62] C. Perigaud. Sea level oscillations observed with Geosat along the two shear fronts of the North Equatorial Counter Current. *J. Geophys. Res.*, 95:7239–7248, 1990.

[63] C. Perigaud, C. Cassou, B. DeWitte, and L.-L. Fu. Using data and intermediate coupled models for seasonal-to-interannual forecasts. *Mon. Wea. Rev.*, 128:3026–3049, 2000.

[64] C. Perigaud, F. Melin, and C. Cassou. Enso simulated by intermediate coupled models and evaluated with observations over 1970-98. Part I: role of off-equatorial variability. *J. Climate*, 13:1605–1634, 2000.

[65] S.G.H. Philander. Instabilities of zonal equatorial currents. *J. Geophys. Res.*, 81:3725–3735, 1976.

[66] R.A. Pielke and C.N. Landsea. La Nina, El Niño, and Atlantic hurricane damages in the United States. *Bull. Am. Met. Soc.*, 80:2027–2033, 1999.

[67] K. Polzin. Statistics of the Richardson number: mixing models and finestructure. *J. Phys. Oceanogr.*, 26:1409–1425, 1996.

[68] J.F. Price, R.A. Weller, and R. Pinkel. Diurnal cycling: observations and models of the upper ocean response to diurnal heating, cooling, and wind mixing. *J. Geophys. Res.*, 91:8411–8427, 1986.

[69] J.F. Price, R.A. Weller, and R.R. Schudlich. Wind-driven ocean currents and Ekman transport. *Science*, 238:1534–1538, 1987.

[70] WOCE Product. Mean surface wind fields from the ERS-AMI and ADEOS-NSCAT microwave scatterometers, August 1991 to May 2000. In *WOCE Global Data, Version 2.0, CD ROM*. WOCE International Project Office, Southampton, UK, 2001.

[71] C.F. Ropelewski and M.S. Halpert. North American precipitation and temperature patterns associated with the El Niño/ Southern Oscillation (ENSO). *Mon. Wea. Rev.*, 114:2352–2362, 1986.

[72] C.F. Ropelewski and M.S. Halpert. Precipitation patterns associated with the high index phase of the Southern Oscillation. *J. Climate*, 2:268–284, 1989.

[73] C.F. Ropelewski and M.S. Halpert. Quantifying the Southern Oscillation-precipitation relationships. *J. Climate*, 9:1043–1059, 1996.

[74] P.M. Saunders. The temperature at the ocean-air interface. *J. Atmos. Sci.*, 24:269–273, 1967.

[75] R.S. Schudlich and J. F. Price. Diurnal cycles of current, temperature, and turbulent dissipation in a model of the equatorial upper ocean. *J. Geophys. Res.*, 97:5409–5422, 1992.

[76] J. Scinocca. The mixing of mass and momentum by Kelvin-Helmholtz billows. *J. Atmos. Sci.*, 52:2509–2530, 19945.

[77] T. Shinoda and H.H. Hendon. Mixed layer modeling of intraseasonal variability in the tropical western Pacific and Indian Oceans. *J. Climate*, 11:2668–2685, 1998.

[78] T. Shinoda, H.H. Hendon, and J. Glick. Intraseasonal variability of surface fluxes and sea surface temperature in the tropical western Pacific and Indian Oceans. *J. Climate*, 11:1685–1702, 1998.

[79] J. Shukla. Predictability in the midst of chaos: A scientific basis for climate forecasting. *Science*, 282:728–730, 1998.

[80] S.D. Smith. Coefficients for sea surface wind stress, heat flux, and wind profiles as a function of wind speed and temperature. *J. Geophys. Res.*, 93:15467–15472, 1988.

[81] S.R. Smith and J.J. O'Brien. Regional snowfall distributions associated with ENSO: Implications for seasonal forecasting. *Bull. Am. Met. Soc.*, 82:1179–1191, 2001.

[82] W.D. Smyth and K.B. Winters. Turbulence and mixing in Holmboe waves. *J. Phys. Oceanogr.*, 33:694–711, 2003.

[83] E. Strang and H. Fernando. Entrainment and mixing in stratified shear flows. *J. Fluid Mech.*, 428:349–386, 2001.

[84] S. Thorpe. Turbulence in stably stratiefied fluids: A review of laboratory experiments. *Boundary-Layer Meteor.*, 5:95, 1973.

[85] C. Torrence and G.P. Compo. A practical guide to wavelet analysis. *Bull. Am. Met. Soc.*, 79:61–78, 1998.

[86] C. Torrence and P.J. Webster. Interdecadal changes in the ENSO-Monsoon system. *J. Climate*, 12:2679–2690, 1999.

[87] R.P. Trask, R.A. Weller, W.M. Ostrom, and B.S. Way. Pan American Climate Study, Mooring Recovery and Deployment Cruise Report, *R/V Thomas Thompson*, cruise number 73. Technical report, Woods Hole Oceanographic Institution, Technical Report 98-18, Woods Hole, MA, 1998.

[88] C. Wang and R.H. Weisberg. The 1997-98 El Niño evolution relative to previous El Niño events. *J. Climate*, 13:488–501, 2000.

[89] B.S. Way, W.M. Ostrom, R.A. Weller, J.D. Ware, R.P. Trask, R. Cole, and J. Donovan. Pan American Climate Study, Mooring Deployment Cruise Report, *R/V Roger Revelle*, cruise number Genesis 4. Technical report, Woods Hole Oceanographic Institution, Technical Report 98-07, Woods Hole, MA, 1998.

[90] R.A. Weller. Observations of the velocity response to wind forcing in the upper ocean. *J. Geophys. Res.*, 86:1969–1977, 1981.

[91] R.A. Weller, S.A. Baumgartner, S.A. Josey, A.S. Fischer, and J.C. Kindle. Atmospheric forcing in the Arabian Sea during 1994-1995: observations and comparisons with climatology and models. *Deep Sea Research II*, 45:1961–1999, 1998.

[92] R.A. Weller, F. Bradley, and R. Lukas. The interface or air-sea flux compontent of the TOGA Coupled Ocean-Atmosphere Response Experiment and its impact on subsequent air-sea interaction studies. *Manuscript submitted to J. Atmos. Ocean. Tech.*, 2003.

[93] R.A. Weller and R.E. Davis. A vector measuring current meter. *Deep Sea Res.*, 27, 1980.

[94] R.A. Weller and A.J. Plueddemann. Observations of the vertical structure of the oceanic boundary layer. *J. Geophys. Res.*, 101:8789–8806, 1996.

[95] W.B. White. Annual forcing of baroclinic long waves in the tropical north Pacific Ocean. *J. Phys. Oceanogr.*, 7:50–61, 1977.

[96] K. Wyrtki. Equatorial currents in the pacific 1950 to 1970 and their relations to the trade winds. *J. Phys. Oceanogr.*, 4:372–380, 1974.

[97] K. Wyrtki. Sea level during the 1972 El Niño. *J. Phys. Oceanogr.*, 7:779–787, 1977.

[98] K. Wyrtki. The response of sea surface topography during the 1976 El Niño. *J. Phys. Oceanogr.*, 9:1223–1231, 1979.

[99] X. Zang, L.-L. Fu, and C. Wunsch. Observed reflectivity of the western boundary of the equatorial Pacific Ocean. *J. Geophys. Res.*, 107, 2002.

[100] X. Zang and C. Wunsch. The observed dispersion relationship for North Pacific Rossby wave motions. *J. Phys. Oceanogr.*, 29:2183–2190, 1999.

[101] R. Zhang and S. Levitus. Interannual variability of the coupled tropical Pacific ocean-atmosphere system associated with the El Niño-Southern Oscillation. *J. of Climate.*, 10:1312–1330, 1997.